



TECHNISCHE
UNIVERSITÄT
WIEN



Dissertation

Investigation of Multi-Photon Processing Parameters and Materials

carried out for the purpose of obtaining the degree of Doctor technicae (Dr. techn.),
submitted at TU Wien, Faculty of Mechanical and Industrial Engineering, by

Dipl.-Ing. Wolfgang Steiger

Mat.Nr.: 00754329

under the supervision of

Univ.Prof. Dipl.-Phys. Dr. Aleksandr Ovsianikov
Institute of Materials Science and Technology, E308

reviewed by

Univ.Prof. Dipl.-Ing. Dr.mont. Jürgen Stampfl
Institute of Materials Science and Technology, TU Wien

Prof. Vygantas Mizeikis, PhD
Dept. of Electronics and Materials Science, Shizuoka University

This work was supported by the European Research Council within the framework of the projects Laser-engineered Biomimetic Matrices with Embedded Cells (ERC Starting Grant Nr. 307701) and Photo-Hydrogels (FWF, Proj. Nr. I2444 N28).

I confirm, that going to press of this thesis needs the confirmation of the examination committee.

Affidavit

I declare in lieu of oath, that I wrote this thesis and performed the associated research myself, using only literature cited in this volume. If text passages from sources are used literally, they are marked as such. I confirm that this work is original and has not been submitted elsewhere for any examination, nor is it currently under consideration for a thesis elsewhere.

Signature

Abstract

Multi-photon polymerization is a microfabrication and nanofabrication technology with a rapidly growing field of applications. It is based on the simultaneous absorption of two or more photons to excite a molecule to an energy state higher than the energy of the individual photons. This phenomenon was initially seen as a scientific curiosity with limited practical applications. Due to the advancement of ultrashort pulsed lasers, this phenomenon has been employed for stereolithographic methods such as 2-photon polymerization (**2PP**). By tightly focusing a pulsed laser into photosensitive resin, arbitrary 3-dimensional (**3D**) structures with feature resolution of a few hundred nanometers can be produced. Compared to conventional additive manufacturing (**AM**) technologies, 2PP can produce intricate geometries within the resin without the need to deposit new material in a layer-by-layer fashion. Its unrivaled spatial resolution allows the production of microscaffolds which are of interest for biomedical applications.

This thesis presents a comprehensive study of parameters governing 2PP and materials for tissue engineering. To render 2PP of interest for *in vivo* applications requires high processing speeds. However, the resolution of 2PP creates a major bottleneck, as the fabrication time is significantly higher than for conventional AM methods. In addition, most photoinitiators (**PIs**) used for 2PP require long exposure times to initiate polymerization, leading to slower scanning speeds. In an initial step, a z-scan setup was developed, capable of characterizing the 2-photon absorption (**2PA**) in a wide spectral range. This allowed the screening of newly synthesized PIs and the determination of the peak absorption wavelength. Matching the wavelength used for 2PP to the maximum 2PA absorption, significantly improved the performance of the 2PP system and allowed to increase the writing speed. As a thorough understanding of the material performance at higher writing speeds is essential when upscaling the fabrication process, a closer examination of the required laser power for polymerization (P_{th}) for fabrication speeds up to 100 mm s^{-1} was carried out. From the results, it was concluded that for these fabrication speeds, P_{th} was significantly lower than predicted by the established model. It was therefore possible, to increase the scanning speed, without exceeding the available laser power.

Recently, 2PP was proposed as a third strategy in tissue engineering to bridge two distinct trends. This synergetic approach aims to load highly porous microscaffolds with dense cell spheroids. Based on the principle of self assembly multiple scaffolds are able to fuse and create tissue while the 3D-scaffolds provide initial mechanical support. Materials processable with 2PP, that exhibit these properties, are based on glass like matrices, which cannot be degraded by the body, limiting the natural remodeling capacity of the tissue. In this work, polymers based on biodegradable polycaprolactone (**PCL**) were studied to produce biocompatible scaffolds.

The versatility of 2PP for biomedical applications was demonstrated in two studies. Microcages were produced to trap neurons using standing Faraday waves. Lastly, microscaffolds for hair implants were produced, which successfully induced the growth of human hair follicles from human induced pluripotent stem cells (**hi-PSC**). The fast production of highly detailed, biodegradable microscaffolds via 2PP showcases the tremendous potential of this technology for tissue engineering.

Kurzfassung

Multi-Photonen Polymerisation ermöglicht die Produktion hochauflösender dreidimensionaler (3D) Strukturen. Sie basiert auf dem Phänomen der nichtlinearen Absorption, bei dem ein Molekül zwei oder mehrere Photonen simultan absorbiert. Die Energiedifferenz zum angeregten Zustand beträgt die Summe der einzelnen Photonen. Anfänglich noch als wissenschaftliches Kuriosum mit limitierter Anwendung wahrgenommen, erlaubten Ultrakurzpulslaser eine Vielzahl neuer Applikationen. Eine solche ist die 2-Photonen Polymerisation (2PP). Hierbei wird gepulstes Laserlicht in ein photosensitives Harz fokussiert, wodurch 3D-Geometrien mit einer Auflösung von einigen hundert Nanometern produziert werden können. Verglichen mit konventionellen Additiven Fertigungstechniken besteht keine Notwendigkeit für eine Schicht-für-Schicht Auftragung des zu verarbeitenden Harzes. Die Auflösung von 2PP ist unerreicht in der Additiven Fertigungstechnik und erlaubt die Produktion präziser Gerüststrukturen für biomedizinische Anwendungen.

Diese Doktorarbeit umfasst eine umfangreiche Studie von Parametern, die den 2PP-Prozess beeinflussen. Für *in vivo* Anwendungen wird ein hoher Durchsatz benötigt. Hier stellt die Auflösung der Technologie einen möglichen Engpass dar, da die Produktionsgeschwindigkeit von 2PP um ein vielfaches höher ist, als bei konventionellen stereolithographischen Verfahren. Des Weiteren benötigen 2-Photonen Photoinitiatoren lange Belichtungszeiten, wodurch langsame Scangeschwindigkeiten bedingt werden. Eine vollständig automatisierte Z-Scan Messanordnung wurde entwickelt, um die spektrale Absorption von 2-Photon-aktiven Komponenten zu vermessen. Eine Übereinstimmung der Wellenlänge, welche für 2PP verwendet wurde, mit dem Maximum der 2-Photonen Absorption sorgte für eine deutliche Erhöhung der Prozesseffizienz. Um das Polymerisationsverhalten von Materialien bei erhöhten Scangeschwindigkeiten zu verstehen, wurde die minimal benötigte Laserleistung (P_{th}) für Geschwindigkeiten von bis zu 100 mm s^{-1} untersucht. Die ermittelten Werte für P_{th} lagen deutlich unter den berechneten Trends, welche auf vergleichbaren Studien basierten. Die Ergebnisse erlaubten eine deutliche Steigerung der Fabrikationsgeschwindigkeit.

Ein weiterer Fokus wurde auf Materialien mit Potential für Anwendungen in der regenerativen Medizin gelegt. Hierfür wurden Präpolymere basierend einem biokompatiblen und biodegradierbaren Polycaprolacton-Backbone untersucht. Das Potential von 2PP als Werkzeug für neuartige Lösungsansätze in der Gewebezüchtung wurde in zwei Studien veranschaulicht. Periodisch angeordnete Mikrostrukturen wurden produziert. Diese wurden mithilfe stehender Wellen mit neuronalen Zellen besiedelt. In der zweiten Studie wurden 2PP-Strukturen für Haarimplantate produziert, die mit Keratinozyten und induzierten pluripotenten Stammzellen beladen wurden. Nach Implantation generierten die Zellen menschliche Haarfollikel.

Die rasche Produktion von Gerüststrukturen basierend auf biodegradierbaren und biokompatiblen Materialien veranschaulicht das Potential von 2PP für biomedizinische Anwendungen.

Acknowledgements

First, I would like to thank my supervisor Aleksandr Ovsianikov for his guidance. His vast knowledge of this interdisciplinary field of research gave valuable input to overcome major obstacles when designing setups and planning experiments. The cooperations with a multitude of research groups he provided significantly shaped the course of this thesis and I am grateful that he entrusted me with these projects.

I want to express my gratitude to the multiple cooperation partners. Aysu Arslan and Jasper Van Hoorick, as well as their supervisors Peter Dubruel and Sandra Van Vlierberghe, provided many materials used in this work. Additionally, they offered valuable scientific input. The cooperation with Antonella Pinto under the supervision of Alexey Terskikh was exemplary. A reliable, professional and flexible working relationship allowed significant progress. Furthermore, I want to thank Pu Chen, Tanchen Ren and Utkan Demirci for their work using Faraday waves. I want to highlight the contributions by Karin Wieland under the supervision of Bernhard Lendl. Her thorough work and reliability helped to find a red through line among the many measurements done.

I want to thank the secretaries of our institute Silvia Windisch, Tanja Grünwald, Dagmar Fischer and Andrea Novak, for their reliability and straightforward support for countless administrative tasks. I thank Stefan Zellhofer for managing laser safety and providing the occasional helpful comment, Gerhard Kern for technical support, Thomas Koch for nanoindentation measurements and Christian Zaruba for excellent management of SEM at the institute.

I am particularly grateful for the assistance and additional guidance by Jürgen Stampfl, who provided a great working environment at the Additive Manufacturing Technologies group. I thank Robert Gmeiner, Philipp Neubauer and Bernhard Steyrer for their technical competence and assistance. In addition to giving valuable scientific input, I want to thank Sonja Baumgartner, Bernhard Buseti and Christoph Hofstetter for regular moral support.

Over the last years, our 2PP-group has grown significantly compared to when I started my diploma thesis and this is in no small part due to the collaborative, inspiring and friendly group members. In particular, I want to thank the following: Elise Zerobin, for having an open ear for even the most basic questions about chemistry. Markus Lunzer, for advice on experiments and many educational corrections. Katja Hölzl, for valuable counsel and thorough research. Agnes Dobos, for an amazing collaboration and professional competence. Marica Markovic, for doing all the necessary stuff in the background to keep our group running in addition to her work in cell culture and her always having an open ear.

I will never be able to fully express my gratitude for the supervision by Peter Gruber. His open mind, helpful nature and his incredible technical expertise in various technical fields was a constant inspiration, to learn more and try harder.

The students I supervised probably taught me as much during their respective projects as I taught them (Michael Aufreiter, Franek Bartnik, Dominik Theiner, Franziska Gantner and Xander Berger). Thanks to my fellow students Alexander Haber, Georg Harrer, David Müller, Franz-Stephan Strobl and Sebastian Schönhuber. To a large part they supported me in finishing a degree program despite the many doubts along the way.

Lastly, I want to thank my parents for their continuous support, their openness and trust. My sister Elisabeth, who is always there for me and convinced me that I could study physics. And my girlfriend Julia, who helped me through the many ups and downs of this thesis.

I could not have done this without you.

Contents

1	Introduction	1
1.1	State of the Art	1
1.2	Motivation	3
2	Theory	7
2.1	Tissue Engineering	7
2.1.1	Scaffold-Based Tissue Engineering	7
2.1.2	Scaffold-Free Tissue Engineering	7
2.1.3	Third Strategy in Tissue Engineering	8
2.1.4	Regeneration of Hair Follicles	8
2.2	Additive Manufacturing	9
2.2.1	Photopolymerization	11
2.3	2-Photon Lithography	12
2.3.1	Photoinitiators	13
2.3.2	Prepolymers	14
2.3.3	Measurement of Material Properties	16
2.4	Nonlinear Absorption	17
2.5	Generation of Ultrashort Pulses	19
2.5.1	Tunable Lasers	20
2.5.2	Dispersion Compensation	20
2.5.3	Autocorrelation	22
2.5.4	Laser Intensity Measurement	22
2.6	Volume Pixel	25
2.6.1	Focused Gaussian Beam	25
2.6.2	Writing Resolution	27
2.6.3	Threshold Intensity	28
2.6.4	Polymerization Threshold	31
2.7	Photodynamic Therapy	33
2.8	Z-Scan	34
2.8.1	Thermal Lensing	40
3	Materials and Methods	41
3.1	Z-Scan Setup	41
3.1.1	Power and Diode Range	43
3.1.2	Beamprofiler	43
3.1.3	Autocorrelator	45
3.1.4	Thermal Effects	45
3.1.5	Sample Preparation and Measurement	45
3.2	2PL-Setup	47
3.2.1	Acousto-Optical Modulator	47

3.2.2	Scanning Mode	48
3.2.3	Objectives	50
3.2.4	Large Field 2PP	50
3.3	Laser Source	52
3.4	2PP	53
3.4.1	ETA:TTA	53
3.4.2	Ormocomp®	54
3.4.3	Sol-Gels	54
3.4.4	PCL-Based Prepolymers	54
3.4.5	GelMod	56
3.4.6	Activated Glass	56
3.5	Material Characterization	56
3.5.1	Nanoindentation	57
3.5.2	Raman Spectroscopy	57
3.5.3	Polymerization Threshold	58
3.6	Photodynamic Therapy	60
3.7	Microscaffolds	60
3.8	Microcages	62
3.9	Hair Follicles	64
3.9.1	Microwells	64
3.9.2	Encapsulation and Transplantation	65
4	Results Z-Scan	67
4.1	System Calibration	67
4.1.1	Beam Profiler Optimization	70
4.2	Reference Z-Scan	73
4.3	Photoinitiators	75
4.4	Measurement Algorithm	78
4.5	2P-PDT	79
4.6	Discussion	81
5	Results PCL	83
5.1	Di-Functional Prepolymer	83
5.1.1	No Photoinitiator Added	83
5.1.2	Photoinitiator Added	83
5.2	Hexa-Functional Prepolymer	85
5.3	Discussion	87
6	Results Polymerization Threshold	89
6.1	Ascending Scan	89
6.2	Single Line [1D]	89
6.2.1	Voxel Increase	91
6.2.2	Threshold Lines	92
6.2.3	Minimum Feature Resolution	94
6.3	Double Line [2D]	96
6.4	Cubes [3D]	96
6.5	Discussion	99

7	Results Large Field 2PP	103
7.1	Discussion	107
8	Results Microscaffolds	109
8.1	Microcages	109
8.2	Hair Follicles	112
	8.2.1 Zr-Hybrid	112
	8.2.2 PCL-Based-Prepolymer	114
8.3	Discussion	114
9	Conclusion	117

Die approbierte gedruckte Originalversion dieser Dissertation ist an der TU Wien Bibliothek verfügbar.
 The approved original version of this doctoral thesis is available in print at TU Wien Bibliothek.

Abbreviations and acronyms

1D, 2D, 3D	1-,2-, 3-dimensional	KC	keratinocyte
2PA	2-photon absorption	MG63	human osteosarcoma cell line
2PEF	2-photon excited fluorescence	mKC	mouse keratinocyte
2PL	2-photon lithography	NLA	nonlinear absorption
2PP	2-photon polymerization	NLR	nonlinear refraction
4,4'-Bis	4,4'-Bis(diethylamino) benzophenone	OPA	optical parametric amplifier
AFM	atomic force microscope	PBS	phosphate buffered saline
AM	additive manufacturing	PCL	polycaprolactone
AOM	acousto-optical modulator	PDMS	polydimethylsiloxane
CAD	computer aided design	PDT	photodynamic therapy
DAPI	4'-6-diamidino-2-phenylindole	PEG	polyethylene glycol
DBC	double bond conversion	PI	photoinitiator
DMSO	dimethyl sulfoxide	PMMA	poly(methyl methacrylate)
DP	dermal papilla	PS	photosensitizer
DSC	differential scanning calorimetry	PSF	point spread function
ECM	extracellular matrix	ROS	reactive oxygen species
FDM	fused deposition modeling	SEM	scanning electron microscopy
FN	fieldnumber	SFOV	squared field of view
FOV	field of view	SHG	second harmonic generation
fs	femtosecond	SLA	stereolithography
FTIR	Fourier transform infrared	SLM	selective laser melting
GDD	group delay dispersion	SLS	selective laser sintering
GFP	green fluorescent protein	THF	tetrahydrofuran
GVD	group velocity dispersion	Ti:Sa	titanium-doped sapphire
hiPSC	human induced pluripotent stem cell	UV	ultraviolet
HMDS	hexamethyldisilazan	WLC	white light continuous z-scan
hTERT	human telomerase reverse transcriptase	WOW-2PP	widened objective working range 2PP

1 Introduction

1.1 State of the Art

2-photon polymerization (**2PP**), sometimes also referred to as multiphoton polymerization, is a microfabrication and nanofabrication technology with a rapidly growing field of explored applications ranging from the fabrication of microlenses [1, 2], photonic crystals [3, 4], to micromechanical and microfluidic devices [5–7]. Its main advantage compared to available additive manufacturing (**AM**) methods is the capability to produce complex three-dimensional (**3D**) structures at unrivaled spatial resolution in the sub-micrometer range [8]. This is achieved via 2-photon absorption (**2PA**), a nonlinear process, which allows the highly localized deposition of light into a photosensitive resin. There is no need to add material in a layer-by-layer fashion, as done in conventional AM-technologies [9]. While initially limited to fabrication speeds of a few micrometers per second, the fabrication duration vastly increased due to galvanometer scanners [10, 11]. Recently, scanning speeds up to 4 ms^{-1} using galvanometer scanners have been reported, rendering 2PP increasingly more attractive for a wide field of research [12].

This increase in scanning speed and subsequent increase in throughput renders 2PP of interest for biomedical applications such as tissue engineering. The resolution of 2PP allows to produce environments at nanometer precision, for example the extracellular matrix (**ECM**) [13]. The ECM is the non-cellular compartment of each tissue and it provides structural and biochemical support [14, 15]. Mimicking conditions that are as close to *in vivo* is especially relevant for the development of therapeutic drugs. The initial outcome of *in vitro* drug testing on two-dimensional (**2D**)-cell culture often decides whether the development of the drug is continued [16]. However, certain limitations of 2D-culture suggest that an alternative method such as higher drug toxicity should be considered. Among other limitations are the lack of cell to cell and cell to ECM signaling which occur in 3D-tissue. These signals are essential for cell differentiation, proliferation, and other cellular functions, suggesting that growing cells as 3D-cell cultures is more representative of the conditions *in vivo* [17, 18]. Therefore, 3D-microenvironments can provide significant insight when testing the safety and efficacy of therapeutic drugs [19, 20]. In the case of 3D-tissue engineering via 2PP, hydrogels have emerged as versatile materials. They act as a highly biomimetic surrounding similar to the natural ECM [21, 22]. The material parameters of hydrogels can be tuned in three dimensions to guide cell adhesion and proliferation [23, 24]. Recent progress has shown the feasibility of structuring hydrogels in the presence of living cells. It allowed new types of cell experiments for cell-laden hydrogels. This approach yields a uniform cell distribution and circumvents the need to seed the scaffolds after production [25]. In addition, 2PP shows great promise to produce structures such as microscaffolds for regenerative medicine. Its high resolution allows to fabricate scaffolds which provide mechanical support for cell spheroids upon implantation in defects such as bone tissue [26]. The size of porous microscaffolds for these experiments was usually less than $300\text{ }\mu\text{m}$. To allow cell migration through the scaffold, the pores need to be a few micrometers in diameter, which cannot be produced using conventional stereolithography (**SLA**). As

1 Introduction

2PP provides the required resolution, it is seen as a potential new way to produce scaffolds used for the regeneration of bone tissue [27–29]. Another field of particular interest for 2PP is the regeneration of hair follicles for implantation. The hair follicle is induced by dermal papilla (**DP**) cells. While differentiation of human induced pluripotent stem cells (**hiPSC**) into DP-like cells has been reported [30], they lose their folliculogenic properties upon growth in culture dishes [31]. It is assumed that under these conditions cells lack contextual and positional cues from the surrounding 3D tissue. When culturing DP cells as spheroids, they partially regain their folliculogenic properties and the gene expression pattern characteristic of the freshly dissociated human dermal papillae [31]. However, a major stepping stone to render 2PP of interest for these applications is the processed material. The material must provide the mechanical support while being biodegradable at the same time. While there are many works about biocompatible microscaffolds fabricated with 2PP, these materials are usually sol-gel based, so the implant will not degrade over time [32–34].

1.2 Motivation

This thesis was written at the Institute of Materials Science and Technology, TU Wien, to investigate materials used for 2PP such as photoinitiators (**PIs**) and prepolymers. 2PP is based on radical chain polymerization. The resins used consist of one or more monomers or prepolymers and a radical PI. Upon excitation via 2PA the PI can cleave and yield radicals. These chemical species are highly reactive and will attack C=C double bonds, producing a new carbon-carbon single bond and another radical species (discussed in detail in Sec. 2.2.1). The prepolymers crosslink into a dense network, which is required for solid 3D-structures. When increasing the fabrication speed of 2PP, a thorough understanding of the processing parameters is required to ensure reproducible results and allow upscaling for future *in vivo* experiments.

The scope of this thesis was

- Design of a z-scan setup to measure the nonlinear absorption properties of 2-photon active compounds in a broad spectral range.
- Study of prepolymers based on a biodegradable and cytocompatible PCL-backbone.
- Comparative study of polymerization performance for various materials and the required minimum laser power (P_{th}) for writing speeds of 100 mm s^{-1} .
- Fabrication of microscaffolds for biomedical applications.

As an initial step, a z-scan setup was developed to measure the 2PA cross section (σ_2 , given in GM). In most cases such z-scan experiments are confined to a limited wavelength window due to complicated setups or cumbersome alignment for each wavelength [35, 36]. With easily tunable fs-laser sources a broad spectral range is available for 2PP structuring. Matching the laser wavelength to the peak of the 2PA spectrum of a particular compound can result in a few-fold increase of the PI's performance [36]. This optimization is of particular importance when the fabrication speed is increased. Low 2PA absorption requires high exposure times, leading to an overall longer fabrication process [37], as shown in Fig. 1.1. The 2PP setup used for this thesis allows the change of wavelength in a range from 690 to 1040 nm [12]. With this broad window available for structuring, the z-scan setup was required to cover the same spectral range to efficiently characterize newly synthesized PIs. The compounds characterized with this z-scan setup were predominantly intended for 2PP applications. As this setup studied nonlinear absorption behavior it was also intended as a tool to characterize compounds used for other 2PA based processes such as photodynamic therapy (**PDT**). In PDT chemical agents are activated using light to specifically destroy cancerous tissue among others [38].

After the working window and effectiveness of certain PIs was determined, the next step was the study of newly synthesized prepolymers for their 2PP-processability. The data acquired from z-scan results helped to select an optimal wavelength range for a given PI. Prepolymers based on the biocompatible and biodegradable polyester polycaprolactone (**PCL**) [40] were studied as alternative to current sol-gel materials [41, 42].

In addition to this, the performance of 2PP for fabrication speeds up to 100 mm s^{-1} was inspected. Understanding the polymerization behavior at high scanning speed is key when up-scaling for clinical applications is seen as the long term goal. The correlation between required power for polymerization (P_{th}) and scanning speed v must be known in order to extrapolate polymerization behavior at faster speeds and estimate the maximum working window of a given

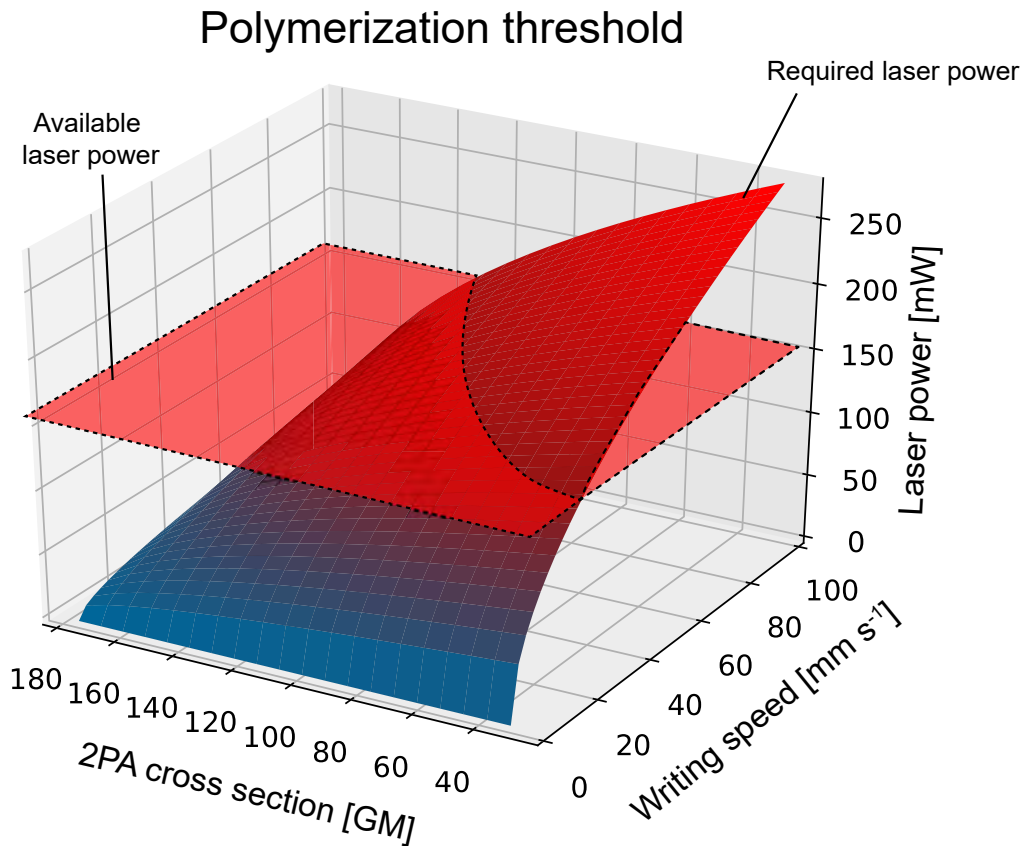


Figure 1.1: Dependence of the polymerization threshold P_{th} from 2PA cross section and writing speed. The 3D-area represents the minimum laser power P_{th} for a given writing speed and 2PA cross section (given in GM). The red 2D-plane represents the laser power limit. Faster writing speeds demand higher laser powers, as the individual points are illuminated for a shorter time ($P_{th} \propto v^{0.5}$). The 2PA absorption is given in GM. As can be seen from the intersection of power limit and minimum laser power, faster writing speeds require higher 2PA cross section. Increasing fabrication speed from 10 to 50 mm s⁻¹ would double the required laser power, while a writing speed of 100 mm s⁻¹ would necessitate thrice the power. On the other hand an increase in cross section from 20 to 50 GM or 100 GM would lead to a reduction of P_{th} by 30 % or 50 % respectively. Displayed data was simulated for 2PA compounds requiring a minimum laser power of 50 mW at a writing speed of 1000 mm s⁻¹ and 2PA cross section of $\sigma_2 = 100$ GM. A limit of 150 mW was chosen as this is the maximum laser power for commercially available systems [39].

material composition. This study was motivated by the fact that P_{th} for cube structures produced at writing speeds from 20 to 100 mm s^{-1} did not correspond with the predicted trend established by Serbin et al. (Fig. 1.2) [43]. These observations were based on qualitative analysis and therefore prone to errors due to the method. A more thorough but time consuming method to evaluate P_{th} is the fabrication of single lines. However, the correlation between single lines and complex 3D systems is rarely studied. Therefore, thorough polymerization studies of materials used for 2PP were done using fabrication speeds up to 100 mm s^{-1} to correlate P_{th} observed for single lines with P_{th} seen for fully 3D-structures. From these results the polymerization rate was extracted for various materials in order to determine the efficiency of materials for 2PP structuring [43]. Moreover, this research added to the fundamental understanding of the performance of 2PP. Current studies of the correlation between required laser power and the writing speed were only done in the range of 10 to 100 $\mu\text{m s}^{-1}$ [44, 45].

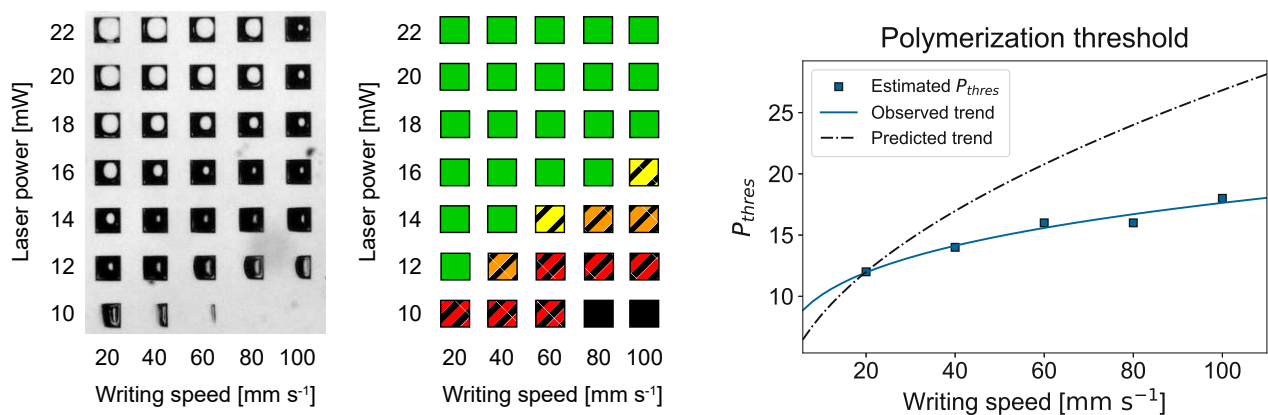


Figure 1.2: Evaluation of required laser power P_{th} for increasing fabrication speeds. For 3D-structures there is no clearly defined power, which can be selected as P_{th} (left). Therefore P_{th} is often times only qualitatively described by color schematics, depending on the quality of the fabricated cubes (middle). Trends roughly estimated by this method show a clear deviation from the trend predicted by established models (right). A more thorough understanding of P_{th} was required to accurately describe this deviation from the model prediction.

Optimizing the PI performance, studying new materials for 2PP and establishing their polymerization behavior for fast fabrication speeds were prerequisites to operate the 2PP system at peak efficiency. It allowed to produce stable scaffolds with sufficient mechanical properties for implantation at the fastest possible scanning speeds. The versatility of 2PP was showcased with two different methods. Firstly the structures were produced in periodic array to act as microcages. The microcages were then loaded with fibroblasts and neurons in separate experiments using Faraday waves [46, 47]. Secondly, biocompatible scaffolds were used for implantation of hair DP cells to grow hair follicles [30, 48].

2 Theory

A general overview of 3D-tissue engineering, as well as selected approaches to create 3D-tissue are presented. In particular the use of Faraday waves and hair follicle regeneration are described. The fundamentals for AM are briefly summarized with a focus on photopolymerization and 2PP. The applications of 2PP for tissue engineering are elaborated. The principles of ultrashort pulse generation and tunable femtosecond (**fs**)-lasers are given. A particular focus is placed on autocorrelators, which are used to determine the pulse duration of a fs-laser. The model behind volume pixels (voxels) and the resolution limit of 2PP are outlined to illustrate P_{th} . Another segment focuses on 2-photon-PDT (**2P-PDT**) as an alternate application field of 2PA. As the 2PA behavior for various compounds was characterized over the course of this thesis, the fundamentals for z-scan measurements to measure 2PA cross section (σ_2) are given.

2.1 Tissue Engineering

Tissue engineering aims to restore, maintain, or improve damaged tissues or whole organs [49]. In tissue engineering two main approaches can be distinguished: scaffold-based and scaffold-free [26].

2.1.1 Scaffold-Based Tissue Engineering

The scaffold-based strategy relies on the use of biomaterials to create a temporary structure supporting cells throughout the tissue formation. A scaffold is either a classical 3D construct with interconnected pores, a hydrogel with cells embedded in it, or a combination of the two approaches. The solid, porous and (ideally) biodegradable polymeric scaffolds are fabricated in advance and seeded afterwards with cells [21]. Alternatively, the use of a decellularized ECM is another promising trend for tissue engineering [50]. However, this scaffold-based approach presents some challenges. Large constructs are cumbersome to seed with cells, leading to inhomogeneous cell distribution [51]. Another big drawback of this method is the timescale to achieve high enough cell densities for transplantation [52].

2.1.2 Scaffold-Free Tissue Engineering

Originating from the idea of self-assembly the scaffold-free approach is based on tissue spheroids. The term spheroid is used to describe a particular case of 3D cell culture, where multiple cells are fused to form a 3D spheroid [53, 54]. Here, the capacity of cell spheroids to fuse shows great promise, as tissues in the human body such as liver, brain, and pancreatic islets comprise densely packed cells with a minimal ECM fraction [55]. Tissue spheroids or aggregates can also be used as building blocks to form complex tissue architectures through tissue fusion [56]. Two methods of producing these spheroids are hanging drop and non-adhesive surfaces. While

2 Theory

hanging drop has shown promise for spheroid fabrication [57], spheroids produced using non-adhesive hydrogels show a more regular size and shape distribution. For this method non-adhesive wells are used. As the cells cannot attach to the well they are forced to attach to each other and form spheroids [58]. Cell spheroids produced from adipose mesenchymal stem cells (MSCs) were cultured in a cylindrical mold as a possible approach for osteochondral defect regeneration [59]. However, concerns about the mechanical stabilities of these constructs have been voiced [26, 60].

Another promising scaffold-free approach in tissue engineering is to form densely packed-cell constructs using Faraday waves, nonlinear standing waves, which appear on liquids enclosed by a vibrating receptacle. Applying standing Faraday waves to cells in medium induces hydrodynamic drag force

$$F_d = 6\pi\eta r\nu, \quad (2.1)$$

which is defined by the dynamic viscosity η , particle radius r and flow velocity relative to the particle ν . This drag force drives the particles to the nodes of the standing waves where the amplitude is zero. This approach allows a wide variety of assembly patterns based on the wavefunction used [46, 47].

The relationship between the Faraday wavelength λ and frequency f is given by

$$(\lambda f) = \left(\frac{g\lambda}{2\pi} + \frac{2\pi\sigma}{\rho_l\lambda} \right) \tanh\left(\frac{2\pi H}{\lambda} \right), \quad (2.2)$$

with the gravitational acceleration constant g , surface tension σ , liquid density ρ_l and the layer thickness H [61]. This approach also allows fabrication of dense cell spheroids. Within a few seconds complex structures can be assembled. The generated 3D-assembly can be dynamically tuned to diverse patterns by altering the wave frequency [62]. Similarly to other scaffold-free approaches, the mechanical stability has to be studied further. Also, because of the wave nature, Faraday waves are not able to produce arbitrary 3D-structures.

2.1.3 Third Strategy in Tissue Engineering

Recently, a third strategy in tissue engineering has emerged, which aims to combine the two previously described approaches. Porous spherical structures of 200 μm diameter were fabricated [26]. These scaffolds were then placed into non-adhesive well plates, together with the desired cell type. As discussed, the cells are driven to form spheroids due a lack of adhesion [28]. Therefore, when the cells sediment, they move through the pores of the scaffold and form the spheroid within the 3D-structure. These base units can then be used as building blocks for directed self-assembly strategies [63]. This approach provides the high cell density required for tissue engineering, while also providing mechanical support due to the microscalfold [27, 28]. 2PP has proven as the the ideal tool to produce these small, 3D and highly porous scaffolds. While many materials have been reported which show excellent 2PP processability and cell-viability, such as sol-gels, they cannot be degraded by the cells [29].

2.1.4 Regeneration of Hair Follicles

A promising field for tissue engineering is the regeneration of human hair follicles. Why some follicles undergo premature inability to regenerate themselves is unclear. There are currently

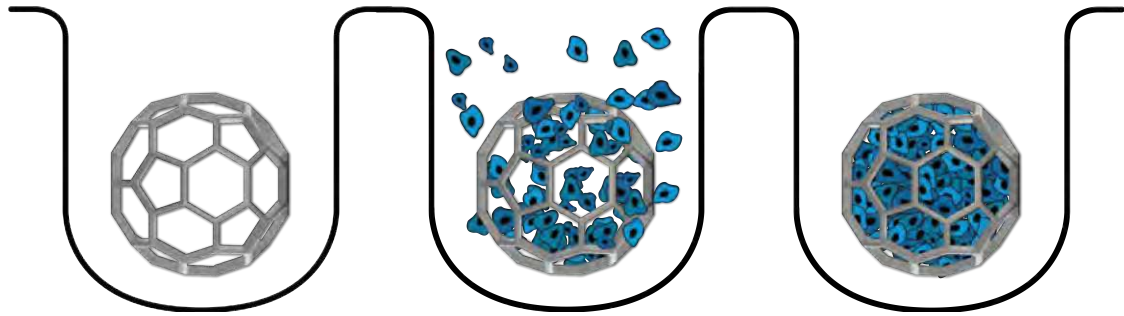


Figure 2.1: Third strategy in tissue engineering. A porous scaffold is fabricated. The scaffold is placed within a non-adhesive well plates (left). Cells are added to the well (middle). Due to the non-adhesive walls the cells naturally form spheroids (right). The structure serves as base unit for self-assembly approaches in tissue engineering with high cell density, while the scaffold provides mechanical support. To fabricate these porous scaffolds high resolution 3D-printing based on 2PP has emerged as a promising method.

limited strategies to overcome baldness. To date, the only two FDA approved drugs available for hair loss treatment are the dihydrotestosterone-suppressing 5 α -reductase inhibitor, finasteride, and the antihypertensive potassium channel opener, minoxidil [64]. However, both options are expensive, prone to side effects, and, most importantly do not provide adequate long-term hair coverage [65, 66]. A second option is hair transplantation, which consists of moving the preexisting hair follicles, usually from the back or side of the scalp to front or top. However, the number of follicles that can be harvested and implanted is limited, and the restoration is temporary due to the progressive nature of hair loss condition [67]. Here, tissue engineering provides the tools to regenerate hair follicles using hiPSC cells which can be differentiated into DP-like cells. This method has already been shown in cell culture dishes. However, DP grown under these conditions are reported to loose their foliculogenic properties, when grown in culture dishes. It is assumed that this is due to the lack of cues from the surrounding tissue [31]. With the proposed third strategy, AM methods with high resolution such as 2PP are seen as potential tools for this field.

2.2 Additive Manufacturing

AM describes the process of joining materials to fabricate parts from 3D-model data, as opposed to subtractive manufacturing and formative manufacturing methods [68, 69]. A physical object is created by successive addition of material based on a virtual 3D-model. In most cases the 3D-model is separated - or sliced - into several 2D-layers which are fabricated consecutively (Fig. 2.2). Depending on the method, the layer positioning is done by moving the building platform in vertical (z) direction or changing the focal plane. The 3D-models for AM can be produced by 3D-scanning or via Computer Aided Design (CAD). A widely used file format for 3D-geometries is **STL** (an abbreviation of stereolithography). The term AM covers a large field of applications. While 3D-printing is often used as an umbrella term for AM, it describes 3D-fabrication similar to inkjet systems where a printhead deposits materials drop wise. After finishing a layer, the next is added on top. This inkjet-based method is frequently used in tissue engineering as it allows to print multiple biomaterials, cells and biochemicals (referred

2 Theory

to as bioinks) [51,70]. The resolution of inkjet based bioprinting is limited to 10–50 μm [71].

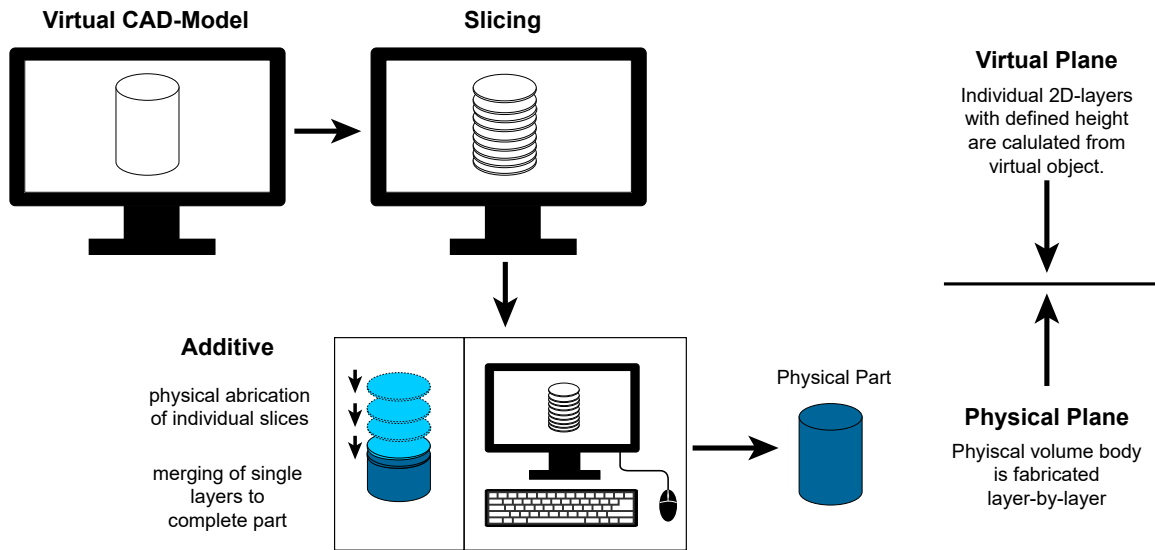


Figure 2.2: Schematic of additive manufacturing. A virtual CAD-model is sliced into multiple 2D-areas. The 3D part is then produced in a layer by layer fashion. Figure modeled after Gebhardt [68].

In extrusion based AM, like Fused Deposition Modeling (**FDM**) or Robocasting, material is dispensed through a nozzle. This application either uses fusible thermoplasts or highly viscous material to deposit individual strands of material layer by layer. Extrusion based 3D printing has been applied using bioinks to create cell-laden constructs [72,73]. Advantages of extrusion bioprinting include the ability to print bioinks (100 mPa s) with very high cell densities into 3D-scaffolds [74,75]. A drawback of this technique is the low resolution (200–1000 μm), potential nozzle clogging and the decreased cell viability due to shear stress [74,76,77]. Laser scanning has been employed in a wide range of AM technologies as it allows high resolution and precision for manufacturing. Heating of powder material via laser scanning is used in selective laser melting (**SLM**) and selective laser sintering (**SLS**). Depending on the thermal energy, the particles are sintered or melted. After one layer is finished a new layer of powder is added. The resolution of this process is 10 to 100 μm [78,79]. The high laser energies used for these processes (in the kW range) allow AM of metal powders [80]. The heat caused by these high energy lasers does not allow processing of materials for tissue engineering. Another laser based approach, known as SLA is based on photopolymerization of liquid monomers via UV-irradiation. This process was also the first additive system presented in 1986 [81]. The liquid monomer is linked via chemical reactions, no heat is produced. Conventional stereolithography setups offer a resolution of 20 μm while nonlinear stereolithography such as 2PP offers resolution in the sub-micron range [8].

As the focus of this thesis was on 2PP, the processes of photopolymerization as well as 2-photon lithography (**2PL**) are described in detail.

2.2.1 Photopolymerization

Photopolymerization describes the usage of light to induce chemical reactions in a photosensitive material, commonly referred to as resin [82]. Radicals initiate cross-linking of prepolymers which leads to cross-linking of resins, forming a solid network insoluble in common solvents. Consequently, solvents can be used to remove unpolymerized resin after the polymerization process. Polymerizations can be divided into step-growth and chain-growth mechanisms. This thesis will only focus on the chain-growth mechanism, in particular the free radical polymerization, as it is the base for 2PP applications [9]. During polymerization, three main types of reactions have to be mentioned:

- Chain initiation.
- Chain propagation.
- Chain termination.

The light brought into the sample is absorbed by the initiating molecule, referred to as PI. Upon excitation of the PI, free reactive species are created. These reactive species break apart the C=C double bonds of the base monomer in the chain initiation phase. Often times the term monomer is inadequate to describe the polymerization rate, as the base unit already comprises of a polymeric structure. Therefore, the term prepolymer is often used for monomer systems which have been reacted to an intermediate molecular mass state. The prepolymer is capable of further polymerization by reactive groups to a high molecular weight state [83]. It then becomes reactive due to one carbon atom requiring an additional electron (Fig. 2.3). The molecule then reacts with a neighboring monomer, creating a chain with the radical moving to the end of the chain. This chain-growth propagation mechanism continues until reactive species are inactivated by termination reactions. This can be due to recombination with another radical, reaction with a second chain which also has a radical ending [84]. Another effect is the reaction of radicals with inhibiting molecules, referred to as quenchers, in the photosensitive material. Quenchers can be added to the resin to inhibit radical diffusion, confining the excited volume and increasing the resolution. Quenching can also occur due to atmospheric oxygen confined in the resin. The effect of quenchers also significantly effects the required light dosage for initial polymerization (Sec. 2.6.2) [85].

2 Theory

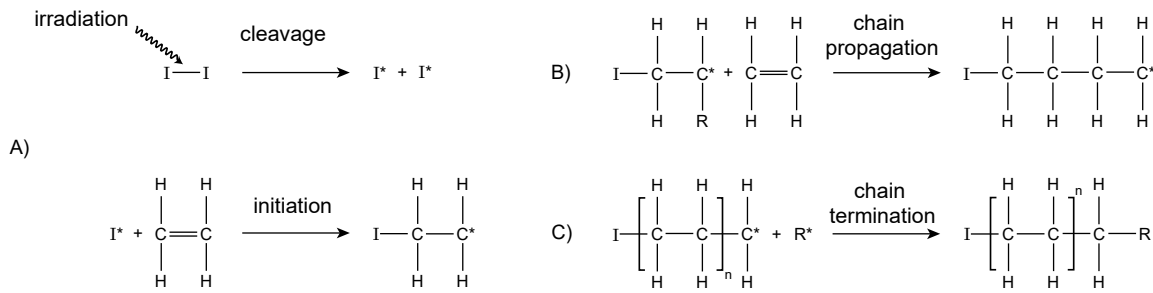


Figure 2.3: Types of reactions during radical polymerization. The PI absorbs the energy through illumination and creates reactive species I^* . Initiator radicals then react with unsaturated base units (monomer or prepolymer), creating reactive base units (A). The $C=C$ double bond is broken apart and the monomer becomes reactive. Subsequent addition of base units leads to the formation of new reactive base units (B). This process is stopped by recombination with a radical, chain-to-chain termination or reactive oxygen species (C).

2.3 2-Photon Lithography

2PL is similar to conventional SLA methods. Using a light source, photons are locally brought into a photosensitive resin. Optical scanning systems control the exposed area, producing custom layers. Repeating this process for multiple layers allows the fabrication of arbitrary 3D-geometries. In conventional SLA new material needs to be applied onto the building area after a single layer has been exposed to the light source. During this process the building platform is moved away from the vat, which contains the liquid resin. A new film of resin is applied and the building platform is placed in the desired layer height. During this step the shear forces need to be kept in mind when the building platform is removed from the vat [86]. In 2-photon lithography this procedure between two layers is no longer required due to the nonlinear nature of the process (discussed in detail in Sec. 2.4) as the absorption process takes place only in the focal volume of the laser, [87]. The excitation of the molecules requires a threshold photon dosage. Until this threshold is reached the resin does not react with the laser light and is transparent to the used wavelength. This eliminates the need for layer-by-layer deposition of new material and is also the reason why 2PL is often referred to as "true 3D-printing" as the structure can be arbitrarily built. Additionally, 2PP doesn't require temporary supports when free standing 3D structures are produced in highly viscous resins [9]. Positioning the laser beam can be done by various methods. Most 2PP systems include three linear actuators to move the sample position in x-, y- and z-direction (Fig. 2.4). Linear motors or piezoelectric actuators can be used. While piezoelectric actuators offer precision positioning in the nm-range, their travel range is limited to a few hundred micrometer. Linear motors provide high speed ($> 1 \text{ cm s}^{-1}$), acceleration and travel range of a few centimeters [9]. Alternatively, galvanometer based laser scanners can be used, which allow positioning of the laser beam in x- and y-direction by two movable mirrors. They are significantly faster than actuators but are limited to the field of view (FOV) of the setup. Furthermore, the scanning speed is linked inversely proportional to the objective magnification [10, 11]. Another drawback of galvanometer scanners is the loss of intensity for larger scanning angles, limiting the effective FOV which can be used for 2PP. This can be compensated by a scan-tube lens system [12, 88]. Usually, a combination of both technologies is used where the galvanometer scanner is scans the available FOV. Afterwards, the

linear motor moves the sample to the next position. Adding multiple FOVs allows to fabricate structures in the range of centimeters without compromising the precision of the process [89–91]. The structuring height of 2PP is usually limited by the refractive index of a given material due to focal spot distortions and the working distance of the objective (discussed in detail in Sec. 3.2.3). These limitations can be overcome by methods such as widened objective working range 2PP (**WOW-2PP**). In WOW-2PP, a glass slide is placed between the objective and the liquid material. This configuration allows to produce structures higher than the field of view but is only applicable for liquid materials [92].

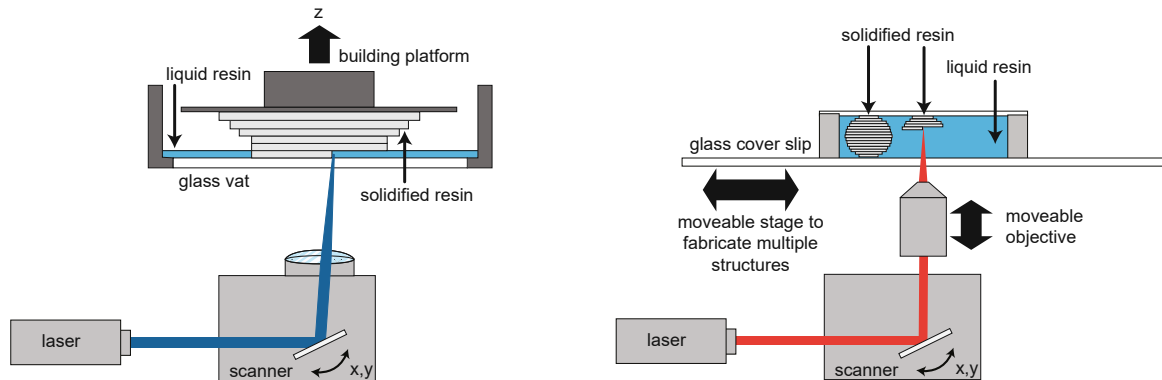


Figure 2.4: Comparison between conventional stereolithography (left) and 2-photon lithography (right). In stereolithography the building platform is moved in z-direction after each layer is finished and a new layer of unpolymerized material is applied. Due to nonlinear absorption this layer-by-layer fabrication is not required in 2PL and 3D structures can be fabricated directly within the resin. A combination of galvoscaner and moveable stage allows to produce multiple objects within a sample.

2.3.1 Photoinitiators

A PI describes a light sensitive molecule able to create reactive species upon excitation. While there is a vast field of applications for PIs, this thesis focused in particular on PIs which form free radical species used for chain polymerization (Sec. 2.2.1). They can be categorized in two types (Norrish Type I and Type II) depending on the mechanism with which they produce radicals. PIs of Type I cleave upon irradiation and form two reactive radicals. This cleavage is an unimolecular process, as the radicals are formed by a single molecule. The covalent bond is cleaved homolytically (the electrons of the cleaved covalent bond are divided equally between the products), creating two radicals. Type II photoinitiators require a co-initiator molecule. The PI abstracts a hydrogen from a hydrogen donor (generally an amine or alcohol). In the case of amines, amino radicals then initiate polymerization. Two free radicals are formed during this process [93]. Type I initiators show excellent cytocompatibility, which is necessary for cell encapsulation experiments in 3D-hydrogels for biomedical applications. Typical PIs for UV encapsulation are Iragcure 2959 [94], VA-086 [95] and Li-TPO-L [21]. Due to the small conjugated π -systems of these initiators they exhibit very low 2PA cross section (σ_2) and require long irradiation times to cleave the covalent bonds, limiting the fabrication speed of the 2PP method [37]. Therefore, most 2PA PIs are of Type II. Commercial 2-photon PIs such as 4,4'-Bis(4,4-Bis(diethylamino)benzophenone) are available and offer good performance for structuring

2 Theory

sol-gels [32]. Cross conjugated electronic π -systems with donor (D) and acceptor (A) groups ($D - \pi - A - \pi - D$) such as M2CMK have shown excellent two-photon performance [96]. However, for 2PP applications based on live cell encapsulation in hydrogels these initiators can not be used as they are cytotoxic and not soluble in water [13].

Specialized water-soluble initiators such as P2CK have been developed with significantly larger σ_2 , which have been used for fabrication of 3D-hydrogel structures [97, 98]. However, these compounds exhibit significant cytotoxicity even in the absence of irradiation above certain concentrations. When irradiated these PIs can cause significant photodamage to cells and it is assumed that this damage results from reactive oxygen species (ROS) such as singlet oxygen (1O_2) [99]. Recently a water soluble initiator was developed by Dobos and Tromayer, which allows 2PP structuring in the presence of living cells. Here, a cleavable water-soluble aryl diazosulfonate photoinitiator, referred to as DAS, was used to encapsulate ASC/TERT1 cells with 2PP [25].

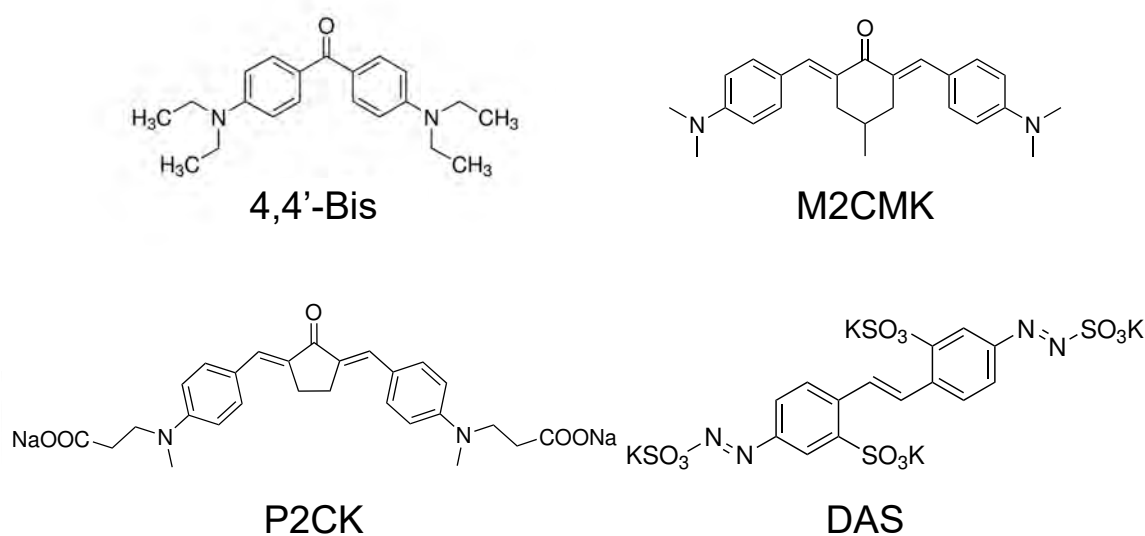


Figure 2.5: Photoinitiators (PIs) used for 2PP applications. 4,4'-Bis is a commercially available PI and used for sol-gel materials [32]. M2CMK has shown excellent two-photon performance. Both 4,4'-Bis and M2CMK are cytotoxic [96]. The water soluble P2CK and DAS were developed to cross-link hydrogels. Upon irradiation P2CK induced cell death, due to the creation of radical oxygen species [25, 97, 98]. DAS shows promise for live encapsulation of cells as it is cytocompatible even after irradiation [25].

2.3.2 Prepolymers

For 2PP applications a wide range of processable prepolymers is available, depending on the application. Organo-soluble materials can be used for fabrication of structures such as photonic crystals or microlenses [1–4]. For 2PP structuring in the presence of living cells the materials need to be water soluble and biocompatible [13, 98].

Triacrylates

Triacrylate based systems such as ETA and TTA are highly reactive and have shown good processability under 2PP conditions [100,101]. A solution of ETA and TTA (50:50 by weight) yields stiff but brittle structures due to the short chain acrylates used as base monomers. 2PP produced structures of ETA:TTA exhibit a reduced Young's modulus ranging from 1200 to 2650 MPa, depending on the laser power and used PI [102].

Sol-Gels

Sol-gels have emerged as versatile photosensitive materials. The sol-gel allows incorporation of optically active organic molecules into a glassy matrix to form doped gels [103]. These materials are easy to synthesize [104], have shown high mechanical strength and low shrinkage after development, rendering them as reliable materials for high precision 2PP [32]. The materials have also been shown to be biocompatible, although due to the glassy matrix they are not biodegradable [105]. Due to their rigidity sol-gels allow large stable structures without the need for support overhangs. However, it should be kept in mind that this also limits the height of the produced structure due to the working distance of the objective. An approach like WOW-2PP, which allows for structures many times higher than the actual objective working distance by dipping the objective into the liquid resin is not applicable for sol-gel constructs [92]. The exact reduced Young's modulus of the material has yet to be determined as the samples crack upon nanoindentation [12].

Hydrogels

Hydrogels are cross-linked 3D-networks of hydrophilic polymers, extensively swollen with water. These materials are important to fabricate scaffolds, which are able to mimic roles of the ECM. They provide essential cues for cell adhesion and proliferation, while still allowing the diffusion of nutrients, metabolites and growth factors [106,107]. Nature-based materials provide certain advantages for cell adhesion and proliferation. Gelatin, derived from collagen provides all these requirements [108]. Methacrylamide modified gelatin, also known as GelMOD belongs to the group of nature based hydrogels. It is produced by partial hydrolysis of collagen extracted from skin, bone, or connective tissue of animals. Since a major part of the ECM is composed of collagen, gelatin or GelMOD are capable of mimicking the natural cell environment. GelMOD has a low cytotoxicity and in cell culture medium, the cells can be in contact with the monomer for a prolonged time. Furthermore, the stability and tunability of mechanical properties, as well as biodegradability renders GelMod of interest for tissue engineering [23]. Introducing norbornene groups (Gel-NB) allows for the use of a thiol-ene photo-click reaction, thereby further increasing the reactivity and leading to improved processability [109]. Recently a new material has been developed by Houben et al. where a semi-crystalline backbone is connected with flexible acrylate spacers. This prepolymer was synthesized using a polyethylene glycol (PEG) backbone, resulting in a water soluble material which could cross-link under UV-conditions without the addition of PI [42].

2.3.3 Measurement of Material Properties

As structures produced with 2PP exhibit dimensions in the micron range, it is not possible to apply conventional material testing such as tensile testing. These methods require sample dimensions in the millimeter range. Therefore, producing probes using 2PP within a manageable time frame would only be possible by compromising the resolution of the technology [101,110]. Comparing data obtained from UV-polymerized bulk material with 2PP produced geometries, showed discrepancies in material performance such as stiffness [111]. These are assumed to be caused by the different illumination processes. Bulk polymer is formed by UV flooding illumination, whereas 2PP structures are produced voxel-by-voxel. This makes a direct correlation between bulk polymerization and 2PP difficult [101,110]. One way to determine the stiffness of 2PP produced scaffolds is atomic force microscopy (AFM). The forces between material surface and tip are measured via a cantilever. Thereby, a detector recognizes deflected signal due to movement of the cantilever [111]. Due to the sensitivity of the method, hydrogels can be measured with AFM [112]. The high spatial resolution (fractions of a nanometer) and a measurement area of a few micrometers logically decrease the throughput of AFM [113–115]. Alternatively, the reduced Young's modulus of 2PP structures can be measured via nanoindentation, which provides sufficiently high resolution for micrometer large structures while offering a faster measurement procedure [116]. For nanoindentation, a hard tip with known material properties is pressed into the sample. As the tip is moved into the sample, the force on the tip increases until it reaches a predefined value. The indentation process is then stopped and the tip remains in the material for a given time. Afterwards, the tip is removed and the area of residual indentation in the sample is measured to calculate the hardness [117]. From these data, the reduced Young's modulus is calculated, which can be correlated to the Young's modulus if the Poisson's ratio for both nanoindenter tip and sample material, as well as the Young's modulus of the tip are known [118]. Several material properties of polymers are a direct consequence of the double bond conversion (DBC). Generally speaking, DBC is the ratio of unreacted prepolymers to prepolymers, which have already been cross-linked, forming the polymer. Therefore, the DBC is often correlated to material properties [110]. Methods to measure the DBC include differential scanning calorimetry (DSC), Fourier transform infrared (FTIR) and Raman spectroscopy [119,120]. While DSC is the industry standard for evaluating DBC, it is not suited for 2PP structures because the part weight needed is higher than parts produced via 2PP. While FTIR can be used, poor spatial resolution and distinct sample preparation are some of the drawbacks of this technique. Raman spectroscopy has emerged as an optimal tool to characterize 2PP microstructures [110,121]. It allows for in situ and nondestructive monitoring of specific bond vibrations with excellent spectral resolution and minimum sample preparation. It relies on inelastic scattering of light to collect information about the vibrational modes of molecules [110]. This can be done by relating the signal of C=O to C=C moieties. The higher the DBC, the lower the signal of unreacted C=C moieties. To allow comparison, the C=O signal is used to normalize the data. Comparing the integrated signal areas of the unpolymerized reference ($A_{C=O}$ and $A_{C=C}$) with the polymerized sample ($A'_{C=O}$ and $A'_{C=C}$), yields the DBC [121]

$$\text{DBC} = \left[1 - \frac{A'_{C=C}/A'_{C=O}}{A_{C=C}/A_{C=O}} \right]. \quad (2.3)$$

2.4 Nonlinear Absorption

2PA was first postulated by Maria Goeppert-Mayer in 1931. Two or more photons combine to bridge an energy gap too large for the individual photons. In theory, a photon excites the molecule to a short-lived (fs-long) state. The molecule can reach the excited state if a second photon is absorbed within this short lifetime [122]. The probability for 2PA is given by the 2PA cross section σ_2 in Goeppert-Mayer units defined as

$$1 \text{ GM} = 10^{-50} \text{ cm}^4 \text{ s photon}^{-1} \text{ molecule}^{-1}. \quad (2.4)$$

Because of the technical limitations to create the necessary photon flux it took until 1961 to be proven by Kaiser and Garrett, who observed 2PA using a solid state laser [123]. As 2PA requires high photon densities, the invention of pulsed lasers with a pulse duration in the fs-range was key (discussed in detail in Sec. 2.5). Because of the nonlinear behavior, the highest probability for excitation is confined to a small volume at the laser focus where in the linear case the absorption takes place along the entire light path (Fig. 2.6) as described by the Beer-Lambert law. After excitation (be it linear or nonlinear) the molecule can release the energy via emission of a photon (fluorescence), which can be used for high resolution two-photon microscopy [124, 125]. Alternatively, the molecule can change from the excited state S_1 to the triplet state T_1 via intersystem crossing [29]. In this state, the excited molecule can initiate reactive species, such as radicals produced from PIs (Sec. 2.2.1), which is the basis of SLA. The reactive species can alternatively be used to damage cell tissue, which has found application in PDT (Sec. 2.7) applications, where cell death is locally induced in cancer cells.

The n-photon absorption rate k_n is given by

$$k_n = \frac{R \cdot \sigma_n}{(E_{\text{phot}})^n} \cdot \int_0^{T=\frac{1}{R}} I^n(t) dt, \quad (2.5)$$

where $I(t)$ denotes the intensity, σ_n the n-photon cross-section, R the repetition rate, and $E_{\text{phot}} = \frac{hc}{\lambda}$ the energy of a photon with a wavelength of λ [126]. For $\tau \ll R^{-1}$ the integral can be approximated by

$$k_n = g^{(n)} \cdot \frac{\sigma_n}{(R\tau)^{n-1}} \cdot \left(\frac{I_{\text{avg}}}{E_{\text{phot}}} \right)^n \quad (2.6)$$

Here, I_{avg} denotes the time-averaged intensity. This time averaged expression is usually used as most energy detectors are too slow to follow $I(t)$. From this it can be seen that the peak intensity I_0 is approximately $R \cdot \tau$ times larger than the average intensity I_{avg} [126]. The constant $g^{(n)}$ is the time-zero n-order temporal coherence, which depends on the pulse shape [127]. The dependence of pulse duration and repetition rate by the order of $n - 1$ shows that pulse duration does not impact the absorption rate for linear absorption and only affects 2PA and higher ordered absorption phenomena. For the 2PA case Eq. 2.6 simplifies to

$$k_n = g^{(2)} \cdot \frac{\sigma_n}{R\tau} \cdot \left(\frac{I_{\text{avg}}}{E_{\text{phot}}} \right)^2. \quad (2.7)$$

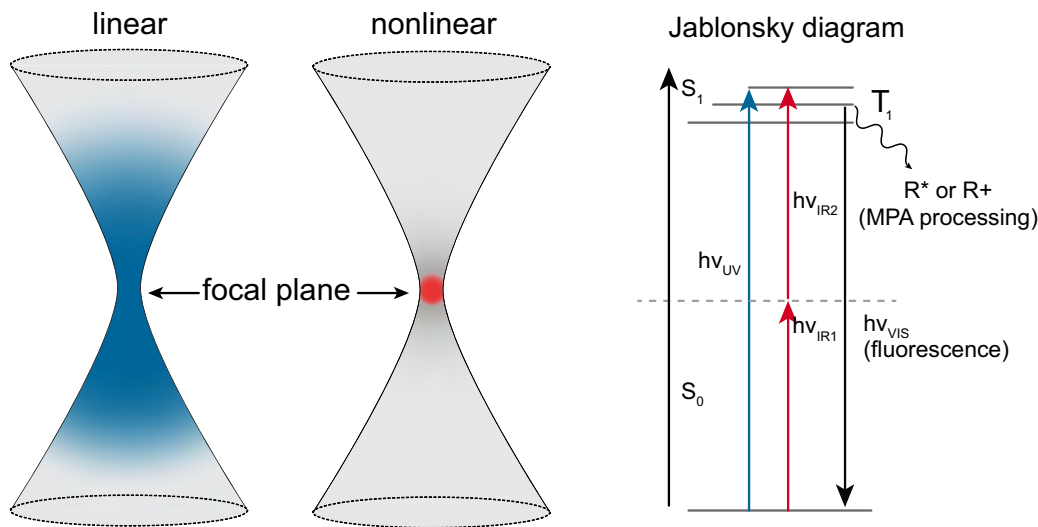


Figure 2.6: Linear and nonlinear absorption principle. In the linear case photons of energy $h\nu$ are absorbed along the focused Gaussian beam in accordance with the Beer-Lambert law (left). Nonlinear absorption requires high local photon density within a short time window of a few fs. Therefore, the absorption probability rapidly decrease away from the focus of the laser beam (middle). In the Jablonsky diagram (right) the linear and 2-photon cases are further illustrated. The required energy to excite a molecule can be absorbed by a single photon of $E_{phot} = h\frac{c}{\lambda_{UV}}$ or simultaneous absorption of two photons of half the energy $E_{phot} = h\frac{c}{\lambda_{IR}}$. From the excited state, the molecule can emit a photon (fluorescence) or relax via intersystem crossing into the triplet state T_1 . In this excited state the molecule can generate radicals which can be used for lithography-based applications.

Depending on the pulse shape and the order of the absorption the factor $g^{(n)}$ is defined, which can be calculated by solving using the respective intensity distribution. For a Gaussian pulse shape the 2PA rate is given by [126]

$$k_{2,Gauss} = 0.66 \cdot \frac{\sigma_2}{R\tau} \left(\frac{I_{avg}}{E_{phot}} \right)^2 \quad (2.8)$$

with the relation between average and peak intensity [128]

$$I_0 = 0.94 \cdot \frac{I_{avg}}{R \cdot \tau}. \quad (2.9)$$

For a sech^2 shape the 2PA rate is

$$k_{2,sech^2} = 0.59 \cdot \frac{\sigma_2}{R\tau} \left(\frac{I_{avg}}{E_{phot}} \right)^2 \quad (2.10)$$

with [128]

$$I_0 = 0.88 \cdot \frac{I_{avg}}{R \cdot \tau}. \quad (2.11)$$

From these equations it is evident that nonlinear processes such as 2PA requires short pulse durations to generate sufficiently high peak intensities [126].

2.5 Generation of Ultrashort Pulses

Because of the short lifetime span of the virtual state 2PP requires ultrashort laser pulses. These pulses are defined with a pulse duration τ of 1 ps or less. For a given average laser power, the intensity (and therefore the photon density) is higher by six orders of magnitude for a system with repetition rate of 80 MHz and pulse duration τ of 100 fs (described in detail in Sec. 2.6.1). Because of average laser powers of a few hundred mW [39], there is almost no heating of the sample during the process when comparing 2PP to high energy processes such as SLM and SLS, where average laser powers of a few hundred Ws are used [79]. For such short durations, optical shutters or Q-switching can no longer be used. The most common method to generate these pulses is mode locking [129]. This can be done actively by periodic modulation of the laser losses at the same frequency as the pulse repetition rate. This is usually achieved by the use of acousto-optic modulators (AOMs). Passive modelocking is done by the use of saturable absorber, as their modulation frequency is higher than that of an electronic modulator. These components introduce a fixed phase-relation for the individual cavity modes. This phase-relation leads to constructive interference within a limited time-window, creating ultrashort pulses (Fig. 2.7, left) A third method of mode locking, is regenerative mode locking, which, similarly to the active case, uses an AOM to periodically modulate the losses [130]. In the active case this is done via radiofrequency signal generated by a stable crystal oscillator at a fixed frequency. For regenerative mode locking, the modulation frequency is derived directly from the laser cavity itself. This is done to allow changes in the laser cavity. For active modelocking the radiofrequency signal needs to be closely matched to the cavity length, as the modulation frequency must match one round-trip time of the laser. A mismatch will cause relaxation oscillations. As the frequency is derived directly from the laser cavity, changes in

2 Theory

the laser cavity can be adjusted. This is especially important, since the cavity length has to be adjusted to compensate group velocity dispersion (GVD) [131].

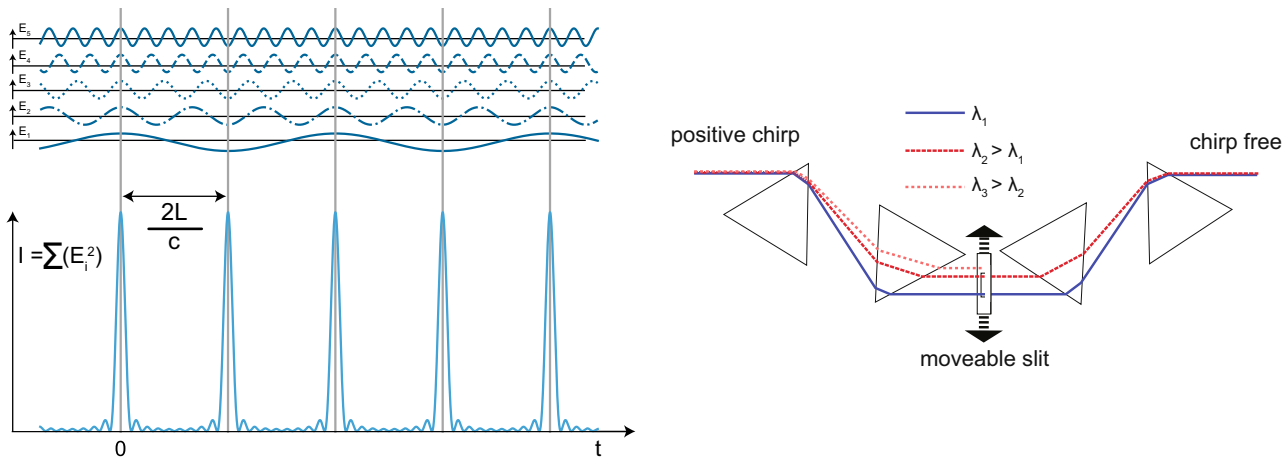


Figure 2.7: Mode locking principle (left). If all modes within a laser cavity have a fixed phase relation, constructive interference only happens in a short time window creating ultrashort laser pulses. Four prism sequence for a tunable laser (right). This sequence is required to compensate GVD caused within the laser cavity. An adjustable slit is added to this sequence to allow narrow tuning windows for ultrashort pulses.

2.5.1 Tunable Lasers

Tunable lasers are lasers with adjustable output wavelength. While tunable lasers are usually operated under continuous wave conditions, it is also possible to realize tunable fs-lasers. The gain-bandwidth of the laser is determined by the atomic or molecular energy levels of the gain medium. Atomic gas lasers tend to have relatively narrow bandwidth. Molecular dye and solid state systems exhibit broader bandwidth. Doping the laser gain medium with transition metal ions allows for a broad gain bandwidth [132]. A commonly used example is the titanium (Ti^{3+} doped sapphire (**Ti:Sa**), which offers tuning ranges from 650–1100 nm. However, due to the longer lengths of material (compared to tunable dye-lasers) the GV within the cavity needs to be compensated (see also Sec. 2.5.2). Tuning of the laser is done by an adjustable slit placed between two prisms which separate the spectral components (Fig. 2.7, right) [131, 133].

2.5.2 Dispersion Compensation

Dispersion is a phenomenon describing the dependence of the phase velocity by the frequency of the traveling electromagnetic wave. Dispersion caused by optical components, also called chromatic dispersion, is an undesired effect as it affects the pulse duration. As the 2PA rate is inversely proportional to τ , a pulse broadening can severely limit 2PP applications. This effect can be counteracted by increasing the average laser power P and with it I_{avg} . However as $I_0 \propto \tau^{-1}$, the required laser powers would quickly exceed the limit of available laser systems. Decreasing the scanning speed increases the processing time. Therefore, compensating pulse broadening is essential for the effective performance of 2PL setups. In general, dispersion de-

scribes a change in the phase velocity v_{Ph} of a traveling wave within an material with refractive index n , which depends on the wavelength. The phase velocity is given by

$$v_{Ph} = \frac{c}{n} = \frac{\omega}{k}, \quad (2.12)$$

with the speed of light c , the wavenumber k and the angular frequency ω . It describes the velocity at which the phase of a frequency component of the electromagnetic wave propagates. The group velocity of a wave

$$v_G = \frac{d\omega}{dk} \quad (2.13)$$

gives the rate at which the amplitude propagates and therefore information is transported [128]. The differential $d\omega$ can be described by

$$\begin{aligned} \nu \cdot \lambda &= \frac{\omega}{2\pi} \cdot \lambda = c \Rightarrow \omega = \frac{2\pi c}{\lambda} \\ \frac{d\omega}{d\lambda} &= -\frac{2\pi c}{\lambda^2} \Rightarrow \frac{d}{d\omega} = -\frac{\lambda^2}{2\pi c} \cdot \frac{1}{d\lambda} \end{aligned} \quad (2.14)$$

Using Eq. 2.12 to express the wavenumber as $k = \frac{2\pi n}{\lambda}$ leads to

$$\frac{dk}{d\omega} = -\frac{\lambda^2}{2\pi c} \cdot \frac{1}{d\lambda} \left(2\pi c \frac{n(\lambda)}{\lambda} \right) = \frac{1}{c} \left(n - \lambda \frac{dn}{d\lambda} \right). \quad (2.15)$$

Therefore, the velocity v_G in a homogeneous medium is given by

$$v_G = \frac{d\omega}{dk} = \frac{c}{n - \lambda \cdot \frac{dn}{d\lambda}} = \frac{v_{Ph}}{1 - \frac{\lambda}{n} \cdot \frac{dn}{d\lambda}}. \quad (2.16)$$

To now describe the effect of a dispersive medium on the duration of the optical pulse, the GVD is given by the second derivate of the wavenumber by the angular frequency [134]. Continuing the approach from Eq. 2.14 gives

$$\text{GVD} = \frac{d}{d\omega} \left(\frac{1}{v_G} \right) = \frac{d^2 k}{d\omega^2} = \frac{\lambda^3}{2\pi c^2} \left(\frac{d^2 n}{d\lambda^2} \right). \quad (2.17)$$

While the first order derivative ($\frac{dk}{d\omega} = \frac{1}{v_G}$) represents the overall delay of the pulse, the GVD describes the change in pulse shape. For most optical dispersive systems such as optical glass the GVD is positive

$$\frac{d^2 k}{d\omega^2} > 0, \quad (2.18)$$

meaning that longer wavelengths are traveling faster in the dispersive medium than the shorter wavelengths. Due to the bandwidth of fs-laser pulses the pulse is broadened, which is called a positive chirp (Fig. 2.8, top). Multiplying the GVD with the length of the respective dispersive element leads to the group delay dispersion (**GDD**) given in fs^{-2} . As 2PP requires high photon densities, such a chirped pulse can drastically affect the system performance [135]. For dispersion compensation, negative GVD is added to the pulse before the optical elements. This can be done for specific wavelengths using mirrors, which apply negative chirp to the

beam during reflection [136]. Alternatively, a two-prism construction can be used (Fig. 2.8, bottom). Here, the wavelength dependent angle of refraction leads to a runtime difference for the individual wavelengths. The position of the prisms can be changed by a motor to increase or reduce the negative GVD [137].

2.5.3 Autocorrelation

An autocorrelator is the most common instrument to measure ultrashort optical pulses. A pulsed laser beam is split into two beams of equal intensity. Using an adjustable mirror a runtime difference of Δ_x is introduced along one beam path. This change in runtime results in a phase change of $\tau = \frac{\Delta_x}{c}$. The two beams are then recombined in a nonlinear crystal for second harmonic generation (SHG). The frequency doubled signal of the crystal depends on the pulse overlap. By recording the output system over the runtime difference, the pulse duration can be extracted. There are two types of autocorrelator systems. The interferometric autocorrelator recombines the two beams in a collinear fashion. This method exhibits a constant background signal due to the two beams and the second harmonic generation SHG-crystal signal being emitted in the same direction. For background-free autocorrelation the two beams are displaced by retro prisms and then recombined using a focusing lens with the SHG crystal placed positioned at the focal length of the lens. With this setting (visualized in Fig. 2.9) the background signal can be cut off by a pinhole, allowing only the SHG signal to reach the recording photo diode. The recorded autocorrelator signal over runtime difference Δt represents the time integration over two convoluted functions. Therefore, one needs to take the pulse shape to calculate the pulse duration τ from the FWHM of the autocorrelator curve τ_{AC} . This relation is $\tau = \frac{1}{\sqrt{2}} \cdot \tau_{AC}$ for Gaussian-shaped pulses and $\tau \approx 0.648 \cdot \tau_{AC}$ for hyperbolic secant-shaped pulses [138, 139].

2.5.4 Laser Intensity Measurement

The ultrafast nature of pulsed laser makes direct measurement of the time dependent intensity distribution $I(t)$ a technically challenging task (as discussed in Sec. 2.4). Because of this $I(t)$ is usually given by the peak intensity

$$I_0 = \frac{2 \cdot P_0}{\pi w_0^2}. \quad (2.19)$$

The relationship between I_0 and the average intensity I_{avg} was shown in Eq. 2.9. P_0 has to be calculated indirectly by measuring the energy of a single pulse E_p and the pulse duration τ . Usually, the average output power P is measured by methods such as powermeters and E_p is calculated using the pulse repetition rate R [128]. The pulse duration is determined via autocorrelator. For a Gaussian beam profile, P_0 and I_0 turn to

$$\begin{aligned} P_0 &= 2 \cdot \sqrt{\frac{\ln(2)}{\pi}} \frac{E_p}{\tau} = 2 \cdot \sqrt{\frac{\ln(2)}{\pi}} \frac{P_{out}}{\nu \cdot \tau}, \\ I_0 &= \frac{2 \cdot P_0}{\pi w_0^2} = 4 \cdot \sqrt{\frac{\ln(2)}{\pi}} \cdot \frac{P_{out}}{\pi w_0^2 R \cdot \tau}. \end{aligned} \quad (2.20)$$

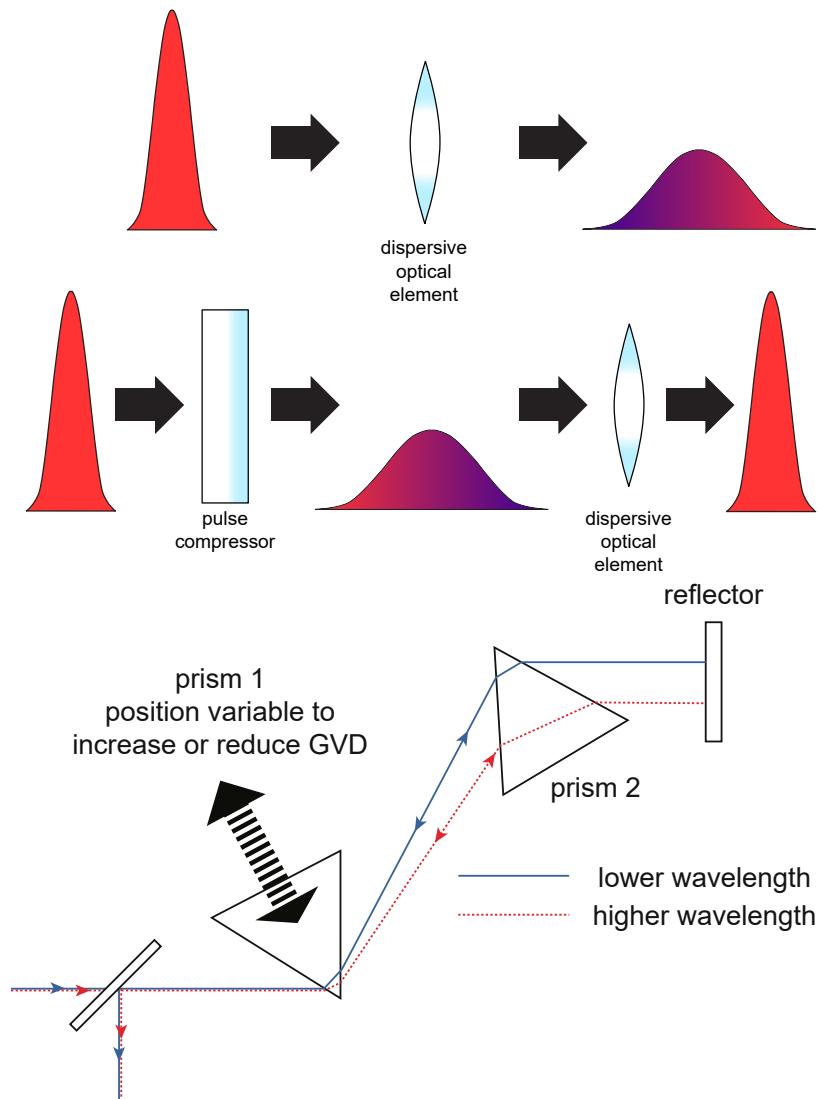


Figure 2.8: Dispersion compensation (top). Due to the bandwidth of a laser pulse, optical elements induce positive GVD, which leads to a broadening of the pulse. This effect can be compensated by introducing negative GVD before the optical elements so that the pulse duration is minimized after the optical components. This can be done by introducing a longer runtime for higher wavelengths. As these wavelengths later travel faster through the dispersive optics, this runtime is precompensated by two prisms (bottom). Using a motorized prism allows more flexibility when adjusting the runtime difference.

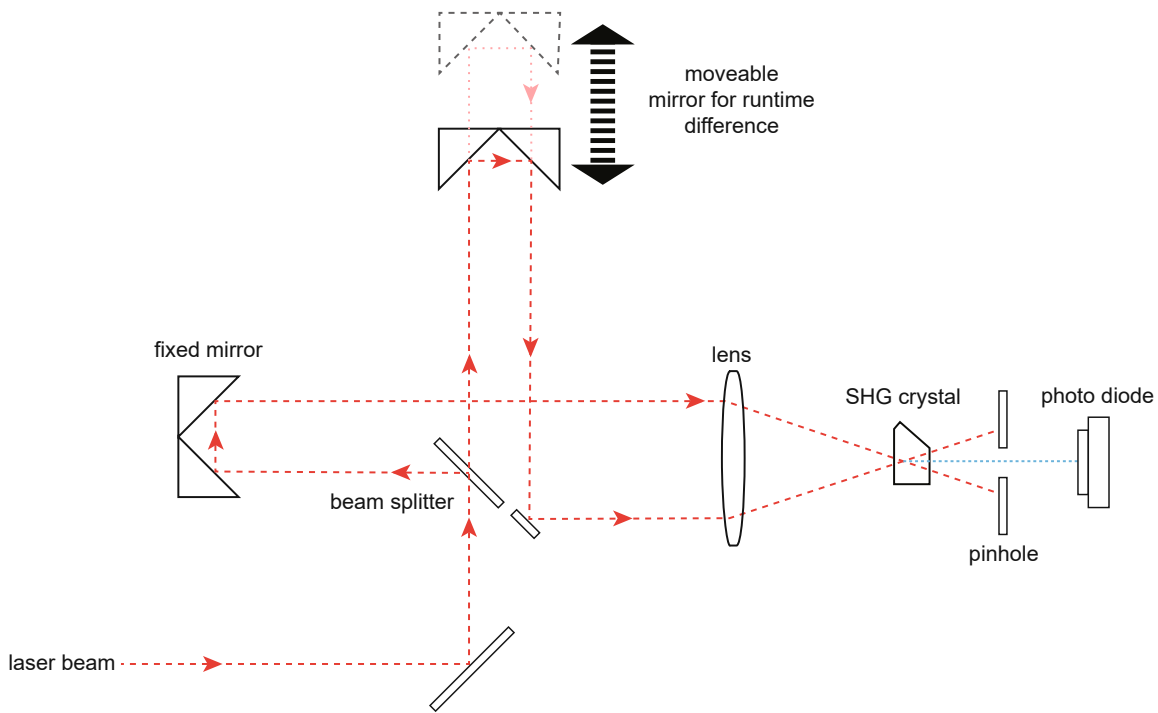


Figure 2.9: Autocorrelator principle. The incoming laser beam is split in two beams of equal intensity. A moveable mirror allows to add a runtime difference to one beam before both are recombined into a SHG crystal using a lens. The frequency doubled output signal is recorded by a photodiode. Correlating the signal strength and runtime difference allows to calculate the pulse duration τ .

2.6 Volume Pixel

In 2PP the polymerization is confined to a limited voxel. This volume is determined by optical considerations, as well as chemical ones. First, the number of photons required to initiate 2PA-processes is determined by the intensity distribution of a focused Gaussian beam. Secondly, the density of radicals ρ produced by fs-laser pulses has to reach a threshold concentration. This section focuses on the various processes affecting the dimensions of the voxel by first introducing the general theory of a focused Gaussian beam (Sec. 2.6.1). This model is then modified to consider the case of nonlinear absorption (Sec. 2.6.2). Lastly, the chemical considerations governing the polymerization threshold are discussed (Sec. 2.6.3).

2.6.1 Focused Gaussian Beam

When focusing a laser with a lens the waist ω_0 at the focal plane is given by the geometries of the lens [128]

$$2 \cdot \omega_0 = \frac{4 \cdot \lambda \cdot f}{\pi \cdot D}, \quad (2.21)$$

where λ is the laser wavelength, f the focal length of the lens and D the diameter of the lens. This equation assumes that the beam is of the same size as the lens diameter D . For smaller beams the diameter of the incoming collimated beam has to be used. Therefore, a larger beam leads to a smaller beam waist ω_0 and a higher photon density. Because of this relation, beam expanders are used in optical setups to enlarge the beam before focusing, in order to gain higher energy density at the focal point.

The width of the beam $\omega(z)$ for any position along the z -axis can be described by the following relation

$$\omega(z) = \omega_0 \cdot \sqrt{1 + \left(\frac{z}{z_R}\right)^2}, \quad (2.22)$$

where z is the distance along the z -axis, ω_0 the beam waist and z_R the Rayleigh length [140]. The Rayleigh length is the distance z_R from the center, where the area of the beam has doubled (or alternatively $\omega(z_R) = \sqrt{2} \cdot \omega_0$ as shown in Fig. 2.10) [128].

$$z_R = \frac{\pi \cdot \omega_0^2}{\lambda} \quad (2.23)$$

Eq. 2.22 and 2.23 describe an ideal Gaussian beam. The discrepancy between measured $z_{R,real}$ to the ideal Gaussian $z_{R,ideal}$ is known as M^2 or beam quality factor and calculated by

$$M^2 = \frac{z_{R,real}}{z_{R,ideal}} = z_{R,real} \cdot \frac{\lambda}{\pi \cdot \omega_0^2}, \quad (2.24)$$

Knowing, z_R , λ and ω_0 the beam can be fully described. For larger distances from the focus $\omega(z)$ increases linearly, which gives the total divergence angle

$$\Theta = 2 \cdot \theta \approx 2 \cdot \frac{\lambda}{\pi \omega_0}. \quad (2.25)$$

As this angle is inversely proportional to ω_0 , a smaller beam shows a larger divergence behavior.

2 Theory

Because of this relation, beam expanders are also used in optical setups where the laser beam needs to travel longer distances. In these systems a beam expander increases the beam size in order to reduce the beam divergence angle. That way, a better collimation is upheld for longer optical paths [128].

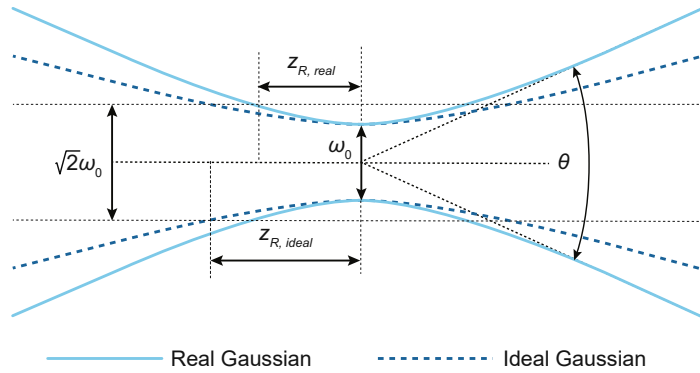


Figure 2.10: Width $w(z)$ of a focused beam (solid line) and the ideal focused Gaussian beam (dashed line) along the z -axis. The Rayleigh length z_R is defined as the distance from the waist ω_0 where the width has increased to $\sqrt{2} \cdot \omega_0$. As the real Gaussian diverges faster, $z_{R,real}$ is smaller than the ideal $z_{R,ideal}$. Θ is the total divergence angle, which can be used to approximate the beam in the far field.

The previously discussed beam waist ω_0 is defined by a 2D-Gaussian distribution

$$I(\tilde{x}, \tilde{y}) = I_0 \cdot \exp\left(-\frac{1}{2} \cdot \left(\frac{\tilde{x} - x_0}{\sigma_x}\right)^2\right) \cdot \exp\left(-\frac{1}{2} \left(\frac{\tilde{y} - y_0}{\sigma_y}\right)^2\right), \quad (2.26)$$

which describes the local intensity distribution of the beam at any position z along the axis. The waist is then defined as the radial distance where the intensity drops to $I_0 \cdot e^{-2}$. This can easily be extracted from Eq. 2.26 which was simplified to

$$I(x, y) = I_0 \cdot \exp\left(-\frac{1}{2} \cdot \left(\frac{x}{\sigma_x}\right)^2\right) \cdot \exp\left(-\frac{1}{2} \left(\frac{y}{\sigma_y}\right)^2\right), \quad (2.27)$$

by the use of coordinate translation ($x = \tilde{x} - x_0$, $y = \tilde{y} - y_0$). To extract the radial position ω_x of the waist, the requirement is

$$I(\omega_x, y) = I_0 \cdot \exp -2 \cdot \exp\left(-\frac{1}{2} \left(\frac{y}{\sigma_y}\right)^2\right) = I_0 \cdot e^{-\frac{1}{2} \left(\frac{\omega_x}{\sigma_x}\right)^2} \cdot e^{-\frac{1}{2} \left(\frac{y}{\sigma_y}\right)^2}. \quad (2.28)$$

After canceling, this simplifies to

$$\exp(-2) = \exp\left(-\frac{1}{2} \left(\frac{\omega_x}{\sigma_x}\right)^2\right), \quad (2.29)$$

$$2 = \frac{1}{2} \left(\frac{\omega_x}{\sigma_x}\right)^2. \quad (2.30)$$

From this derives the relation between σ_x and ω_x

$$\omega_x = 2 \cdot \sigma_x. \quad (2.31)$$

The same approach can be used for ω_y

$$\omega_{x,y} = 2 \cdot \sigma_{x,y}. \quad (2.32)$$

An alternative description for the beam shape is the full width at half maximum (FWHM), where the characteristic point is the distance from the distribution's peak to the point where the intensity has dropped to half its maximum value:

$$\begin{aligned} I(x_f, y) &= \frac{1}{2} \cdot I_0 \cdot \exp\left(-\frac{1}{2}\left(\frac{y}{\sigma_y}\right)^2\right), \\ I(x_f, y) &= I_0 \cdot \frac{1}{2} \cdot e^{-\frac{1}{2}\left(\frac{y}{\sigma_y}\right)^2} = I_0 \cdot e^{-\frac{1}{2}\left(\frac{x_f}{\sigma_x}\right)^2} \cdot e^{-\frac{1}{2}\left(\frac{y}{\sigma_y}\right)^2}, \\ \ln\left(\exp\left(-\frac{1}{2}\frac{x_f^2}{\sigma_x^2}\right)\right) &= \ln\left(\frac{1}{2}\right) = \ln\left(2^{-1}\right) = -\ln(2). \end{aligned} \quad (2.33)$$

Therefore, the full width at half maximum is defined as

$$\text{FWHM}_x = 2 \cdot x_f = 2 \cdot \sqrt{2 \cdot \ln(2)} \cdot \sigma_x. \quad (2.34)$$

This is also valid for FWHM_y . A radially symmetric Gaussian distribution is assumed ($\omega_x = \omega_y = \omega_0$ and $\text{FWHM}_x = \text{FWHM}_y$) for a non astigmatic laser beam.

2.6.2 Writing Resolution

The shape of the focused beam determines the minimum line spacing in lateral and vertical direction required for 2PP processing. For linear absorption the point spread function (**PSF**) can be approximated by a Gaussian distribution (Sec. 2.6.1)

$$I_{1P} = I_0 \exp\left(-\frac{2r^2}{\omega_0^2}\right) = I_0 \exp\left(-\frac{r^2}{2\sigma^2}\right). \quad (2.35)$$

The beam waist ω_0 for given wavelength λ and numerical aperture of an objective (NA) can be calculated by expressing the variance as [141]

$$\sigma \cong \frac{0.255 \cdot \lambda}{\text{NA}}. \quad (2.36)$$

From this definition the relationship for the beam radius $\omega_{xy,1P}$ defined by e^{-2} (Sec. 2.6.1) is derived as

$$\omega_{xy,1P} \cong 2 \cdot \sigma = \frac{0.45 \cdot \lambda}{\text{NA}}. \quad (2.37)$$

To describe the PSF for the nonlinear case the PSF is squared

$$I_{1P}^2 = I_0^2 \exp\left(-\frac{4r^2}{\omega_0^2}\right). \quad (2.38)$$

Eq. 2.38 shows, that for a given wavelength λ 2PA can achieve a $\sqrt{2}$ higher resolution than linear absorption without taking chemical processes into account (Fig. 2.11).

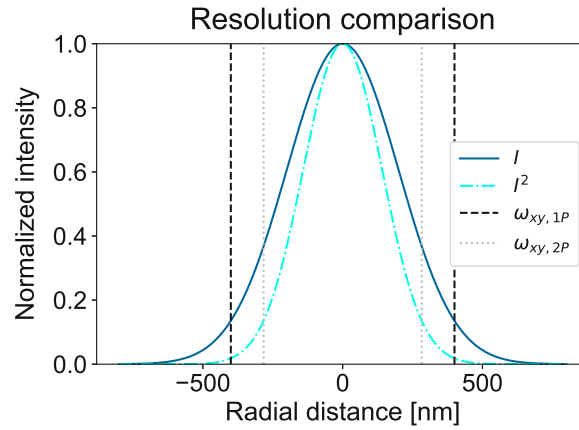


Figure 2.11: Intensity distributions for linear and nonlinear absorption. As 2PA is a nonlinear process its probability scales with the squared intensity I^2 (normalized to the linear maximum I_0 for better comparison). Therefore, 2PA allows offers an increase in resolution of $\sqrt{2}$.

For the 2-photon case this waist is reduced by $\sqrt{2}$. An in-depth analysis and calculation of the 2-photon voxel dimensions was done by Zipfel et al. [142], based on numerical calculations done by Richards and Wolf [143]. The calculated voxels were used for multiphoton microscopy calculation, but they also apply for the 2PP-voxel. For a given NA and λ the lateral voxel radius can be estimated by Eq. 2.39.

$$\omega_{xy,2PP} = \begin{cases} \frac{0.320 \cdot \lambda}{\sqrt{2} \cdot \text{NA}}, & \text{NA} \leq 0.7 \\ \frac{0.325 \cdot \lambda}{\sqrt{2} \text{NA}^{0.91}}, & \text{NA} > 0.7 \end{cases} \quad (2.39)$$

The horizontal voxel radius also depends on the refractive index n and is given by

$$\omega_{z,2PP} = \frac{0.532 \cdot \lambda}{\sqrt{2}} \left(\frac{1}{n - \sqrt{n^2 - \text{NA}^2}} \right). \quad (2.40)$$

All estimates were calculated by using e^{-1} , therefore the added $\sqrt{2}$ in the respective denominators. The volume of the voxel can be approximated by using the model by Zipfel et al. and written as

$$V_{Voxel,2PP} = \pi^{\frac{3}{2}} \cdot \frac{\omega_{xy,2PP}^2 \cdot \omega_{z,2PP}}{0.68} \quad (2.41)$$

The ellipsoid volume is modified by 0.68 to take the wings of the PSF far from the focus into account [142].

2.6.3 Threshold Intensity

In addition to these optical considerations, chemical processes need to be taken into account when defining the voxel dimensions. The density of radicals ρ produced by fs-laser pulses determines the degree of polymerized material. This distribution is given by the rate equation

$$\frac{\partial \rho}{\partial t} = (\rho_0 - \rho) \sigma_2 N^2. \quad (2.42)$$

It is defined by the primary initiator particle density ρ , the photon flux $N(r, t, z)$ and the 2PA cross section σ_2 (Sec. 2.4) [43]. At the focal plane ($z = 0$) the light distribution can be approximated by the Gaussian distribution

$$N(r, t) = N_0(t) \cdot \exp\left(\frac{-2r^2}{\omega_0^2}\right). \quad (2.43)$$

The photon flux is assumed constant over time ($N_0(t) = N_0$). Solving Eq. 2.42 returns

$$\frac{\rho_0 - \rho}{\rho_0} = \exp\left(-\sigma_2 N^2 t\right). \quad (2.44)$$

Polymerization of the resin occurs when the density of radicals ρ exceeds a certain minimum concentration, referred to as threshold concentration ρ_{th} . The voxel diameter d is defined as the region where this condition is met ($\rho \geq \rho_{th}$) [144].

$$\begin{aligned} \frac{\rho_0 - \rho_{th}}{\rho_0} &= \exp\left(-\sigma_2 t \cdot N^2\right) \\ \ln\left(\frac{\rho_0 - \rho_{th}}{\rho_0}\right) &= -\sigma_2 t \cdot N^2 \Rightarrow \ln\left(\frac{\rho_0}{\rho_0 - \rho_{th}}\right) = \sigma_2 t \cdot N^2 \end{aligned} \quad (2.45)$$

Substitution of Eq. 2.43 into Eq. 2.45, with

$$C_{mat} = \ln\left(\frac{\rho_0}{\rho_0 - \rho_{th}}\right) \quad (2.46)$$

yields

$$\begin{aligned} C_{mat} &= \sigma_2 t \cdot \left(N_0 \exp\left(\frac{-2r^2}{r_0^2}\right)\right)^2 \Rightarrow \sqrt{\frac{C_{mat}}{\sigma_2 N_0^2 t}} = \exp\left(\frac{-2r^2}{\omega_0^2}\right) \\ \ln\left(\sqrt{\frac{C_{mat}}{\sigma_2 N_0^2 t}}\right) &= \frac{-2r^2}{\omega_0^2} \Rightarrow \frac{1}{2} \cdot \ln\left(\frac{\sigma_2 N_0^2 t}{C_{mat}}\right) = \frac{2r^2}{\omega_0^2} \\ r &= \frac{d}{2} = \frac{\omega_0}{2} \cdot \sqrt{\ln\left(\frac{\sigma_2 N_0^2 t}{C_{mat}}\right)}. \end{aligned} \quad (2.47)$$

For a fs-laser, the pulse duration τ and repetition rate ν need to be taken under consideration in addition to the exposure time t ($t \Rightarrow n \cdot \tau$ with $n = \nu \cdot t$) [144]. Therefore, the lateral voxel diameter ($d = 2 \cdot r$) is given by

$$d = \omega_0 \cdot \sqrt{\ln\left(\frac{\sigma_2 N_0^2 n \tau_L}{C_{mat}}\right)}. \quad (2.48)$$

The horizontal voxel length l is obtained by substituting an axial Gaussian distribution

$$N(z) = \frac{N_0}{1 + \frac{z^2}{z_R^2}} \quad (2.49)$$

into Eq. 2.45. Solving for $l = 2 \cdot z$ yields

$$l(P, t) = 2z_R \cdot \sqrt{\left(\frac{\sigma_2 N_0^2 n \tau_L}{C_{mat}}\right)^{\frac{1}{2}} - 1}. \quad (2.50)$$

The number density of photons N_0 depends on the laser system used for the 2PP experiments. It is described as the number of photons per area

$$N_0 = \frac{n_{phot}}{\omega_0^2 \pi} = \frac{1}{\omega_0^2 \pi} \cdot \frac{E}{\hbar \omega_L} = \frac{I_0}{\hbar \omega_L}, \quad (2.51)$$

with the single photon energy $E_{phot} = \hbar \omega_L$ and the laser intensity I_0 . Inserting the I_0 for pulsed lasers (Eq. 2.20), the number density of photons is given by

$$N_0 = \frac{1.87}{\omega_0^2 \pi} \cdot \frac{P}{\nu \tau \hbar \omega_L}. \quad (2.52)$$

For a given wavelength most parameters can be assumed constant such as the photon energy $\hbar \omega_L$, pulse duration τ_L , repetition rate ν , Rayleigh length z_R , beam diameter ω_0 and 2PA cross section σ_2 . Therefore, these parameters in Eq. 2.48 and 2.50 can be summed up as optical constant $C_{opt,\lambda}$ as shown in Eq. 2.53,

$$\frac{\sigma_2 N_0^2 n \tau_L}{C_{mat}} = \frac{\sigma_2 \nu \cdot t \cdot \tau_L}{C_{mat}} \cdot \left(\frac{1.87}{\omega_0^2 \pi} \cdot \frac{P}{\nu \tau \hbar \omega_L}\right)^2 = P^2 \cdot t \cdot \frac{C_{opt,\lambda}}{C_{mat}} \quad (2.53)$$

Using this expression the voxel diameter and voxel length for a given wavelength can be written as functions depending on the laser power P and the exposure time t as

$$d(P, t) = r_0 \cdot \sqrt{\ln\left(\frac{P^2 \cdot t \cdot C_{opt,\lambda}}{C_{mat}}\right)}. \quad (2.54)$$

$$l(P, t) = 2z_R \cdot \sqrt{\left(\frac{P^2 \cdot t \cdot C_{opt,\lambda}}{C_{mat}}\right)^{\frac{1}{2}} - 1}. \quad (2.55)$$

From Eq. 2.54 and 2.55 it can be seen that the lateral resolution increases significantly with higher intensities (Fig. 2.12).

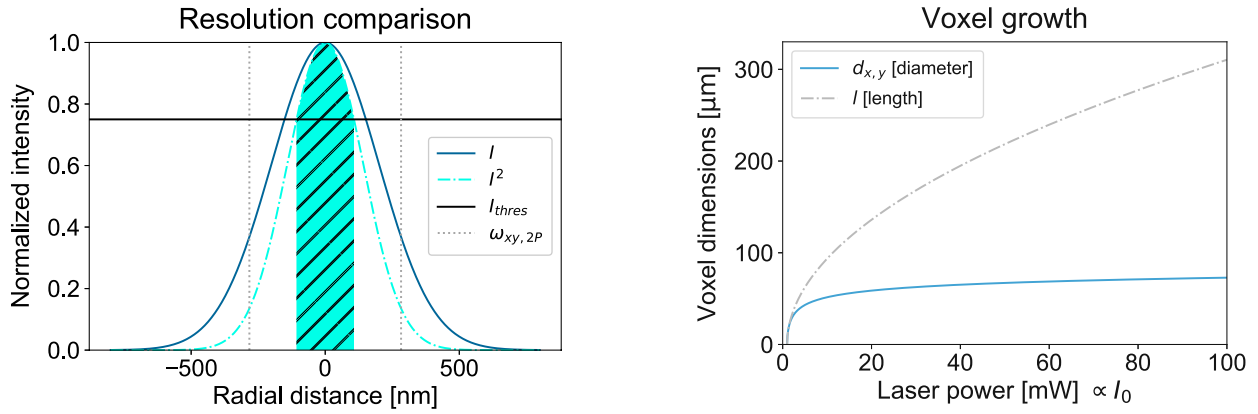


Figure 2.12: Polymerization threshold (left). In addition to a $\sqrt{2}$ increase in resolution, the voxel diameter is determined by a threshold intensity I_{thres} (black line). At I_{thres} sufficient radicals are created to form non-reversible polymers. Comparison between voxel diameter and length (right). The lateral diameter increases significantly faster for higher laser powers.

2.6.4 Polymerization Threshold

The polymerization threshold is given by a hypothetical zero-sized voxel

$$\begin{aligned}
 V_{Voxel}(P_{thres}, t) &= d(P_{thres}, t) \cdot l(P_{thres}, t)^2 = 0 \\
 \Rightarrow d(P_{thres}, t) &= 0 = \omega_0 \cdot \sqrt{\ln\left(\frac{P^2 \cdot t \cdot C_{opt,\lambda}}{C_{mat}}\right)} \\
 e^0 &= 1 = P_{thres}^2 \cdot t \cdot \frac{C_{opt,\lambda}}{C_{mat}} \\
 P_{thres} &= \frac{C_{mat}}{C_{opt,\lambda}} \cdot \sqrt{t^{-1}} = \sqrt{\tilde{C} \cdot t^{-1}}.
 \end{aligned} \tag{2.56}$$

The material parameter C_{mat} is assumed to be constant for a fixed PI-concentration and material. As mentioned the optical parameters $C_{opt,\lambda}$ are assumed constant for a given setup and a selected wavelength. Under these assumptions the threshold power P_{th} is inversely proportional to the square root of the exposure time t or proportional to the square root of the writing speed v

$$P_{thres} = \tilde{C} \cdot \sqrt{t^{-1}} \propto \sqrt{v}. \tag{2.57}$$

This relation also holds true for the voxel length

$$\begin{aligned}
l(P_{thres}, t) = 0 &= 2z_R \cdot \sqrt{\left(\frac{P_{thres}^2 \cdot t \cdot C_{opt,\lambda}}{C_{mat}}\right)^{\frac{1}{2}} - 1} \\
1 &= \left(P_{thres}^2 \cdot t \cdot \frac{C_{opt,\lambda}}{C_{mat}}\right)^{\frac{1}{2}} \\
P_{thres} &= \sqrt{\frac{C_{mat}}{C_{opt,\lambda}} \cdot t^{-1}} \propto v^{\frac{1}{2}}
\end{aligned} \tag{2.58}$$

For experimental evaluation of P_{th} , it is evidently not possible to observe voxel of size zero. Instead the voxel diameters for varying power settings are fitted to Eq. 2.55 to interpolate P_{th} . Alternatively, a minimum diameter size can be selected as the scaling of $P_{th} \propto v^{\frac{1}{2}}$ also applies for a non-vanishing diameter d_{min} . This correlation between writing speed and laser power has been previously reported by various sources for writing speeds in the range of 10 to $100 \mu\text{m s}^{-1}$ [43–45].

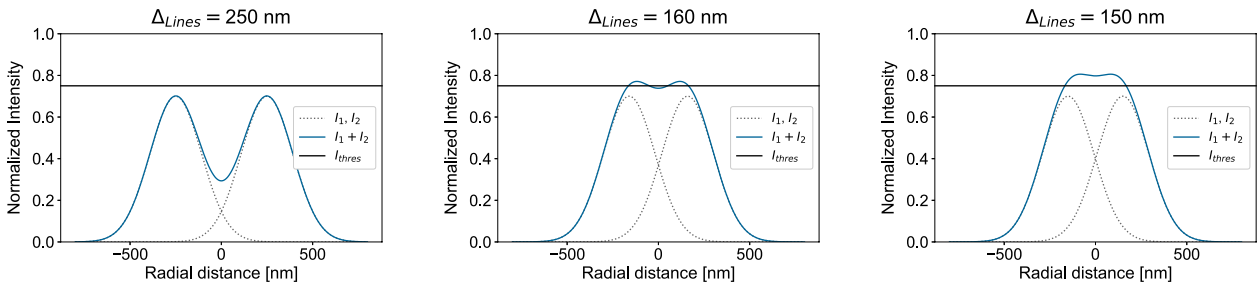


Figure 2.13: Effect of inhibiting molecules such as oxygen on the polymerization threshold. Two voxels are produced at subdiffraction distance of each other. While the individual intensity is below the required threshold intensity I_{thres} (or threshold power P_{th}), the overlap and subsequent depletion of inhibiting molecules at the interstice allows polymerization when exposing the adjacent voxel.

In addition to these geometric considerations, quenching molecules which inhibit the formed radicals affect the resolution and P_{th} . While quenchers can be added to the resin atmospheric oxygen also acts as a quencher. The inhibiting oxygen needs to be consumed before polymerization starts [145]. Quenching directly competes with photopolymerization and is usually considered detrimental to the process, but adding a quencher can be used to increase the feature resolution of single lines [85]. Another effect, which can be observed in most system based on radical polymerization is the formation of features below the threshold intensity, when writing two adjacent lines at sub-diffraction distance. In this case, the quencher in the interstice of the two voxels is consumed. In case of sub-diffraction distance between two lines, the oxygen in the interstice is totally consumed and can not act as a quencher. Therefore, the threshold in polymerization is reduced compared to the case of a single line (Fig. 2.13, right) [146]. This effect is also observed during 2PP of 3D-structures such as cubes, where the required P_{th} is significantly lower than in the single line case.

2.7 Photodynamic Therapy

PDT is a light activated treatment method for cancer and other diseases. It utilizes light-sensitive drugs or photosensitizers (PS), which can be preferably localized in malignant tissues. Compared with traditional therapies such as surgery, radiotherapy, and chemotherapy, PDT has advantages like minimal invasion, and localized (non-thermal) killing of tumor tissue [147]. As a first step the inert PS have to be introduced in the organism. Afterwards they are exposed to light of a specific wavelength, that can be absorbed by the PSs and excite them, which generates cytotoxic species following two further processes. Type I reactions can produce free radicals or superoxide ions resulting from hydrogen or electron transfer and Type II refers to interactions between oxygen and the excited PSs to initiate formation of highly reactive singlet oxygen ($^1\text{O}_2$). While both types occur simultaneously, cell death is predominantly induced by type Type II processes [148]. PDT still faces several problems. The preparation of PS for parenteral use is challenging and cell and tissue damage are depending on the precise localization of the PSs, because of the limited diffusion distance of the generated cytotoxic species in the tissue (~ 20 nm). Furthermore, PDT is limited by the possibility to focus the light source and its penetration depth in the tissue, which is defined by the laser wavelength. Currently approved PDT sensitizers absorb in the visible spectral region up to 700 nm, so the penetration into the tissue is limited by the wavelength to a few millimeters. Potential applications of this technologies are among others cardiovascular diseases, arteriosclerosis, endometriosis or carcinoma in situ and osteosarcoma [149, 150]. PDT was FDA first approved for photofrin (porfimer sodium) in 1993 [151] and in 2016 using a laser source of 630 nm [152].

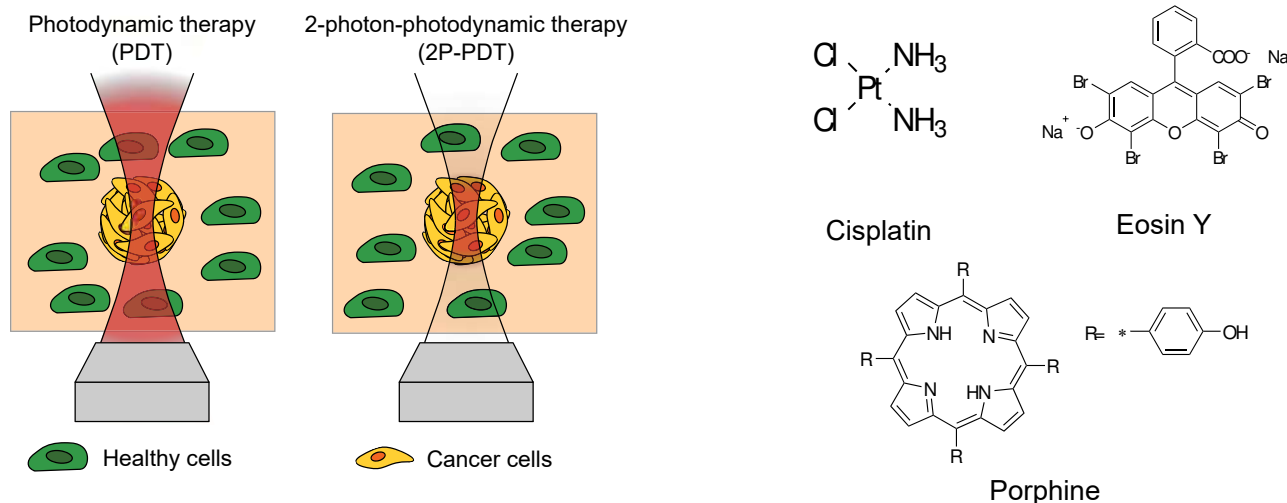


Figure 2.14: PDT principle (left). Conventional PDT uses UV-light sources to activate photosensitive substances which cause cell death. 2P-PDT is localized to the laser focus due to nonlinear absorption. Chemical compounds for cancer-treatment (right). Cisplatin is a commonly used agent for chemotherapy [153], eosin-y is mostly used as acidic red stain for cytoplasm [154] but has also found applications in 2PP [155]. Porphine is a porphyrin derivative which have been reported to exhibit high 2PA cross section σ_2 [156].

2P-PDT shows promise in increasing the light penetration due to the near-infrared nature of

the process (Fig. 2.14). Its principle is nearly the same, but the PS can only absorb the light if they are located in the focus of the exposure laser due to the fact, that a high photon density is necessary for 2PA. The small excitation volume of 2PA promises enhancement of the spatial resolution and therefore less damaging of to healthy tissue around the cancer. A major issue for two-photon application is the poor solubility in of 2PA active sensitizers and low σ_2 (below 50 GM) [157].

In cancer treatment cisplatin is commonly used chemotherapeutic agent. It cross-links with the purine bases on the DNA, which disturbs the DNA repair mechanisms and damages it. Cell death thereby induced in both cancer cells and other cell types. Due to the faster proliferation of cancer cells, this cell type is attacked more frequently than healthy cell types with lower proliferation rate [153]. PS are the main component for PDT. Eosin-y is mostly used as an acidic red stain for cytoplasm [154] but has also been used for 2PP at 1040 nm [155]. Porphine is an achiral porphyrin derivative dye, its large molecules have been previously reported to exhibit high σ_2 [156, 158]. The chemical structures of these materials are shown in Fig. 2.14.

2.8 Z-Scan

The z-scan technique has become a standard method to characterize higher order nonlinearities such as 2PA cross section of PIs [159], which have found broad applications in 3D-nanolithography such as 2PP and PDT [38]. There is an increasing need to characterize the 2PA spectra of newly synthesized PIs for biomedical applications. On the one hand, when such z-scan measurements are performed at the wavelength later used for 2PP, the obtained results might be sufficient for comparison of the expected practical performance of different PIs. On the other hand, the true potential of a certain PI design stays unrevealed, if its complete nonlinear absorption spectrum is not characterized. Matching the laser wavelength to the peak of the 2PA spectrum of a particular compound can result in a few fold increase of the PI's performance. Most z-scan setups are based on optical parametric amplifiers (**OPA**) operating at a single wavelength and are not practical for characterization of 2PA spectra of a PI. 2-photon excited fluorescence (**TPEF**) is also popular for spectral measurements [160]. However, this technology is limited to compounds with fluorescent behavior and extracting absolute values depends on the reference standard or requires a complex setup [161]. White light continuum z-scan (**WLC**) is able to determine absolute cross section values but also requires a complicated optical path [36, 162]. Pulsed fs-lasers offer an alternative approach to the amplified systems, however the high repetition rate tends to cause thermal effects, which have to be eliminated [163].

The z-scan was introduced in 1990 [164] and has been widely employed due to its relatively simple setup [165]. A thin sample (sample length L smaller than the Rayleigh length z_R) is moved in and out of a focused laser beam (see Fig. 2.15) along an axis (usually called the z -axis, hence the name of the technique). Ideally, the laser focus is at the center of the translation stage. A photo diode at the end of the stage collects the transmitted light. The discussed open aperture setup records changes in transmission, which can then be used to extract the 2PA behavior. Adding an aperture before the measurement diode allows measurement of the nonlinear refractive index of a material (dashed line in Fig. 2.15) as it registers the change in the divergence of the beam.

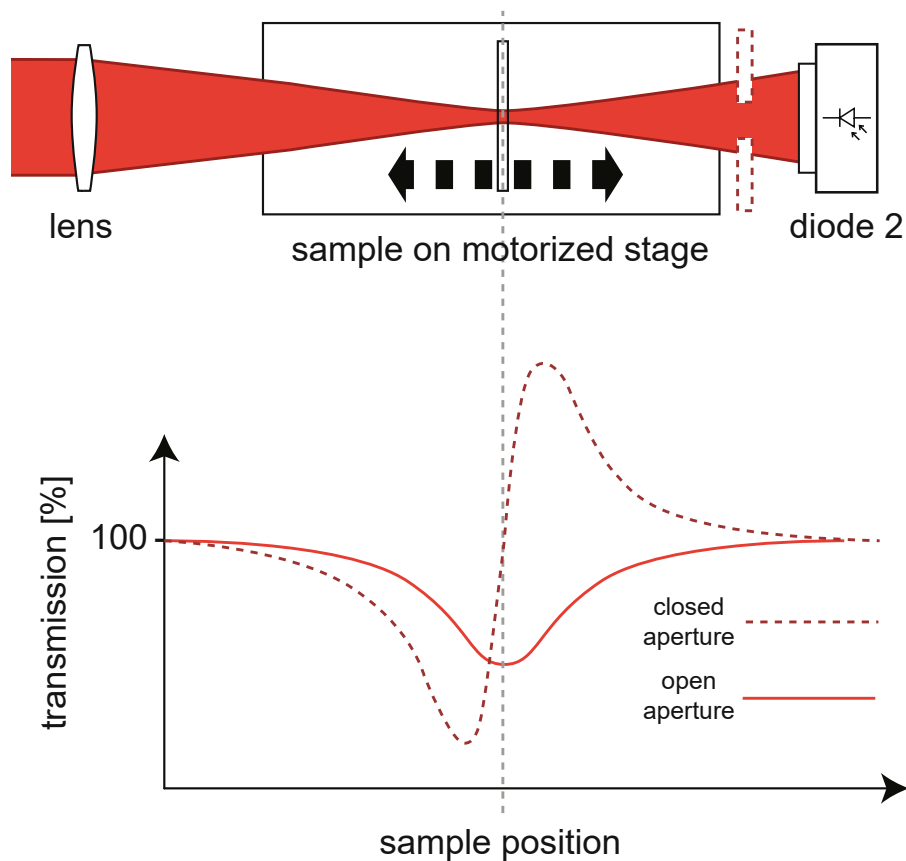


Figure 2.15: Z-scan principle. A thin sample is moved in and out of the focused laser beam. The drop in transmission (solid line) determines the 2PA cross section. The drop depends on a multitude of systemic parameters, which need to be known in advance of the scan. This setup can be modified by adding an aperture (dashed squares before diode) to measure the nonlinear refractive index (dashed line).

2 Theory

To theoretically describe the z-scan, the effects of nonlinear self-action - nonlinear refraction (**NLR**) and nonlinear absorption (**NLA**) - need to be observed. Assuming nearly monochromatic laser light passing through the sample, the nonlinear self-action causes loss in transmission (ΔT).

The polarization is given by

$$P(t) = \epsilon_0 \int_{-\infty}^{\infty} \chi^{(2)}(t-t_1)E(t_1)dt_1 + \int_{-\infty}^{\infty} \int_{-\infty}^{\infty} \chi^{(2)}(t-t_1, t-t_2)E(t_1)E(t_2)dt_1dt_2 + \int_{-\infty}^{\infty} \int_{-\infty}^{\infty} \int_{-\infty}^{\infty} \chi^{(3)}(t-t_1, t-t_2, t-t_3)E(t_1)E(t_2)E(t_3)dt_1dt_2dt_3 + \dots, \quad (2.59)$$

where $\chi^{(n)}$ describes the n-th order response or susceptibility function [166]. The polarization is dependent on the electric field

$$|E(t)| = \text{Re} \left\{ E(t) \cdot e^{i(kr-\omega t)} \right\}, \quad (2.60)$$

which varies slowly over time. For a single frequency input the field can be approximated in the external self-action limit [166]. For this to be applicable, the sample length L needs to be thin compared to the Rayleigh length z_R . In addition, the intensities have to show an integrated phase shift of less than π . This allows us to write the polarization as

$$P(t) = \epsilon_0 \chi E(t) = \epsilon \left[\chi^{(1)} + \chi^{(3)} \frac{|E(t)|^2}{2} \right] \cdot E(t). \quad (2.61)$$

The external self action limit later allows a separation of the wave equation into an equation describing the phase Φ and intensity I . For readability the time dependence was omitted in the following equations ($E = E(t)$, $P = P(t)$). The wave equation

$$\frac{d^2 E}{dz^2} - \frac{1}{c^2} \frac{d^2 E}{dt^2} = \mu_0 \frac{d^2 P}{dt^2} \quad (2.62)$$

is approximated by keeping only susceptibilities up to the 3rd order. Additionally, the slowly varying envelope approximation [167] is used where the complex amplitude of the field $E(r, t)$ varies slowly with r and t . Thus, the higher ordered derivatives

$$\left| \frac{\partial^2 E}{\partial k^2} \right| \ll \left| k \cdot \frac{\partial E}{\partial k} \right| \quad \text{and} \quad \left| \frac{\partial^2 E}{\partial t^2} \right| \ll \left| \omega \cdot \frac{\partial E}{\partial t} \right| \quad (2.63)$$

are ignored. Applying these approximations leads to the wave equation

$$\frac{dE}{dz} + \frac{1}{c} \frac{dE}{dt} = i \frac{\omega}{2\epsilon_0 c} \cdot P. \quad (2.64)$$

A coordinate transformation applied to the system of the traveling wave ($\tau = t - \frac{z'}{x}$, $z' = z$) and with the substitution of the polarization (eq. 2.61) gives

$$\frac{dE}{dz'} = i \frac{\omega}{2c} \cdot P = i \frac{\omega}{2c} \cdot \epsilon \left[\chi^{(1)} + \chi^{(3)} \frac{|E|^2}{2} \right] \cdot E. \quad (2.65)$$

Writing the electric field as $E = E_0 \cdot e^{i\phi}$ then allows splitting the equation into a real and an imaginary part:

$$\frac{dE_0}{dz'} = -\frac{\omega}{2c} \left[\text{Im} \{ \chi^{(1)} \} + \text{Im} \{ \chi^{(3)} \} \frac{E_0^2}{2} \right] \cdot E_0, \quad (2.66)$$

$$\frac{d\Phi}{dz'} = -\frac{\omega}{2c} \left[\text{Re} \{ \chi^{(1)} \} + \text{Re} \{ \chi^{(3)} \} \frac{E_0^2}{2} \right]. \quad (2.67)$$

Since $I \propto E_0^2$ it can be seen that $\chi^{(3)}$ causes phase shifts $d\Phi$ depending on the intensity. Rewriting eq. 2.66 and 2.67 in terms of intensity (considering only the nonlinear induced phase changes) leads to [166]

$$\frac{dI}{dz'} = -\underbrace{\frac{\omega}{2nc} \cdot \text{Im} \{ \chi^{(1)} \}}_{\alpha} \cdot I - \underbrace{\frac{\omega}{n^2 c^2 \epsilon_0} \cdot \text{Im} \{ \chi^{(3)} \}}_{\beta} \cdot I^2 \quad (2.68)$$

and

$$\frac{d\Phi}{dz'} = \frac{\omega}{c} \frac{1}{2n^2 c \epsilon_0} \text{Im} \{ \chi^{(3)} \} \cdot I, \quad (2.69)$$

with the linear refractive index n , the linear absorption coefficient α and the two photon absorption coefficient β . For 2-photon applications the 3rd order nonlinearity is being observed which is a complex quantity

$$\chi^{(3)} = \chi_R^{(3)} + \chi_I^{(3)} \quad (2.70)$$

and can be written as [164]

$$\chi_R^{(3)} = 2n_0^2 \epsilon_0 c \gamma, \quad \chi_I^{(3)} = \frac{n_0^2 \epsilon_0 c^2}{\omega} \cdot \beta. \quad (2.71)$$

A Gaussian beam is used (TEM₀₀) to describe the electrical field's transmission:

$$E(z, r, t) = E_0(t) \cdot \frac{\omega_0}{\omega(z)} \cdot \exp \left(-\frac{r^2}{w(z)} - \frac{ikr^2}{2R(z)} \right) e^{-i\Phi(z,t)}, \quad (2.72)$$

where $R(z)$ is the wavefront, $E_0(t)$ the amplitude of the electric field, $k = \frac{2\pi}{\lambda}$ the propagation vector and $e^{-i\Phi(z,t)}$ describes the radially symmetric phase shifts [168]. The beam waist $\omega(z)$ along the z-axis is given by

$$\omega(z) = \omega_0 \sqrt{1 + \frac{z^2}{z_R^2}}. \quad (2.73)$$

with the Rayleigh length z_R , (Sec. 2.6.1). Since changes in the refractive index Δn affect the phase shift the eq. 2.69 is the following

$$\frac{d\Delta\Phi}{dz'} = \frac{\omega}{c} \Delta n I = \frac{2\pi}{\lambda} \cdot \Delta n I. \quad (2.74)$$

Changes in I (eq. 2.68) are due to the linear (α) and nonlinear (β) absorption coefficients

$$\frac{dI}{dz'} = -\alpha I - \beta I^2. \quad (2.75)$$

2 Theory

It is important to note that while z denotes the position along the beam path z' describes the propagation depth. With the description of the Gaussian beam (Eq. 2.72) these two relations can be solved for the intensity (I_e) at the exit of the sample

$$I_e(z, r, t) = I(z, r, t) \cdot \frac{e^{-\alpha L}}{1 + q(z, r, t)} \quad (2.76)$$

and the phase shift

$$\Delta\Phi(z, r, t) = \frac{k\gamma}{\beta} \ln[1 + q(z, r, t)], \quad (2.77)$$

with

$$q(z, r, t) = \beta \cdot I(z, r, t) \cdot L_{eff} \cdot \frac{\omega_0^2}{\omega(z)^2}. \quad (2.78)$$

The effective sample length

$$L_{eff} = \frac{1 - e^{-2\alpha L}}{\alpha} \quad (2.79)$$

takes the linear absorption into account to describe the sample length without the effects of linear absorption. Combining eq. 2.76 and 2.77 gives the complex field at the exit surface of the sample:

$$E_e = E(z, r, t) \cdot e^{-\frac{\alpha L}{2}} (1 + q(z, r, t))^{ik\gamma/\beta - \frac{1}{2}} \quad (2.80)$$

To describe the electric field E_a at the aperture (the aperture will later vanish for the open aperture z-scan) Huygens principle and a Hankel transformation of zero order can be applied. An alternative approach, used by Sheik-Bahae et al. [164], is the Gaussian decomposition. Here, the complex electric field after exiting the sample is decomposed into a summation of Gaussian beams. The individual beams are propagated towards the aperture, where they are resummed to E_a . The resulting expression contains both refractive and absorptive transmittances which are coupled by a factor $\frac{\beta}{2k\gamma}$. For open aperture z-scans the transmittance is insensitive towards beam distortions and therefore simplifies to a function depending solely on the nonlinear absorption.

The transmitted power $P(z, t)$ can therefore be obtained by integrating Eq. 2.80 over r without the inclusion of the free-space propagation process. This results in the transmitted power [169]

$$P(z, t) = P_i(t) e^{-\alpha L} \frac{\ln[1 + q(z, t)]}{q(z, t)} \quad (2.81)$$

with

$$q(z, t) = \beta \cdot I(t) \cdot L_{eff} \cdot \frac{\omega_0^2}{\omega(z)^2} \quad (2.82)$$

and

$$P_i = \frac{1}{2} \pi \omega_0^2 I_0(t). \quad (2.83)$$

Integrating Eq. 2.81 over time gives the normalized energy transmittance

$$T(z) = \frac{1}{\sqrt{\pi}q(z, 0)} \int_{-\infty}^{\infty} \ln(1 + q(z, 0)e^{-\tau^2})d\tau. \quad (2.84)$$

For the open aperture case, the change in transmission [165] for a given sample position z is described by

$$T(z) = \frac{1}{\sqrt{\pi} \cdot q_0(z, 0)} \int_{-\infty}^{\infty} \ln \left[1 + q_0(z, 0) \cdot e^{-\xi^2} \right] \cdot d\xi \quad (2.85)$$

with

$$\begin{aligned} q(z, 0) &= q_0 \cdot \frac{\omega_0^2}{\omega(z)^2} \\ q(z, 0) &= q_0 \cdot \frac{1}{1 + \left(\frac{z}{z_R}\right)^2} \\ q_0 &= \beta \cdot I_0(\omega_0, P) \cdot L_{eff} \end{aligned} \quad (2.86)$$

The effective cuvette length $L_{eff} = (1 - e^{-\alpha L})/\alpha$ is defined by the cuvette length L and linear absorption coefficient α . For the z -scan, this factor is assumed to be constant if the linear absorption range does not overlap with the spectral range used in the z -scan measurements. The intensity of a temporally stable focused Gaussian beam

$$I_0(\omega_0, P) = 4 \cdot \sqrt{\frac{\ln(2)}{\pi}} \cdot \frac{P}{\pi\omega_0 R\tau} \quad (2.87)$$

depends on the laser power P , beam radius ω_0 , repetition rate R , and pulse duration τ . Knowing all parameters enables extraction of the 2PA cross section

$$\sigma_2 = \frac{h\nu \cdot \beta}{N_A \cdot \rho} \quad (2.88)$$

with the photon energy $h\nu$, concentration of solution ρ , the Avogadro number N_A and the 2PA absorption coefficient β . If $|q_0| < 1$ we can use the geometric series to write Eq. 2.85 as a discrete sum for numerical calculations [164]

$$T(z) = \sum_{m=0}^{\infty} \frac{-q(z, 0)^m}{(m+1)^{\frac{3}{2}}} \quad (2.89)$$

While R is constant over the entire laser spectrum there are four parameters which change significantly with the individual wavelengths (τ , z_R , ω_0 , and P). Therefore, it is paramount to have a library containing the spectral data of these fitting parameters. As σ_2 is an indirectly measured parameter, uncertainty of the laser beam parameters leads to error propagation (exemplified in Tab. 2.1 for a 2PA compound with σ_2 of 150 GM) which can significantly distort the measurement and the reported cross section. Therefore, it is paramount to have a library containing the spectral data of these fitting parameters to reduce this source of errors.

Table 2.1: Uncertainties in the setup parameters can significantly affect the calculated 2PA cross section (σ_2) by up to 30 %. Change in σ_2 calculated by taking reference data for a 2PA absorbing compound with $\sigma_2 = 150 \text{ GM}$ and Eq. 2.86. A beam diameter of $24 \mu\text{m}$, pulse duration of 70 fs and average laser power of 500 mW were used.

Parameter	Pulse Duration	Laser Power	Beam Waist
Fluctuation	$\pm 7 \text{ fs} / \pm 14 \%$	$\pm 50 \text{ mW} / \pm 10 \%$	$\pm 2 \mu\text{m} / \pm 10 \%$
$\Delta(\sigma_2)$	7%	20%	14%

2.8.1 Thermal Lensing

When exposing a sample to a high-powered laser beam, heating of the sample can cause thermal effects which affect the measured data [170, 171]. The absorbed light heats up the sample and the resulting temperature gradient causes a local variation in the sample density. This in turn changes the refractive index and leads to a lens-like behavior of the sample. The heating persists over a characteristic thermal time

$$t_c = \frac{\omega_0^2}{4D} \quad (2.90)$$

after which the sample returns to thermal equilibrium [172]. This coefficient depends on the beam waist ω_0 and the thermal diffusion coefficient D typically in the range of (10^{-3} to $6 \cdot 10^{-3} \text{ cm}^2 \text{ s}^{-1}$) for liquids. For lasers with a repetition rate higher than 0.1 kHz the time between exposure is shorter than t_c causing cumulative heating [170]. To counteract these effects a beam chopper is required to allow the sample to return to equilibrium after being exposed to the laser source [172].

3 Materials and Methods

The z-scan setup, which was designed and assembled over the course of this thesis is described in detail. The measurement procedure and calibration using autocorrelator, beam profiler, oscilloscope and waveplate are summarized as they are required to calculate the 2PA cross section (σ_2) of nonlinear absorbing compounds over the entire laser spectrum. The 2PL setup is outlined with a focus on four objectives, their respective fabrication resolution and the production of structures larger than a single FOV are discussed. A separate section is dedicated to sample preparation and manufacturing. The various methods used in this thesis to characterize 2PP fabricated structures are listed. The use of 2PL for 2P-PDT is summarized. The design and fabrication of microscaffolds fabricated for biomedical applications are shown. Lastly, two experimental methods for the produced microscaffolds are presented. In the first experiment the scaffolds act as microcages to trap cells using Faraday waves. For the second experiment 2PP scaffolds are loaded with hiPSC to induce the growth of hair follicles.

3.1 Z-Scan Setup

The z-scan setup developed during this thesis was designed to characterize synthesized PIs such as M2CMK and DAS [96, 99]. The spectra obtained from z-scan allow to determine the optimal operation wavelength for 2PL-applications. The focus was on a simplified design with few dispersive optics. Furthermore it was not based on OPA, to allow flexible and fast characterization of 2PA compounds. The setup is powered by a high power fs laser oscillator (MaiTai DeepSee, Spectra Physics, Santa Clara, USA) with a tuning range from 690 to 1040 nm. The beam passes through a number of optical components (Fig. 3.1) through a focusing lens onto the sample. A positive and negative achromatic doublet lens with a focal length of 200 mm focusing is used (AC254-200-B, Thorlabs, Newton, United States), with achromatic coating (650 to 1050 nm). A motorized stage (LCS16-025-2(4)5, SMAC, Carlsbad, USA) operated by a one-axis controller (LCC-10, SMAC, Carlsbad, USA) moves the sample into and out of focus. A photodiode (PDA100A-EC, Thorlabs, Newton, United States) measures the transmitted light and a reference photodiode helps to compensate signal fluctuations. An oscilloscope (DS4024, Rigol, Beaverton, USA) records the signals from both diodes. A custom-built beam chopper (142 Hz rotation frequency, 78 μ s on-time) reduces the exposure time of the sample to eliminate thermal effects [163]. Due to the design of the DeepSee pulse compressor, a GDD of 0 fs² cannot be compensated for all wavelengths. In order to use the pulse compressor with the low dispersion of the z-scan a 10 cm quartz block was introduced. For single wavelength z-scans a Galilean beam expander works well but requires manual adjustment for each wavelength. To avoid this and guarantee collimation when changing the wavelength, the setup contains a reflective beam expander (BE04R/M, Thorlabs, Newton, United States). Furthermore, the mirror based expansion does not introduce further dispersive elements into the beam path, allowing to use the pulse measured via autocorrelator for the fitting. To measure the pulse, a flip mirror directs the beam into the autocorrelator. As previously discussed, fluctuations in

3 Materials and Methods

the system variables can cause significant variance in the calculated σ_2 (see Tab. 2.1), therefore minimizing the dispersion and possible pulse broadening is an important aspect to guarantee correct calculation of σ_2 .

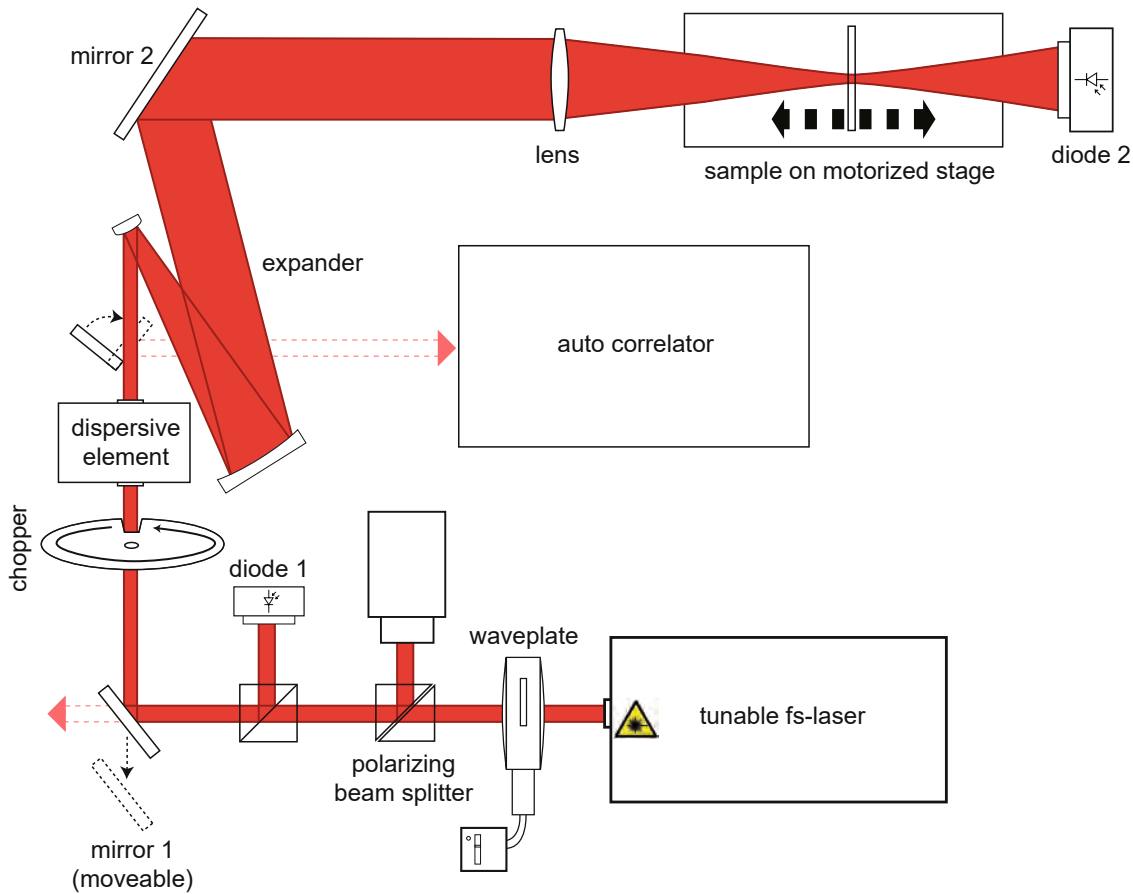


Figure 3.1: Z-scan setup and beam path from the tunable fs-laser to the sample. A waveplate and polarizing beam splitter attenuate the input laser power. Two parabolic mirrors expand the beam by 4x and a lens focuses the beam. A motorized stage moves the sample in and out of focus. Two diodes record the measurement- and reference signal while a mechanical chopper allows to adjust the on/off duration of the signal. A flip mirror directs the beam to the autocorrelator to measure the pulse duration. As this setup is also used for 2PP experiments, mirror 1 can be moved out of the beam path to direct the laser into the 2PP system. To simulate dispersion caused by the 2PP a dispersive element is introduced into the beam path.

An automated Graphical User Interface allows to calibrate the system for a desired spectral range. The calibration routine comprises:

- Relating waveplate angle θ and time averaged laser power P .
- Determining conversion for a given P to voltage recorded by measurement diodes.
- Minimizing pulse duration τ using an autocorrelator.
- Profiling the beam and extracting z_R , ω_0 , and M^2 .

This routine is necessary as the z-scan method extracts σ_2 from the fit parameter q_0 (fitting accuracy previously described in Tab. 2.1). All values are stored in a database within the operating software and data from the z-scan is fitted automatically.

3.1.1 Power and Diode Range

A motorized rotation stage (PRM1Z8, Thorlabs, Newton, United States) controls the angle of the waveplate (467-4210, Eksma Optics, Vilnius, Lithuania) in order to regulate the beam polarization (Fig. 3.1). A polarizing beamsplitter cube (PBS052, Thorlabs, Newton, USA) reflects the s-polarized component of the light while transmitting the p-polarized part. The reflected light is directed into a beam dump. This way, the laser power can be regulated from 1.8 W down to 10 mW. The correlation between waveplate angle and laser power is obtained by fitting the measured power for each rotation angle according to [128]

$$P = P_0 + P_{out} \cdot \cos^2(\theta \cdot a + \phi_0) \quad (3.1)$$

Using a powermeter (Fieldmax II, Coherent Inc, Santa Clara, USA) P is measured before passing the focusing lens for each wavelength in intervals of 5 nm. Due to the periodic nature of the waveplate retarder, rotation angles between 0 and 120° (measurement steps of 3°) are sufficient. To automatically select the optimum measurement window for a given laser power the conversion factor from mW to V is required. Due to the wavelength sensitivity of both measurement diodes (PDA100A-EC, Thorlabs, Newton, United States) as well as the filters (NE20A and NDUV40A, Thorlabs, Newton, United States) the conversion factors from laser power to diode voltage over the entire spectrum need to be known. The system automatically records signals for each wavelength in a given range and step size. The measurement diode triggers the oscilloscope to a minimum signal using the maximum measurement range (2.4 V) to evaluate the optimal signal range. This list of conversion factors guarantees optimal resolution for any given power and wavelength.

3.1.2 Beamprofiler

Because of the possibility to tune the wavelength range in the visible to near infrared spectrum (690 - 1080 nm) the beam profiling is done via CMOS camera (UI-1492LE, IDS, Obersulm, Germany). The camera approach was preferred over the knife edge method since it allowed live imaging without the need for an additional automated component like a movable razor blade. The chip resolution (1.67 μm per pixel) is sufficient to extract the correct beam shape from the image (Fig. 3.2). To calculate the characteristic beam parameters, the 2D-Gaussian beam registered by the camera chip was integrated, resulting in the error function

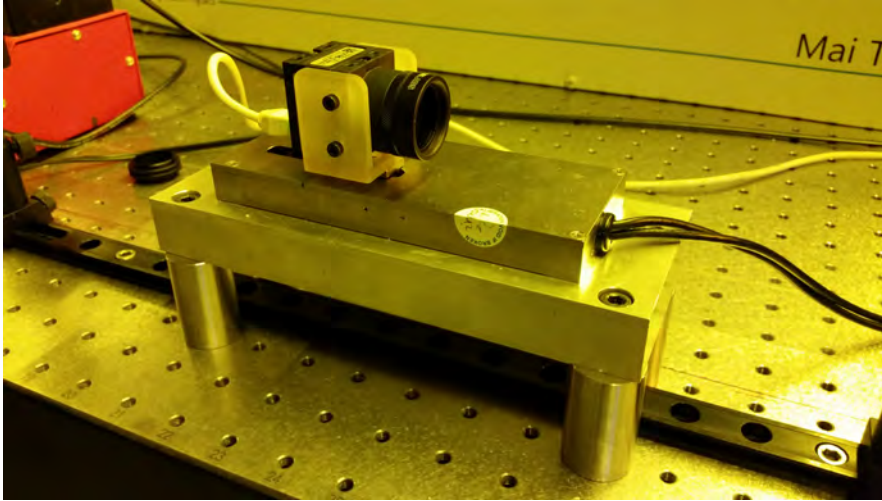


Figure 3.2: Placing a CMOS camera on the movable stage enables profiling of the focused laser beam. The camera is moved in and out of focus and the recorded image is fitted using second order image moments to extract the characteristic beam data.

$$erf = \frac{2}{\sqrt{\pi}} \int_0^x e^{-u^2} du. \quad (3.2)$$

Fitting the integral of the recorded beam was preferred over the standard Gaussian fit as the error is lower for numerical integration compared to differentiation [173]. Depending on the order of the moment the average or variance of a distribution can be extracted. Given a continuous 2D distribution $f(x, y)$, the raw moment of order $p + q$ is defined as [174]

$$M_{pq} = \int_{-\infty}^{+\infty} \int_{-\infty}^{+\infty} x^p y^q f(x, y) dx dy \quad (3.3)$$

with the central moments given by

$$\mu_{pq} = \int_{-\infty}^{+\infty} \int_{-\infty}^{+\infty} (x - \bar{x})^p (y - \bar{y})^q f(x, y) dx dy. \quad (3.4)$$

For a discrete distribution (i.e. a pixel image) Eqs 3.3 and 3.4 are modified to [174, 175]

$$M_{ij} = \sum_x \sum_y x^i y^j I(x, y), \quad (3.5)$$

$$\mu_{pq} = \sum_x \sum_y (x - \bar{x})^p (y - \bar{y})^q f(x, y) dx dy \quad (3.6)$$

With the mean values

$$\bar{x} = \frac{M_{10}}{M_{00}}, \quad \bar{y} = \frac{M_{01}}{M_{00}}. \quad (3.7)$$

The 2nd order moments (M_{20}, M_{02}) correspond to the variances of the Gaussian distribution (μ_x, μ_y). Fitting these moments using least-square algorithms allows to extract the distribution parameters. This process is repeated for multiple stage positions (0-24 mm in 1 mm steps). The obtained results allow to fit the beam waist $\omega(z)$ (Eq. 2.26), extract the Rayleigh length z_R

and determine the focal position z_0 along the stage according to EN ISO 11146-2:2005 [176]. Comparing z_R with the ideal $z_{z,ideal}$ gives the beam quality factor M^2 (Eq. 2.24).

3.1.3 Autocorrelator

The MaiTai DeepSee includes a unit which compensates the GVD of the fs-laser source to achieve minimum pulse duration at the sample. The GVD-compensation is achieved by two prisms which can be moved via remote. The compressor motor was implemented in our software and combined with an autocorrelator. The incoming laser beam is split into two beams of equal intensity. By controlling a motorized stage, an optical delay is imparted upon one of the two beams. The two beams are then recombined within a nonlinear crystal for second harmonic generation. Depending on the stage position (and therefore the runtime difference), the variation in signal intensity allows to calculate the pulse duration [177]. This method is then repeated for multiple compressor positions to minimize the pulse duration for a given wavelength. After successfully fitting the optimal compressor position, this procedure is repeated over the laser spectrum.

3.1.4 Thermal Effects

To avoid thermal effects due to the fs-laser heating the sample, an optical chopper allows for the sample to return to equilibrium temperature. A variable adapter increases the voltage to drive the motor, thereby reducing the on-time. Four different chopper settings with increasing frequency and therefore a shorter on-time (when the sample was exposed to a train of pulses from the oscillator) were compared. For the final z-scan experiments a chopper on time of 78 μs was selected. All settings displayed in Tab. 3.1.

Table 3.1: Settings of the optical chopper used for z-scan experiments.

On-time [μs]	Single Rotation [ms]	Frequency [RPM]	Chopper Diameter [mm]
450	51	62	180
210	31.6	71	180
90	14	91	180
78	7	142	90

3.1.5 Sample Preparation and Measurement

Using the z-scan method a variety of 2-photon active compounds was studied (Tab. 3.2). The respective solution was filled into the cuvette, which was placed onto the stage. The sample was measured under static conditions (Fig. 3.3). Rhodamine B (Sigma-Aldrich / Merck KGaA, Darmstadt, Germany), a common laser dye, was used as a reference substance due to its well documented 2PA cross section σ_2 to verify the z-scan setup [35]. The 2PP PIs M2CMK and DAS were synthesized as previously reported [96, 99]. For the z-scan solutions of 10 mM were prepared by dissolving rhodamine B in methanol and M2CMK in Tetrahydrofuran (**THF**). DAS was dissolved in phosphate buffered saline (**PBS**) for 10 mM solutions. While initially synthesized for 2PP applications, P2CK was studied as a potential PS for 2P-PDT applications due

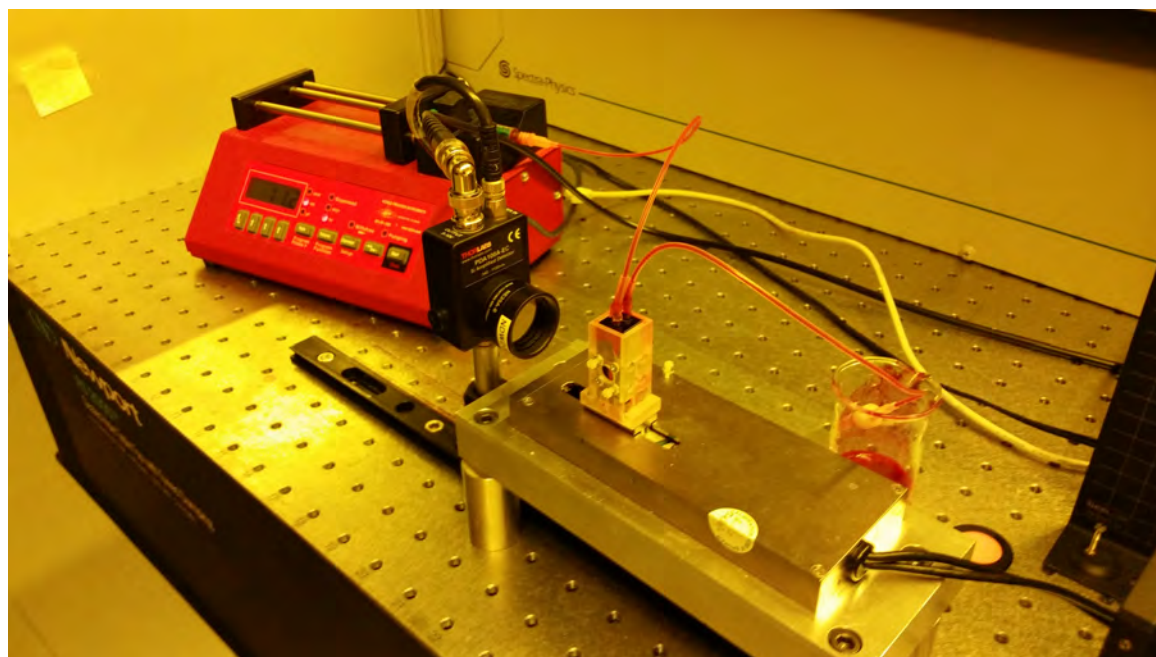


Figure 3.3: Z-scan measurement setup. 3D-printed sample holder with the cuvette is placed on the movable stage. Using a syringe the 2PA-compound is pumped through the cuvette. A photodiode records the transmitted signal at various stage positions. If desired the pump can be activated during z-scan to measure 2PA-cross section under flow conditions.

to the ROS generated by the compound after irradiation [178]. It was synthesized as previously described [25]. Furthermore, eosin-y, cisplatin and porphine (5,10,15,20-Tetraphenyl-21H,23H-porphine) were screened for 2P-PDT application. They were bought from Sigma and used as received. Eosin-y was dissolved in PBS for a 3 mM solution. Two solutions (3 and 10 mM) of cisplatin in dimethyl sulfoxide (DMSO) were prepared. For porphine four solutions (0.5, 1, 2 and 10 mM) in DMSO were used. All solvents were bought from Sigma-Aldrich (Merck KGaA, Darmstadt, Germany) and used as received.

Table 3.2: 2PA materials characterized using the z-scan technique.

Material	Application	Molar Weight [g mol ⁻¹]	Solvent
Rhodamine B	Laser Dye / Reference	479.02	Methanol
M2CMK	PI	374.53	THF
DAS	PI	708.88	PBS
P2CK	PI/PS	506.5	PBS
Eosin-Y	PS	647.89	PBS
Porphine	PS	678.11	DMSO
Cisplatin	Chemotherapy Agent	300.05	DMSO

For the z-scan a cuvette of 1 mm thickness (120 μ l volume, 17.5 \times 6.5 mm² aperture) (170-000-1-40, Hellma-Analytics, Müllheim, Germany) was used. Before the respective z-scan the cuvette was cleaned to avoid potentially unremoved material from previous z-scan experiments

to affect the measurement. This was done using 2-propanol ($\geq 99.5\%$) and lens tissues (MC-5 Lens Tissues, Thorlabs, Newton, USA) for the aperture. The cuvette was then flushed with 2-propanol and placed onto the motorized stage using a 3D-printed socket. A blank z-scan was done at 800 nm and 600 mW with pure 2-propanol. This results in average noise, independent of the sample position. The signal intensity depends on laser wavelength and laser power. This step is especially important to reduce errors during measurement as tiny particles within the cuvette or on the cuvette window can severely affect the locally measured signal. If such errors were detected, the cleaning procedure was repeated until a clean signal was observed. The calibration can also be done with the respective solvent used for the 2PA active compounds. After this calibration the sample was flushed and emptied using pressurized air. After nine consecutive z-scan measurements 100 μ l were pumped through the cuvette to provide fresh material. This number was chosen as usually three measurements at three laser power settings were done for a single wavelength. Therefore, between switching of the wavelength, the material could be pumped through the cuvette. Experiments with flushing new material between each z-scan were done, but did not show significant changes and manually operating the pump after every scan was considered ineffective.

3.2 2PL-Setup

The 2PL system used for the experiments in this thesis is based the same fs-laser source as the z-scan (Sec. 2.5). A number of optical components guide the beam to the sample (Fig. 3.4). The input laser power is regulated using a polarizer as described in Sec. 3.1.1. Using a movable mirror the beam can be directed into the z-scan setup (described in Sec. 3.1) instead of the 2PL-system. An AOM (MT110-B50A1.5-IR-Hk, AA Opto-Electronic, Orsay, France) modulates the laser beam.

3.2.1 Acousto-Optical Modulator

Acoustic waves are sent through a crystal and can be thought of as periodic planes of expansion and compression, which locally changes the refractive index. Therefore, the AOM acts as an optical grating, reflecting a beam under the Bragg condition, given in Eq. 3.8. It depends on the wavelength of the sound Δ and the laser wavelength λ [144]. The angle of reflection θ depends on the order m .

$$2\Delta \sin(\theta) = m \cdot \lambda \quad (3.8)$$

The 0th-order passes through the AOM, while the first order is diffracted and therefore allowed to pass through a pinhole. This optical principle enables fast modulation speed in the range of MHz, which would not be possible using optical shutters. A 5x achromatic beam expander (GBE05-B, Thorlabs, Newton, USA) is mounted before the galvanometer (IntelliSCAN, Scanlab GmbH, Puchheim, Germany), which allows scanning in x- and y-direction. A scan and tube lens system based on two achromatic lenses (Plössl system) is required to translate the pivot point of the laser beam to the backfocal plane of the objective. Without this optical component, the scanning angle is limited by the aperture of the objective, which also causes intensity gradients on the edge of the FOV. The Plössl system allows a high FOV (2.5 mm for 10x/0.3 objective) [12].

Table 3.3: Full width half maximum (FWHM) of the voxel for different objectives at 800 nm. Data reprinted with permission [12].

Objective	FWHM _{xy} [μm]	FWHM _z [μm]	Volume [μm^3]
Plan-Apochromat 10x0.3	0.92	10.88	16.2
Plan-Apochromat 20x/0.8	0.37	2.05	0.49
C Plan-Apochromat 63x/1.4 oil	0.23	0.52	0.047

The objective (Fig. 3.4) focuses the laser beam into the sample. After a layer is finished the objective is moved in z-direction by a motorized stage (Z-Achse Plus 50 Märzhäuser, Wetzlar, Germany) for the next layer. A microscope stage (SCAN^{plus} IM 120 \times 80, Märzhäuser, Wetzlar, Germany) allows positioning of the sample. However, this is not used during the fabrication of a single layer. After a geometry for a given FOV is finished in x-, y- and z-direction, the stage can be moved to allow fabrication of multiple parts within the 120 \times 80 mm² working area.

Before structuring at a given wavelength the output power depending on the voltage used for the AOM is calibrated by measuring the output power at the objective via powermeter (Fieldmax II, Coherent Inc, Santa Clara, USA). Due to the high numerical aperture of the 63x/1.4 objective, measuring the output power with the available powermeter was not possible. Microscope slide power meter sensor heads are available (S170C, Thorlabs, Newton, USA). For this work, the calibration for 63x/1.4 was done using the 20x/0.8 objective [12].

3.2.2 Scanning Mode

Depending on the objective, the hatch distance Δ_h between individual lines of a single plane had to be selected, as the voxel size depends on the numerical aperture (Sec. 2.6.3). This was also the case for z-distance Δ_z between individual layers. The specific Δ_h and Δ_z settings for each experiment are referenced in their respective sections. Estimates for FWHM for a given objective are displayed in Tab. 3.3 based on voxel descriptions discussed in Sec. 2.6.2. A detailed calculation of voxel sizes used as initial structuring parameters for the given objectives was done by Gruber [12] and is the basis for the 2PP settings used in this work.

For structuring the 2PL also allows different writing modes, which determine the fast scanning axis. There can be a single fast scan axis (x or y) for all layers. Long, thin structures such as cylinders are preferably scanned with the fast axis matched to the axis of the cylinder height to reduce the time spent on de- and acceleration of the scanning mirrors. Alternatively the fast axis can be alternated for subsequent layers (xy-alternating). This creates a woodpile like overlap of the individual lines which improves mechanical stability [144]. Lastly, it is possible to fabricate the layer twice, once with x as the fast axis and once with y (xy). This mode doubles the fabrication time. It can be used to increase the energy brought into the system which might not be possible by further increasing the laser power, for example when operating close to the threshold where the light dosage causes bubble formation [135].

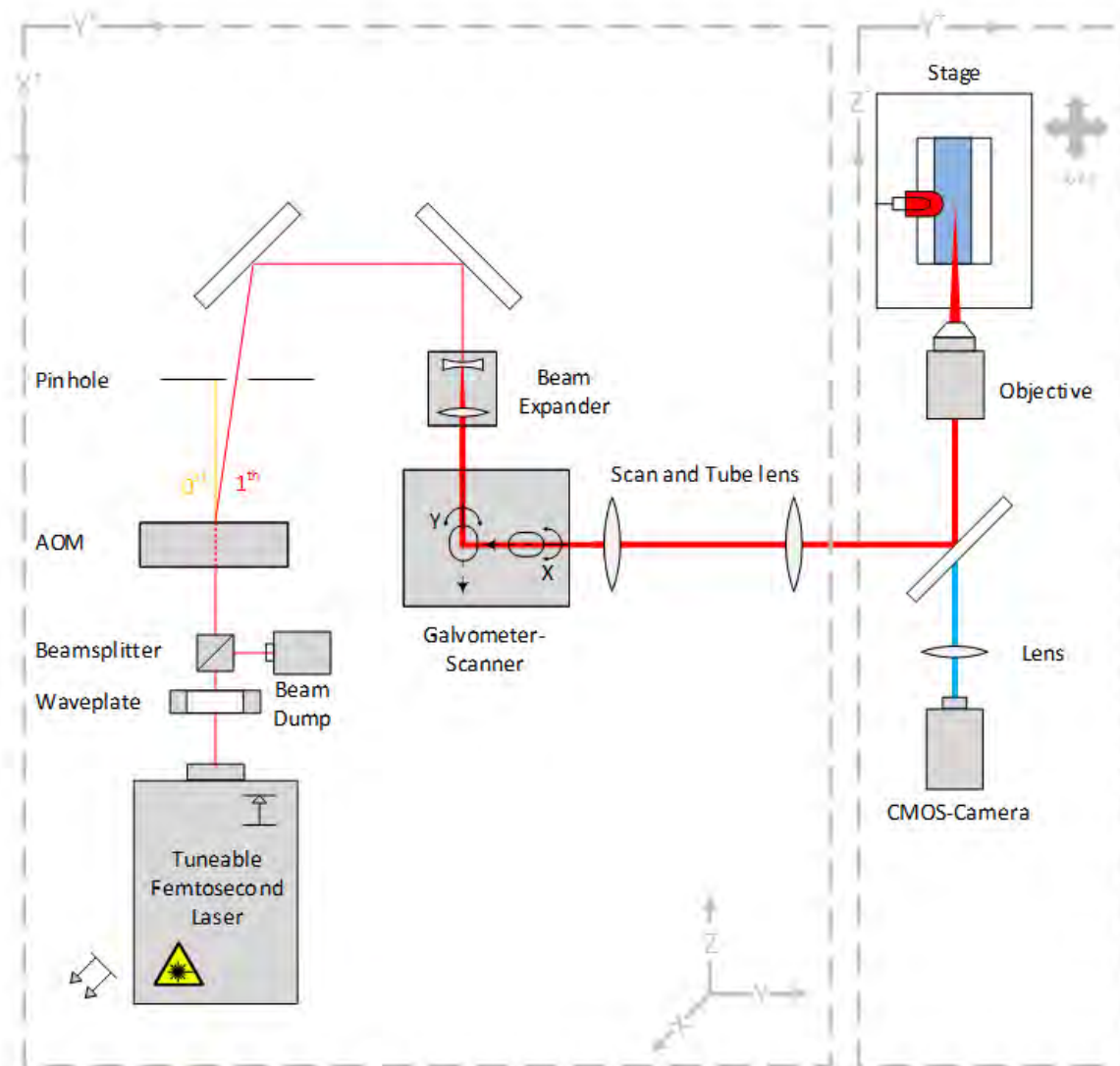


Figure 3.4: 2PL system. The tunable fs-laser allows 2PP structuring from 690-1040 nm. Waveplate and beamsplitter regulate input power. The AOM is used for fast modulation of the laser beam directed into the objective. The achromatic beam expander expands the beam to 5x. For x- and y-scanning a two-mirror galvometer scanner positions the laser beam. Scan and tube lens translate the pivot point of the beam to the objective. The stage, where the sample is placed, can be moved in x-,y- and z-direction. Using an LED light enables live monitoring of the polymerization process via CMOS-camera. Image taken from Gruber, reprinted with permission [12].

3.2.3 Objectives

For this thesis four objectives were used:

- Plan-Apochromat 10x/0.3
- Plan-Apochromat 20x/0.8 M27
- Plan-Apochromat 63x/1.4 Oil

All four objectives were purchased from Zeiss (Zeiss, Oberkochen, Germany) and are displayed in Fig. 3.5.



Figure 3.5: Objectives used in this thesis. 10x/0.3 [179] and 20x/0.8 [180] were used for structures larger than 200 μm . 63x/1.4 [181] was used for high resolution experiments.

The 10x/0.3 and 20x/0.8 objectives were used for structures larger than 200 μm when a high throughput or a large working area was required. Due to the working distance of 6.5 mm structures of 1 mm height can be written in sol-gel materials. However, for highly detailed objects, a maximum working distance of 300 μm is recommended [12]. The mismatch in the refractive indices of air and material distorts the laser focal spot when the laser is focused deep in the material. This mismatch also causes a shift of the focal position away from the objective, leading to distorted geometries. This can be compensated by adjusting the height H_{orig} of the structure by

$$H_{adj} = H_{orig} \cdot \frac{n_{im}}{n_{mat}}, \quad (3.9)$$

with the refractive index of the immersion fluid n_{im} and the material refractive index n_{mat} . For high resolution experiments such as the linetest (Sec. 3.5.3) or microscaffolds of 100 μm the 63x/1.4 oil immersion objective was used. A droplet of immersion oil with $n_e = 1.518$ (Immersol 518 F, Zeiss, Oberkochen, Germany) was put on top of the objective.

3.2.4 Large Field 2PP

The structuring window of 2PP is limited by the FOV for a given objective. In microscopy, the diameter of the FOV is often expressed as field number (**FN**) for 1x magnification. For a

certain objective magnification (M_{obj}) the FOV is given by

$$\text{FOV} = \frac{\text{FN}}{M_{obj}} \quad (3.10)$$

To structure geometries larger than the available FOV, the geometry is divided into multiple units determined by the FOV. For easier calculation, the squared FOV (**SFOV**) (Fig. 3.6) is used for this division

$$\text{SFOV} = \frac{\text{FOV}}{\sqrt{2}}. \quad (3.11)$$

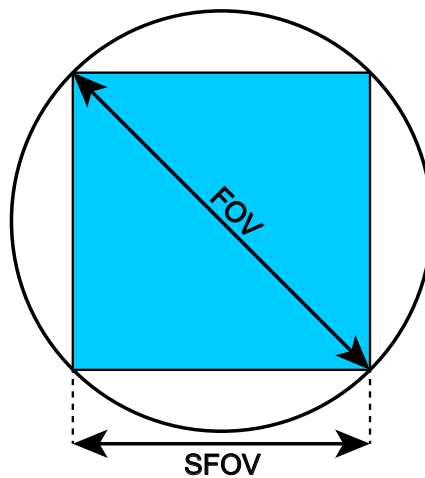


Figure 3.6: FOV for a given objective. For easier calculation of 2PP structures larger than the FOV the SFOV is used to divide a given geometry into equal squares.

Each unit is then fabricated separately. When finished, the stage moves to the next unit, continuously stitching together a structure larger than the available field of view. This process demands precise positioning of the stage and scanner. For this, the conversion factor K is required to correlate the available scanner bits n_{bit} to lateral positions at the focal plane Δ_d . Ideally the available scanning distance is equal to the squared field of view ($\Delta_d = \text{SFOV}$). However, as there might be intensity drops for large scanning angles, Δ_d can be adjusted. For this thesis Δ_d was corresponded to $\text{FN} = 16$, resulting in $\Delta_d \approx 1.13 \text{ mm}$ for 10x/0.3 objective, $\Delta_d \approx 700 \mu\text{m}$ for 20x/0.8 and $\Delta_d \approx 180 \mu\text{m}$ for 63x/1.4 oil immersion objective. The focal length L_f of an objective depends on the length of the scan tube length L_{tube} and the magnification of the objective M_{Obj} . Using L_f and the scanner half-angle θ the maximum lateral traveling distance of the system can be calculated by

$$\Delta_d = 2 \cdot \frac{\theta}{x} \cdot L_f = 2 \cdot \frac{\theta}{x} \cdot \frac{L_{tube}}{M_{Obj}}. \quad (3.12)$$

The total lateral distance Δ_d was modified by the expansion factor x as to the Plössl tube lens expands the incoming beam (for the described 2PP system $x = 2$). For a given objective the conversion factor K_{obj} is calculated by

$$K_{obj} = \frac{n_{bit}}{\Delta_d} = n_{bit} \cdot \frac{x}{2 \cdot \theta} \cdot \frac{M_{Obj}}{L_{tube}}. \quad (3.13)$$

This factor can be expressed independently of the objective:

$$K = M_{corr} \cdot \frac{K_{obj}}{M_{Obj}} = \frac{M_{corr}}{M_{Obj}} \cdot \frac{n_{bit}}{\Delta_d} = M_{corr} \cdot \frac{n_{bit} \cdot x}{2 \cdot \theta \cdot L_{tube}} \quad (3.14)$$

To adjust possible errors due to imperfections of the system alignment a correction factor M_{corr} was introduced to allow manual compensation of the misalignment (Fig. 3.7). The relationship between FOV and M_{corr} is inversely proportional as is evident from the relation $K \propto \Delta_d^{-1}$ (Eq. 3.14). Additionally it was possible to overlap two adjacent FOVs. This feature was implemented to increase stability of the junction by exposing the overlap of two FOVs during each individual structuring window.

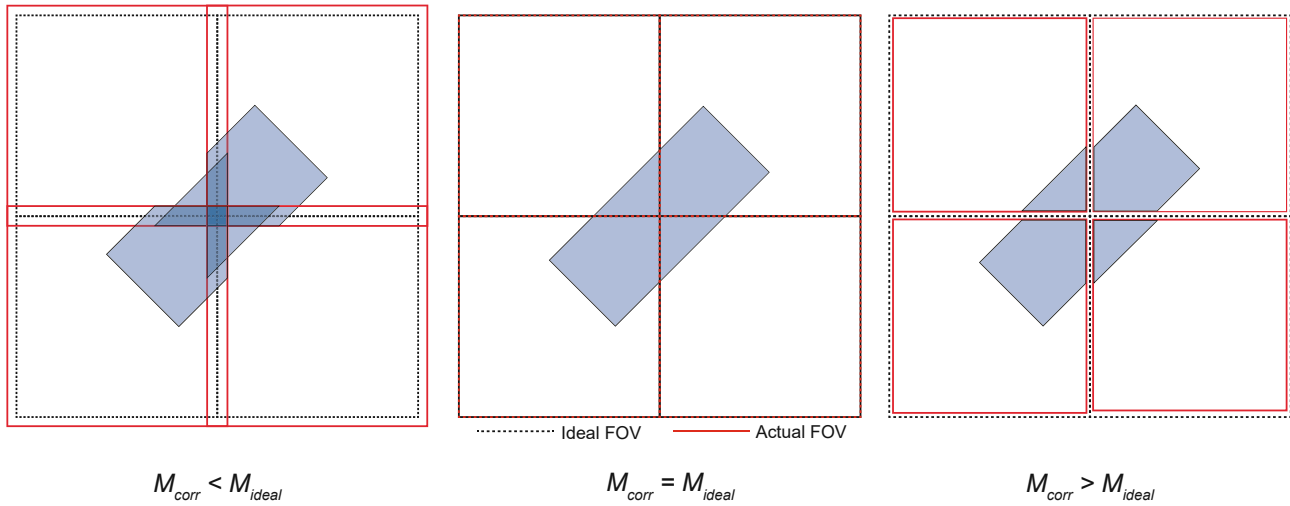


Figure 3.7: Microscope correction factor M_{corr} for structures composed by multiple FOVs. If M_{corr} is smaller than the ideal setting M_{ideal} , the FOVs are larger than intended (left). If ideally calibrated, the regions interface without gap (middle). If M_{corr} is too large the FOVs are smaller than intended, causing gaps between the individual FOVs (right).

3.3 Laser Source

The main laser source in this thesis was a Mai Tai eHP Deep See (Spectra Physics, Santa Clara, USA). The wide tuning range (690 to 1040 nm) and pulse compensation unit allow for a wide application window of 2PA processes. The system is based on two chambers. The first contains two diodes laser ($P = 30 \text{ W}$ at $\lambda = 806 \text{ nm}$ for each diode) which pumps Nd³⁺ ions doped in a yttrium vanadate crystalline matrix (Nd : YVO₄, ($P = 12\text{-}30 \text{ W}$ at $\lambda = 532 \text{ nm}$), generating a 1064 nm beam at 30 W, which is then frequency doubled to $\lambda = 532 \text{ nm}$ using an LBO crystal. This provides an output signal of 5 W at 532 nm. In the second chamber a mode-locked crystal acts as the active medium for the pulsed laser. Pulsing stability is achieved via regenerative

mode-locking (Sec. 2.5). Due to the dispersion caused by the Ti:Sa crystal the group velocity dispersion GVD is compensated within the laser cavity via adjustable prisms (Sec. 2.5.2). This prism configuration also allows the tunability of the laser. A movable slit is placed between the prism which only allows a narrow bandwidth to resonate. After the laser beam leaves the cavity it passes through an additional pulse compression unit (DeepSee). Here the emitted laser pulse is negatively chirped to compensate dispersion caused by the optical components of the optical system. Therefore, the MaiTai eHP Deep See not only allows beam and pulse stability, but also minimum pulse duration at the objective. Using an autocorrelator the optimal pulse duration for a system can be evaluated and stored. Depending on the system a change in wavelength automatically sends the corresponding compressor position to the DeepSee unit, eliminating manual readjustment for the individual systems.

3.4 2PP

Over the course of this thesis various types of materials were used for 2PP. PCL₂, PCL₆ and zr-hybrid (also known as SZ2080) were used to produce microscaffolds. ETA:TTA was used as a reference material when studying the polymerization thresholds to compare the performance of sol-gels (zr-hybrid) with PCL-based crystalline prepolymers (PCL₂ and PCL₆). Initial large field 2PP experiments were done using the commercial photoresist Ormocomp[®] [182]. For cell encapsulation experiments 10 % Gel-NB was used [109]. 10 % methacrylated GelMOD [24] was used for experiments comparing results from z-scan with 2PP. GelMod and Gel-NB were provided by Jasper Van Hoorick under the supervision of Peter Dubrueel and Sandra Van Vlierberghe (Polymer Chemistry and Biomaterials Group, Ghent University).

The photoinitiators used for 2PP applications in this work have been M2CMK [96], 4,4'-Bis [183] and DAS [99]. M2CMK was used for acrylate and methacrylate resins, as well as the solid state PCL-based PCL₂ and PCL₆. The photoinitiator 4,4'-Bis was used for the sol-gel material zr-hybrid and for initial studies of the PCL-based PCL₂. The water-soluble initiators P2CK and DAS were used for hydrogel materials with a high water content for tissue engineering applications.

All samples were placed on glass coverslips which were functionalized in the case of PCL₂, PCL₆ and GelMod to increase adhesion of fabricated structures to the glass surface (Sec. 3.4.6). For zr-hybrid and ETA:TTA systems functionalization was only required structures larger than 500 μm. Microscaffolds exhibiting only a few small contact areas fabricated out of both materials did not require functionalized surfaces to properly attach.

3.4.1 ETA:TTA

For the triacrylate monomer formulation ETA:TTA (50:50 by weight) M2CMK was chosen as PI. It was dissolved in acetone and mixed with the monomer to get a 10 mM stock solution of M2CMK in ETA:TTA. The acetone was afterwards distilled using a rotary evaporator. The desired solution of M2CMK was achieved by mixing the required amount of pure ETA:TTA to the 10 mM M2CMK solution in ETA:TTA. Then, the solution was pipetted onto a glass slide (no activated slides required) for 2PP processing. Due to the liquid nature of ETA:TTA masks of polydimethylsiloxane (PDMS) were required for higher samples. Because of its viscosity ETA:TTA can be used for structures larger than the objective working distance by means of

3 Materials and Methods

WOW-2PP [92]. After 2PP structuring the material was developed in 2-propanol for 30 min and afterwards developed in 2-propanol for an additional 10 min.

3.4.2 Ormocomp[®]

Ormocomp[®] is a commercially available inorganic–organic hybrid photoresist, which was purchased from micro resist technology (micro resist technology, Berlin, Germany). The highly viscous material can be easily handled using a spatula to place the material on a glass slide. After structuring, the material was developed in 1:1 solution of 4-methyl-2-pentanone and 2-propanol for 20 min. Afterwards, the sample was washed with 2-propanol for a min.

3.4.3 Sol-Gels

Zr-hybrid was dissolved in 1-propanol to allow mixing with the PI in the liquid phase. The desired wt% of 4,4'-Bis (Merck KGaA, Darmstadt, Germany) was dissolved in 1-propanol and pipetted into the monomer-solution. The solution was then mixed using a vortexer for five min. Depending on the desired sample height, the material was pipetted in multiple layers (one layer of roughly 0.5 mm height) to allow drying of each layer without the risk of creating air pockets within the sample. The material was dried before 2PP processing using a heating plate set to 40 °C for 2-3 h before the next layer was applied. M2CMK could not be used for zr-hybrid as the shift in absorption frequency band by the mixture of both materials caused the sample to turn dark blue and therefore intransparent for the 2PP setup. The refractive index of zr-hybrid was measured to be 1.52, which is close to the $n_e = 1.518$ used for 63x/1.4 objective. For 10x/0.3 the height of the structure needed to be pre-compensated (Sec. 3.2.3). As zr-hybrid is solid after drying even large free-standing structures can be fabricated without the need for supporting geometries. However, this limits the possible structuring height by the working distance of the objective and does not allow for WOW-2PP applications [92]. Samples of $7 \times 7 \text{ mm}^2$ dimension in custom polymethylmethacrylate holders with a height of 2 mm were produced. When working with these dimensions menisci need to be considered as the material is attracted by the confinement walls. This meniscus can severely affect the sample and while a sample height of 1.5 mm might be reached at the walls, the material height at the center is just a few tens of μm . This meniscus further requires multiple layer depositions before the desired sample height is achieved uniformly across the sample area. After structuring, the samples were submerged in 1-propanol for one hour and afterwards developed for an additional 10 min in 1-propanol.

3.4.4 PCL-Based Prepolymers

In corporation with Ghent University new materials for microscaffolds were synthesized based on the crystalline prepolymer reported by Houben et al. [42]. The synthesis of these compounds was done by Aysu Arslan under the supervision of Peter Dubruel and Sandra Van Vlierberghe (Polymer Chemistry and Biomaterials Group, Ghent University). This material is based on a PCL backbone (Fig. 3.8) as PCL has shown excellent biocompatibility and biodegradability [41]. Two PCL-based prepolymers were studied, the main difference between the two materials being the number of functional groups per molecule. PCL₂ is a diacrylate endcapped prepolymer (one acrylate group at each end), whereas PCL₆ is a hexa-acrylate endcapped prepolymer (three acrylate groups at each end). The chemical structures of both materials are shown in Fig. 3.8.

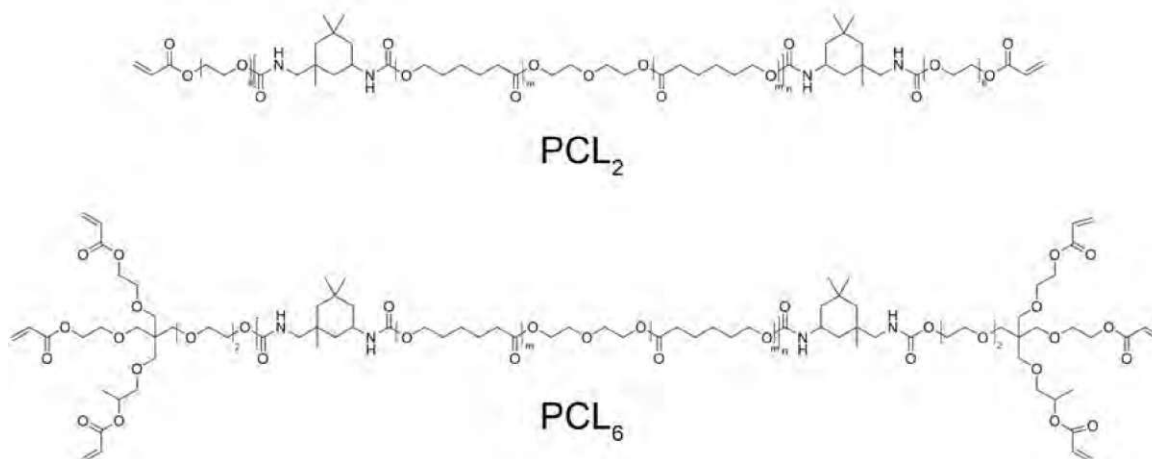


Figure 3.8: Structure of the PCL-based prepolymers. The difunctional PCL₂ has an active group at each end of the molecule. The hexafunctional PCL₆ is tricapped at each end.

For experiments without PI, the material was placed onto a functionalized glass slide and put on a heating plate (60 °C) as the sample was intransparent at room temperature due to its crystalline nature. To add PI, the solid material had to be dissolved and mixed with the PI solution. The PCL-backbone renders the material insoluble in water compared to the PEG-based precursor reported by Houben et. al., therefore the material was dissolved in THF. Using a 10 mM solution M2CMK the PI was added in wt%, knowing the molar weight (374.52 g mol⁻¹). For experiments with 4,4'-Bis the same calculation with the respective molar weight (324.46 g mol⁻¹) was done. For 1 wt% M2CMK in 100 mg PCL₆, 270 μl of M2CMK (10 mM in THF) are required, which is more than sufficient to dissolve the prepolymer. Therefore, initially solving the prepolymer could be skipped. This was especially important to process the material as the solution remained highly viscous and could be pipetted onto the sample without trickling into the mask-glass intersection due to capillary forces. After the material was placed on a glass slide, it was dried on a heating plate set to 50 °C for one hour. Similarly to zr-hybrid, multiple layers (one layer of roughly 0.5 mm height) were required for samples of a few millimeters thickness and dried for one hour before applying the next layer to avoid air confinement. The selected solvent to monomer ratio of 0.37 mg μl⁻¹ also minimized corrosion of the PDMS mask due to the fact that THF is highly caustic for polymers such as PDMS. Adding more THF to the solution only allowed to deposit very thin layers of material (< 0.1 mm) without running the risk of corroding the mask, therefore drastically slowing down the sample preparation time. Alternatively, metal rings were used as masks but the intersection between metal and glass did not allow for a tight junction, therefore material spread through the desired volume. Before the start of 2PP experiments, the sample was put on the heating plate set to 60 °C for ten min to allow transparency. While the material is crystalline, PDMS molds were required to guarantee uniform height as the heated material exhibited lower viscosity. This was especially important for structures with a height larger than 600 μm to efficiently use the whole sample area for

3 Materials and Methods

fabrication. The refractive index was measured to be 1.51, comparable to Sol-Gel materials. As with zr-hybrid the material was suitable for 63x/1.4 oil immersion objective. For 10x/0.3 the mismatch in refractive index had to be precompensated by compressing the geometry (Sec. 3.2.3). After 2PP structuring the material, the sample was developed in THF for 30 min and afterwards developed in THF for an additional 10 min. For experiments using PDMS masks, the material was left to solidify and turn intransparent before the mask was removed. This was done as to not risk damaging the scaffolds while removing the mask. After removing the PDMS mask, the sample was developed in THF, to both preserve the mask and also prevent corrosion of PDMS in the developing solution.

3.4.5 GelMod

For PDT experiments 10 % GelMod Norbonene [109] was used (described in Sec. 3.6). Polymerization threshold experiments were done using 10 % methacrylated GelMod [24] and 2 mM DAS. After structuring the sample was developed in PBS and placed on a heating plate at 36 °C for 20 min.

3.4.6 Activated Glass

For PCL₂, PCL₆ and GelMod the glass coverslips were functionalized by binding methacrylate groups to the surface of the glass. This process is known as silanization. In this process a glass surface is covered with organofunctional alkoxy silane molecules. The glass surface contains hydroxyl groups. These attack the alkoxy groups on the silane, which in turns forms covalent -Si-O-Si-bonds [184]. This functionalization allows for monomers containing acrylates or methacrylates to covalently link to the surface and provide better adhesion of the structure to the glass. This adhesion is especially important for the polymerized resin to remain fixed to the glass coverslip during development. To increase the efficiency of the process the glass slides were plasma treated before silanization to increase the number of free hydroxyl groups on the glass surface. A plasma cleaner (PDC-002, Harrick Plasma, Ithaca, USA) was used at 30 W for 15 min before silanization. A silanization solution of 100 l was prepared by mixing 48 % ethanol, 0.3 % acetic acid (Sigma-Aldrich, Merck KGaA, Darmstadt, Germany) and 49.7 % purified water. Afterwards, 2 % 3-(Trimethoxysilyl)propyl methacrylate (Sigma-Aldrich, Merck KGaA, Darmstadt, Germany) were added dropwise over a short amount of time while continuously stirring with a magnetic stirrer. The plasma cleaned glass slides were put in a 100 ml beaker and incubated for 15 min. The rack was then put in a separate beaker containing purified water. The water was replaced twice. Remaining water droplets on the glass slides were removed by using clean compressed air. The samples were dried in an oven set to 50 °C.

3.5 Material Characterization

To determine the material properties three methods were chosen for this thesis. The reduced Young's modulus measurements were done via nanoindentation. The DBC was evaluated using Raman microscopy. To study the necessary light dosage for polymerization the threshold power P_{th} was compared using different approaches such as ascending scan, freehanging lines and cubes.

3.5.1 Nanoindentation

The reduced Young's modulus of cubes fabricated from PCL₆ was measured using nanoindentation. A standard three-sided Berkovich tip was used to deflect the micro-cantilever to record the displacement and the corresponding load. Multiple positions over the top surface of the cubes were measured. A force of 0.02 mN was selected as limit [102, 117]. Representative measurement is shown in Fig. 3.9.

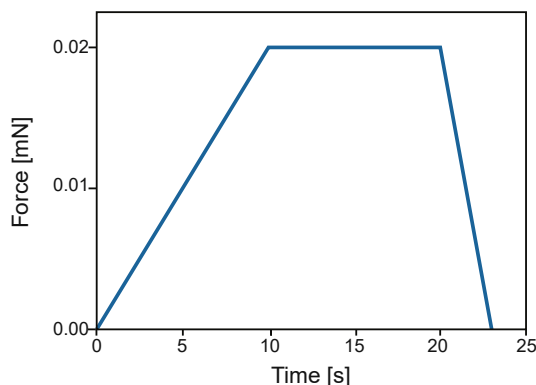


Figure 3.9: Representative measurement of 3D-cubes via nanoindentation. A three-sided Berkovich tip was pressed into the sample. As the tip was moved into the sample, the load on the tip increased until it reached a predefined value. Afterwards, the area of residual indentation in the sample was used to calculate the hardness [117].

3.5.2 Raman Spectroscopy

Raman measurements were performed using the WITec alpha 300RSA+ confocal Raman microscope (WITec GmbH, Ulm, Germany). A near-infrared 785 nm diode laser at 240 mW was focused through a 20x/0.4 objective (EC Epiplan 10x/0.2 HD M27, Zeiss, Oberkochen, Germany), resulting in a theoretical lateral resolution of approximately 800 nm. The backscattered Raman photons were collected in reflection mode. After passing an edge filter, the red shifted Stokes light was guided via fiber (50 μm fiber diameter, confocal pinhole) to a spectrometer (UHTS 300 spectrometer optimized for 785 nm excitation wavelength, f/4, 300 mm focal length) equipped with a 300 grooves/mm grating (BLZ = 750 nm). A highly sensitive, thermoelectrically cooled Deep Depletion Charged-Coupled Device detector allows a spectral resolution of approximately 8 cm⁻¹. Raman measurements were recorded of 2PP-fabricated cubes prepared on a microscope glass slides. The samples were placed on a motorized x-y-stage (< 1 μm reproducibility). Five spectra per cube were recorded at different measurement spots across the surface of a single cube, accumulating 20 scans with an integration time of 1 s for each spectrum. All measurement spots were manually selected and added to a list of coordinates before starting the raster scan option for consecutively collecting Raman spectra on each of the defined spots.

ProjectFOUR software (WITec GmbH, Ulm, Germany) was employed for data processing. Savitzky Golay smoothing (2nd order polynomial, window size 14) was applied before the area of selected bands was integrated using the Sum Filter Option (width: 60 cm⁻¹) with linear

background subtraction. To correct for instabilities in the laser signal over time which would directly reflect in the intensity of the detected Raman signal, band area ratios of the C=C stretch vibration located at 1630 cm^{-1} Raman shift vs. C=O stretch vibration at 1726 cm^{-1} Raman shift were calculated [185]. The Raman spectrum of unreacted prepolymer was used as 100 % C=C reference, the C=C conversion was then calculated relative to this value. Finally, the mean of all five conversion values for each polymer cube was determined including the according standard deviation based on the Gaussian law of error propagation.

3.5.3 Polymerization Threshold

In this thesis various methods have been used to evaluate the polymerization threshold power P_{th} (described in Sec. 2.6.3) for a given material composition, laser wavelength λ and fabrication speed v . This can be done by producing an array of cubes with fixed geometry (Cubes), writing single lines close to the glass surface for various z-positions (Ascending Scan Method) or fabricating free-hanging lines (linetest). The correlation between P_{th} and v was obtained using a Python based least square fit. Afterwards, the coefficient of determination (R^2) [186, 187] was calculated for the fitted data with $R^2 > 0.6$ showing good correlation and $R^2 > 0.8$ high correlation between fit and experiment data.

Cubes

An array of identical cubes (fixed geometry, Δ_z and Δ_h) was structured to evaluate P_{th} . Depending on the material and objective, the dimensions of the voxel change and therefore these settings have to be adjusted to the given material, PI (as well as PI-concentration) and objective used. To study the relation between laser power P and fabrication speed v the 2PP system was calibrated for the selected objective (Sec. 3.2). An array with varying speed in x-direction and power in y-direction was produced. Experiments on the influence of structuring wavelength were done at a fixed writing speed (100 mm s^{-1} for all experiments in this thesis). For a given wavelength the available output power at the objective was calibrated using a powermeter. A one dimensional (1D)-array of cubes with varying laser power was produced. Afterwards the sample was removed from the building platform, the laser wavelength was changed using the software and the output power was again calibrated for the next wavelength. After this calibration, the powermeter was removed and the sample was placed back onto the building platform. This step was repeated for all screened wavelengths.

Ascending Scan

Ascending scan studies were done using the 63x/1.4 oil immersion objective. The laser focus was manually adjusted using the z-stage to be at the intersection between glass slide and resin. Multiple lines were written with varying powers for various speeds. The ascending scan method was done at one z-position instead of various positions. This was done as the voxel dimensions were of no interest for these experiments and just the polymerization threshold P_{th} was studied [43].

Linetest

Instead of the ascending scan method, the majority of polymerization studies was done using free standing lines to study P_{th} in more detail. For each line two pillars were fabricated before the line was produced (Fig. 3.10, left). The line is created between two pillars ($40 \times 40 \times 50 \mu\text{m}^3$) which are spaced $10 \mu\text{m}$ apart. To avoid potential errors due to the de-and acceleration of the scanning mirror, the line was extended $10 \mu\text{m}$ left and right of the pillars. Fabrication of the pillars ($\Delta_h = 0.3 \mu\text{m}$, $\Delta_z = 0.4 \mu\text{m}$) was done with a scanning direction in x and fabrication speed of 150 mm s^{-1} with 63x/1.4 oil immersion objective. The laser power used for the pillars was adjusted for each material and PI-concentration. The scanning speed was varied from a minimum of 0.1 mm s^{-1} to a maximum of 100 mm s^{-1} with a minimum of four writing speeds. Starting with a minimum power of 2 mW , the laser power was increased by $\Delta_P = 2 \text{ mW}$ until a polymerized line was observed. Every speed and power setting was done in triplicates. While lines could be observed during the structuring, the respective setting was often times not the actual threshold power due to the limited resolution of the live camera. The actual polymerization power could only be reliably evaluated after developing the sample. The samples were developed in the respective solvent. However, due to the fine nature of the lines evaporating solvent can cause large capillary forces and lead to rupture of the lines. To decrease these forces and allow study of fine lines close to the polymerization threshold the structures were covered with hexamethyldisilazan (**HMDS**), to replace the solvent with a liquid exhibiting lower surface tension and therefore smaller capillary forces during evaporation [188].

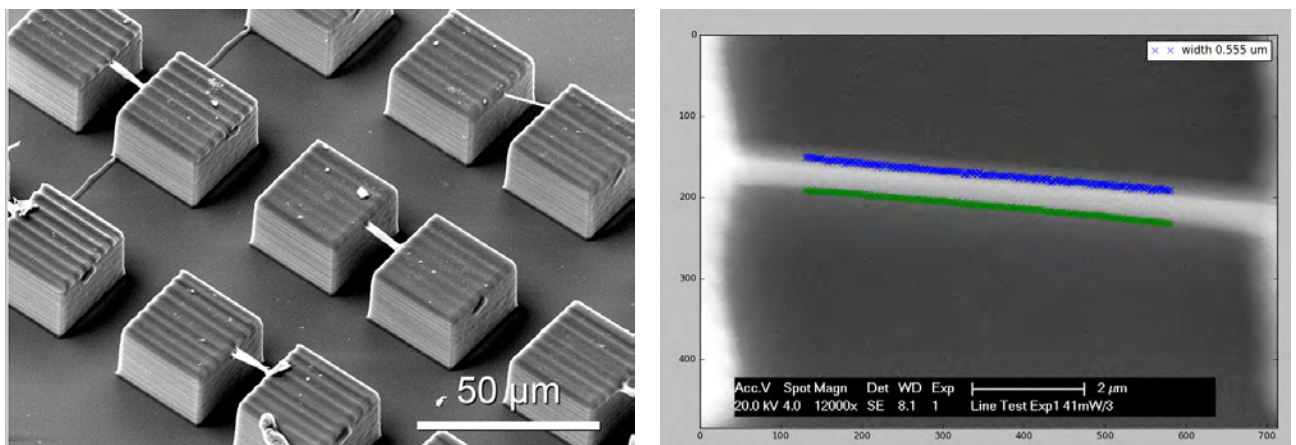


Figure 3.10: SEM images of linetest structures fabricated from PCL_6 with 1 wt% M2CMK (left). Two solid pillars are fabricated before a line is fabricated between the pillars with a given speed and power. Graphical User Interface to fit the measured line images obtained by SEM (right). The threshold pixel intensity, which distinguishes line from background noise, can be adjusted manually. If desired, two separated thresholds are used for both sides of the line. This is important for tilted samples, as the bottom edge is not as clearly pronounced compared to the top edge.

The dried samples were imaged afterwards under optical microscope in case only the minimum power for a specific fabrication speed was of interest. Alternatively scanning electron microscopy (SEM) was used to measure the actual length and height of the polymerized lines (Fig. 3.10, left). Here, each line was recorded individually with a $20 \cdot 10^3 \times$ magnification. Using a custom algorithm up to 800 different positions of each recorded image were measured to extract the

average linewidth. The sample tilt of 45° , when looking at the voxel height was automatically compensated (Fig. 3.10, right). A pixel threshold was manually set, which separates the line from background noise. This pixel threshold can be used for both sides of the line or individually adjusted if ideal exposure conditions have not been met during SEM-imaging. This manual adjustment of upper and lower threshold was especially important when looking at tilted lines, where the surface closer to the detector was more illuminated.

3.6 Photodynamic Therapy

The effect of 2-photon active compounds for PDT applications was studied using the human osteosarcoma cell line (**MG63**, Sigma-Aldrich/Merck KGaA, Darmstadt, Germany) and human adipose-derived stem cells (**ASC**, Evercyte GmbH, Austria). ASCs were immortalized by insertion of human telomerase reverse transcriptase (**hTERT**). This ASC/TERT1 cell line was labeled with green fluorescent protein (**GFP**) to obtain permanently labeled green labeled cells following a previously established protocol [189]. Spheroids of mCherry labeled MG63 were formed in nonadhesive agarose molds leading to spheroids of $200\ \mu\text{m}$ diameter. These were then mixed with ASC/TERT1 ($10^6\ \text{cells l}^{-1}$) in 5% GelNB [109] with $0.15\ \text{mM}$ Li-TPO-L [21] and an equimolar amount of dithiothreitol (DTT, Merck KGaA, Darmstadt, Germany). The sample was encapsulated using a UV-chamber (UV Crosslinker AH (115V/230V), 234100, Boekel Scientific, Feasterville, USA) and a dosage of $1.5\ \text{J cm}^{-2}$. After encapsulation the respective 2PA compounds were added to the sample. The sample was submerged in cell culture medium and incubated for 12 h. For P2CK $0.5\ \text{mM}$ was chosen. For cisplatin the concentration was $0.03\ \text{mM}$.

Using the live camera the focal plane of the laser was adjusted to the bottom of an individual spheroid and then moved $20\ \mu\text{m}$ below. Exactly like in the 2PP case a 3D-object was scanned by the system. Using $10\times/0.3$ objective, a sphere with a radius of $300\ \mu\text{m}$ was scanned with $\Delta_h = 1.0\ \mu\text{m}$ and $\Delta_z = 1.0\ \mu\text{m}$ was writing at a scanning speed of $1000\ \text{mm s}^{-1}$. Operating wavelength and laser power were selected for the individual photosensitizer after z-scan experiments revealed the optimal absorption wavelength. Because of the localized nature of 2PA, areas with encapsulated ASC/TERT1 were not sufficiently irradiated to activate the sensitizers. Afterwards, the samples were kept in the incubator for 3 days, while the medium was regularly refreshed. This was done to remove remaining PS as their inherent fluorescence might be recorded in addition to the fluorescence signal from the cells.

3.7 Microscaffolds

For various applications microscaffolds based on a truncated icosahedron - commonly known as a buckyball (Fig. 3.11, left) after the buckminsterfullerene (C_{60}) molecule [190] - were fabricated as they can be used as porous base units for self assembly in tissue engineering (Sec. 2.1). $7 \times 7\ \text{mm}^2$ samples of zr-hybrid (0.1 wt% 4,4'-Bis) of $600\ \mu\text{m}$ height were prepared. Spaced $50\ \mu\text{m}$ in x- and y-direction, an array of 13×13 buckyballs with a diameter of $300\ \mu\text{m}$ was fabricated. Using $10\times/0.3$ objective the refractive index mismatch was precompensated by compressing the STL to 66% (Sec. 3.2.3). For structuring the laser power was set to $120\ \text{mW}$ at $800\ \text{nm}$ and fabrication speed to $1000\ \text{mm s}^{-1}$ using $\Delta_h = 0.4$ and $\Delta_z = 0.5$. The consecutive layers were scanned in x- and y-direction alternately. The scaffolds were structured

top to bottom as the solid material enables free standing structures without support. The same settings were used for PCL₆ (0.1 wt% M2CMK). These scaffolds were loaded with hiPSC derived DP-cells and keratinocytes. When implanted these cells are able to regulate the growth cycle of a hair follicle [30, 48]. The buckyballs were fabricated to provide mechanical stability for the hiPSC-DP spheroids for transplantation (Sec. 2.1.3). Later experiments demanded a guiding rod to direct the hair growth from the hair follicle. Therefore, a rod of 1.0 mm length was attached to one pentagon area of the buckyballs (Fig. 3.11, middle). Due to the lollipop like appearance, the structures were referred to as lolly-up.

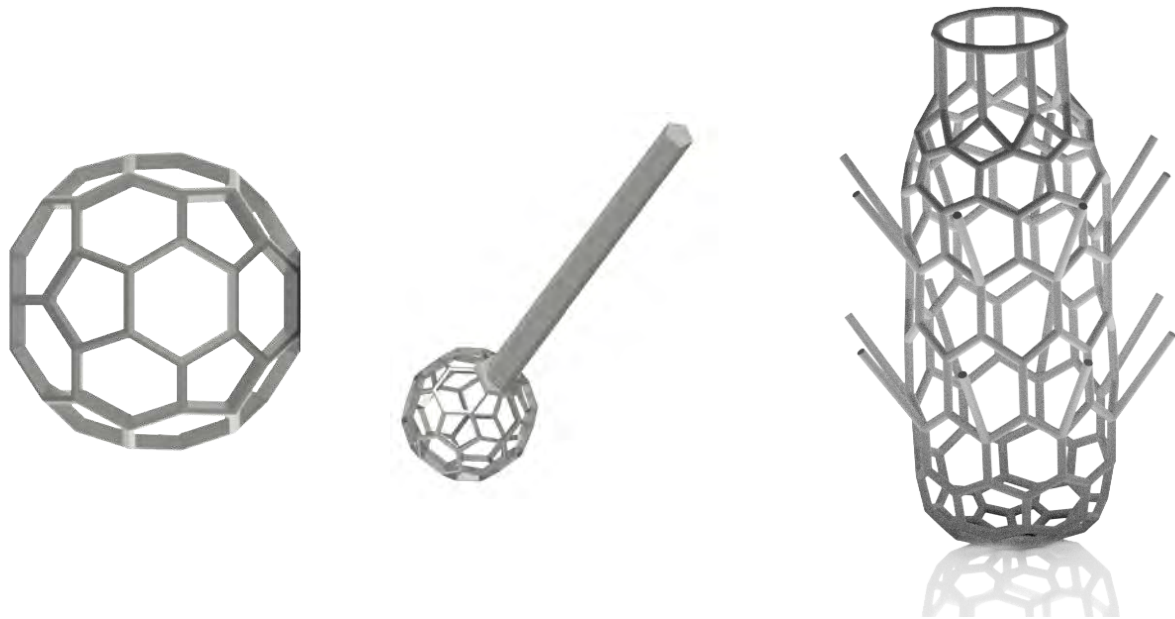


Figure 3.11: Buckyball microscaffolds designed after buckminsterfullerene C₆₀ (left). The scaffolds are used to provide mechanical support for cell spheroids within the scaffold. For visibility only the front half of the scaffold is depicted. A guiding rod was added to direct the growth of the hair (middle). The capilinsler, an alternate scaffold design for hair implants was provided by Vladimir Mironov (right). It exhibits pores large enough to allow cell perfusion. An open top is designed to direct the growing hair follicle while sideways hooks are intended to provide mechanical support after implantation.

An alternative scaffold design for DP-transplantation applications, referred to as capilinsler, was provided by Vladimir Mironov (Regenerative Medicine Institute, Sechenov Medical University, Moscow, Russia). Similar to the lolly-up, the design was intended to direct cell growth in direction of the narrowing at the top, where an opening significantly larger than the adjacent pores was placed. The pore diameters along the side were designed large enough to allow cell perfusion. Sideways hooks are intended to provide mechanical support after implantation. As with the lolly-up structures, PCL₆ (0.1 wt% M2CMK) was used as resin. The same structuring parameters as for the lolly-up were used and due to the refractive index mismatch the STL was precompressed to 66 % of its total height. As the total height of the capilinsler was 1000 μm , PDMS masks were necessary to achieve the sample height.

For cell trapping experiments by means of Faraday waves (Sec. 2.1.2), the buckyball design was adapted. As the scaffolds had to be placed at the nodes of the standing waves, the buck-



Figure 3.12: Buckyball design for Faraday wave experiments. Five rods fix the scaffold to the glass slide. Three designs - conventional buckballs (left), open top buckyballs (middle) and open bottom buckyballs (right) - were modeled to study the effect of geometry on the number of trapped cells. A central barrier for the base-hexagon element was added to reduce the pore-size.

buckyballs needed to be fixed to glass surface. Therefore, five feet were attached to the structure. The diameter of the buckyballs was $100\ \mu\text{m}$, with a pore size of $\approx 32\ \mu\text{m}$ for the pentagon area and $\approx 40\ \mu\text{m}$ for the hexagon area. The hexagon diameter was twice the size of fibroblasts ($10\text{-}20\ \mu\text{m}$), for example mouse embryonic fibroblasts [191]. To decrease the pore size a central rod was added to the hexagon area. The effect of geometry on the trapping efficiency was also studied. For this, three buckyball designs were compared: complete, open top and open bottom buckyball (Fig. 3.12). The fine structures required highest possible resolution. Therefore, the 63x/1.4 oil immersion objective (Sec. 3.2.3) was chosen. Due to the close match in refractive indices for both PCL_6 and zr-hybrid, no pre-compression of the STL was required. Fabrication was done with a laser power of $70\ \text{mW}$, fabrication speed at $40\ \text{mm s}^{-1}$, $\Delta_h = 0.2\ \mu\text{m}$ and $\Delta_z = 0.5\ \mu\text{m}$ with alternative x- and y-scanning direction for subsequent layers.

3.8 Microcages

As experiments using Faraday waves require periodic features, an array of 25×25 buckyballs connected to the glass with feet (Fig. 3.13), spaced $240\ \mu\text{m}$ in x- and y-direction were produced on a glass slide ($9 \times 9\ \text{mm}^2$). After development the scaffolds were coated with $1\ \text{mg ml}^{-1}$ poly-D-lysine (Sigma-Aldrich/Merck KGaA, Darmstadt, Germany) for one hr and washed twice with water. The slide was put into a customized chamber with a size of $10 \times 10 \times 2\ \text{mm}^3$. Initial Faraday wave experiments were done using $2 \cdot 10^6\ \text{cells ml}^{-1}$ MC3T3 fibroblasts (Sigma-Aldrich/Merck KGaA, Darmstadt, Germany), later cortical neurons ($5 \cdot 10^6\ \text{cells ml}^{-1}$) were studied. Primary cortical neurons were isolated from embryonic day 18 CD-1 mice (Charles River, Wilmington, USA). The respective cells were added to the chamber and exposed to Faraday waves at 54 Hz, 80 mV. Two exposure durations (100 and 300 s) were chosen depending on the experiment. For staining of fibroblasts nucleic staining Hoechst 33342 (Thermo Fisher Scientific, Massachusetts, USA) was used. The cytoplasm was stained via CellTrace™ Far Red (Thermo Fisher Scientific, Massachusetts, USA). Fibroblasts were kept in cell medium at $37\ ^\circ\text{C}$

with 95 % relative humidity, and 5 % CO₂ for three days. Cell medium was changed every 24 h. The cortical neurons were suspended in neurobasal medium with B27 supplement (Life Technologies, Carlsbad, USA) and 500 µl glutamine (Life Technologies, Carlsbad, USA). Culture conditions were held stable at 37 °C with 95 % relative humidity, and 5 % CO₂. After 7 days culture the caged cells were fixed with 4 % paraformaldehyde (Electron Microscopy Sciences, Hatfield, USA) in PBS for 30 min at room temperature. The samples were washed thrice for five min with PBS. The 3D-tissues were permeabilized in PBS containing 0.25 % Triton X-100 (Sigma-Aldrich/Merck KGaA, Darmstadt, Germany) for 30 min at room temperature on a shaker. This was followed by three washing steps (5 min each) in PBS. 3D-tissues were incubated in 5 % (w/v) bovine serum albumin (Sigma-Aldrich/Merck KGaA, Darmstadt, Germany) in PBS for 2 h at 37 °C. Afterwards, samples were incubated on a shaker, overnight at 4 °C in a 1:300 mixture of Tuj-1 beta tubulin antibody (Abcam, Cambridge, United Kingdom) and 5 % PBS containing. The following day, samples were subjected to 3 × 5 min PBS washes. The scaffolds were incubated overnight in a 1:500 mix of Alexa 594-conjugated secondary antibodies staining (Donkey anti-rabbit, Abcam, Cambridge, United Kingdom) and 5 % PBS was used. Samples were incubated overnight at 4 °C followed by 3 × 1 hr washes in PBS. 4',6-diamidino-2-phenylindole (**DAPI**, Life Technologies, Carlsbad, USA) was added into the staining solution to stain the nuclei. Samples were imaged using laser scanning confocal microscope (LSM 710, Zeiss, Oberkochen, Germany).

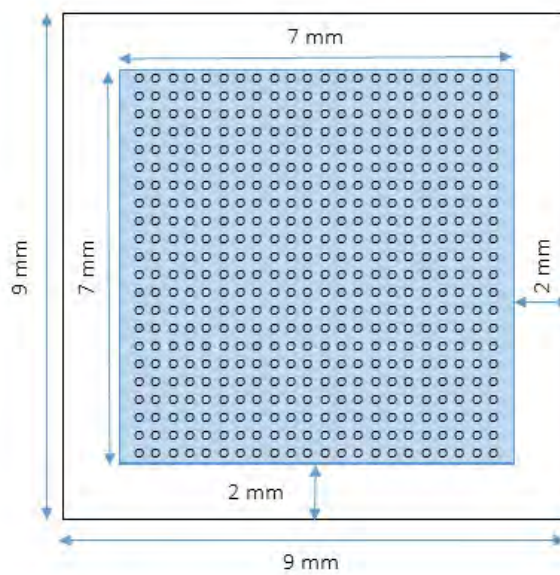


Figure 3.13: Buckyball of 100 µm diameter fixed to the glass sample by five rod extensions (left). An array of 25 × 25 buckyballs was structured on a 9 × 9 mm² for standing wave experiments.

3.9 Hair Follicles

To combine high cell density with mechanical stability, the previously discussed buckyballs and lolly-ups were used to provide mechanical stability for experiments focusing on hair-inducing cells. The microscaffolds were loaded with iPSC derived DP cells and keratinocytes (KC), which provide the environment required by the DP cells in their natural state. Furthermore, KC enhance the crosstalk between dermal and epidermal cells upon transplantation. After seeding, the scaffolds provided a tool to facilitate the transplantation of the 3D-follicular units into the back of nude mice and to enhance the hair growth through the skin, mimicking the biological event of hair follicle formation in human beings (Fig. 3.14). Initial experiments were done using zr-hybrid buckyballs without guiding rod as a proof of principle. Afterwards, lolly-ups fabricated from PCL₆ were seeded with cells to showcase the cell compatibility of the material. For this method custom microwells were designed for the specific experimental needs.

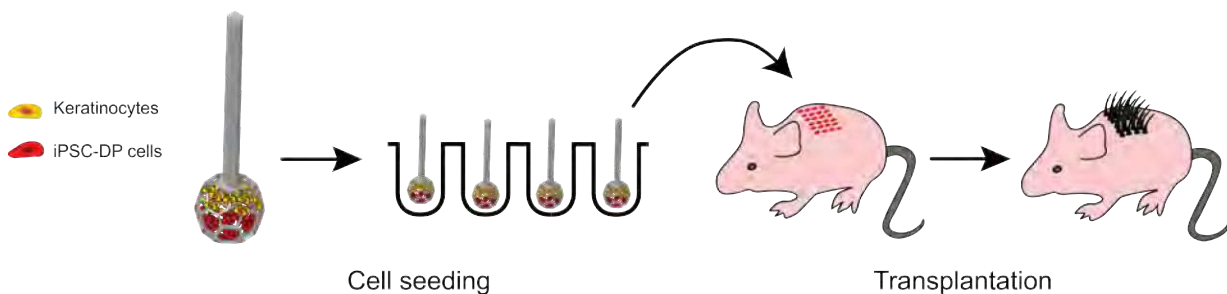


Figure 3.14: Schematic representation of the method developed to create an aggregate of keratinocytes and dermal papilla cells using lolly-up microscaffolds. After 3 days of culture, the scaffolds filled with cells are transplanted into mice to evaluate the ability to generate hair follicles.

3.9.1 Microwells

A stamp was designed to fit 9×9 wells on a 30 mm circle. The wells were designed as V-shapes with a top diameter of 2 mm and a bottom diameter of 300 μm . This design was chosen to allow cells to drop to the bottom of the well without clinging to the extension rod of the lolly-up structures. The stamp was cleaned after fabrication using a 1:1 solution of acetone and 2-propanol for 30 min. After drying, the stamp was UV-treated and covered with gold particles using sputter coating to render the material chemically inert. To produce the negative, Sylgard 184 silicone elastomer and Sylgard 184 curing agent, purchased from Sigma-Aldrich (Merck KGaA, Darmstadt, Germany, used as received), was used to produce a silicone negative of the stamp. This acted as a negative for agarose molds. Curing agent and silicone elastomer were manually mixed at 1:10 ratio for ten min. Afterwards air bubbles caused by the manual stirring were removed by centrifuging the sample for five min. The material was poured over the stamp, which was enveloped in aluminum foil to prevent leakage (Fig. 3.15, middle). This process entrapped air within the pores of the stamp. Therefore, the sample was put in the desiccator. The desiccation was repeated three times to assure that no air was confined within the elastomer. The sample was placed in the oven at 100 $^{\circ}\text{C}$ for 30 min. After this procedure the material was left for ten min at room temperature before removal from the negative to avoid fracture of the elastomer.

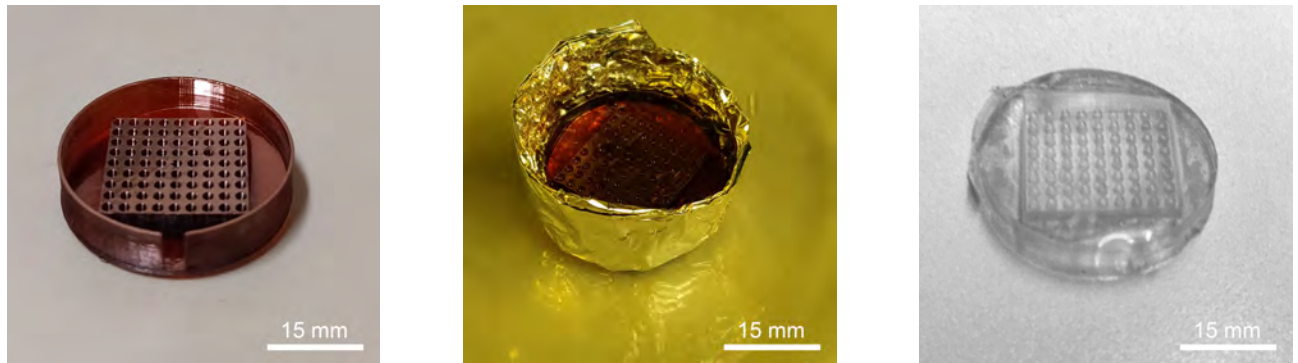


Figure 3.15: Fabrication of negative for agarose microwells. A stamp containing 9×9 microwells was produced using SLA (left). Sylgard 184 silicone elastomer and curing agent were used to produce a negative. In order to avoid leakage, the well was enveloped with aluminum foil (middle). After curing the silicone positive could be removed from the stamp (right).

A solution of 2% Agarose (Sigma-Aldrich/Merck KGaA, Darmstadt, Germany) in purified water was heated using a microwave until the material was completely dissolved. The liquid agarose was then poured into a 35 mm culture dish. The silicone positive, which was cut along the edges to create a square stamp, was placed up-side-down on the agarose solution. After 10 min, the positive stamp could be removed from agarose. The result was a culture dish with 63 V-shape microwells. The custom plate was then transferred in the incubator and equilibrated overnight with the cell medium.

3.9.2 Encapsulation and Transplantation

To ensure the presence of a single scaffold per microwell and allow spheroids formation within the structure, the individual scaffolds were manually transferred to each well. In case of the lolly-up geometry, ball portion was at the bottom and rod faced toward the top of resection. This placement was chosen to avoid cell aggregation towards the guiding rod. Transfer was conducted under a stereomicroscope (Leica MZ6, Leica Microsystems GmbH, Wetzlar, Germany). After differentiation of hiPSCs into DP-like cells and expansion in monolayer, hiPSC-DP cells were harvested with trypsin, centrifuged and resuspended in AmnioMAX™ II medium (Gibco, Thermo Fischer Scientific, Waltham, Massachusetts, USA) at the density of 10^6 cells in 250 μ l. For mouse keratinocytes (**mKC**), the truncal skin was removed from E18.5 C57BL/6 embryos and rinsed in Ca^{2+} and Mg^{2+} free PBS. The skin was oated on 0.2% dispase overnight at 4 °C to separate epidermis from dermis. The dermis was then digested with 0.2% collagenase (Sigma-Aldrich, St.Louis, USA) at 37 °C for 60 min, while the epidermis was digested with 0.25% trypsin/EDTA (Sigma-Aldrich, St.Louis, USA) for 10 min at 37 °C. Single-cell suspensions were strained through 40 μ m filters and pelleted at 1200 rpm. 1×10^6 mouse dermal cells and 1×10^6 single epidermal cell were resuspended in a total volume of 250 μ l of AmnioMAX™ II medium (Gibco, Thermo Fischer Scientific, Waltham, Massachusetts, USA) and Keratinocytes growth medium (PromoCell GmbH, Heidelberg, Germany) respectively. The mKCs were then mixed together with hiPSC-DP cells or mouse dermal cells and homogeneously distributed over the microwell in the culture dish. To ensure a proper settlement of the cell mix at the bottom of the resections, the culture dish was briefly centrifuged for 3 min at 500 rpm. At this point,

3 Materials and Methods

fresh medium, made of an equal amount of AmnioMAX™ II medium and keratinocytes growth medium, was carefully added to the culture dish, which was incubated at 37 °C for 3 days.

In order to evaluate the hair-inducing properties of iPSC-DP cells generated in vitro, the zr-hybrid buckyballs were transplanted into the back skin of Athymic nude mice. Athymic nude mice were obtained from Envigo (Envigo, Placentia, USA). All animal procedures were performed in accordance with the PHS Policy on Humane Care and Use of Laboratory Animals [192] and with the approval of the Sanford Burnham Prebys Medical Discovery Institute IACUC Committee. Under anesthesia (isofluorane), a shallow stab wound nearly parallel to the skin surface was made using a 20-G ophthalmic V-lance. The scaffolds were manually transferred inside the wound, which was covered with bandages for about 1 week to allow the healing. After recovery from anesthesia, mice were kept under normal husbandry conditions. The skin sites that had received the injected cells, referred to as “patch”, were harvested 14-18 days later. The generated hair follicles were next analyzed via immunohistochemical staining, using the Anti-Keratin 14 antibody (**K14**) and the human-specific antibody (MAB1273, Merck Millipore, Massachusetts, USA) to detect the epithelial compartment of the follicle and the presence of human DP-like cells respectively. DAPI was used to stain nuclei. All of the images were obtained via z-stack projection using confocal microscope (Apotome, Zeiss, Oberkochen, Germany).

4 Results Z-Scan

Z-scans of different 2PA compounds are presented. An initial system calibration was done, which was required to completely characterize the focused laser beam. The measurement algorithm was optimized to reduce calibration time. Initial z-scans of rhodamine B were conducted to study the effect of a chopper in order to prevent accumulated heating caused by the high repetition rate. Afterwards, the PIs M2CMK and DAS, which are used for 2PP structuring, were characterized and the 2PA spectrum was compared with polymerization performance for variable structuring wavelengths. Lastly a study of 2PA compounds of interest for 2P-PDT (P2CK, eosin-y, cisplatin, and *porphine*) was carried out and preliminary 2P-PDT experiments were done using the optimal working window of cisplatin and P2CK.

4.1 System Calibration

The parameters (τ , z_R , ω_0 , and P) required for the fitting of q_0 were collected in a spectral range from 700 to 1000 nm (see 2.8). To study the effect of wavelength dependence on the beam collimation a Galilean beam expander and a reflective beam expander were compared. Without manual readjustment for each wavelength, the focal position of the laser beam shifted substantially for the Galilean beam expander while it remained constant for the reflective expander (Fig. 4.1). Therefore, the reflective expander was ideally suited for the automatic z-scan setup.

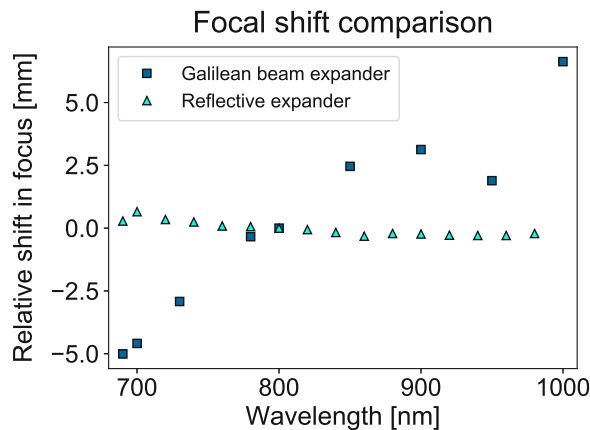


Figure 4.1: Focal position for over the laser tuning range. Using a Galilean beam expander caused large shifts in the focal position if the collimation was not manually adjusted for each wavelength. A reflective expander collimates the beam over the entire laser spectrum, causing only negligible shifts in focus.

After acquiring the output laser powers for each wavelength, the conversion factors were

4 Results Z-Scan

determined. These factors calculate the signal range in mV for a given laser power. They are especially important, as the change in signal for the z-scan can be below one percent. This narrow window has to be carefully selected before the measurement to ensure highest possible accuracy. The conversion factors were recorded in 5 nm intervals for the entire laser spectrum. The resolution limit was 0.02 % signal fluctuation at 1.0 W and 800 nm.

During initial z-scans, a reflection of the laser beam was observed when the sample was moved into the laser focus (as seen in Fig. 4.2, left). A part of the beam was reflected by the cuvette and traversed the path right back to the reference diode. To counteract this reflection and guarantee a stable reference signal, the angle of the cuvette was slightly tilted as it was initially placed perpendicular to the incoming beam.

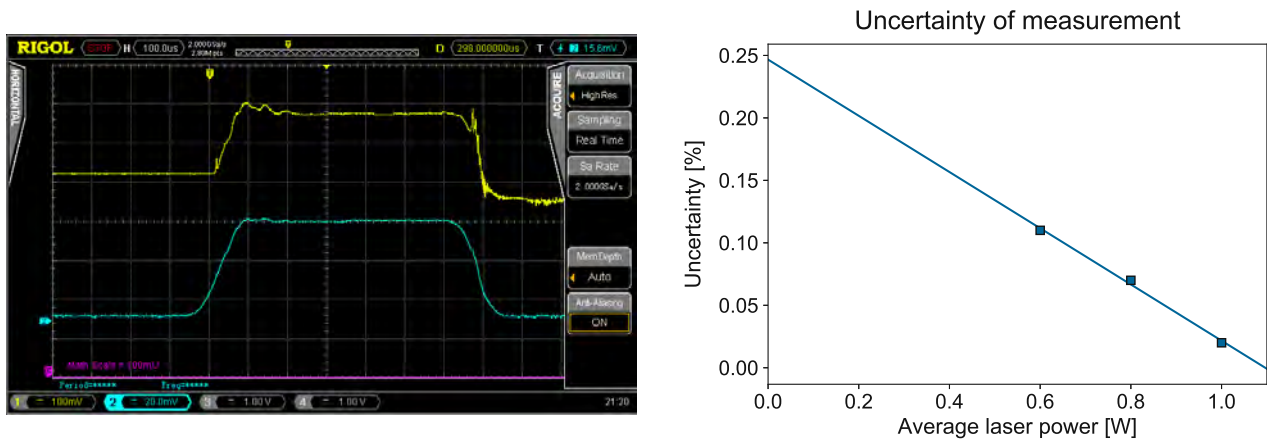


Figure 4.2: Reflected signal at reference diode (D1, yellow) when the sample was moved into focus (left). If the reference signal increases due to reflection it cannot be used to properly normalize the measured data. By slightly tilting the cuvette, this reflex was avoided. Resolution limit of the z-scan (right). The uncertainty due to internal noise of the measurement diodes increased from 1.0 W to 0.6 W, limiting the measurement window of the z-scan.

To determine the systematic uncertainty of measurements three laser powers at 800 nm (0.6, 0.8 and 1.0 W) were selected and 100 signals recorded without any 2PA compound in the beam path. Uncertainty decreased from 0.11 % at 0.6 W, to 0.02 % at 1.0 W. This trend was a logical result as higher laser powers result in higher diode current and therefore the diode noise does not affect the signal as much (Fig. 4.3). For each wavelength the relationship between waveplate angle θ and output power was fitted according to Eq. 3.1. This was done in 5 nm steps over the laser spectrum. Measurements showed a maximum power of 1.9 W at 790 nm and a decrease in laser power to 0.5 W at 700 and 1040 nm (Fig. 4.3, left). The conversion factors for each wavelength were acquired (Fig. 4.3, right).

Directing the beam into an autocorrelator via flip mirror allowed measurement of the pulse duration (Fig. 4.4). The pulse compressor of the laser unit can be adjusted by changing the motor position of the prism configuration (Fig. 4.5, left). By changing the motor position and subsequent measurement of τ for each position the pulse duration was minimized to 70 fs from 750 to 950 nm. The pulse duration increased towards the flanks of the available laser spectrum to 110 fs at 700 nm and 75 fs at 1000 nm (Fig. 4.5, right). Since the output laser power decreases towards the end of the laser spectrum and pulse broadening takes place, no second harmonic

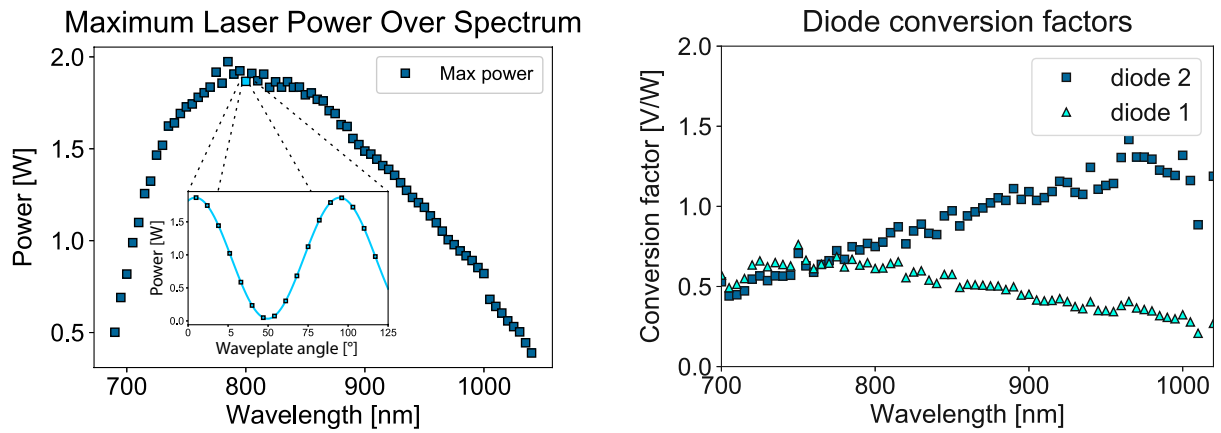


Figure 4.3: Maximum laser power (left). For each wavelength the relationship between waveplate angle θ and output power was fitted (insert). This was repeated in 5 nm steps over the laser spectrum. Diode conversion factors for reference and the measurement diode (right). The change in sensitivity depending on the wavelength is important to find the optimal signal range for each wavelength, thereby guaranteeing the highest possible resolution and accurate measurement.

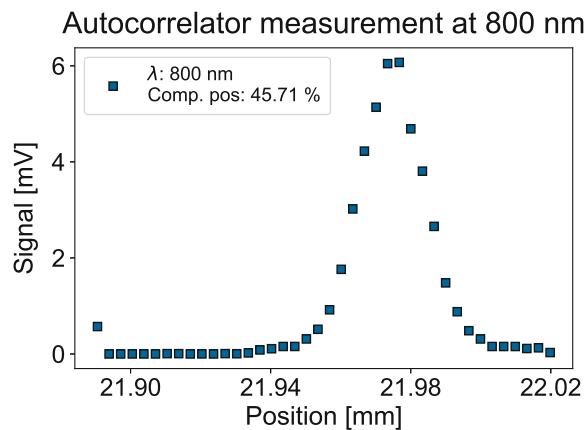


Figure 4.4: Optimizing the pulse duration using an autocorrelator. The laser beam is split in two beams of equal intensity. Using a motorized stage the optical path difference of the two beams is in- or decreased depending on the stage position. A photodiode records the signal produced by second harmonic generation.

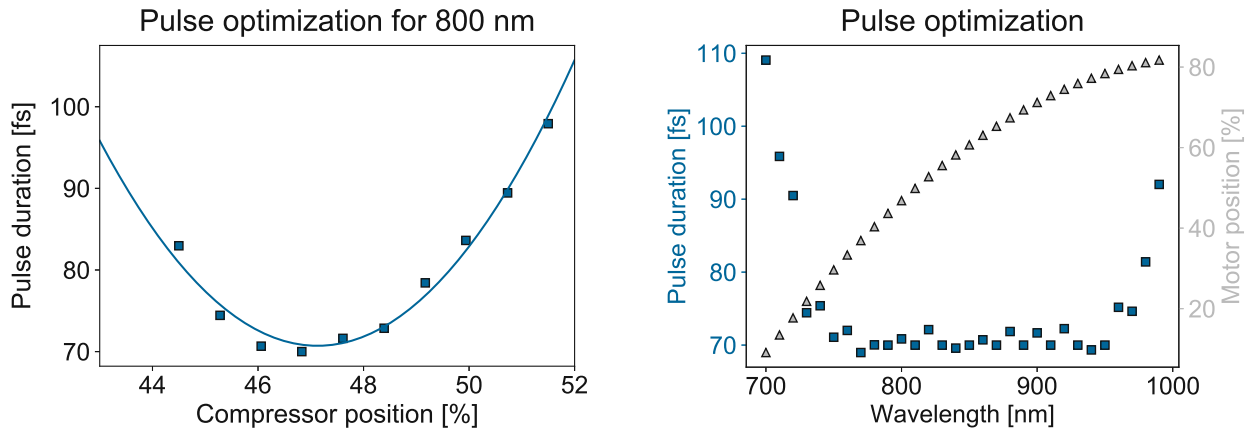


Figure 4.5: For each motor position the autocorrelator measurement was done to find the minimum pulse duration for a given wavelength (left). Minimum pulse duration (squares) for all measured wavelengths (right). For each wavelength an optimal motor position for the compressor was determined (triangles).

generation was observed for wavelengths above 1000 nm.

The beam data was measured over the entire laser spectrum and the Rayleigh lengths were fitted to $z_R \propto \frac{1}{\lambda}$ (Fig. 4.6, left). Using the minimum beam waist ω_0 and z_R the beam quality M^2 could be calculated for a given wavelength λ (Eq. 2.24). M^2 was almost exclusively below 1.2 and on average 1.1 over the entire spectrum indicating good beam quality (Fig. 4.7) [193].

4.1.1 Beam Profiler Optimization

To fit the Gaussian distribution using image moment, the algorithm summed over the entire camera pixel array (3840×2748 pixels). As the computation time for a single image took up to 14 seconds, the process had to be reduced to a fraction of a second for the profiler to work in an appropriate amount of time. In order to achieve this, the algorithm scanned the entire image to find the pixel with the highest intensity, which served as estimate for the center of the beam. This pixel was then used as the center of a square which was cut out from the original pixel to have less data points for computing. When assuming a beam diameter of around $300 \mu\text{m}$, 10 mm at the end of the travel range of the motorized stage and $40 \mu\text{m}$ at the focus point, all the necessary data for the fit can be confined to an array of 350×350 pixels thereby reducing the amount of pixels by 90%. This image reduction is visualized in Fig. 4.8.

Furthermore, the fitting algorithm itself was improved by optimizing the initial estimates for the least square fitting. Using constant estimates for σ_x , σ_y required longer fitting times as the beam waist contracts and expands along the stage. The time for fitting 25 stage positions was 19.26 s. The second fitting approach, using the second order image moments as estimates for the least square fitting, reduced the total time by 20%. As this method is based on the same algorithm later used for least-square fitting its efficiency depends on an optimally cut-out array by the image reduction algorithm. Otherwise the computation time increase as again the method sums up over a discrete grid. The fastest computation performance was achieved by estimating σ_x and σ_y by intersecting a 1D-array in x- and y-direction and using these coordinates for the highest peak pixel. The estimates for ω_x and ω_y were taken from the

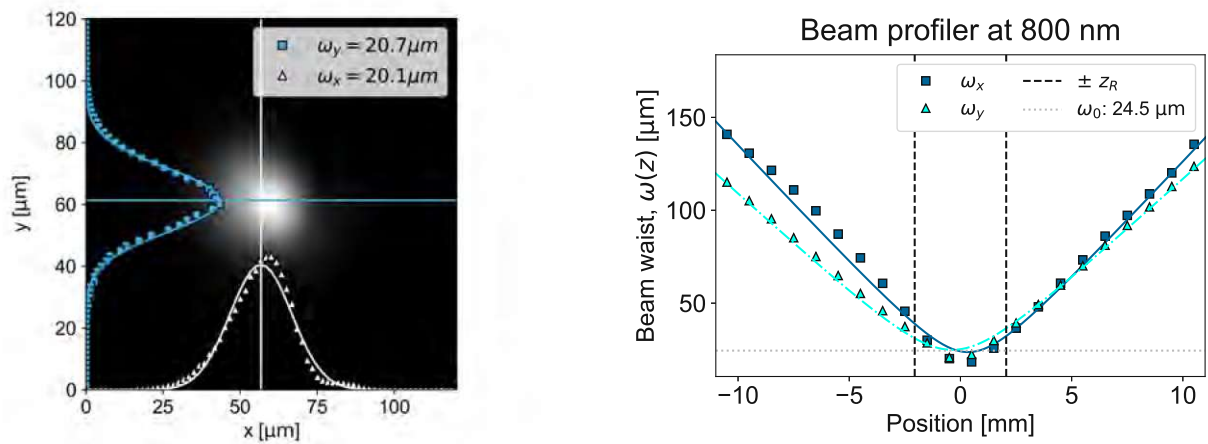


Figure 4.6: Beam profiling algorithm (left). From the recorded image the intensity distribution is fitted to a Gaussian distribution. As can be seen there is a slight astigmatism inherent from the fs-laser module. The profiling is done for multiple stage positions to determine the beam parameters ω_0 , z_R and M^2 for a given wavelength λ (right). Due to the astigmatism the beam is elliptical and the minimum beam waist ω_0 is derived ω_x and ω_y .

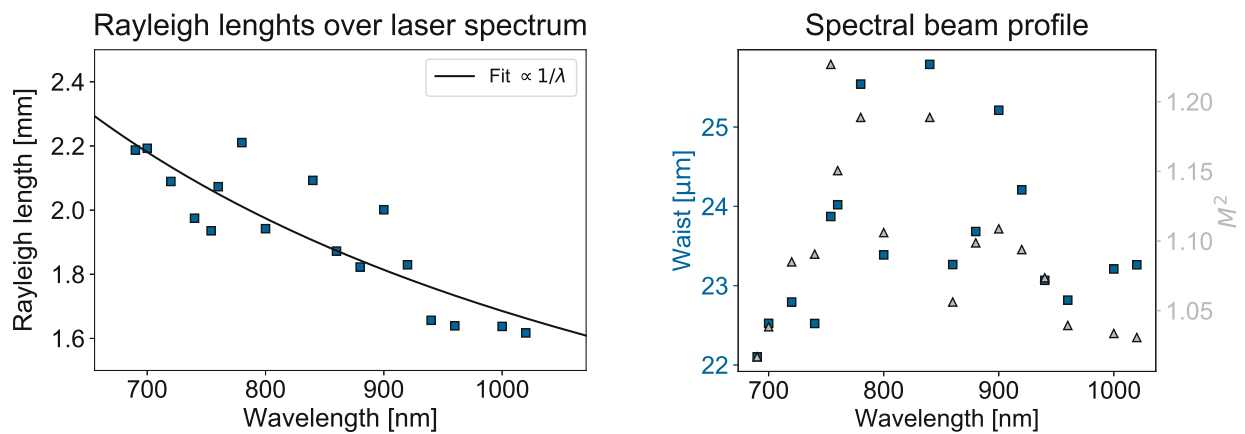


Figure 4.7: Beam profiler results over the laser spectrum. The Rayleigh length z_R was fitted to $z_R \propto \lambda^{-1}$ (left). Measurement of z_R and ω_0 for a given wavelength allowed to calculate the beam quality factor M^2 for a given wavelength λ (right). M^2 was on average 1.1, indicating good beam quality.

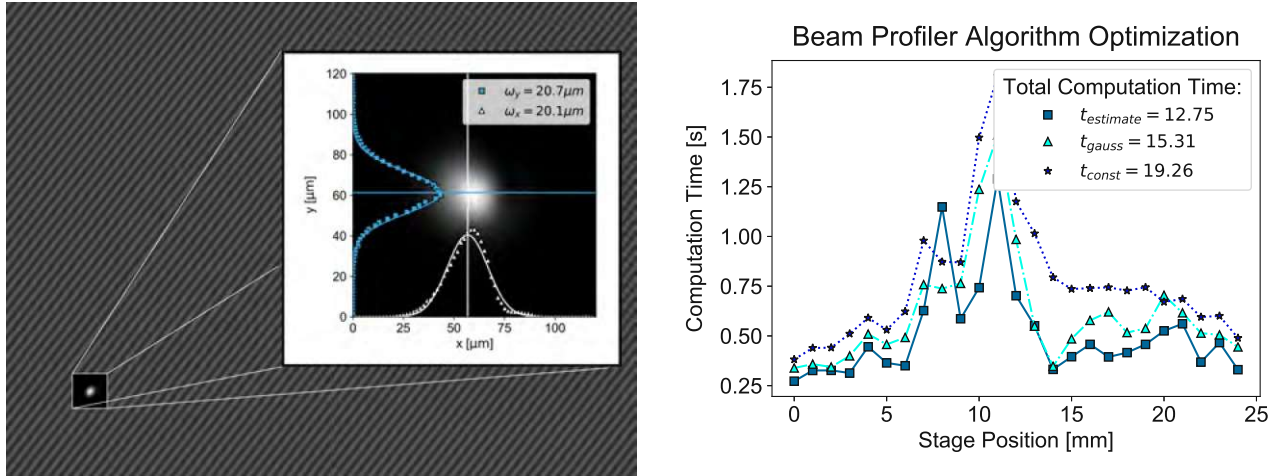


Figure 4.8: Visualization of the image reduction algorithm (left). The striped area is the data ignored for the image moments algorithm to increase the speed of the program. The insert shows the fit done by the software. Optimization of computation time (right). As the beam waist changes for each position using constant estimates for the fitting required longer fitting times (t_{const}). Using estimates based on image moment calculations reduced the time but required optimal selection of the cut out image area (t_{gauss}). Estimating the parameters by two representative arrays yielded a decrease of 33% in fitting time ($t_{estimate}$)

distance where the pixel intensity drops to $I_{pixel} \cdot e^{-2}$, using the relation between beam waist and variance (Eq. 2.32). This approach decreased the measurement time by 33% compared to the initial method using constant estimates (displayed in Fig. 4.8). The image acquisition was also optimized to reduce the time required to record an individual image. For each position the exposure time was dimmed by a factor (0.8 or 0.5) until no overexposed pixels were detected or the minimum exposure time of the camera was reached. A factor of 0.5 resulted in almost 50% decrease in measurement time compared to 0.8. As $\omega(z)$ was given by a focused Gaussian beam (Eq. 2.22), this was taken into account by a floating reduction of the initial exposure time. Here, the initial exposure time was only used at the zero position. For all other positions the initial exposure time was changed with respect to the in- or decrease of intensity expected from the Gaussian beam model. The degree of this reduction could be changed by a dampening factor. A dampening of 0.7 decreased the total fitting time by 5 seconds. A dampening of 0.5 lead to erroneous fitting of the beam as regions with low intensity at the end of the stage were underexposed and not properly fitted. Experiments with an initial exposure time of 62 ms were done to study the possible improvement in computation speed. However, the low exposure time lead to underexposed images at the fringes. Therefore, 500 ms was kept as initial exposure time for all experiments (all results for the different approaches displayed in Tab. 4.1).

Table 4.1: Fitting algorithm optimization. For each position the initial exposure was decreased by a reduction factor until no overexposed pixels were recorded. Floating reduction changed the initial exposure depending on the stage position while dampening additionally reduced this initial exposure time by a factor ≤ 1 . A dampening of 0.5 caused erroneous recording of the beam profile at the fringe positions of the stage. Globally reducing the initial exposure lead to erroneous fitting without significantly decreasing the measurement time. All measurements were done using constant width guess method.

Initial exposure [ms]	Reduction factor	Floating reduction	Dampening	Time [s]	Successful fitting
500	0.8	False	1	236	True
500	0.5	False	1	119	True
500	0.5	True	1	117	True
500	0.5	True	0.7	112	True
500	0.5	True	0.5	98	False
62	0.5	False	1	79	False

4.2 Reference Z-Scan

To illustrate accumulative thermo-optical effects caused by high repetition rate lasers, measurements of a 10 mM solution of rhodamine B in methanol at 800 nm were performed without a chopper (Fig. 4.9, left). These measurements exhibited a significantly larger drop than reported values [35]. To optimize the system, four different chopper on-times from 470 to 78 μ s were compared at two different laser power values (1.0 and 1.4 W). Each scan was repeated three times. Varying the power should not affect the calculated σ_2 . An increase of σ_2 with at intensity is an indication, that the observed absorption is no longer just caused by 2PA alone. For the longest exposure time the cross section at 1.4 W was 20 % larger than the extracted cross section at 1.0 W. This was not the case for higher chopper frequencies, where the increase of average laser power resulted measured σ_2 within the error margins. (Fig. 4.9, right) and corresponded to previous findings [35, 36]. Spectral studies of rhodamine B were also independent of the laser power used for scanning (500 and 700 mW in 10 nm steps) and showed high absorption close to 700 nm, a secondary maximum between 790 and 850 nm and a low 2PA cross section above 900 nm (Fig. 4.10). The spectral data were in good agreement with reference values from literature [35, 36].

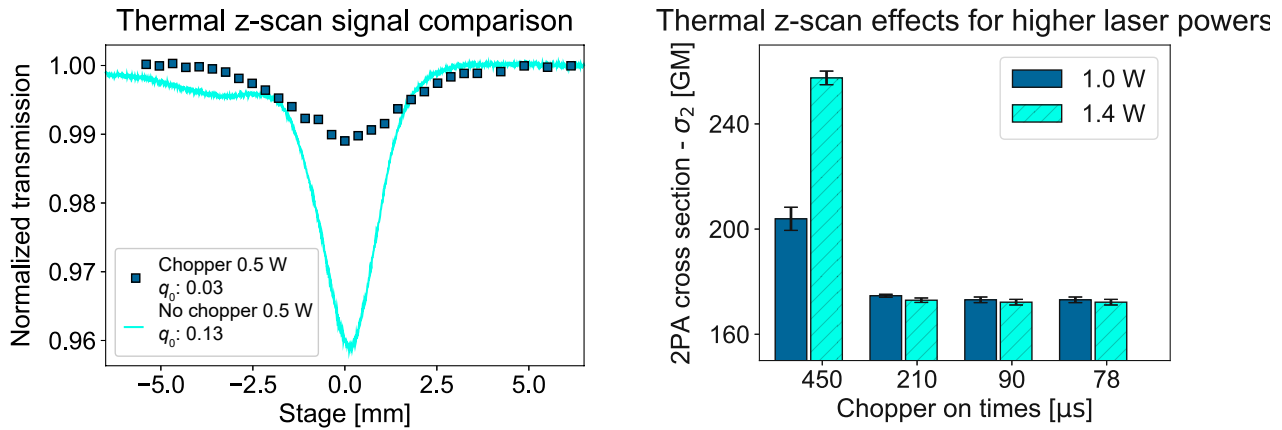


Figure 4.9: Thermal z-scan comparison of rhodamine B (10 mM in Methanol at 800 nm) measured with and without chopper (left). The signal drop without chopper (straight line) was four times larger than when a chopper was used (squares). Four different chopper exposure times were selected to study the impact of thermal effects on the extracted cross section (right). For each exposure time the cross section was measured at 1.0 and 1.4 W and the relative change in cross section was calculated. At 450 μ s exposure time the change in extracted cross section was more than 20 % indicating thermo-optical effects caused by the high repetition rate. In contrast, at chopper on-times of 210 μ s and below such behavior was not observed.

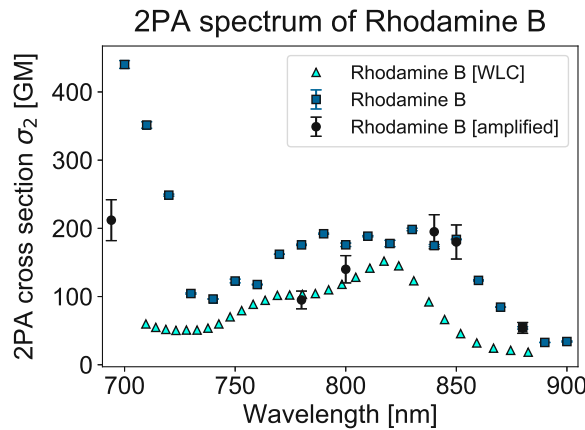


Figure 4.10: 2PA-spectrum of rhodamine B. The solid squares show the data measured using the tunable z-scan setup. Black circles are reference values using a z-scan setup based on an OPA [35], whereas triangles are measured using a z-scan setup based on WLC [36] (no error bars provided by source). The data follow similar trends exhibiting high absorption in the region between 760 and 840 nm and lower absorption for longer wavelengths. Close to 700 nm the values obtained with the tunable system and the OPA setup increase.

4.3 Photoinitiators

For M2CMK at 300 mW onwards, the fit parameter q_0 - which corresponds to the 2PA absorption coefficient β - increased exponentially with the laser power (Fig. 4.11). Under pure 2PA conditions q_0 scales linearly to the used laser power (Eq. 2.86). Higher laser powers also lead to a notable sharpening of the transmission curve, with 76 % of the signal drop within $\pm 1.3 z_R$ compared to 65 % (Fig. 4.12). A trend of 65 % signal drop within this limit was also observed for rhodamine b. Therefore, the measurement power was reduced to 250 mW for each wavelength to obtain σ_2 . The 2PA values obtained for the spectrum of M2CMK were higher than the reference spectrum measured with the WLC and due to the lower laser powers the measurement error increased compared to the results for rhodamine B. However, the trend of WLC and the tunable setup was comparable with a maximum absorption between 720 and 800 nm and a decrease in 2PA cross section below 50 GM above 900 nm (Fig. 4.13, left).

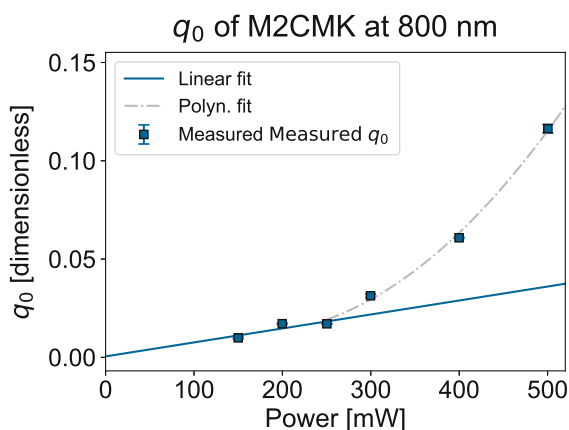


Figure 4.11: 2PA studies of M2CMK (10 mM solution in THF) at 800 nm. In the pure 2PA case q_0 is expected to follow a linear trend, which was observed for measurement powers up to 250 mW (left, solid line). From 300 mW on q_0 followed an exponential trend (dashed line).

To correlate the absorption spectrum with 2PP-performance an array of cubes ($60 \times 60 \times 60 \mu\text{m}^3$, at 100 mm s^{-1} , 10x/0.3 objective) was structured for varying wavelength and laser powers to compare the minimum power required to yield visible structures, which can be correlated to the polymerization threshold. Polymerization performance significantly increased from 820 to 800 nm with minor fluctuations in polymerization threshold from 800 to 700 nm (Fig. 4.13).

The spectrum of DAS correlated well with the previously reported findings, showing an absorption maximum of 100 GM at 700 nm [36]. To compare 2PA with polymerization efficiency 1 mM DAS was used in the presence of methacrylated GelMod to produce cubes ($100 \times 100 \times 100 \mu\text{m}^3$, at 1000 mm s^{-1} , using 10x/0.3 objective). The structuring was performed at four different wavelengths. As can be observed from the array of cubes produced by 2PP in (Fig. 4.14, right), the required laser power was 40 mW for 700 and 720 nm, whereas it increased to 60 mW for 800 nm. This correlation was further quantified as

$$P_{th} \propto \sqrt{\sigma_2}^{-1}. \quad (4.1)$$

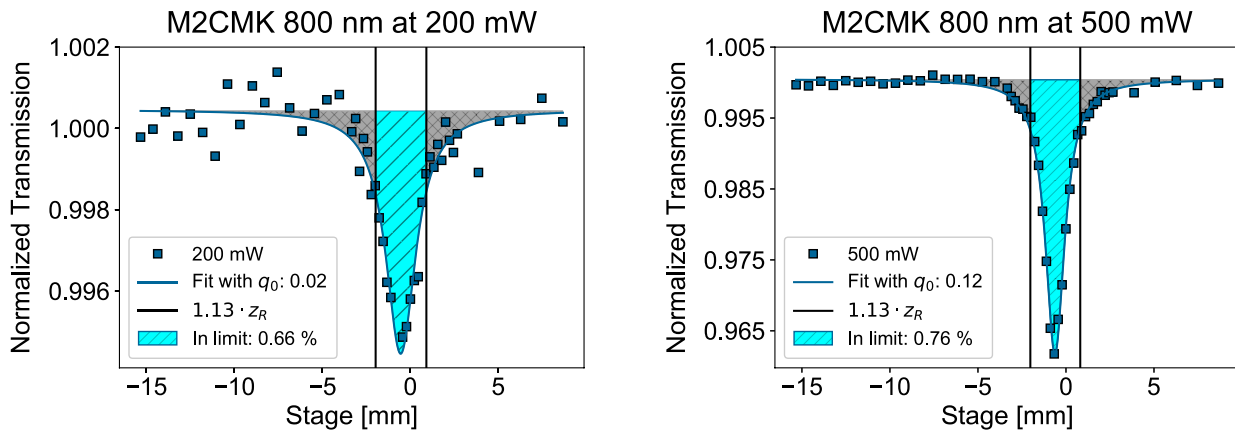


Figure 4.12: Z-scans of M2CMK (10 mM solution in THF) at 800 nm. The exponential increase in absorption was also visible in the recorded transmission signal, where a notable sharpening of the curve can be seen when comparing 200 mW (left) and 500 mW (right). While at 200 mW 650% of the signal drop occurs within a distance of $\pm 1.13 \cdot z_R$ around the focus, at 500 mW 77 % of the signal drop is happening within this section.

This relation was taken from Eq. 2.54. As there is no clearly defined threshold for cube structures (compared to the linetest method), two conditions were studied and correlated to σ_2 . The power required for clearly pronounced cube features ("Stable cubes" in Fig. 4.15) and the power where first polymerization was observed ("First cubes" in 4.15) were both plotted. The dependence of threshold from σ_2 could be observed for both M2CMK and DAS. The trend was more clearly pronounced for M2CMK. This was probably due to the significantly larger cross section of M2CMK when compared with DAS. These results indicate a clear correlation between the absorption maximum of the PI and its performance during 2PP structuring.

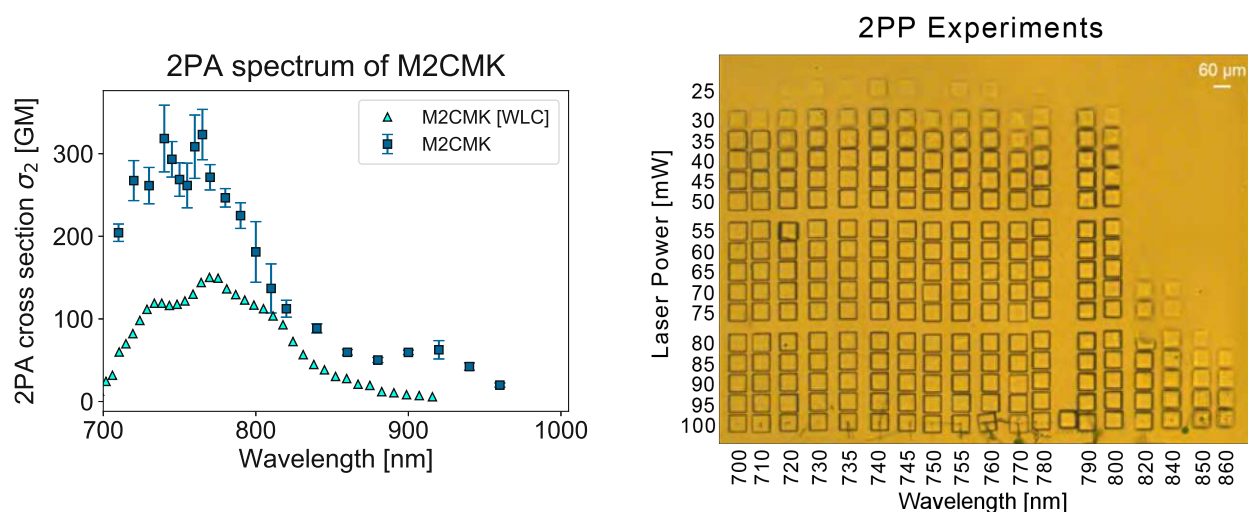


Figure 4.13: 2PA-spectrum of M2CMK (left) in Methanol (10 mM) measured with the tunable system (squares) was compared to the referenced WLC [36, 99] (triangles, no error bars given in source). While larger than results from WLC experiments, the spectral behavior of σ_2 followed a comparable trend with the absorption maximum between 720 and 800 nm and a decrease in 2PA cross section above 900 nm. 2PP experiments of PCL₆ with 1 wt% M2CMK correlated to this absorption behavior as the structuring power for required for polymerization increased significantly for 810 nm and higher wavelengths (right).

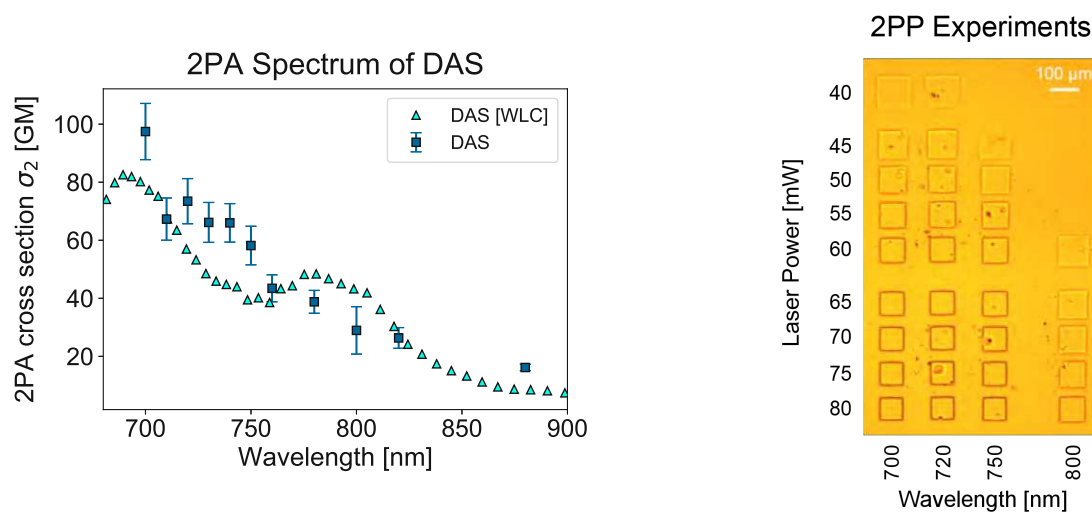


Figure 4.14: The 2PA spectrum of 10 mM DAS (left) in PBS (2 mM) measured with the tunable system (squares) was compared to the data obtained from WLC [36, 99] (triangles, no error bars given in source). It exhibits a maximum absorption of 90 GM at 700 nm. The 2PP structuring wavelength was matched to the absorption peak, which resulted in reduction of the polymerization threshold (right).

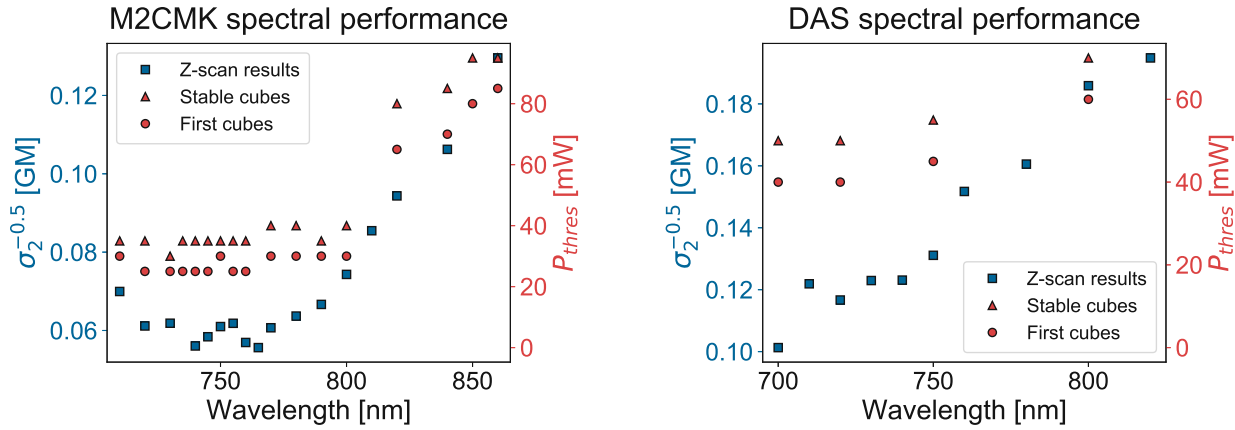


Figure 4.15: Correlation between σ_2 and necessary laser power. The polymerization threshold power is inversely proportional to $\sqrt{\sigma_2}$. As the threshold power for cubes can only be described qualitatively, two threshold conditions were studied. Both the minimum power for clearly defined cubes (Stable cubes, triangles) and the minimum power for first polymerized features (First cubes, circles) showed clear correlation to σ_2 . The trend was more pronounced for M2CMK (left), compared to DAS (right), which was probably due to the significantly higher σ_2 of M2CMK and therefore steeper change.

4.4 Measurement Algorithm

The results for rhodamine B (Sec. 4.2) as well as for the PIs (Sec. 4.3) allowed to establish a measurement procedure for the tunable z-scan system. As the laser power significantly decreased towards the edge of the laser spectrum, 600 mW was chosen as the initial laser power P_{init} . The initial measurement was done at 800 nm in a power range of from $P_{init} \pm \Delta_P$ with $\Delta_P = 100$ mW. For each power setting three z-scans were recorded. If the average σ_2 was within $\pm 15\%$ the measurement was accepted. If the fluctuation was higher than this criterion, an additional three z-scans were recorded at $P_{init} - 2 \cdot \Delta_P$. The procedure was repeated until σ_2 extracted from the lowest three laser powers was within the criterion or the minimum power $P_{min} = 200$ mW had been reached. If the latter were the case, the data in the power range where q_0 behaved linearly were selected to extract σ_2 . This approach needed to be adjusted for $\sigma_2 < 100$ GM, as a 15% of fluctuation in this range was below ± 10 GM and consumed long measurement times without yielding further insight, as the nonlinear scaling of q_0 was only observed for $\sigma_2 > 100$ GM. Therefore, for lower σ_2 it was deemed sufficient to accept the measurements of $\sigma_{error} \leq \pm 10$ GM. To further increase the time efficiency of the method, P_{init} was dynamically adapted when changing to a new wavelength λ_{new} depending on the results for a previous wavelength λ_{old} . If the initial power range $P_{init} \pm \Delta_P$ was lowered to $P_{new} = \pm n \cdot \Delta_P$ with $P_{new} = P_{init} - n \cdot \Delta_P$, this setting was used as the initial power for λ_{new} . Using this floating measurement window significantly reduced the number of required z-scans to reliably extract σ_2 .

4.5 2P-PDT

Eosin-y was dissolved in PBS (1 mM). As the linear absorption was at 460 nm [154], the 2PA absorption region was estimated to be in around 920 nm. Z-scans were performed in triplicates at 500 mW from 800, 920, 960, 980 and 1000 nm. A change in signal at the focus was only observed at 1000 nm. However, this change was already within the noise range of the setup (Sec. 4.1) and did not allow reliable extraction of σ_2 . The concentration was increased to (3 mM) and the z-scan was repeated from 800 to 1000 nm in 20 nm steps. The laser power was 500 mW for all scans. This operating power was chosen as to avoid possible heating of the sample, while still being sufficiently far away from the resolution limit at 150 mW. The absorption window of eosin-y was found to be 960-1000 nm (Table 4.2). For cisplatin, a 10 mM solution in DMSO was required to measure the nonlinear absorption from 980-1000 nm. While both compounds exhibited nonlinear absorption behavior, σ_2 was comparatively low and exclusively below 100 GM, as can be seen in Tab. 4.2.

Table 4.2: 2PA spectrum of eosin-y dissolved in PBS (3 mM) and cisplatin dissolved in DMSO (10 mM). The absorption window was at the upper end of the laser spectrum and all compounds exhibited $\sigma_2(\lambda)$ below 100 GM, indicating low 2PA performance.

λ [nm] \ σ_2 [GM]	Eosin-y	Cisplatin
960 nm	57.50 ± 4.41	-
980 nm	62.20 ± 5.19	16.07 ± 1.02
1000 nm	58.99 ± 0.07	24.68 ± 0.24

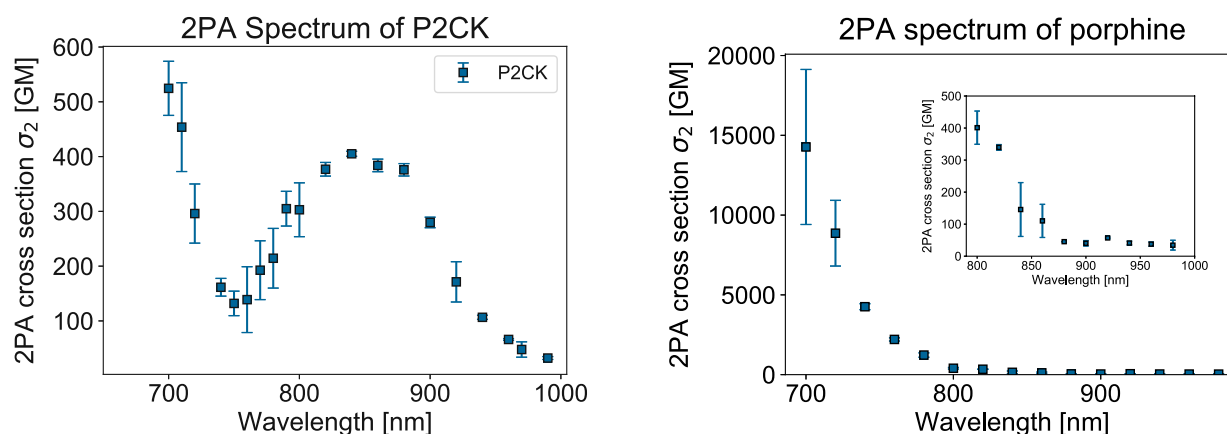


Figure 4.16: The 2PA spectrum of porphine (10 mM in DMSO) exhibited a drastic increase in σ_2 towards 700 nm. Insert shows that σ_2 is already above 100 GM at 860 nm.

While the watersoluble P2CK has been developed as a PI for 2PP structuring in hydrogels, cell death was observed when the PI was activated in close proximity of living cells due to ROS being produced [194]. Therefore, this PI was chosen as a possible candidate for PDT applications. The z-scans of a 10 mM solution in PBS revealed an increase in σ_2 towards 700 nm, as well as a local absorption maximum at 840 nm (Fig. 4.16, left). Z-scans of porphine

4 Results Z-Scan

were performed using a 10 mM solution in DMSO. The wavelength range was 700 to 1000 nm in 20 nm steps. An average laser power of 400 mW was selected. The 2PA activity of porphine significantly increased towards 700 nm. While 400 mW lead to a total signal drop of 0.36 % at 820 nm, the same average power at 700 nm caused a signal drop of 60 %. Therefore, from 820 to 1000 nm, the power was set to 300 and 400 mW. Each z-scan setting was done in triplicates. From 700 to 800 nm the power range was chosen to be 150, 250 and 350 mW to study a possible influence of laser power on q_0 , indicating thermo-optical effects. However, no significant changes of $\sigma_2(\lambda)$ in the selected power ranges were observed. The results for $\sigma_2(\lambda)$ showed a cross section of 112.96 GM at 860 nm which decreased to 34.44 GM at 980 nm. At 1000 GM the signal drop was below the detection limit. The 2PA cross section increased drastically towards 700 nm, where the extracted cross section was in the range of a several thousand GM (Fig. 4.16, right).

Due to this high σ_2 a concentration study was carried out. This was done to see if variation in concentration affected the 2PA behavior. Also, since the signal drop at 700 nm was 60 %, significantly higher than other compounds measured with the z-scan setup, a reduction of the concentration was possible due to this high signal drop. Three additional concentrations of porphine in DMSO (2, 1 and 0.5 mM) were selected.

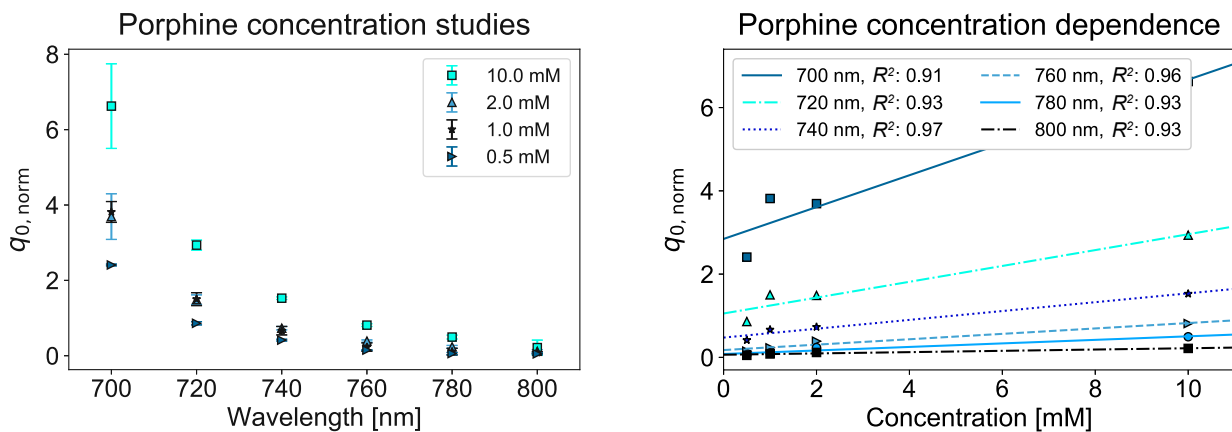


Figure 4.17: Concentration studies of porphine (left). Z-scans with varying porphine concentrations were conducted. To focus on the concentration dependence, q_0 was divided by the respective laser power ($q_{0,\text{norm}} = \frac{q_0}{P}$) to allow comparison. $q_{0,\text{norm}}$ decreased with the concentration (left). Since $q_{0,\text{norm}} \propto \rho$, the concentration dependence for each wavelength was plotted (right). As can be seen the linear fit describes the absorption behavior with R^2 exclusively above 0.9.

As expected, the total signal drop was lower, as less 2PA active compounds were being in the exposed volume. However, even at 0.5 mM the signal drop at 700 nm was still 17 %, again exhibiting significantly higher 2PA activity than previously screened substances. As the power range had to be adapted due to the lower signal caused by the reduced concentrations, $q_{0,\text{norm}} = \frac{q_0}{P}$ was used for comparison. The reduction of concentration lead to a decrease in $q_{0,\text{norm}}$ (Fig. 4.17, left). Since $q_{0,\text{norm}} \propto \rho$ (Eq. 2.86) the results were interpolated using a linear fit and least squares approximation. The linear correlation between $q_{0,\text{norm}}$ and ρ was fitted with R^2 values exclusively above 0.9 (Fig. 4.17, right). 2P-PDT experiments with MG63 spheroids and ASC/TERT1 stem cells encapsulated in GelMod showed excellent cytocompatibility for P2CK without irradiation. The laser light control (no PS or chemotherapy agent added) also

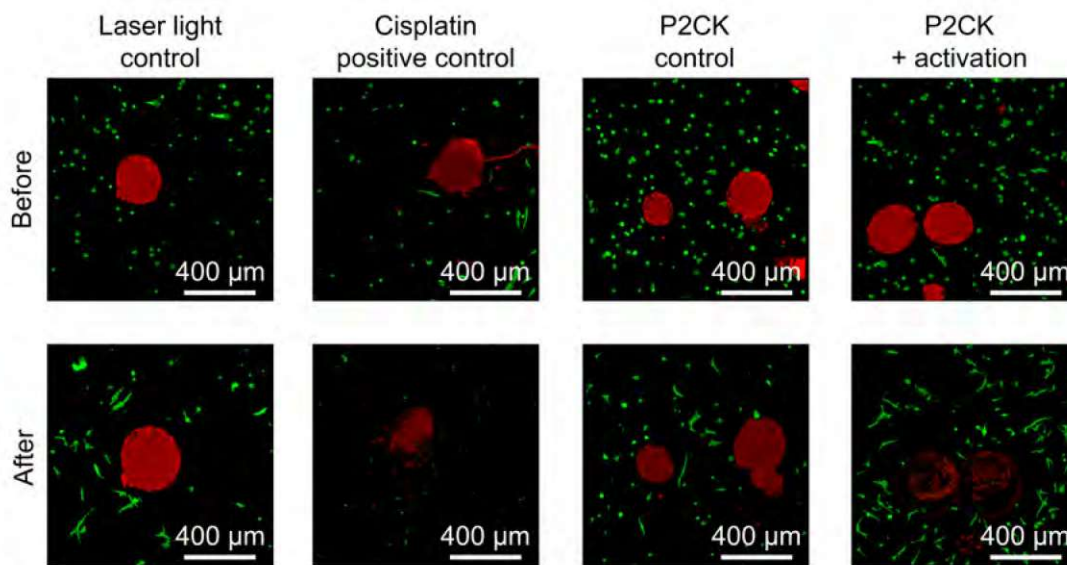


Figure 4.18: 2P-PDT experiments. Spheroids of MG63 (mCherry labeled, red) were formed to mimic solid tumor tissue. The spheroids were encapsulated in 5% GelNB. Using the 2PL setup the spheroids were exposed to laser light. Without sensitizer the laser light did not damage the cells (laser light control). As cisplatin is a chemotherapeutic agent the induced cell death by the agent was not confined to the exposed area (cisplatin positive control). P2CK showed excellent cytocompatibility without irradiation (P2CK control) and caused local cell death in the MG63 spheroids after irradiation (P2CK + activation) without affecting the surrounding ASC/TERT1 cells (GFP labeled, green). Experiments conducted by Agnes Dobos under the supervision of Aleksandr Ovsianikov.

showed that laser irradiation alone did not damage the cells. Cisplatin was cytotoxic even in unexposed areas causing cell death of healthy ASC/TERT1 cells as well as cancerous MG63. After irradiation, P2CK proved cytotoxic in the exposed volume. The solid spheroid was locally targeted and cell death occurred within the confined volume, without harming surrounding ASC/TERT1 cells. Laser scanning microscope images of the experiments are displayed in Fig. 4.18. The laser power for all experiments was set to 100 mW for better comparison. For cisplatin 960 nm (see Tab. 4.2) was chosen as operating wavelength due to the fact that due to losses along the optical path the output laser power at the objective did not reach 100 mW for wavelengths above 960 nm. For P2CK 850 nm was selected as operating wavelength. While P2CK showed maximum σ_2 at 700 nm (Fig. 4.16) the pulse duration increased towards the end of available spectrum. Therefore, the local maximum at 850 nm was preferred as the pulse duration was minimized in this range. Cell experiments were done by Agnes Dobos under the supervision of Aleksandr Ovsianikov, TU Wien.

4.6 Discussion

A completely automated z-scan setup for spectral characterization of 2PA cross-sections in a wide wavelength range was developed. An extensive calibration routine was implemented in a

4 Results Z-Scan

custom software, automatically gathering large amount of data and storing it in a comprehensive library. This database enables reliable and thorough calculation of the cross-section values at different wavelengths. The use of an optical chopper eliminates thermal effects and a reflective mirror expander guarantees a collimated beam over the entire spectral range without the need to readjust the setup between measurements. Because of its simplicity, the presented z-scan setup is a cost efficient alternative to complex amplified systems and the fully automated software allows rapid 2PA characterization of various compounds.

Using the tunable z-scan setup allowed fast screening of agents for 2PP and 2P-PDT applications. Polymerization experiments indicated a clear correlation between 2PA cross section and polymerization performance. The polymerization threshold was reduced when operating the 2PP system at the wavelength with its highest σ_2 . This increase in polymerization performance for same power, speed and concentration settings broadens the processing window of PIs. The better performance at the same PI concentration is of special interest for tissue engineering application as in the case of DAS, where a too high PI concentration can have cytotoxic effects on the cells [99]. The optimal working window for DAS was determined to be 700 to 720 nm. M2CMK exhibited high σ_2 in a broad window from 700 to 800 nm, where little change in polymerization performance was observed. For follow-up experiments with M2CMK in this thesis, 800 nm was chosen as working wavelength, as it showed excellent σ_2 while at the same time being a standard operating wavelength for 2PP-systems.

While initially designed as a PI, it turned out that P2CK could be used as an efficient PS. From the z-scan experiments an optimal working window of P2CK could be determined at 840 nm. To showcase the efficiency and localization of 2P-PDT, it was demonstrated that P2CK was cytocompatible before irradiation and cell death was only induced at the exposed cell spheroid area. This showcases the efficiency of 2P-PDT, especially when compared to chemotherapeutic agents like cisplatin, where cell death was caused even in non-irradiated areas. As low σ_2 is a major bottleneck for this technology porphine was screened as potential new PS. It exhibited extremely high σ_2 at 700 nm. Concentration studies of porphine revealed that this effect scaled as expected linearly with ρ and that these high σ_2 values were not caused by heating of the sample due to the fs-laser source. With σ_2 of several thousand GM porphine can be used at low concentrations, which is important for cytocompatibility of 2P-PDT experiments.

5 Results PCL

Results for the PCL-based prepolymers (di-function PCL₂ and hexa-functional PCL₆) are presented. As previous reports showed cross-linking of PEG-based prepolymers, the 2PP-processability was initially studied without added PI [42]. Experiments on the effect of added PI on the polymerization threshold were conducted. Afterwards, the mechanical stability of arbitrary 3D-constructs was investigated.

5.1 Di-Functional Prepolymer

5.1.1 No Photoinitiator Added

The first experiments were done with pure PCL₂ (no added PI) as the comparable PEG-based material was previously reported to be cross-linkable under UV conditions without added PI [42]. On a heating plate the sample became transparent at 60 °C.

Race car structures were written (100 mW) using a 63x/1.4 oil immersion objective. During development in THF the structures detached from the surface and strong deformation happened which was probably caused by evaporation of the solvent and the fact that the glass slides used were not methacrylated in advance (see Fig. 5.1) Additionally, fine buckyball structures were produced ($d_h = 0.3 \mu\text{m}$, $d_z = 0.3 \mu\text{m}$, 100 mm s^{-1}). Structures were only observed at energies above 70 mW. No remaining scaffolds could be seen after development in THF.

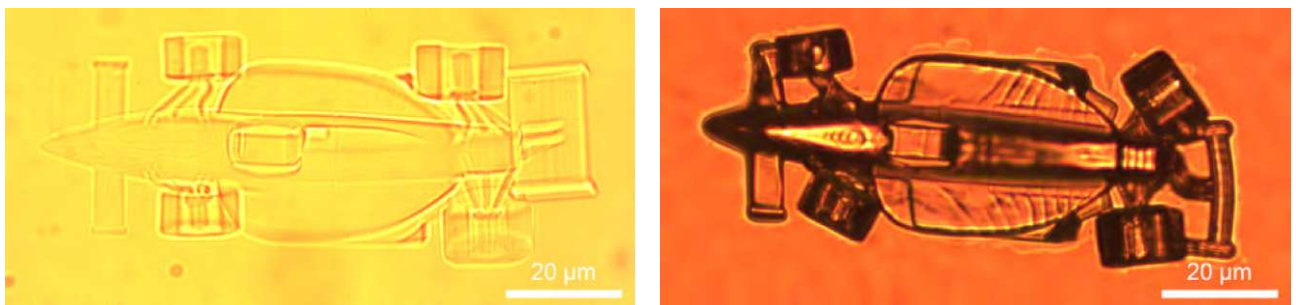


Figure 5.1: Race car structured with PCL₂ without added PI using the 63x/1.4 objective. While the sample was developed in THF deformations could already be observed under the direct light (left). After the solvent evaporated the structure got deformed (right).

5.1.2 Photoinitiator Added

The material was placed on a methacrylated glass slide (Sec. 3.4.6) and heated to 60 °C to allow transparency for 2PP structuring. Using 63x/1.4 oil-immersion objective cubes were fabricated ($50 \times 50 \times 50 \mu\text{m}^3$, $d_h = 0.4 \mu\text{m}$, $d_z = 0.3 \mu\text{m}$) with varying laser powers (10 – 150 mW).

5 Results PCL

To compare the polymerization efficiency, samples with 4,4'-Bis and M2CMK were prepared. For this PCL₆ was dissolved in THF and added the desired wt% of PI to the solution. After structuring, the resin was submerged in THF to remove the unpolymerized material. The initial comparison between pure PCL₂ and PCL₂ with 1 wt% 4,4'-Bis showed that structuring without initiator was possible but the polymerization threshold was significantly lowered from 100 to 40 mW, while it further decreased down to 10 mW for 1 wt% M2CMK (Fig. 5.2). As results for M2CMK showed the lowest necessary laser power (P_{th}), it was chosen as the PI for subsequent 2PP experiments. The already low polymerization threshold allowed to decrease the PI concentration of M2CMK further to 0.5%.

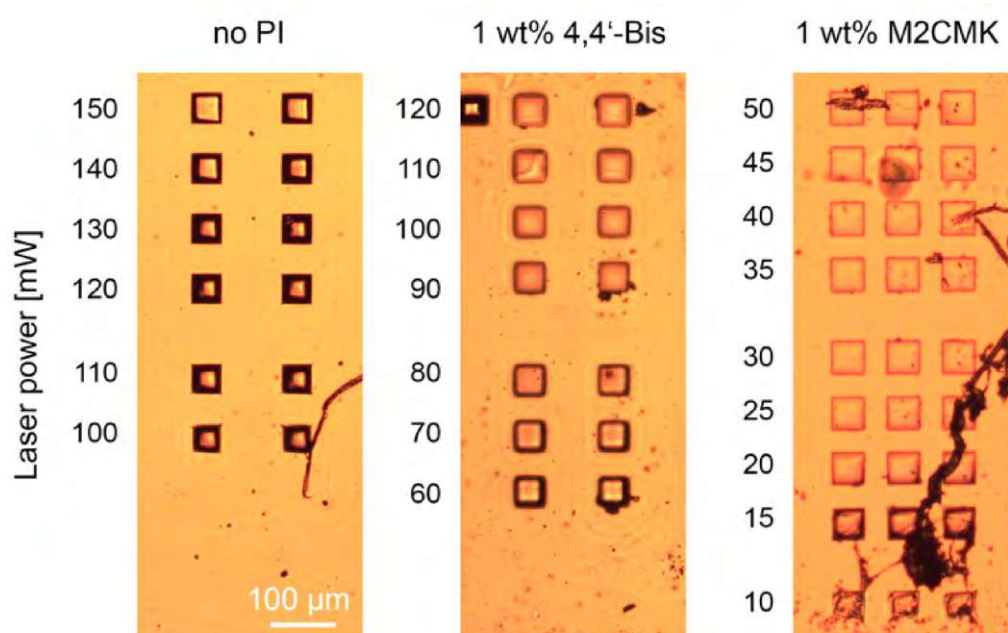


Figure 5.2: Polymerization threshold studies. Cubes ($50 \times 50 \times 50 \mu\text{m}^3$) were structured with decreasing laser power (150 to 10 mW). Without added PI 100 mW was necessary for P_{th} (left). 4,4'-Bis reduced the required power to $P_{th} = 40$ mW (middle). With M2CMK it was possible to reduce P_{th} down to 10 mW (right).

Buckyballs (Sec. 3.7) were structured with $P = 200$ mW, $v = 100$ mm s⁻¹, $d_h = 0.2$ and $d_z = 0.5$. These parameters were chosen as they allowed structuring just below the threshold where the deposited energy caused bubble formation. Working close to this limit was done as to avoid structures collapsing simply due to insufficiently cross-linked material. Despite these settings, the material was not stiff enough to support free standing structures such as microscaffolds (Fig. 5.3, left) after development. Trimethylolpropanetriacrylate (TTA, Sec. 3.4) was added as a short-chained monomer to increase the rigidity of the structures due to its three acrylate groups. For 1 g PCL₂, 60 mg TTA were added. This ratio was chosen to achieve a 1:1 ratio of double bonds (PCL₂: 0.6 mmol g⁻¹ double bonds, TTA: 0.2 mmol g⁻¹ double bonds). As this did not improve the stability of the structures, the ratio subsequently increased from 1:1 to 1:4 (Fig. 5.3). Since the polymerization threshold was already low for M2CMK (with 10 mW), no significant decrease in the polymerization threshold was observed when writing cube structures.

To assure the highest amount of polymerized material in a voxel the structuring was done

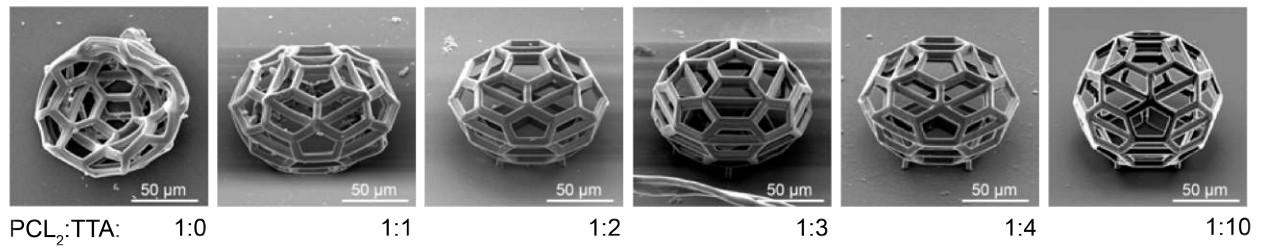


Figure 5.3: Fabrication of microscaffolds with increasing amount of shortchained cross-linking monomers (TTA). Without cross-linker the scaffold collapsed under its own weight (left). Adding enough TTA to achieve a 1:1 ratio of double bounds avoided complete collapse. A 1:10 ratio of PCL₂ to TTA was required to have stable structures (right).

at 200 mW with $d_h = 0.2 \mu\text{m}$ and $d_z = 0.3 \mu\text{m}$. While the increase in TTA yielded more stable structures, the whole scaffold collapsed under its own weight. Finally, the PCL₂:TTA ratio was increased towards 10:1. This amount led to overpolymerization during the structuring process. Therefore, the laser power was decreased from 200 to 130 mW. This ratio allowed fabrication microscaffolds, which were stable even after the development process (Fig. 5.3). While these results showed the processability and stability of PCL₂, the high amount of added TTA meant a large amount of non-biodegradable material in the microscaffolds.

5.2 Hexa-Functional Prepolymer

Because of the softness of PCL₂ a hexafunctional prepolymer was synthesized (see Sec. 3.4) to increase the rigidity without the need to add additional monomers. Contrary to PCL₂ no structures could be produced without added PI. Squared shapes of fabricated cubes were visible during the live imaging of the 2PP process, but these polymerized areas did not remain after development. Increasing the laser power caused bubble formation and was not feasible. Therefore, 0.5 wt% M2CMK was added to the material to produce 3D-structures (63x/1.4 objective, $P = 100 \text{ mW}$ $v = 100 \text{ mm s}^{-1}$, $d_h = 0.2 \mu\text{m}$ and $d_z = 0.3 \mu\text{m}$). Even freehanging parts were stable after development as can be seen in Fig. 5.4. This was also the case for microscaffolds which did not collapse under their own weight (Fig. 5.5), as had been the case with PCL₂.

To measure the reduced Young's modulus eight cubes of $200 \times 200 \times 70 \mu\text{m}^3$ were produced using the 20x/0.8 objective was used due its larger field of view. With 100 mm s^{-1} the structures were written with $\Delta_h = 1.0 \mu\text{m}$ and $\Delta_z = 1.0 \mu\text{m}$ and 35 mW. The power and speed parameters were chosen after writing an array of cubes with increasing powers in steps of $\Delta_P = 5 \text{ mW}$. Bubble formation was observed during structuring at 40 mW. Therefore, 35 mW was chosen as the maximum power for stable structures. The storage modulus was measured to be $39.7 \pm 9.8 \text{ MPa}$ (Tab. 5.1). Nanoindentation measurements were done by Thomas Koch, TU Wien.

After this initial tests for processability under 2PP conditions, more complex geometries were fabricated. As the PCL-backbone has been reported to exhibit cytocompatibility and biodegradability [40, 195, 196], capilinsers as potential scaffolds for dermal papilla experiments were fabricated. As the total height of the scaffolds was 1 mm, significantly larger than the previously structured $100 \mu\text{m}$ buckyballs, the 10x/0.3 objective was required (fabrication settings listed in Sec. 3.7). The capilinsers were stable after development and did not collapse under

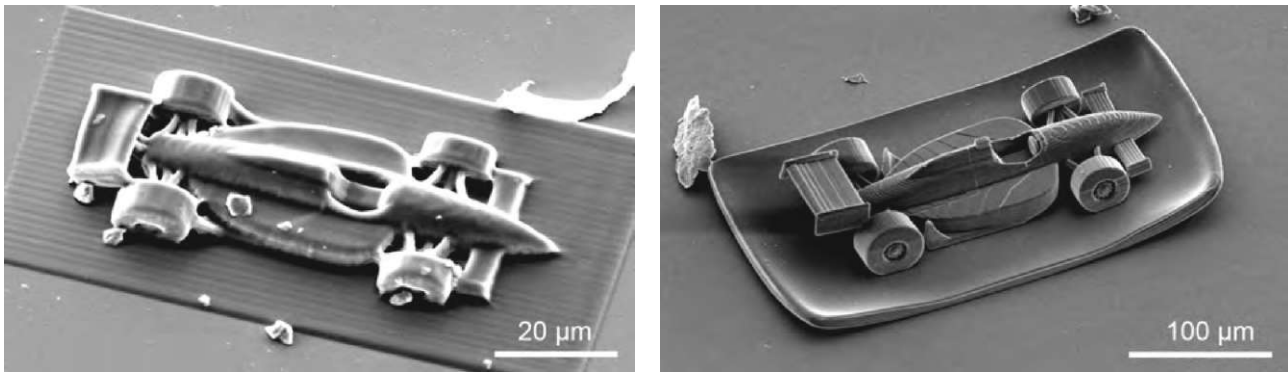


Figure 5.4: SEM images of 2PP structures. Freehanging structures collapsed after development with PCL₂, as can be seen by the spoiler of the race car (left). With PCL₆ the geometry was stable after development in THF (right). The improvement in rigidity is especially impressive considering that the PCL₆ race car is five times larger than the one out of PCL₂, yet the features are clearly defined.

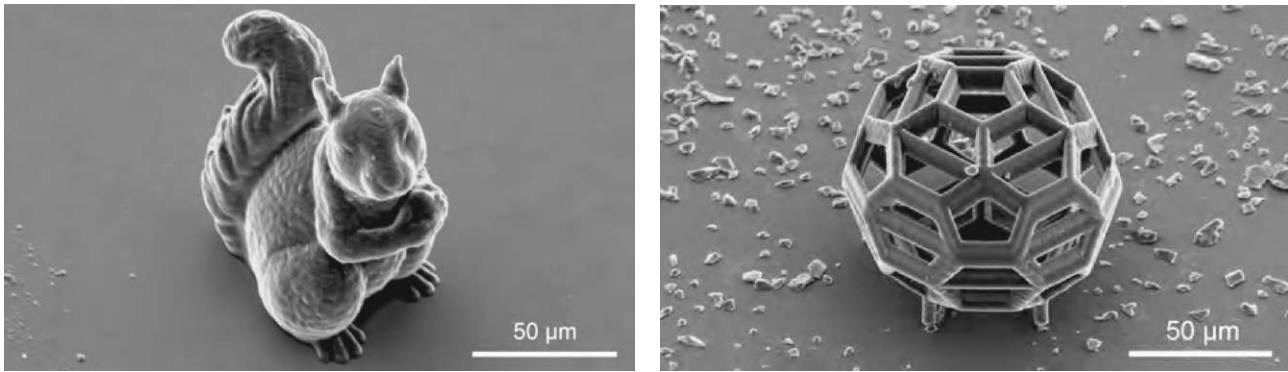


Figure 5.5: SEM images of freestanding 3D-structures based on PCL₆. 3D-models with detailed surfaces such as the squirrel were fabricated (left). Fine microscaffolds like buckyballs also remained stable after development and did not collapse under their own weight (right) as had been observed with PCL₂.

Table 5.1: Results for nanoindentation results for 2PP cubes fabricated from PCL₆. Measurements were done by Thomas Koch, TU Wien.

Cube Nr.	Reduced Young's modulus [MPa]	Nr of Measurements
1	41.8 ± 12.4	7
2	34.4 ± 11.5	5
3	40.0 ± 12.4	11
4	39.4 ± 9.5	9
5	39.0 ± 11.1	8
6	39.9 ± 9.2	12
7	39.6 ± 8.2	11
8	41.1 ± 8.4	11
Total	39.7 ± 9.8	74

the higher weight due to the larger geometry (Fig. 5.6).

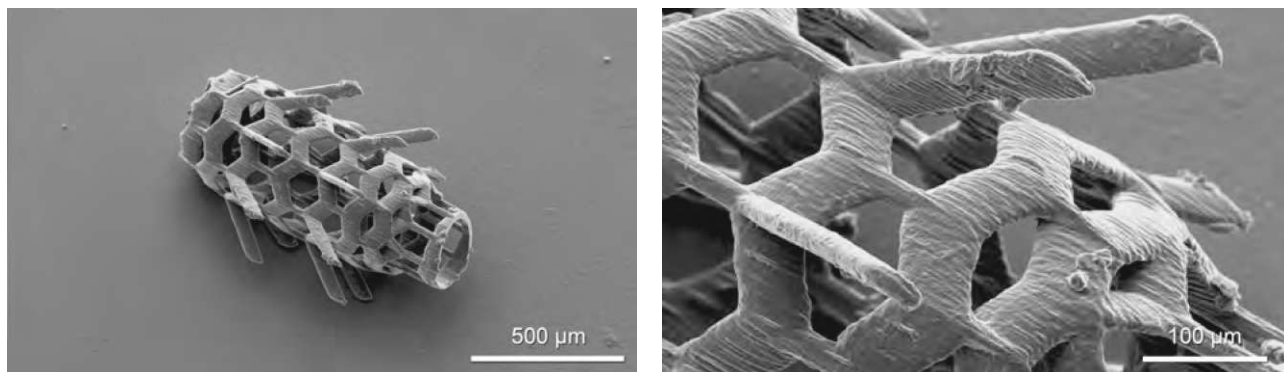


Figure 5.6: Capilinser micro scaffold for DP-cell seeding experiments fabricated from PCL₆ (left). The total height of the structure was 1 mm, significantly larger than previously fabricated scaffolds such as the buckyballs. Despite the larger dimensions the geometry remained stable after development. Close up of the hooks designed to anchor the scaffold in the skin of the patient after implantation (right).

5.3 Discussion

Two PCL-based prepolymers have been studied as potential materials for biomedical applications. PCL₂ was cross-linkable under UV conditions even in the absence of PI, similar to the previously reported PEG-based prepolymers [42]. The hexafunctional PCL₆ was not cross-linkable without PI. Adding PI (4,4'-Bis or M2CMK) reduced P_{th} in the case of PCL₂ and made structuring possible in the case of PCL₆. As microstructures fabricated from PCL₂ collapsed under their own weight, TTA was added to PCL₂. While increasing rigidity, this method was deemed undesirable for tissue engineering applications as highly reactive triacrylates were added. PCL₆ exhibited none of these rigidity issues and is a promising material for biofabrication due to its 2PP processability, stability after development and biocompatibility due to the PCL-based backbone [41]. Even for larger structures of 1 mm total height, the material was stable. The reduced Young's modulus of 39.7 ± 9.8 MPa was measured using nanoindentation. It is comparable to values obtained for commercially available 2PP-photoresists [197]. Due to the effect of the 2PP fabrication process on the material properties, these values are difficult to directly compare with values reported for samples fabricated with conventional AM methods (discussed in Sec. 2.3.3). Further studies are required to determine, if the mechanical properties can be significantly improved by increasing laser power and scanning speed [116]. This is of particular interest as PCL-based micro scaffolds fabricated via SLM have been reported by Williams et al. as a potential material for bone and cartilage repair [198]. Reliable reproduction of complex 3D scaffolds such as the capilinser design showed the processability of PCL₆ using 2PP and renders this a potential material for scaffold based tissue engineering applications.

6 Results Polymerization Threshold

The required laser minimum laser power P_{th} was studied for three materials at different fabrication speeds, to evaluate the respective light dosage to observe polymerization. Initial experiments similar to ascending scan were done to study the polymerization performance with literature values [43, 44]. Afterwards, various ways to determine P_{th} for freehanging lines were approached and compared. Finally, the scaling of P_{th} with increasing writing speeds v was studied in a simplified 2D-environment (two lines closely spaced towards each other). This method was chosen to correlate findings for the single line with conditions more closely resembling the 2PP process, where multiple lines are scanned (Sec. 2.6.2). Lastly, the polymerization behavior for fully 3D-structures was evaluated by measuring the DBC of fabricated cubes via Raman spectroscopy (Sec. 2.3.3). The results allowed to correlate simplified 1D-systems like a single line with complex 3D-parts and to extrapolate the required laser power for higher writing speeds, which could not be reliably fitted to the predicted model. All experiments are summarized at the end of the chapter in Tab. 6.2, including the respective coefficients of determination for the fits (discussed in Sec. 3.5.3). Regardless of material, PI or concentration of PI, a similar trend was observed when increasing the scanning speed. The required P_{th} for scanning speeds of 100 mm s^{-1} was significantly lower than predicted from the established model. Lastly, potential causes for this reduced trend are discussed.

6.1 Ascending Scan

Zr-hybrid (1 wt% 4,4'-Bis) was used for conditions similar to the ascending scan method (Sec. 3.5.3) to study the polymerization behavior under exposure conditions reported in literature [43, 44]. Using 63x/1.4 oil immersion objective, single lines of $30 \mu\text{m}$ were written directly onto the glass starting from 25 mW and decreasing the power by 0.5 mW in y-direction. Comparatively low writing speeds from 10 to $40 \mu\text{m s}^{-1}$ (Fig. 6.1, left) were selected. After developing the sample in 1-propanol, the lines were analyzed using SEM (Fig. 6.1, left). As the scaling of $P_{th} \propto v^{0.5}$ also applies for a constant voxel length l_{min} (Sec. 2.6.2), the polymerization threshold P_{th} was determined as the last power setting, where the structured line did not tilt over. Tilted lines indicated a voxel length $l < l_{min}$, too small to connect to the glass. The observed threshold was comparable to the previously reported dependence $P_{th} \propto \sqrt{v}$ and could be fitted with $R^2 = 0.88$ (Fig. 6.1, right). As described in Sec. 3.5.3, $R^2 > 0.8$ indicates good description of observed data by the fit.

6.2 Single Line [1D]

To closer study the polymerization behavior, the freehanging linetest was employed. Structuring power for the connecting pillars was 40 mW (all parameters listed in Sec. 3.5.3) for zr-hybrid with 1.0 wt% 4,4'-Bis. For later experiments with varying PI-concentration the laser power

6 Results Polymerization Threshold

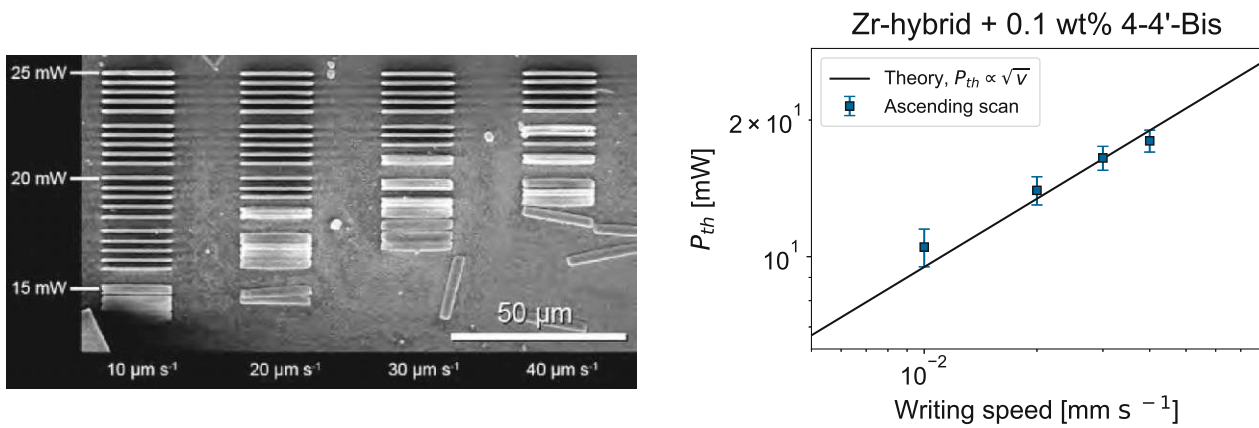


Figure 6.1: SEM images of single lines fabricated at writing speeds from 10 to 40 $\mu\text{m s}^{-1}$. The polymerization threshold P_{th} was determined as the power setting before the lines tilted due to the voxel being too small to attach to the glass (left). The behavior of the polymerization threshold was in agreement with previous findings (right) [43, 44].

was varied depending on the material and PI-concentration to guarantee stable pillars after development. The linetest was done in triplicates with laser powers from 2 to 100 mW steps of $\Delta P = 2$ mW. This broad range of powers was chosen as the change in P_{th} for higher fabrication speeds (ranging from 0.1 to 40.0 mm s^{-1}) was unknown. For each speed an individual sample was prepared. After developing the samples, the individual lines were recorded via SEM (Fig. 6.2, left). A custom Python based algorithm (as described in Sec. 3.5.3) extracted the average line diameter d and height h from each image (Fig. 6.2, right).

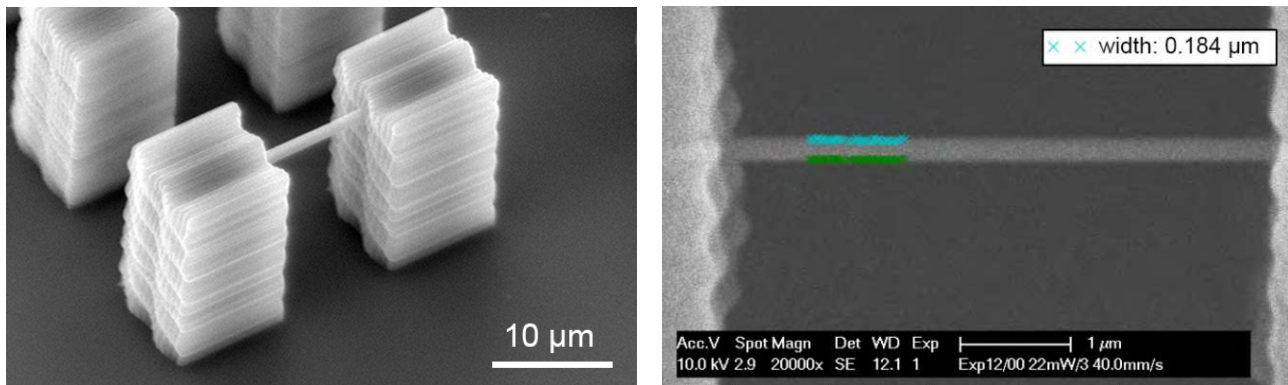


Figure 6.2: SEM images of linetest structure (left). A line was fabricated between two pillars spaced 10 μm apart. Each setting (laser power and writing speed) was done in triplicates and the line diameter was measured using a custom Python algorithm, which extracted the width from the top view (right). For the voxel height the sample was tilted 45° and the measured width was modified by $\sqrt{2}$ to account for the tilt.

6.2.1 Voxel Increase

While the measured voxel height could be reliably fitted to Eq. 2.55 (Fig. 6.3, left), results for voxel diameters diverged from Eq. 2.54 for higher laser powers (Fig. 6.3, right). Initially this was suspected to be an effect similar to avalanche ionization or heat accumulation, caused by high exposure doses [135]. However, as no clear photon dosage could be extracted to globally describe this divergence for all writing speeds, only data from 20 mW away from the first observed line for each speed were used as in this window the results behaved comparable to the model ($R^2 > 0.9$ for all data). Therefore, the polymerization threshold P_{th} could be interpolated through the data points to a hypothetical threshold of a voxel with $d = 0$.

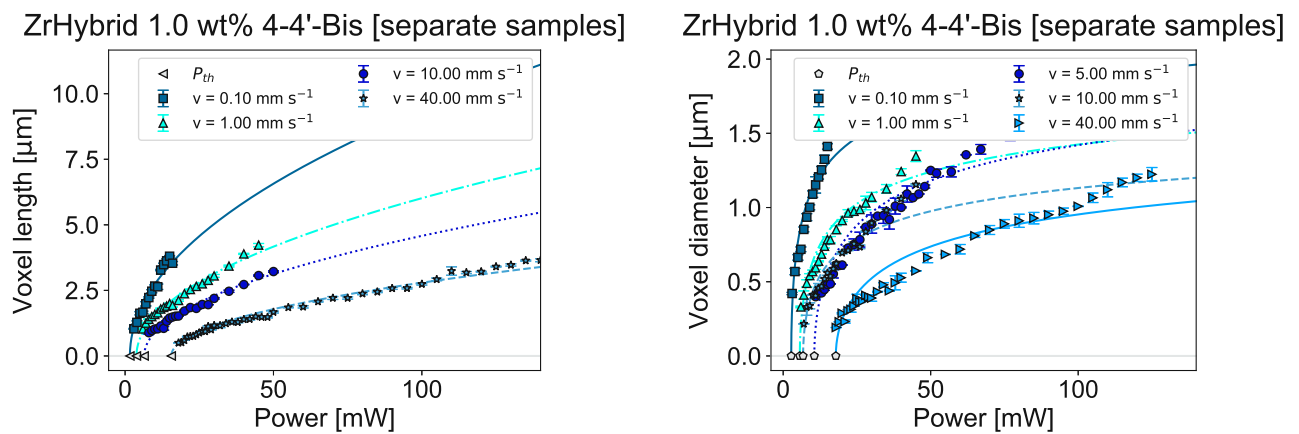


Figure 6.3: Data for voxel height obtained from SEM images followed the trend described by the model (left) [43]. The voxel diameters saw a sharp increase not predicted by the established theory for all writing speeds (right) potentially caused by processes such as avalanche ionization [135]. Therefore, only results close to the threshold (20 mW from first observed line) were used to fit both height and diameter. The polymerization threshold (P_{th}) was interpolated and is represented by the gray markers for both cases. Each speed setting was done on an individual sample. Therefore the lower P_{th} for 10 mm s^{-1} compared to 5 mm s^{-1} was probably due to slight variation in composition of the individual samples.

As can be seen in Fig. 6.3, the results for 5.0 mm s^{-1} and 10.0 mm s^{-1} exhibited an irregular behavior, as for 5.0 mm s^{-1} the required a higher laser power was necessary to produce similar features as with 10.0 mm s^{-1} , despite longer illumination times at 5.0 mm s^{-1} . This discrepancy was assumed to be caused by the fact that the individual experiments were done on separate samples. Slight changes in sample densities due to systematic errors during preparation could have been the reason for this trend. Therefore, the experiment was repeated using a single sample zr-hybrid with 1 wt% 4,4'-Bis. Evaluation of the line diameters again showed a drastic increase for each fabrication speed (Fig. 6.4) with increased laser power. Again, no universal photon dosage could be extracted from the obtained data to adequately describe the divergence behavior for higher laser powers.

For each writing speeds, a 20 mW window from the first observed line was chosen for interpolation, as the data in this area could be fitted to $R^2 > 0.9$ and divergence for increased laser power was probably due to accumulative effects not accounted for in the polymerization

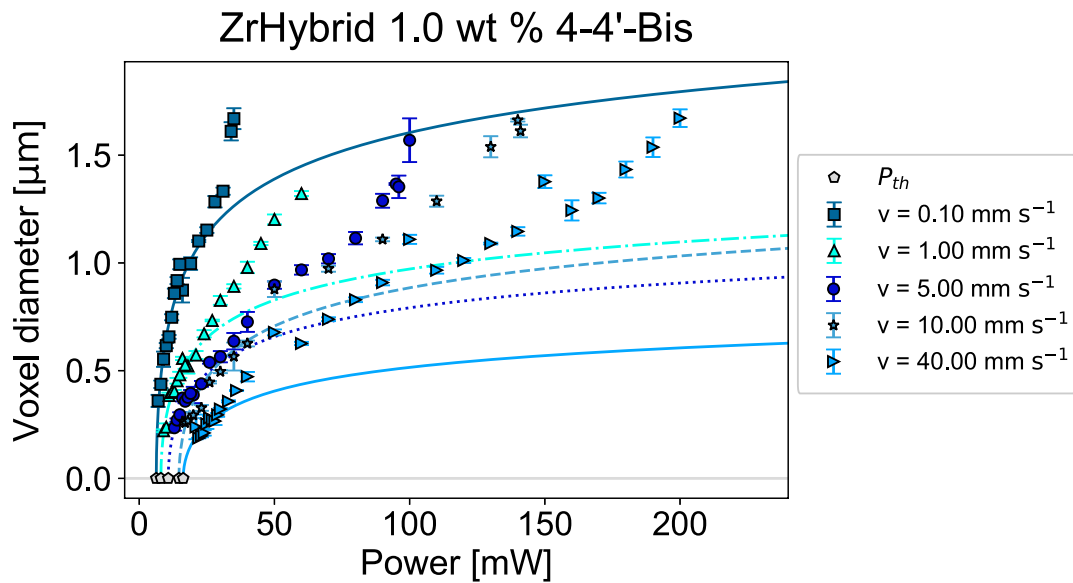


Figure 6.4: Voxel diameters for five different fabrication speeds all done on the same sample which yielded an expected increase of P_{th} (gray pentagons) for increasing writing speeds. As with the previous experiment a sharp increase in diameter could be seen, but from the available data no uniform photon dosage could be extracted. For the fit the first ten laser powers for which polymerization was observed were used.

model [43,135] From this fit P_{th} (gray pentagons in Fig. 6.5, left) was interpolated. The scaling of $P_{th} \propto v^i$ was done using least square fit. The best fit yielded a dependence of $P_{th} \propto v^{0.16}$ with $R^2 = 0.96$. Fitting the data to the predicted trend of $P_{th} \propto v^{0.5}$ (Eq. 2.56) resulted in $R^2 = 0.10$. All scaling factors and coefficients of determination are summarized at the end of this chapter in Tab. 6.2.

6.2.2 Threshold Lines

A comparable trend of $P_{th} \propto v^{0.21}$ ($R^2 = 0.98$) could be extracted by defining P_{th} as the required laser power which results in a visible line after development (Fig. 6.5). Again, fitting this data to the expected model returned a low coefficient of correlation ($R^2 = 0.18$). Interpolating P_{th} from multiple line measurements was a time consuming task and not feasible for the screening of multiple materials with various PI-concentrations. For follow-up experiments P_{th} was extracted from the first visible lines. This was done because the scaling factor - while different in both cases - still diverged from the postulated model and the comparison of multiple materials could be done in a much more time-efficient manner.

The developed samples were observed under optical microscope. P_{th} was defined as the first laser power where a line could be seen between all three pillars. This approach allowed a much faster evaluation of the required photon dosage for a multitude of compounds. Three materials were compared: zr-hybrid, PCL₆ and ETA:TTA. For each material varying PI concentrations were chosen to study a possible effect of PI-concentration on the dosage. The photon dosage for zr-hybrid at 0.1 and 1.0 wt% scaled with $v^{0.25}$ and $v^{0.21}$ respectively (see Fig. 6.6, left).

Results for ETA:TTA and PCL₆ also scaled with $P_{th} \propto v^i$ with $i \in \{0.19 - 0.30\}$ for different

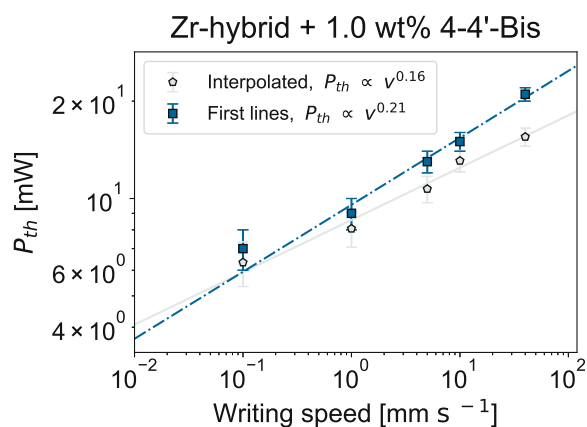


Figure 6.5: Polymerization threshold. The threshold power P_{th} was interpolated from the fit (gray pentagons). The scaling of P_{th} was no longer proportional to \sqrt{v} but instead scaled with $v^{0.16}$. If P_{th} was defined as the first power setting where lines could be seen after development, the scaling was $\propto v^{0.21}$. Both results were obtained using least square fitting with R^2 of 0.96 and 0.98. Fitting to the predicted trend of $P_{th} \propto v^{0.5}$ (not plotted) resulted in fits with $R^2 < 0.2$.

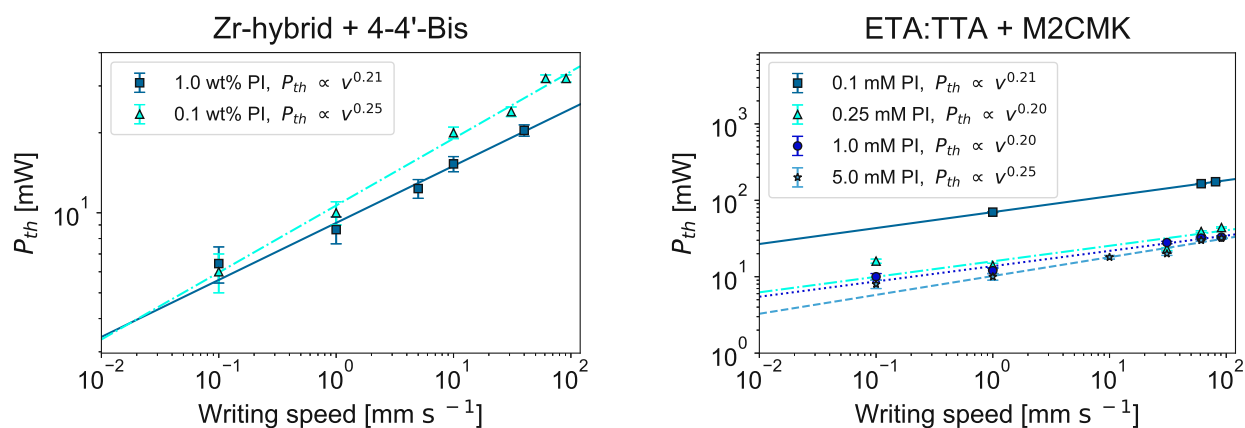


Figure 6.6: Studies for zr-hybrid with different concentrations of 4,4'-Bis (left) and ETA:TTA with different concentrations of M2CMK (right). While an increase in PI decreased the overall polymerization threshold, no significant effect of concentration on the scaling factor could be observed. Therefore, fluctuations in the fitted scaling factor were likely to be systematic errors of the chosen method.

6 Results Polymerization Threshold

concentrations of M2CMK (Fig. 6.6 and Fig. 6.7). No clear effect of PI concentration and scaling factor could be seen. The scaling factor increased to 0.25 for the highest concentration (5 mM) of M2CMK in ETA:TTA while it increased to 0.25 for the lowest concentration (0.1 wt% of 4,4'-Bis). As the scaling factor the optimal value calculated using least square fit, fluctuations in the fitted variable were probably due to the measurement uncertainty of the selected method. As a control, all experiments were fitted using the two extreme values ($i = 0.2$ and $i = 0.25$) obtained. All fits showed $R^2 > 0.85$.

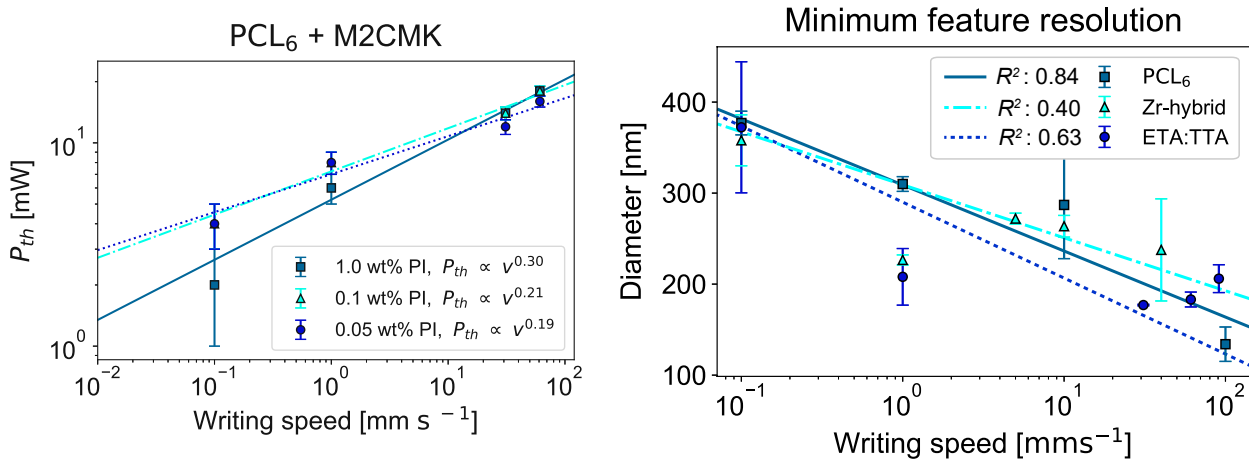


Figure 6.7: PI concentration studies with PCL₆ (left) yielded comparable scaling factors with $i \in \{0.19 - 0.30\}$. Average line diameter for different writing speeds (right). For all three materials the largest initial lines were measured at 0.1 mm s^{-1} and decreased with increasing writing speed. The observed trend could be fitted using logarithmic regression with $R^2 \geq 0.4$.

For PCL₆ little variation in the required laser power was observed for writing speeds of 61 and 91 mm s^{-1} . At the lowest writing speed 0.1 mm s^{-1} , the change in threshold was still within the error margins. Therefore, the step increase from $v^{0.19}$ at 0.05 wt% to $v^{0.30}$ at 1.0 wt% can be due to the power step size of $\Delta_P = 2 \text{ mW}$ defined by the selected method. This window is comparatively large at a writing speed of 0.1 mm s^{-1} . As with ETA:TTA, the data from all three experiments was fitted using the two extremes for i , with $R^2 > 0.8$ for all fits.

6.2.3 Minimum Feature Resolution

The smallest lines produced were also measured for ETA:TTA (5 mM M2CMK) and PCL₆ (0.1 wt% 4,4'-Bis) to compare the minimum feature sizes with those of zr-hybrid. Results for all three materials showed the largest initial lines at 0.1 mm s^{-1} ($377 \pm 13 \text{ nm}$ for PCL₆, $372 \pm 72 \text{ nm}$ for ETA:TTA, and $378 \pm 28 \text{ nm}$ for zr-hybrid) with smaller initial features for increased fabrication speeds. Results were fitted using logarithmic regression with R^2 ranging from 0.4 to 0.84 (Fig. 6.7, full data displayed in Tab. 6.1).

Table 6.1: Minimum feature resolution. For three different materials the diameter of first lines produced for a given fabrication speed was measured. For all three materials, largest initial features were observed at 0.1 mm s^{-1} . Analysis of variance showed significant difference between 0.1 mm s^{-1} and higher writing speeds for all materials.

PCL ₆ + 1 wt% M2CMK		
Writing speed [mm s^{-1}]	Laser power [mW]	Diameter [nm]
0.1	6	377 ± 13
1.0	10	310 ± 8
10.0	14	287 ± 59
100.0	18	143 ± 18
Zr-hybrid + 1.0 wt% 4,4'-Bis		
Writing speed [mm s^{-1}]	Laser power [mW]	Diameter [nm]
0.1	7	378 ± 28
1.0	9	229 ± 1
5.0	12	272 ± 3
10.0	16	2555 ± 35
40.0	21	202 ± 56
ETA:TTA + 5.0 mM M2CMK		
Writing speed [mm s^{-1}]	Laser power [mW]	Diameter [nm]
0.1	8	372 ± 72
1.0	10	208 ± 31
31	20	177 ± 2
61	30	183 ± 10
91	32	206 ± 15

6.3 Double Line [2D]

For the next experiments a second line was written next to the area exposed to the single line, to study the effect of the reduction of P_{th} (discussed in Sec. 2.6.2), as well as the scaling factor. These experiments were done in an attempt to correlate findings from the simplified single line experiments, to conditions more similar to the additive process where multiple lines are produced in a single layer. Two material compositions were studied (zr-hybrid with 0.1 wtP 4,4'-Bis and ETA:TTA with 1 mM M2CMK). The lines were placed next to each other at five distances from 0.1 to 0.5 μm in steps of 0.1 μm . A decrease of P_{th} could only be observed at lines spaced 0.1 μm next to each other. Results for zr-hybrid showed no reduction of P_{th} at 0.1 and 1 mm s^{-1} (Fig. 6.8, left). At 61 and 91 mm s^{-1} , the required laser power 12 mW was lower than results for single line experiments. For ETA:TTA a decrease in P_{th} of 2 mW occurred at 1 mm s^{-1} and above with a difference of 5 mW at 91 mm s^{-1} (Fig. 6.8, right). Fitting the individual threshold powers to the fabrication speed resulted in $P_{th,ZrH} \propto v^{0.16}$ and $P_{th,ETA:TTA} \propto v^{0.18}$ which was comparable to findings discussed in Sec. 6.2.

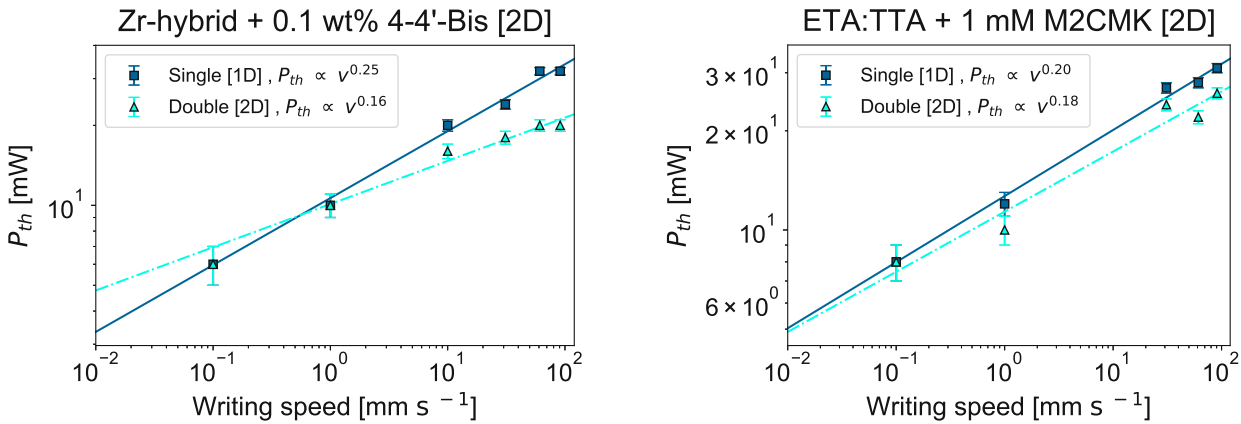


Figure 6.8: Polymerization threshold for two lines spaced 0.1 μm apart. For zr-hybrid a reduction of P_{th} was observed at 10 mm s^{-1} and above (left). For ETA:TTA a reduction in P_{th} was seen at 1 mm s^{-1} and above. The scaling factor of the required laser power was both comparable with findings. Fitting to the predicted trend of $i = 0.5$ (not plotted) resulted in $R^2 < 0.5$.

6.4 Cubes [3D]

To study the photon dosage for the 3D case cubes of $100 \times 100 \times 35 \mu\text{m}^3$ were produced. Using $\Delta_h = 0.3 \mu\text{m}$, $\Delta_z = 0.2 \mu\text{m}$ with alternate xy-hatch for individual layers. As with the previous 1D and 2D experiments 63x/1.4 oil immersion objective was used. A power range from 2 to 40 mW with $\Delta_P = 2 \text{mW}$ and five writing speeds (20, 40, 60, 80 and 100 mm s^{-1}) were selected. After developing the sample in 1-propanol for 30 min, the Raman spectra of each cube (Fig. 6.9, left) were recorded (Sec. 3.5.2). Raman measurements were done by Karin Wieland under the supervision of Bernhard Lendl, TU Wien.

As the results describe the decrease of carbon double bonds, this trend was inverted and

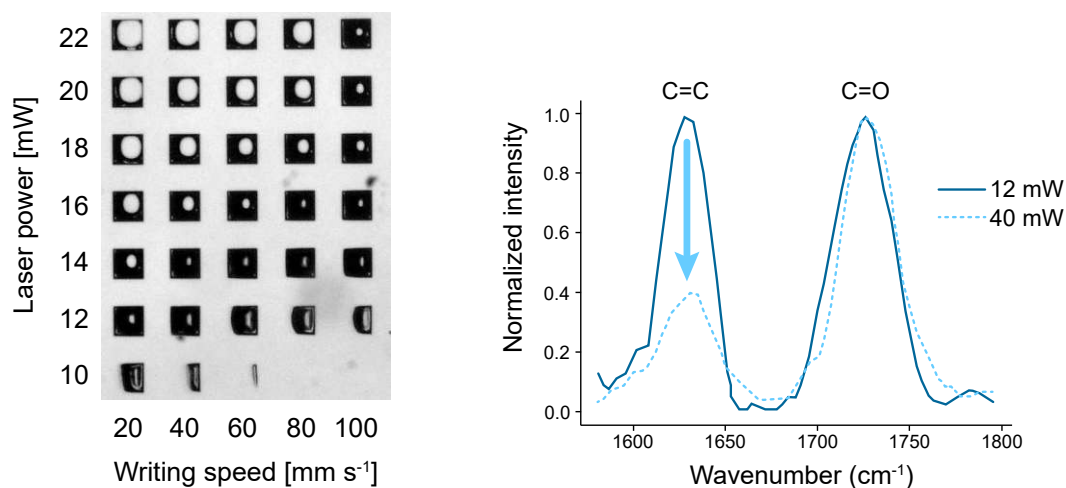


Figure 6.9: Effect of laser power on the resulting polymer cubes for a given writing speed. Cubes were manufactured from ETA:TTA (5 mM M2CMK) with writing speed from 20 to 100 mm s⁻¹ and varying laser power in the range of 10-40 mW (left). Raman spectra of two different laser power settings at 20 mm s⁻¹ (solid line: 12 mW dashed line: 40 mW) were chosen for demonstration. Higher laser power reduced the signal from C=C band. Spectra were processed as described in Sec. 3.5.2. For better visualization and the purpose of better comparison, the data were normalized with respect to the carbonyl band.

fitted to Eq. 2.54, to see if results from the Raman measurements could be compared to trends observed in the linetest experiments (Sec. 6.2). As can be seen in Fig. 6.10 the data could be fitted to the voxel theory with R^2 above 0.85 for each speed. From the five fitting curves P_{th} was interpolated with the condition $DBC(v, P_{th}) = 0$ (inverted triangles along zero y-axis in Fig. 6.10). This threshold power scaled $\propto v^{0.29}$ with $R^2 = 0.67$.

The experiment was repeated with ETA:TTA and 1 mM M2CMK. The lowered concentration required laser powers above 20 mW for all writing speeds. Similarly to the results from the single linetest experiments the change in concentration caused a global shift in P_{th} , yet it had little effect on the scaling of the required photon dosage for different writing speeds. At 1 mM the polymerization threshold (gray Xs in Fig. 6.11) scaled $\propto 0.26$ with $R^2 = 0.94$. While this study focused on the dependence of P_{th} , an interesting observation was gained from the Raman measurements as faster writing speeds result in more efficient DBC for laser powers higher than P_{th} . This was first seen for ETA:TTA and 5 mM M2CMK, where the highest DBC was reached with 80 and 100 mm s⁻¹ at 40 mW (Fig. 6.10). A comparable, yet better pronounced trend could be seen for ETA:TTA and 1 mM M2MCK (Fig. 6.11, left). These results might seem counter intuitive upon first observation as a higher amount of photons is locally brought into the volume at lower writing speeds. A possible explanation could be an overabundance of radicals and therefore an increased likelihood of radical to radical termination. Additionally, the high irradiation energy might drastically increase the viscosity of the material. This could hinder the diffusion of radicals towards unreacted sites, resulting in less efficient cross-linking [9, 146]. This effect was not observed laser powers close to P_{th} , which is probably due to the fact that there needs to be a minimum concentration of radicals to start polymerization and there are not enough radicals to block each other.

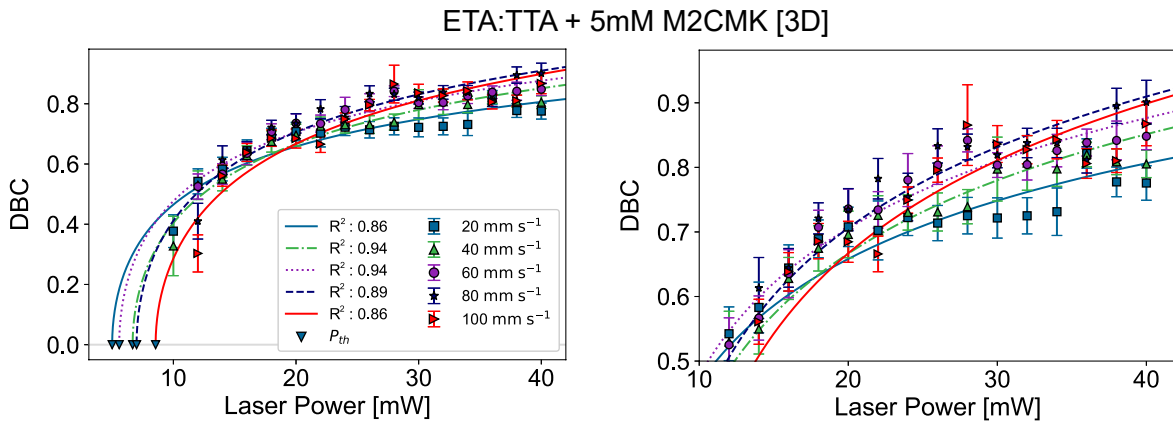


Figure 6.10: DBC for cubes with different writing speeds and powers (ETA:TTA with 5 mM M2CMK) were fitted $\propto \sqrt{\ln(P^2)}$ (left). R^2 was exclusively above 0.85. From this fit P_{th} was interpolated (inverted triangles at DBC = 0). While higher writing speeds necessitated higher P_{th} , this trend was inverted at laser powers above 20 mW, where increased writing speeds resulted in a higher degree of DBC (right, section magnified for better visibility). This trend was also seen for 1 mM M2CMK (Fig. 6.11). Raman spectra measured by Karin Wieland under the supervision of Bernhard Lendl.

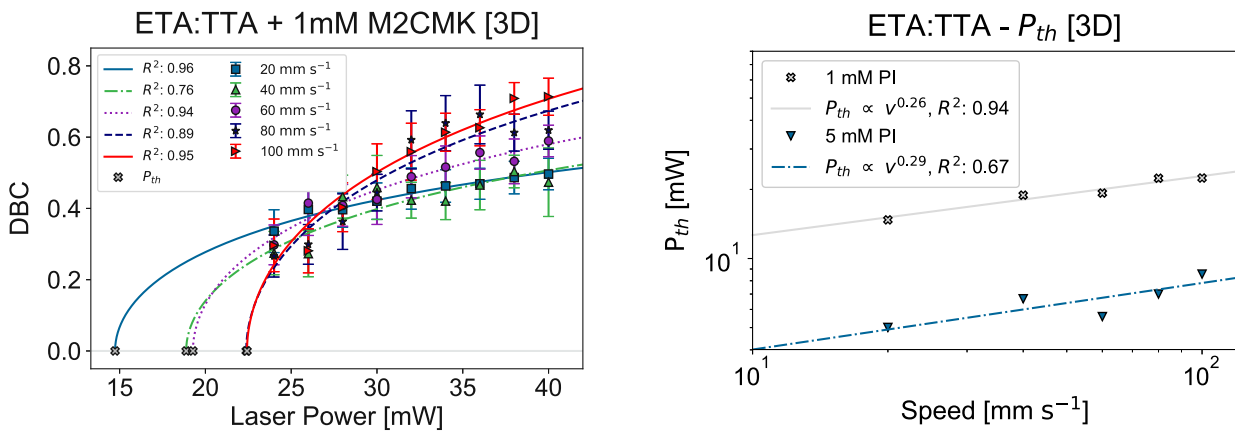


Figure 6.11: Raman measurements performed on cubes at lower PI concentration (ETA:TTA with 1 mM M2CMK) to study a possible dependence on PI concentration. As before the DBC followed the same trend as the linetests (left). Raman spectra measured by Karin Wieland under the supervision of Bernhard Lendl. The extracted P_{th} (gray Xs at DBC = 0) were fitted to v^i (right). Results for 5 mM (triangles) and 1 mM (Xs) scaled $\propto v^{0.29}$ and $v^{0.25}$ respectively with a significantly higher R^2 for 1 mM M2CMK. Results were again both comparable to 1D and 2D linetests while fits to the expected trend were done with $R^2 = 0.26$ and $R^2 = 0.29$ for 1 and 5 mM respectively (fit not plotted). As with 5 mM a higher DBC conversion for faster writing speeds could be reached at laser powers away from P_{th} (left).

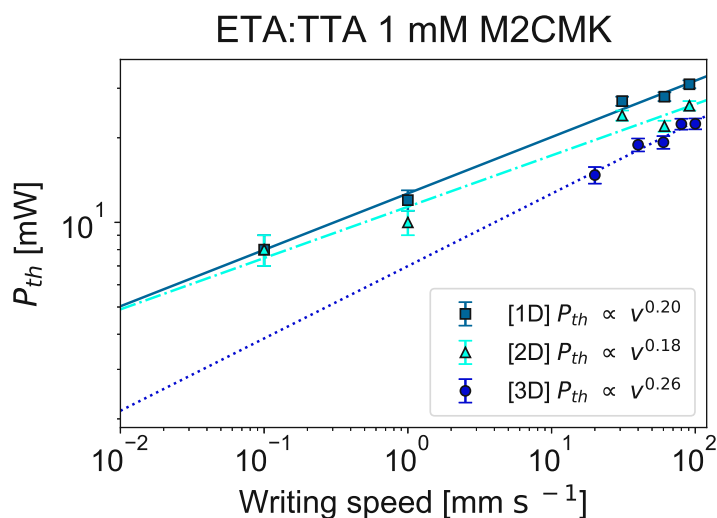


Figure 6.12: Comparison of three different conditions for P_{th} studied with ETA:TTA with 1 mM M2CMK. The highest laser power was required to produce a single freestanding line [1D]. This threshold was reduced by fabricating two lines spaced $0.1 \mu\text{m}$ apart. This reduction of P_{th} was even more significant when writing fully 3D-cubes. While not exactly matching, the scaling factors for all 3 cases were comparable and fitted with $R^2 > 0.8$, compared to fits with the postulated $i = 0.5$ ($R^2 < 0.6$, not plotted).

6.5 Discussion

Two approaches to evaluate P_{th} were compared. While interpolating P_{th} through multiple measured line lengths allowed for an accurate description, it was a time consuming task which made this approach not feasible for a broader material study where multiple materials, initiators and initiator concentrations were compared. Taking the first lines which remained after developing the sample as the minimum laser power for a given writing speed allowed much faster processing and characterization of the individual systems while the scaling of the photon dosage ($v^{0.21}$) was comparable with the interpolation ($v^{0.16}$). This estimation process did not require time consuming SEM imaging and could be done via optical microscope. It allowed to evaluate the photon dosage for three different materials (zr-hybrid, ETA:TTA, PCL₆) and two PIs (4,4'-Bis and M2CMK). For all material compositions studied the photon dosage did significantly divert from previously reported experiments. These findings indicate a much higher efficiency of 2PP for increased fabrication speeds. Instead of $P_{th} \propto v^{0.5}$ as predicted by the established theory (Sec. 2.6.3), the average scaling factor was $i_{mean} = 0.22 \pm 0.03$ for single lines. Furthermore, comparable scaling was observed in detail for more complex circumstances such as double lines ($i_{mean} = 0.17 \pm 0.02$) and three-dimensional cubes ($i_{mean} = 0.28 \pm 0.02$). While the required laser power was reduced with increasing complexity (Sec. 2.6.2), the scaling factor relating P_{th} and v_{th} was comparable for all three conditions for ETA:TTA (1 mM, Fig. 6.12).

These findings have significant impact on the limitations of 2PP as this scaling factor could potentially be used to estimate the required photon dosage for a given component. By producing

6 Results Polymerization Threshold

cubes for a given speed v_1 the polymerization threshold can be evaluated by increasing the laser power until $P_{1,th}$ is reached. From this correlation one can then estimate the required laser power at the highest available scanning speed and quickly estimate if the material can be processed under these conditions. A possible explanation for this phenomenon could be the fact that the initial model was based on static exposure conditions (Fig. 6.13, left). The photosensitive resin was exposed for a certain duration time but there was no scanning movement and therefore the experiment did not take the fabrication kinetics into account.

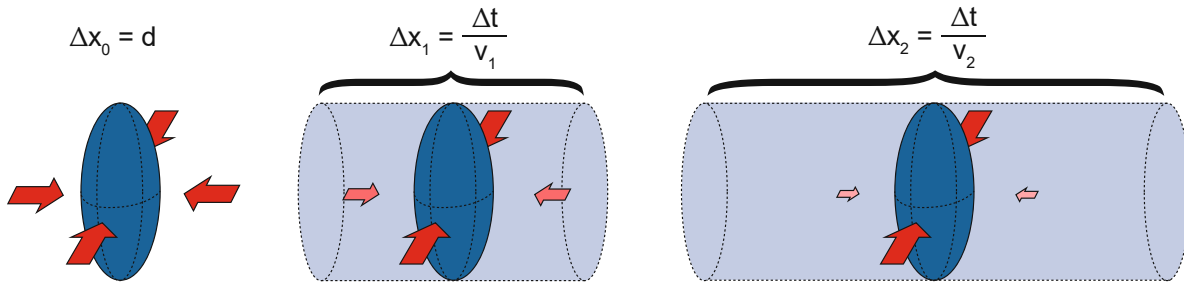


Figure 6.13: Possible model for the photon conversion for different writing speeds. Under static conditions (left), the illuminated area is given by the voxel diameter d . Inhibiting oxygen can diffuse into the voxel and terminate radicals. Afterwards the inhibitor concentration is recovered due to diffusion. When the beam is scanned, a volume is created (middle). Therefore the inhibitor cannot diffuse into the center voxel in time to terminate the radicals. The time required for this diffusion is given by the writing speeds and increases for faster speeds (right). Therefore, even though the same amount of radicals is created, fewer radicals are terminated and less photons are required for polymerization when compared with the static case.

If P_{th} is reached, the oxygen is depleted in the focal volume to allow cross-linking of the prepolymer. After illumination, the initial inhibitor concentration is recovered due to diffusion. In the case of a scanning focal spot, the same amount of radicals is created in a single spot. However, due to the scanning process, a deoxygenated tail is produced along the scanned path (Fig. 6.13, middle), where the inhibitor is also depleted. No inhibitors can diffuse sufficiently fast into the central voxel along the tail. Therefore, a higher writing speed yields higher conversion despite the same number of radicals produced during illumination (Fig. 6.13, right). This could also explain the reduced feature size for first lines observed (Sec. 6.2.3) as the largest features for all three materials were observed at the lowest writing speed of 0.1 mm s^{-1} . A similar decrease in minimum feature size for higher writing speeds was previously reported by Stocker et al. [199]. Using above argumentation, the same amount of radicals created in the voxel can lead to a more efficient conversion of radicals into polymerized resin due to the longer deoxygenated tail within a shorter timespan. As an overview the scaling factors for all experiments discussed are displayed in Tab. 6.2.

Lastly, the correlation between DBC and fabrication speed demands closer inspection as these results indicate that a higher degree of DBC can be reached for laser powers larger than P_{th} for faster writing speeds. This result seems counter intuitive, as less photons are locally brought into the volume for higher writing speeds at a given laser power. This effect could be due to radical to radical recombination when a large number of radicals is produced. Increased

Table 6.2: Overview of scaling factors for the scaling factor i , which determines the relation between threshold power and fabrication speed ($P_{th} \propto v^i$). For the single line (1D) experiments the scaling factor was on average 0.22 ± 0.03 for all studied materials. Data labeled Zr-hybrid_{int} indicates experiments where P_{th} was interpolated from the measured lines. For two lines spaced $0.1 \mu\text{m}$ apart the scaling factor was $i_{mean} = 0.17 \pm 0.02$. For 3D-structures interpolated from Raman measurements of DBC the necessary light dosage scaled with $i_{mean} = 0.28 \pm 0.08$. For each fit, the R_{fit}^2 is given, which is significantly higher than R_{theory}^2 , obtained from fits according to the predicted trend of $i = 0.5$.

Prepolymer	PI	Concentration	Method	Scaling Factor	R_{fit}^2	R_{theory}^2
ETA:TTA	M2CMK	0.1 mM	1D	0.21 ± 0.001	0.99	0.62
ETA:TTA	M2CMK	0.25 mM	1D	0.20 ± 0.076	0.81	0.58
ETA:TTA	M2CMK	1.0 mM	1D	0.20 ± 0.019	0.81	0.58
ETA:TTA	M2CMK	5.0 mM	1D	0.25 ± 0.038	0.95	0.72
PCL ₆	M2CMK	1.0 wt%	1D	0.30 ± 0.031	0.99	0.90
PCL ₆	M2CMK	0.1 wt%	1D	0.21 ± 0.028	0.95	0.43
PCL ₆	M2CMK	0.05 wt%	1D	0.19 ± 0.038	0.98	0.63
Zr-hybrid _{int}	4,4'-Bis	1.0 wt%	1D	0.16 ± 0.014	0.96	0.10
Zr-hybrid	4,4'-Bis	1.0 wt%	1D	0.21 ± 0.016	0.98	0.18
Zr-hybrid	4,4'-Bis	0.1 wt%	1D	0.25 ± 0.022	0.99	0.74
ETA:TTA	M2CMK	1.0 mM	2D	0.18 ± 0.016	0.95	0.43
Zr-hybrid	4,4'-Bis	0.1 wt%	2D	0.16 ± 0.033	0.98	0.08
ETA:TTA	M2CMK	1.0 mM	3D	0.26 ± 0.038	0.94	0.29
ETA:TTA	M2CMK	5.0 mM	3D	0.29 ± 0.122	0.67	0.40

viscosity could also play a role in this as radicals are no longer able to diffuse through the pre-formed network [9, 146]. This effect was less pronounced for higher concentrations of PI. For 1 mM the difference in DBC for at 40 mW was 23 %, compared to 13 % at 5 mM.

7 Results Large Field 2PP

To write structures larger than the available FOV, the correction factor M_{corr} of the 2PP system (described in Sec. 3.2) was evaluated by structuring $300 \times 100 \times 50 \mu\text{m}^3$ of Ormocomp[®]. Using 10x/0.3 objective a writing speed of 100 mm s^{-1} , laser power of 100 mW, $\Delta_h = 0.5 \mu\text{m}$ and $\Delta_z = 1 \mu\text{m}$ were chosen. The structure was rotated 45° and placed at the edge of the available writing area Δ_d . For a uniform power gradient, the available FOV was set to $\Delta_d = 1.2 \text{ mm}$. Multiple structures with varying M_{corr} were produced to optimize the stitching of two scan fields. The optimal M_{corr} setting was 1.275 (displayed in Fig. 7.1). Furthermore, the overlap of adjacent FOVs was increased, as no overlap resulted in gaps between the individual parts. Overlapping $2 \mu\text{m}$ resulted in a solid structure with the stitching area still visible. An overlap of $10 \mu\text{m}$ yielded structures with only minimal visibility of the overlay (Fig. 7.2).

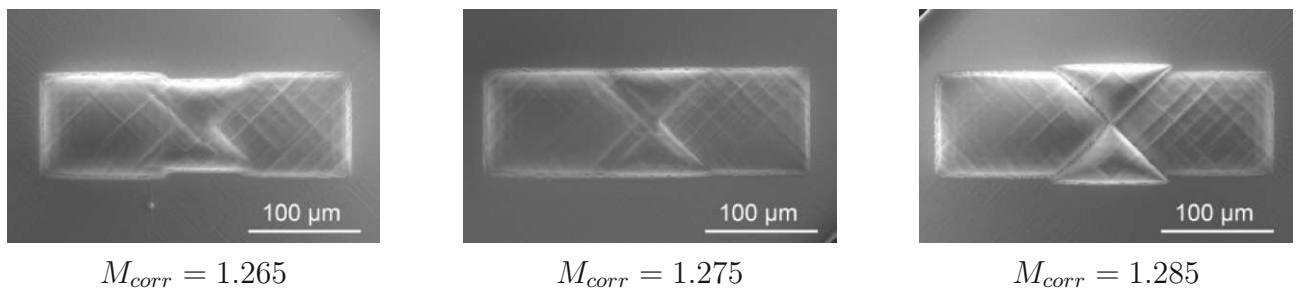


Figure 7.1: Microscope correction factor M_{corr} to match structures composited by multiple FOVs. The optimal setting was determined to be 1.275 (middle). Lowering M_{corr} caused an increase of the FOV (left), while an increase in M_{corr} resulted in a reduced FOV (right). SEM images recorded at USTEM, TU Wien.

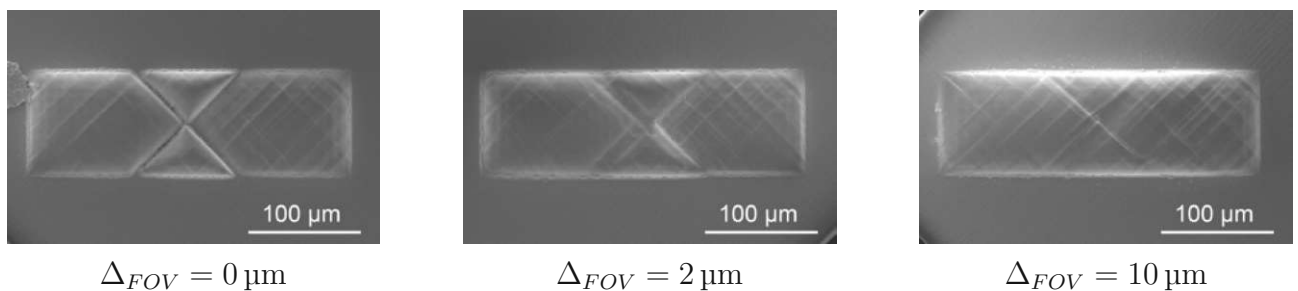


Figure 7.2: A FOV overlap (Δ_{FOV}) determines the area used for adjacent FOVs. Without this overlap gaps are visible (left). Increasing to $\Delta_{FOV} = 2 \mu\text{m}$ allowed a seamless junction (middle), which was improved by an overlap of $\Delta_{FOV} = 10 \mu\text{m}$ (right). SEM images recorded at USTEM, TU Wien.

Using the established parameters ($M_{corr} = 1.275$, $\Delta_{FOV} = 10 \mu\text{m}$) microscaffolds were structured using the 10x/0.3 objective from two material compositions: Zr-hybrid (0.1 wt% 4,4'-Bis)

7 Results Large Field 2PP

and PCL₆ (0.1 wt% M2CMK). The settings for both materials were identical (Sec. 3.7). Stable microscaffolds with a total length of 1.3 mm (0.3 mm buckyball and 1.0 mm rod) could be produced (Fig. 7.3). Because of the FOV overlap method, the scaffolds could be closely packed. Both materials were observed using SEM microscopy. The different resolution in lateral and vertical direction was evident. While clearly visible, the overlap region was correctly fabricated (Fig. 7.3). Zr-hybrid was previously found to be too brittle for nanoindentation measurements [12] and for PCL₆ a storage modulus of 39.7 ± 9.8 MPa (Sec. 5.2) was measured. This material behavior could also be observed under SEM observation where zr-hybrid exhibited micro-fractures, whereas PCL₆ retained an overall smooth surface area.

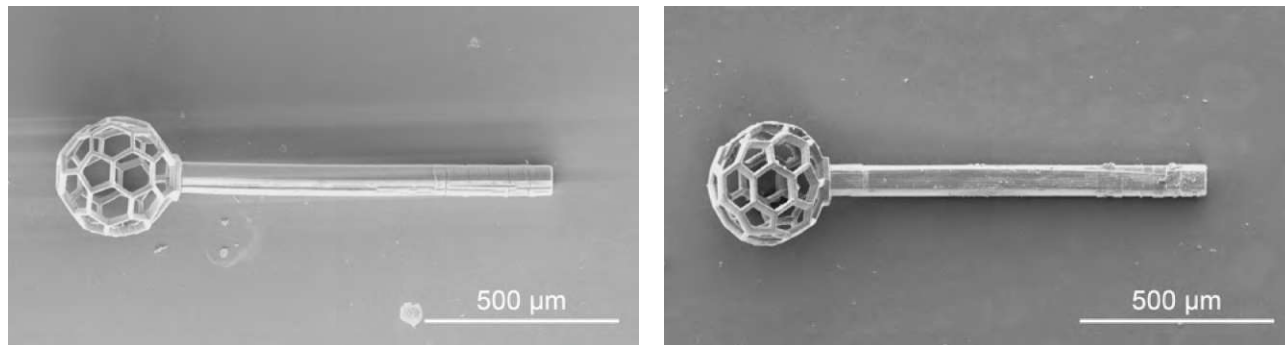


Figure 7.3: SEM-images of buckyball-scaffolds with added guidance rod fabricated from zr-hybrid (left) and PCL₆ (right). Using the previously determined parameters for M_{corr} and Δ_{FOV} allowed to fabricate structures larger than the available FOV.

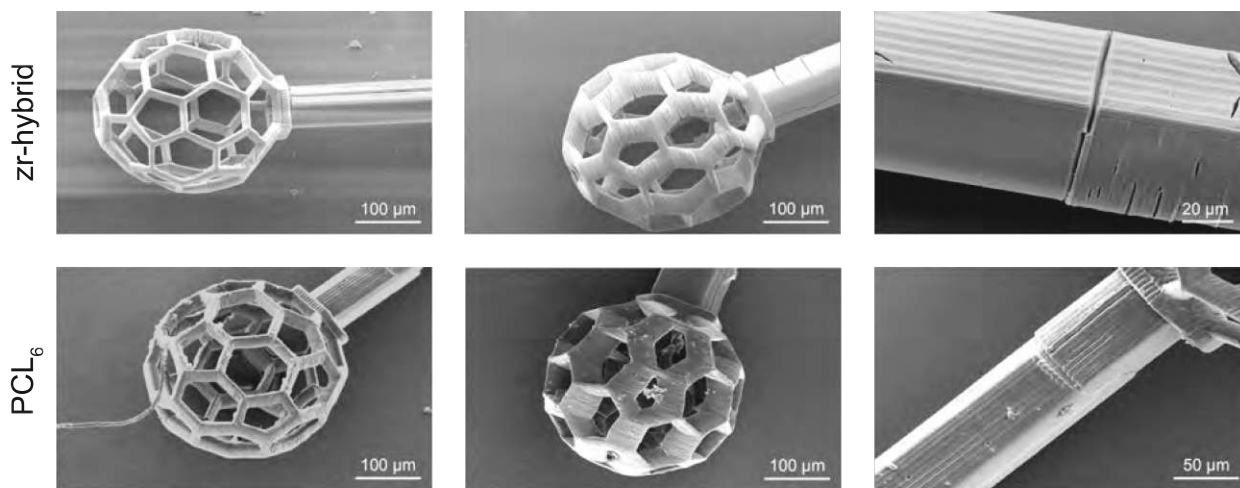


Figure 7.4: Close up of zr-hybrid and PCL₆ scaffolds. Comparison of top (left) and side view (right) showcases the difference in lateral and horizontal resolution. As the structure was larger than the available FOV, it was composited by multiple FOVs, using the previously evaluated parameters to connect the adjacent FOVs (right). As the material was found to be less brittle than zr-hybrid, fewer microfractures were observed. As with zr-hybrid there was a significant difference in the lateral (left) and horizontal (middle) resolution. Close up of the overlap area of two FOVs (right).

To further illustrate the advantages of combining multiple FOVs for high resolution applica-

tions, two connected buckyballs were fabricated. With a diameter of $100\ \mu\text{m}$ each and a $50\ \mu\text{m}$ connection, the total length was $250\ \mu\text{m}$, which was fitting for $10\times/0.3$ objective, but was too large for $63\times/1.4$ oil immersion objective using a single FOV. The first structures were produced with $10\times/0.3$ objective and the same fabrication as for the buckyballs was done with zr-hybrid ($0.1\ \text{wt}\%$ 4,4'-Bis). The voxel height was too large to create pores large enough for cell experiments. While the pore-diameter for the hexagon opening on top was $20\ \mu\text{m}$ the side-view revealed pores with a diameter below $5\ \mu\text{m}$. (Fig. 7.5).

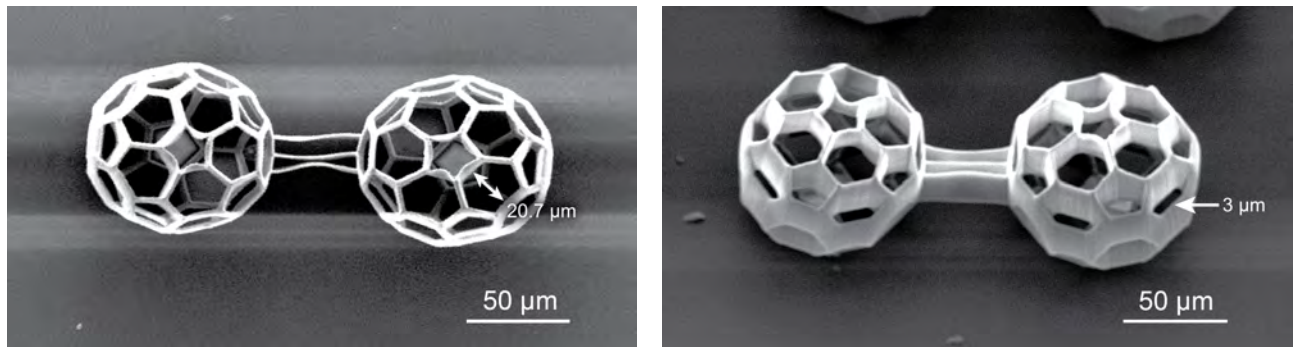


Figure 7.5: Connected buckyballs with a total length of $250\ \mu\text{m}$ written in a single FOV using $10\times/0.3$ objective from zr-hybrid ($0.1\ \text{wt}\%$ 4,4'-Bis). While the diameter of the top pores was on average $20\ \mu\text{m}$, the voxel height of the objective caused a reduction of the lateral pores to $3\ \mu\text{m}$, which is insufficient for cell migration into the scaffold.

The connected buckyball geometry was then fabricated using $63\times/1.4$ oil immersion objective and overlapping FOVs. For structuring, $70\ \text{mW}$, $200\ \text{mm s}^{-1}$, $\Delta_h = 0.4\ \mu\text{m}$ and $\Delta_v = 0.5\ \mu\text{m}$ were chosen. Two rods of $5\ \mu\text{m}$ diameter spaced $8\ \mu\text{m}$ apart connected the scaffolds. The overlapping FOV approach allowed to fabricate large enough geometries without compromising the resolution associated with too small pore sizes. After these preliminary results, the distance between the scaffolds was increased. Choosing two rods as a connection over a $18\ \mu\text{m}$ solid plate was preferred due to the weight of the connecting structure. Initial experiments with a solid connection showed the connection collapsing under its own weight at spacings above $150\ \mu\text{m}$ after drying. This was not observed with two individual rods. Similarly to findings of linetest structures, evaporation of the solvent caused high capillary forces, deforming the free-standing rods. While stable in the solvent (Fig. 7.6, left) the rods were squashed together after drying (Fig. 7.6, right). Replacing the solvent with HMDS, to reduce the surface tension during drying [188], did not counteract these effects. As a solution suspension blocks were introduced to grant stability and this method was studied for two buckyballs connected by $400\ \mu\text{m}$ rods. The connections were stabilized by either a single strut at the center of the connection ($\Delta = 200\ \mu\text{m}$) or two equidistantly spaced pillars ($\Delta = 133\ \mu\text{m}$). SEM revealed stable connections for the two-pillar approach. A single supporting pillar did not grant enough stability to counteract deformations (Fig. 7.7). The total length of the structure was $600\ \mu\text{m}$, which was more than three times the available FOV of the $63\times/1.4$ oil immersion objective, without compromising the resolution as in the case for $10\times/0.3$ objective.

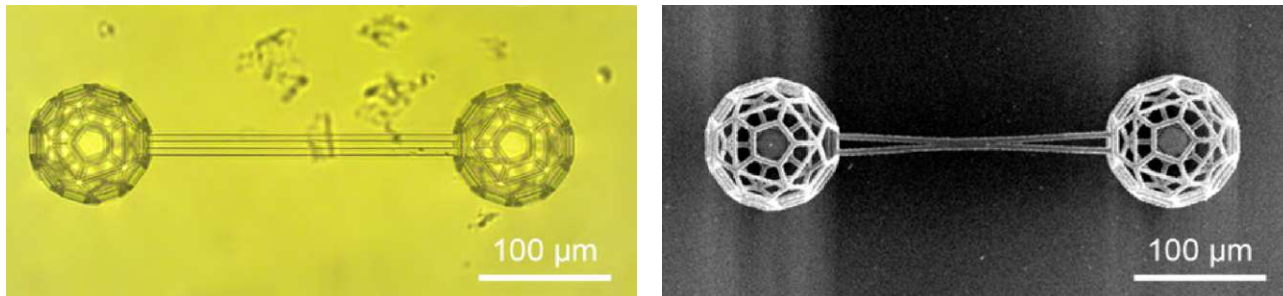


Figure 7.6: Two buckyballs connected by two 5 µm thick rods. While the structure was stable in the solvent (left), the two rods were squashed together after drying (right). Adding HMDS to reduce capillary forces due to the evaporating liquid did not prevent this process.

Die approbierte gedruckte Originalversion dieser Dissertation ist an der TU Wien Bibliothek verfügbar. The approved original version of this doctoral thesis is available in print at TU Wien Bibliothek.

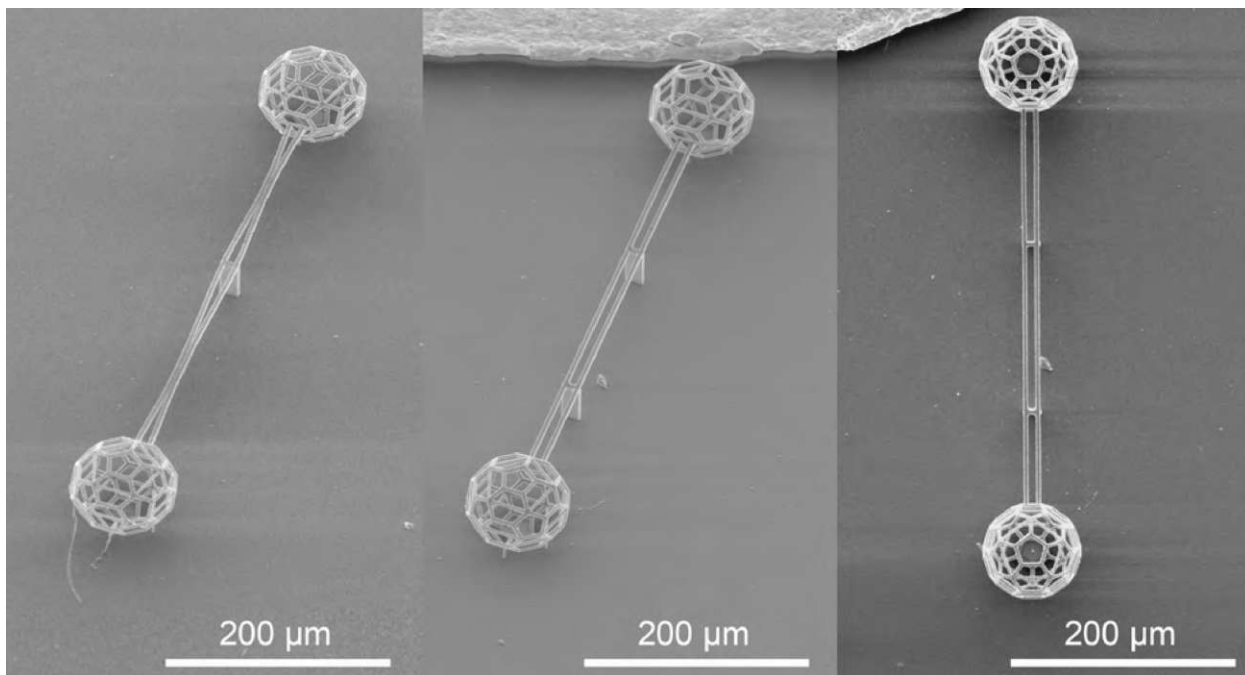


Figure 7.7: Buckyballs connected by 400 µm rods. To prevent deformation after drying, pillars were introduced to stabilize the rods. While a single pillar was insufficient to prevent deformation of 400 µm rods (left), two pillars spaced 133 µm apart allowed for stable structures even after development (middle and right). The total length of the structure was more than three times the available FOV of the 63x/1.4 objective.

7.1 Discussion

By combining multiple FOVs, complex microstructures were produced without compromising the resolution of 2PP. To match adjacent FOVs, the microscope correction factor M_{corr} was optimized. This factor correlates the beam position. If not properly adjusted, intersections were not properly polymerized or overpolymerized. To assure stable junctions, a FOV overlap was introduced. The selected overlap is exposed twice to guarantee sufficient cross-linking. An overlap of $10\ \mu\text{m}$ yielded best results. Combining multiple FOVs with 10x/0.3 objective allowed to produce microscaffolds consisting of a $300\ \mu\text{m}$ buckyball and an added rod of $1.0\ \text{mm}$ from zr-hybrid and PCL₆. While the production of millimeter high structures was previously shown using techniques such as WOW-2PP [92], the structure was still limited in x- and y-direction by the FOV. By combining multiple FOVs, scaffolds in the range of millimeters in lateral direction could be produced. This is especially important for sol-gel materials, as WOW-2PP is not applicable for solids and the working distance in z is therefore limited. This allows production of scaffolds for specific biomedical applications such as the regeneration of hair follicles [26, 30]. The benefit of combining multiple FOVs was further illustrated by comparing zr-hybrid structures of $600\ \mu\text{m}$ length within a single FOV (10x/0.3 objective) and multiple FOVs (63x/1.4 oil immersion). For this, buckyballs were connected via $400\ \mu\text{m}$ rods. The increase in voxel length for lower numerical apertures was shown by the different pore diameters. Using 10x/0.3 objective the lateral pores exhibited a diameter of $20\ \mu\text{m}$, while the diameter of vertical pores was $3\ \mu\text{m}$. Such pore dimensions would not be insufficient for propagation of cells into the scaffolds [191]. Producing the same structure using 63x/1.4 oil immersion objective and combined FOVs, yielded the same scaffold size ($3 \times \text{FOV}_{63x}$, with $\text{FOV}_{63x} = 190\ \mu\text{m}$) without compromising the resolution. Evaporation of the solvent caused deformation of the unsupported rods. This effect could not be prevented by adding HMDS to reduce capillary forces. As a solution, pillars were introduced, providing stability. Various pillar spacings were studied. For a connection of $400\ \mu\text{m}$ a pillar spacing of $133\ \mu\text{m}$ prevented deformation of the scaffolds. These highly resolved structures could potentially used to model neuronal networks. For this, the scaffolds could be seeded with neurons (for example by means of Faraday waves [46, 47]). The connection between the scaffolds could direct the network formation [200].

8 Results Microscaffolds

Two studies of cell seeded scaffolds were conducted. Periodically arranged microcages of 100 μm diameter were produced on a glass slide with feet attaching the cages to the slides. This periodicity allowed the seeding of fibroblasts and later on neurons by way of Faraday waves. Different geometries were compared to study the efficiency of the process. Experiments with fibroblasts were carried out by Pu Chen. Follow up experiments with neurons were done by Tanchen Ren. Both experiments were supervised by Utkan Demirci (Bio-Acoustic MEMS in Medicine Laboratories, Canary Center, Stanford, USA).

The second study involved the production of buckyballs of 300 μm diameter, which were seeded with KC and DP-like cells to induce hair follicles. This new approach for the regeneration of hair was initially done using zr-hybrid to test the feasibility of the method. Lastly, scaffolds produced from PCL₆ (Sec. 5) were seeded with the same cells to demonstrate the application and cytocompatibility of this material. DP experiments were carried out by Antonella Pinto under the supervision of Alexey Terskikh (Alexey Terskikh Lab, Sanford Burnham Prebys Medical Discovery Institute, La Jolla, USA).

8.1 Microcages

For the microcage experiments using Faraday waves buckyballs of 100 μm diameter were produced with 63x/1.4 oil immersion objective (Sec. 3.7) in a 25×25 array. The structure is displayed in Fig. 8.1.

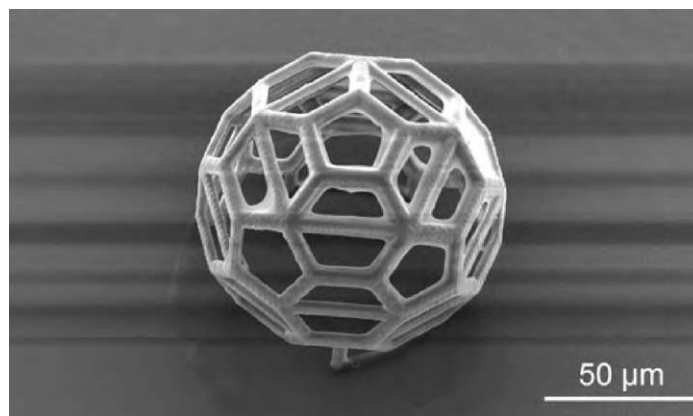


Figure 8.1: SEM image of buckyball structure with 100 μm diameter. The geometry was fixed to the glass sample by five rod extensions.

Initial experiments were done with MC3T3 fibroblasts ($2 \cdot 10^6$ cells ml^{-1}) for three samples to study the optimal Faraday wave parameters before neurons were used. A control sample was done without standing waves. Fibroblasts were only exposed to gravitational settlement. Fibroblasts in sample 2 and 3 were exposed to standing Faraday waves at a frequency of 54 Hz

Table 8.1: Faraday wave experiments. Significantly higher encapsulation of fibroblasts was observed for standing wave conditions compared to control sample where cells were solely exposed to gravitational force.

	nr. of cages	nr. of cells	avg. nr. of cells	std. deviation
control	79	93	1,177	1,217
54 Hz, 80 mV, 100s	68	214	3,147	2,152
54 Hz, 80 mV, 300s	61	221	3,623	2,368

and amplitude of 80 mV for 100 and 300 s, respectively. Results showed significantly higher cell encapsulation for standing wave conditions compared to the control sample (displayed in Tab. 8.1).

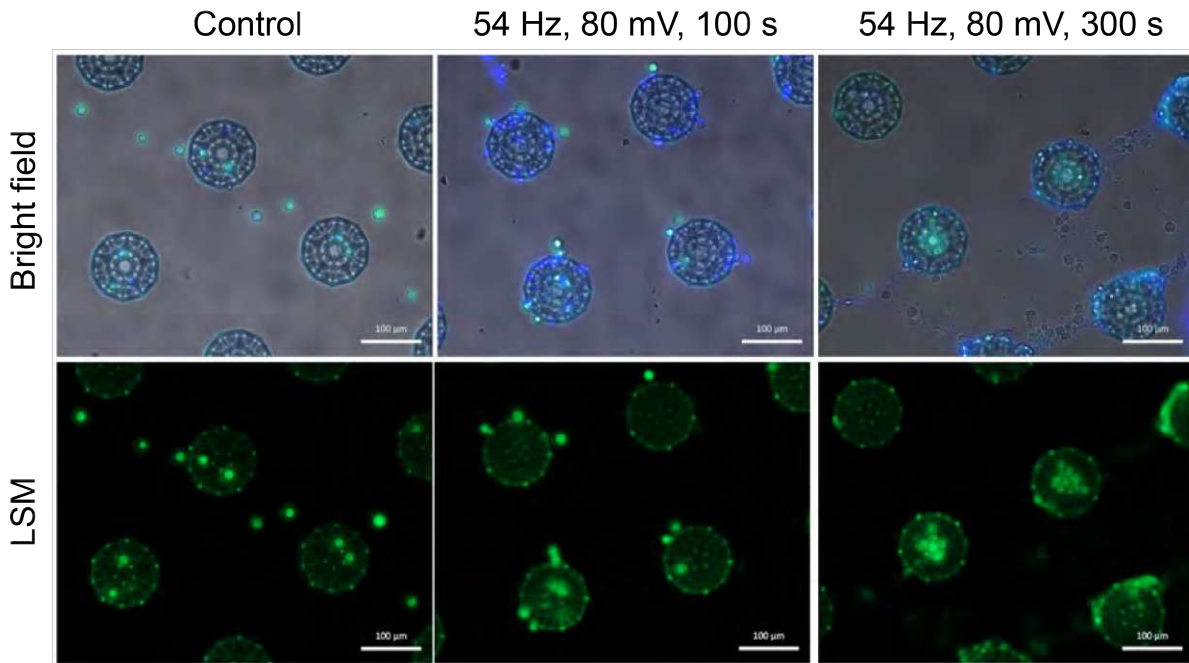


Figure 8.2: Preliminary Faraday wave experiments. Encapsulation of MC3T3 fibroblasts was studied using two different experiment times. Control sample was done without Faraday waves and fibroblasts were only exposed to gravitational force. Experiments done by Pu Chen under the supervision of Utkan Demirci.

For follow up experiments, the effect of different buckyball geometries was studied. Three samples with complete buckyballs, two samples with open top buckyballs, and two samples with open bottom buckyballs were produced (discussed in Sec. 3.7) with the previous 2PP-settings. Cortical neurons (isolated from embryonic day 18 (E18) CD-1 mice) were seeded on the scaffolds ($5 \cdot 10^6$ cells ml⁻¹ per sample) via Faraday waves. The parameters for the Faraday waves from the initial experiment were used (50 Hz, 80 mV) and 300 s was chosen for the experiment runtime due to the higher cell number in the scaffolds. After 10 days, the cell counting was done under confocal microscope. The experiments yielded highest cell density for complete buckyballs geometries (10.48 ± 2.5 cells per scaffold), lower cell density for buckyballs

with open top (6.2 ± 2.6) and significantly less for open bottom structures (1.3 ± 1.0). The full data are displayed in Fig. 8.3.

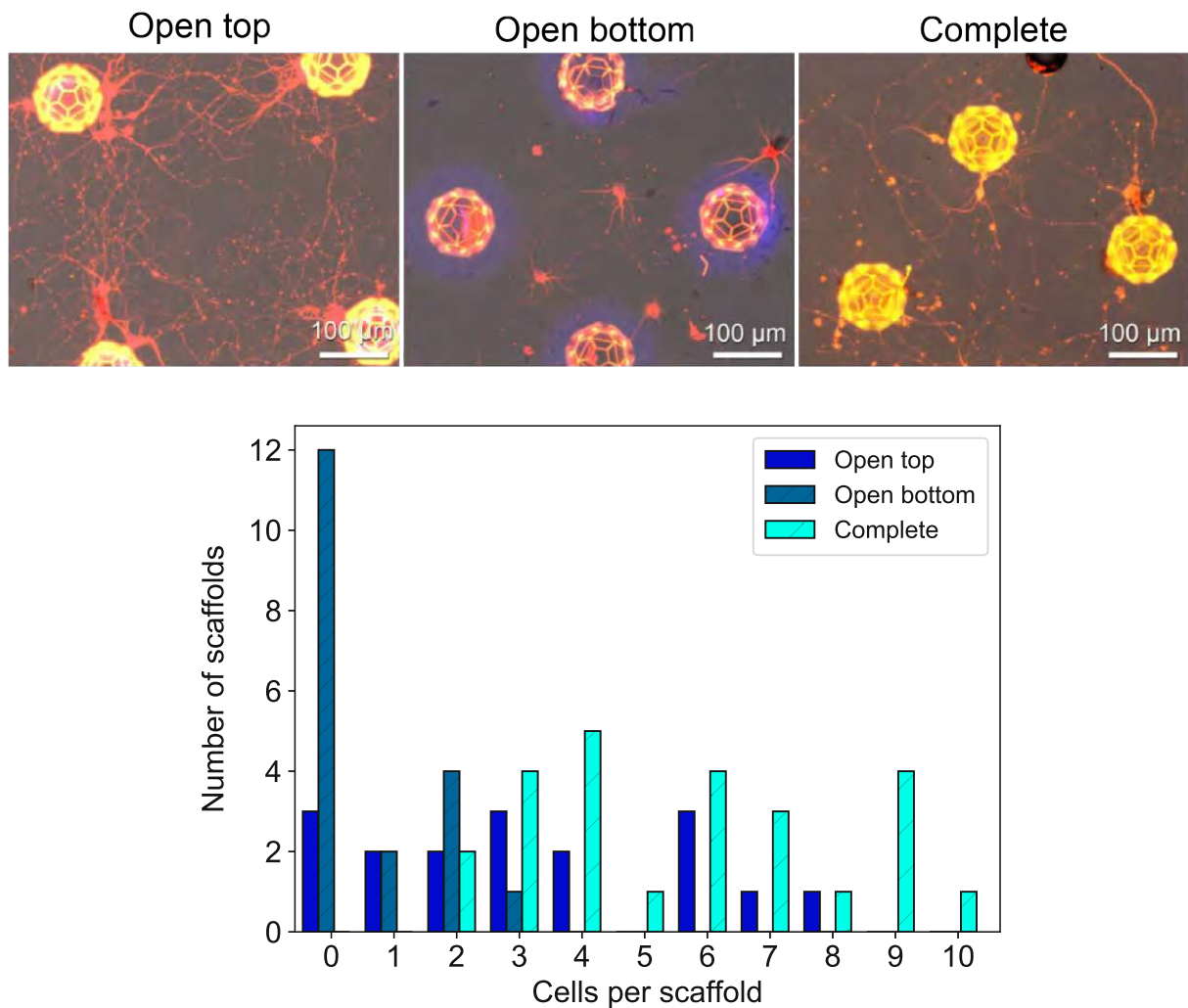


Figure 8.3: Neurons trapped by buckyballs of in 100 μm diameter obtained with LSM (top row). Higher encapsulation of neurons was already visible for open top and complete buckyball structures when compared to open bottom geometries. The number of trapped cells was obtained via z-stack. Counting of trapped cells for each scaffold revealed most efficient cell trapping for the complete buckyball structure (lower) while open bottom contained the least amount of cells. Experiments done by Tanchen Ren under the supervision of Utkan Demirci.

8.2 Hair Follicles

Initial experiments were done using buckyball microscaffolds fabricated from zr-hybrid (Sec. 3.7). The seeded scaffolds were then implanted to study if hair growth was induced after transplantation. After this initial test, the PCL₆ scaffolds were seeded with cells to evaluate the usability of the biodegradable material for this method.

8.2.1 Zr-Hybrid

The zr-hybrid buckyballs were placed manually into the micro-molded agarose dish produced from the silicone positive (described in detail in Sec. 3.9.1). Three different seeding methods were chosen. The negative control consisted of only mKCs. Mouse embryonic DP cells in combination with mKCs were used as positive control to showcase follicle growth using only cell types derived from mice. Lastly, DP-like cells derived from hiPSCs and mKCs were combined to study the growth of human hair follicles. Cell encapsulation was observed already at 24 h after plating and was stable for the following 48 h (Fig. 8.4). Furthermore, this method was highly reproducible as the majority of the scaffolds held the encapsulated cells in the same manner.

The buckyballs were then transplanted on the back of nude mice by manually transferred the scaffold underneath the murin skin. 14 days post-transplantation, hair shafts were observed (Fig. 8.5). Transplantation of a combination of E18 mouse dermal cells (mDCs) and mKCs induced robust hair growth (positive control), mKCs alone resulted in minimal hair induction (negative control), as previously reported [201,202]. However, human iPSC-DP cells combined with mKCs induced robust hair growth, comparable to that seen in a positive control.

The number of hair follicles formed in each patch assay was quantified by manually counting the black hair shafts. The generated hair follicles were next analyzed via immunohistochemical staining, using the K14 antibody and a human-specific antibody to detect the epithelial compartment of the follicle and the presence of human DP-like cells, respectively. DAPI was used to stain nuclei (Fig. 8.5). Immunolabeling of the newly generated hair follicle with human cytoplasm-specific antibody revealed human cells in stereotypic positions of dermal papilla, except in the mouse cell-derived positive control. Therefore, it could shown that the follicles observed using stereomicroscopy were indeed produced by human DP-like cells.

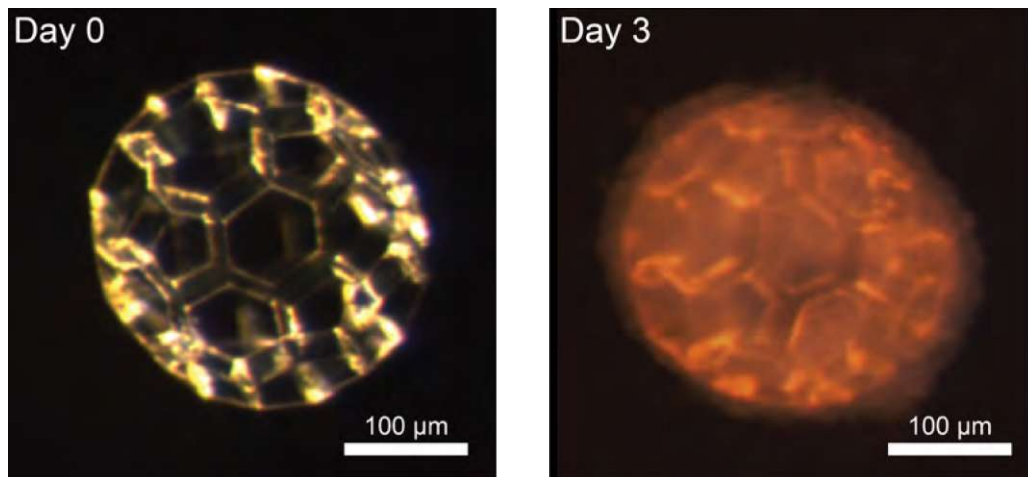


Figure 8.4: Representative images of the scaffolds used for the encapsulation of hair-inducing cells into the buckyballs. Pictures were taken under a stereo-microscope at different time points, as indicated in each quadrant. Experiments done by Antonella Pinto under the supervision of Alexey Terskikh.

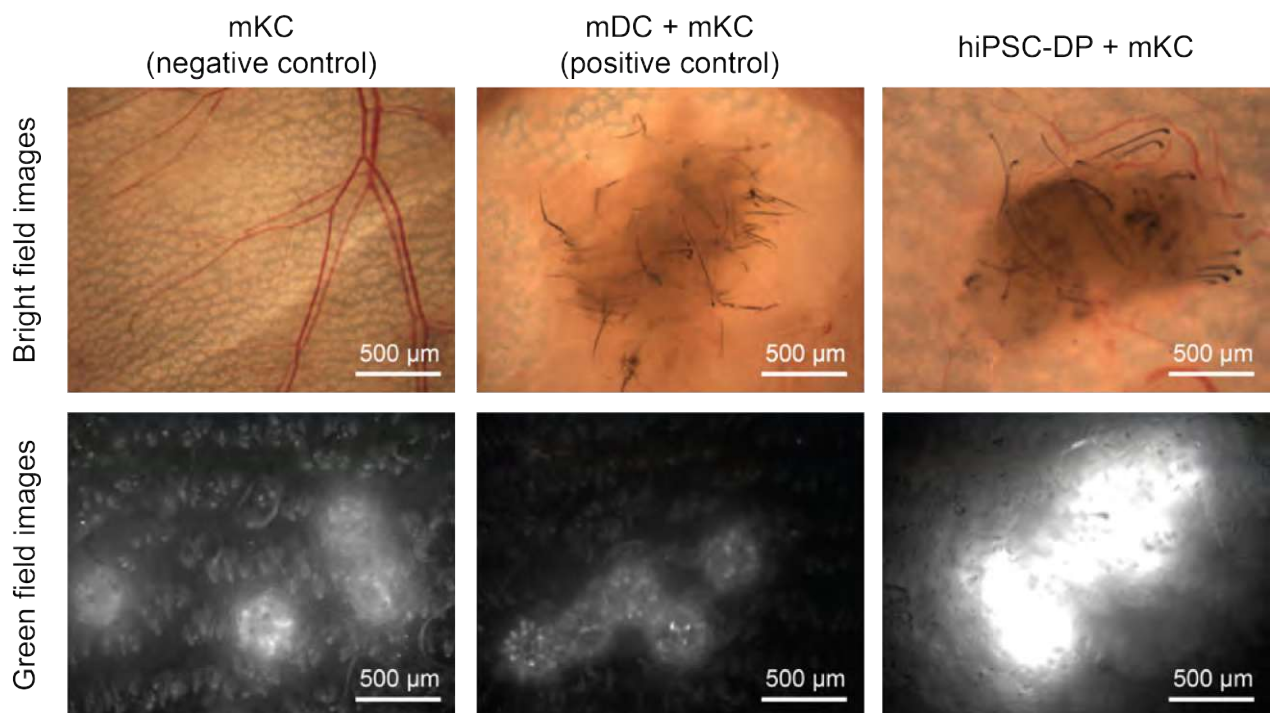


Figure 8.5: Intradermal transplantation of iPSC-DP cells into the back skin of nude mice. Hair shafts were observed underneath the skin, as shown by the stereo images of the whole mounts of embryonic mKCs transplanted alone (negative control) or in combination with mouse dermal cells (mDC, positive control) and DP-like cells derived from hiPSCs (upper). After 14 days, the scaffolds were still visible at the site of transplantation as shown in the pictures taken with a fluorescent microscope (lower). Experiments done by Antonella Pinto under the supervision of Alexey Terskikh.

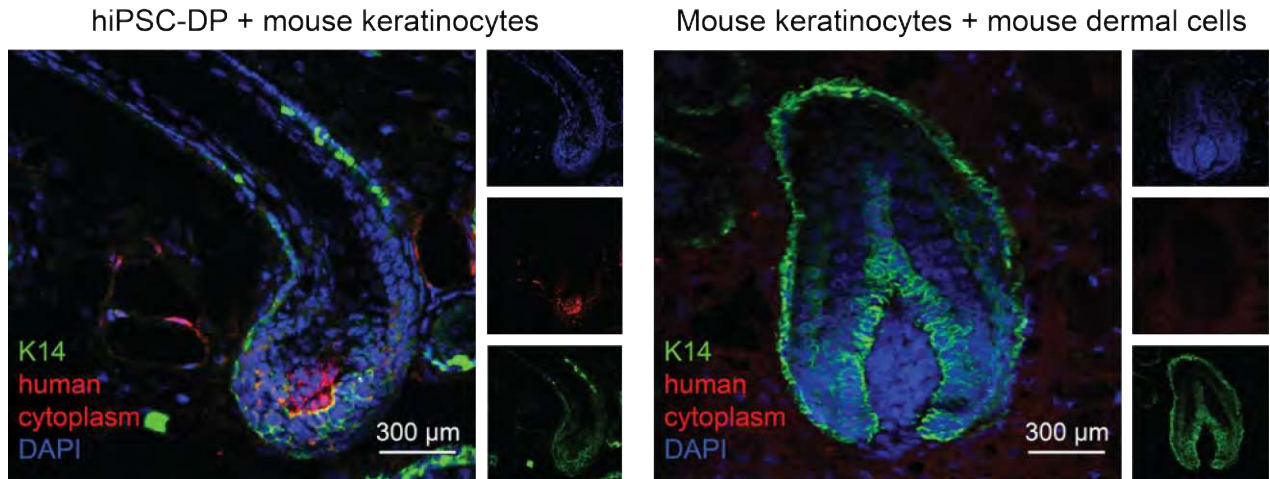


Figure 8.6: Immunohistochemical images of generated hair follicle after transplantation of embryonic mouse keratinocytes combined with human iPSC-derived DP cells (left), or embryonic mouse dermal cells (right). Human cytoplasm was stained using the human-specific antibody MAB1273 (in red). It recognizes only human cells, while K14 (in green) stained keratinocytes. DAPI (blue) was used to identify nuclei. Therefore, it was demonstrated that the observed follicles were indeed produced by the human DP-like cells and mouse keratinocytes. Experiments done by Antonella Pinto under the supervision of Alexey Terskikh.

8.2.2 PCL-Based-Prepolymer

After this prove of principle, the lolly-up scaffolds produced were studied with a special focus on PCL₆ due the biodegradability of the PCL-backbone. The lolly-up scaffolds were seeded in the agarose microwells with hiPSC-DP cells and mouse keratinocytes (Fig. 8.7) in the same manner as the zr-hybrid based buckyballs. After a gentle centrifugation, to enhance gravity-driven sedimentation, it was observed that the cells were easily confined in the small space of the resection, ensuring contact with the ball portion of the scaffold (Fig. 8.7).

After 48 h the cells aggregated within the lolly-up scaffold, forming dense spheroids at the bottom buckyball (Fig. 8.8).

8.3 Discussion

Cell loading of 2PP-produced scaffolds via Faraday waves was successfully demonstrated for fibroblasts and neurons. Complete buckyballs showed the most effective cell trapping, which was probably due to the stability provided by the geometry. Neurons trapped in open top buckyballs were probably exposed to stronger convection during the washing steps, while open bottom structures likely did not provide sufficient support for cells. This new method shows promise to develop 3D-neural structures, which can significantly broaden the understanding of the wiring and mapping mechanisms of neurons [200]. Producing these highly complex patterns could be done via 2PP by combining the high resolution required with previously produced bridge-connections between buckyballs (Sec. 7). These connected structures could be used as guides to direct neuron growth to create custom neuron networks.

2PP-fabricated scaffolds were used for a new approach for the regeneration of hair follicles.

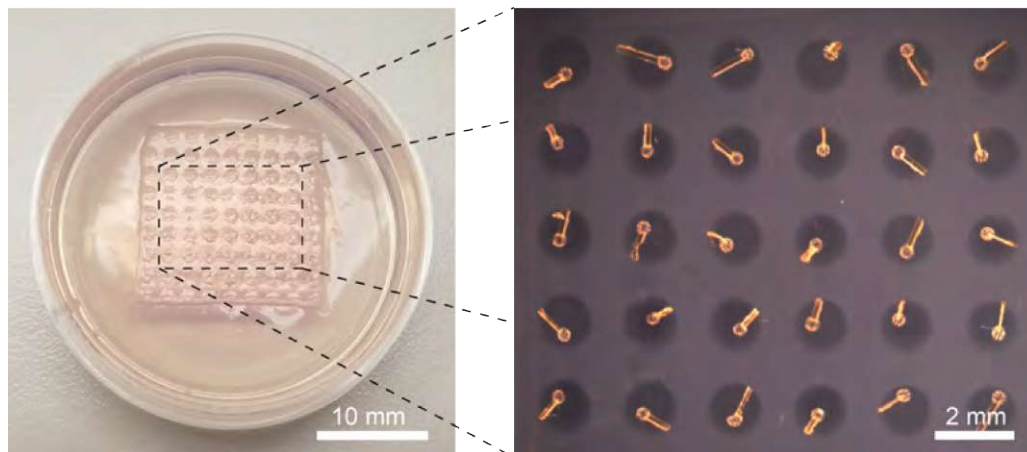


Figure 8.7: Picture of the micro-molded agarose culture dish with single lolly-up scaffolds placed into each resection, as shown in the insert. Experiments done by Antonella Pinto under the supervision of Alexey Terskikh.

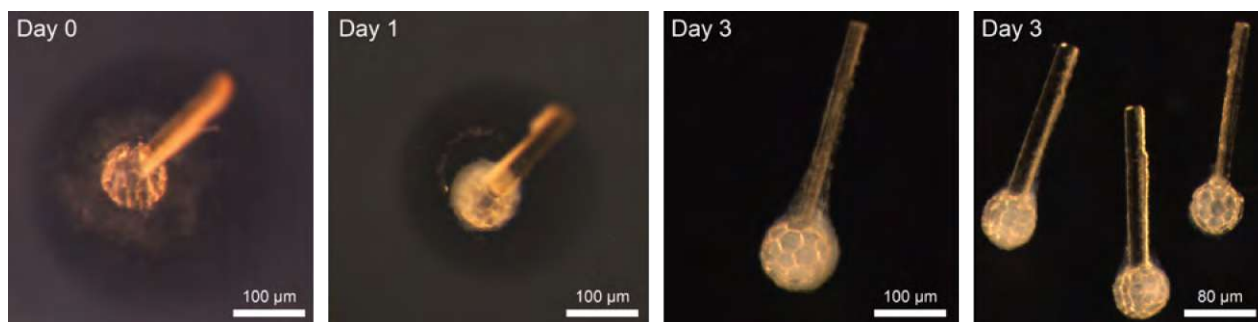


Figure 8.8: PCL₆-based lolly-up scaffolds in agarose molds. After seeding (day 0), hiPSC-DP cells and mouse keratinocytes aggregated within the bottom buckyball and formed a dense spheroid. Pictures were taken under a stereo-microscope at different time points, as indicated in each quadrant. Experiments done by Antonella Pinto under the supervision of Alexey Terskikh.

The high porosity of the buckyball geometry allow to combine iPSC-DP and mKC cells to provide the shape required by the cells in their natural state and to enhance the crosstalk between dermal and epidermal cells. Moreover, the scaffolds provide a new tool to facilitate the transplantation of the three-dimensional follicular units into the back of nude mice and to enhance the hair growth through the skin, mimicking the biological event of hair follicle formation in human beings. This was demonstrated by the use of buckyballs fabricated from zr-hybrid. As this glass-like material is not biodegradable, the cell seeding was also done with PCL₆ as its PCL-based backbone is cytocompatible and biodegradable. The use of hiPSC-DP cells in micro-scaffolds for the neogenesis of hair follicles from autologous adult cells could contribute to create a highly customized approach to stem cell treatment for hair loss disorder, to overcome the limitations currently present in this field [31, 65, 66].

9 Conclusion

A comprehensive study of 2PA processes and materials was carried out. The 2PA cross section σ_2 of NLA compounds was characterized in a range from 690 to 1040 nm. Assembling a completely automated z-scan setup allowed for fast screening of the compounds. A mechanical chopper was required to reduce effects of higher order caused by the high repetition rate laser.

Furthermore, the use of reflective optics minimizes dispersion and enables an automated measurement procedure without manual readjustment when changing the wavelength. Because of an extensive calibration routine, σ_2 could be reliably measured, rendering this setup as a viable alternative to conventional OPA or WLC z-scan systems [35, 36]. As the laser source is the same for 2PP and z-scan experiments, the correlation of absorption and polymerization studies could be directly studied. A correlation between $\sigma_2(\lambda)$ and the required threshold power P_{th} was shown as described by the established model. Matching the wavelength used for 2PP to the 2PA maximum reduced the required lower laser powers and allowed for higher fabrication speeds. In addition, various PS were screened for potential 2P-PDT applications [203]. The water soluble P2CK was used to locally induce cell death in cancer cells without causing damage in the surrounding environment. In addition, the 2PA spectrum of porphine exhibited a σ_2 several magnitudes larger than P2CK. Therefore, concentrations of porphine in the μM -range can be used for future 2P-PDT experiments, as for these concentrations it is not cytotoxic, [204].

The power required for polymerization (P_{th}) was extensively studied with a close inspection of the scaling factor, moderating the correlation of scanning speed (v) and P_{th} . Previous works reported a quadratic correlation between those two components ($P_{th} \propto v^{0.5}$, blue area in Fig. 9.1). However, these works were conducted using writing speeds in the range from 10 to 100 $\mu\text{m s}^{-1}$ [43–45]. In the current work the scanning speed was increased up to 100 mm s^{-1} . The polymerization threshold was studied under three different conditions with increased complexity. Initial experiments were conducted using single lines. Afterwards, two lines were produced spaced 0.1 μm apart. Lastly P_{th} of fully 3D-structures was evaluated using Raman spectroscopy. For all experiments the scaling factor was in the range $i \in \{0.16 - 0.30\}$. Fitting data in accordance with the established $i = 0.5$ resulted in fits with R^2 values almost exclusively below 0.65, indicating that the current model is not properly describing 2PP processes at higher fabrication speeds. This is possibly due to the fact that models were based on experiments under static exposure conditions and did not take diffusion of radicals into account. The results of this work demonstrate, that an increase from 10 to 100 mm s^{-1} requires an increase of laser power by 78 % (green area in Fig. 9.1), instead of the previously assumed 216 % percent as one would expect from quadratic dependence.

Combining multiple FOVs allowed to produce microscaffolds larger than the FOV of a given objective. By matching the overlapping regions, objects of 0.6 mm length could be produced using a 63x/1.4 oil immersion objective, without compromising the excellent resolution. A promising application of this was shown using Faraday wave experiments. Here, microcages were produced from sol-gel materials [32–34] to seed the scaffolds with fibroblast or neurons. By placing structures in a periodic grid, the nodes of the Faraday waves were matched to these

9 Conclusion

positions to drive the cells towards the microcages. The effective trapping of neurons shows great promise for the development of 3D-neural structures that can significantly broaden the understanding of the wiring and mapping mechanisms of neurons [200]. For future experiments the previously discussed combination of multiple FOVs will prove vital, as the connected microcage structure presented in this work could be used to direct the growth of neurons.

Over the course of this work, novel PCL-based prepolymers were tested for their 2PP-processability. While the initial PCL₂ did not require PI for polymerization, the fabricated structures were too weak for self support. The addition of shortchained triacrylates allowed for sufficient cross-linking. Structures produced from the hexafunctional PCL₆ were stable after development even without the addition of additional cross-linking prepolymers. The reduced Young's modulus was measured via nanoindentation to be 39.7 ± 9.8 MPa. This yielded flexible scaffolds which did not fracture during handling as previously used sol-gels [12]. Loading 2PP produced scaffolds with iPSC-DP cells and mKC induced the growth of human hair follicles after implantation in mice. The viability of scaffolds produced from PCL₆ was shown by successful loading of the scaffold and cell survival after 3 days. Due to the fact that PCL₆ is based on a biocompatible and biodegradable PCL-backbone, this newly synthesized material shows immense potential for future application in tissue engineering.

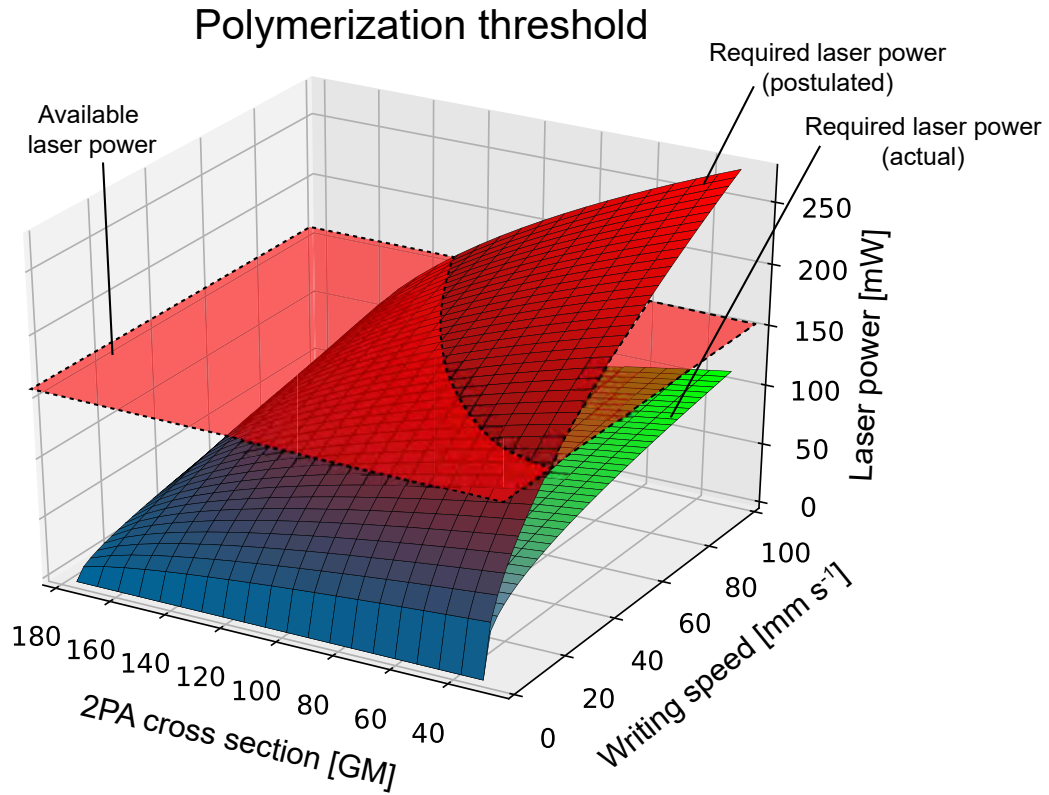


Figure 9.1: Dependence of the polymerization threshold P_{th} from 2PA cross section and writing speed. The blue-red 3D-area represents the required minimum laser power P_{th} for a given writing speed and 2PA cross section (given in GM). While previous models predicted a dependence of $P_{th} \propto v^{0.5}$ [43], the results presented in this project yielded a significantly lower scaling of required laser power for writing speeds of 100 mm s^{-1} . As represented by the blue-green area, the writing speed can be increased further than predicted by the established model ($P_{th} \propto v^{0.22}$). The red 2D-plane represents the laser power limit of commercially available systems [39].

Bibliography

- [1] Simon Thiele, Kathrin Arzenbacher, Timo Gissibl, Harald Giessen, and Alois M. Herkommer. 3d-printed eagle eye: Compound microlens system for foveated imaging. *Science Advances*, 3(2):e1602655, February 2017.
- [2] Rui Guo, Shizhou Xiao, Xiaomin Zhai, Jiawen Li, Andong Xia, and Wenhao Huang. Micro lens fabrication by means of femtosecond two photon photopolymerization. *Optics Express*, 14(2):810, 2006.
- [3] M. Deubel, M. Wegener, S. Linden, G. von Freymann, and S. John. 3d-2d-3d photonic crystal heterostructures fabricated by direct laser writing. *Optics Letters*, 31(6):805–807, March 2006.
- [4] Mark D. Turner, Gerd E. Schröder-Turk, and Min Gu. Fabrication and characterization of three-dimensional biomimetic chiral composites. *Optics Express*, 19(10):10001–10008, May 2011.
- [5] Lorenzo Amato, Yu Gu, Nicola Bellini, Shane M. Eaton, Giulio Cerullo, and Roberto Osellame. Integrated three-dimensional filter separates nanoscale from microscale elements in a microfluidic chip. *Lab on a Chip*, 12(6):1135–1142, February 2012.
- [6] Charalampos Schizas, Vasileia Melissinaki, Arune Gaidukeviciute, Carsten Reinhardt, Christoph Ohrt, Vassilis Dedoussis, Boris N. Chichkov, Costas Fotakis, Maria Farsari, and Dimitris Karalekas. On the design and fabrication by two-photon polymerization of a readily assembled micro-valve. *The International Journal of Advanced Manufacturing Technology*, 48(5):435–441, May 2010.
- [7] Péter Galajda and Pál Ormos. Rotation of microscopic propellers in laser tweezers. *Journal of Optics B: Quantum and Semiclassical Optics*, 4(2):S78, 2002.
- [8] Wojciech Haske, Vincent W. Chen, Joel M. Hales, Wenting Dong, Stephen Barlow, Seth R. Marder, and Joseph W. Perry. 65 nm feature sizes using visible wavelength 3-D multiphoton lithography. *Optics Express*, 15(6):3426–3436, March 2007.
- [9] Jürgen Stampfl and Robert Liska. *Multiphoton Lithography: Techniques, Materials, and Applications*. John Wiley & Sons, December 2016. Google-Books-ID: 5xEPDQAAQBAJ.
- [10] Steven Goodman and Paul Campagnola. Free-Form Nanofabrication Using Multi-Photon Excitation, March 2001. CIB: A61K47/48; A61K9/00; A61L27/36; A61L27/50; B29C67/00; C07K1/06; C07K14/75; C07K14/765; C07K17/04; C12N11/04; G01Q80/00; G02B21/32; G03F7/00; G03F7/029; G03F7/038; G03F7/20; (IPC1-7): G03C5/00; G03F7/00; G03F7/20.

Bibliography

- [11] Ruth Houbertz-Krauss, Matthias Beyer, Joern Probst, and Thomas Stichel. Method for Generating Biologically Friendly, Three-Dimensional Objects or Surfaces Using Laser Radiation, Such Objects, Use of Same and Starting Material for the Method, December 2012. CIB: B29C67/00; C07H9/04.
- [12] Peter Gruber. *Development of a novel wavelength-tunable high-speed 2-photon lithography setup*. PhD thesis, TU Wien, May 2018.
- [13] Jan Torgersen, Xiao-Hua Qin, Zhiquan Li, Aleksandr Ovsianikov, Robert Liska, and Jürgen Stampfl. Hydrogels for Two-Photon Polymerization: A Toolbox for Mimicking the Extracellular Matrix. *Advanced Functional Materials*, 23(36):4542–4554, May 2013.
- [14] Hynda K. Kleinman, Deborah Philp, and Matthew P. Hoffman. Role of the extracellular matrix in morphogenesis. *Current Opinion in Biotechnology*, 14(5):526–532, October 2003.
- [15] Jennifer Patterson, Mikaël M. Martino, and Jeffrey A. Hubbell. Biomimetic materials in tissue engineering. *Materials Today*, 13(1):14–22, January 2010.
- [16] Susan Breslin and Lorraine O’Driscoll. Three-dimensional cell culture: the missing link in drug discovery. *Drug Discovery Today*, 18(5-6):240–249, March 2013.
- [17] Mina J Bissell, Aylin Rizki, and I Saira Mian. Tissue architecture: the ultimate regulator of breast epithelial function. *Current opinion in cell biology*, 15(6):753–762, December 2003.
- [18] V. M. Weaver, O. W. Petersen, F. Wang, C. A. Larabell, P. Briand, C. Damsky, and M. J. Bissell. Reversion of the Malignant Phenotype of Human Breast Cells in Three-Dimensional Culture and In Vivo by Integrin Blocking Antibodies. *The Journal of Cell Biology*, 137(1):231–245, April 1997.
- [19] Andrew L Hopkins. Network pharmacology: the next paradigm in drug discovery. *Nature Chemical Biology*, 4(11):682–690, November 2008.
- [20] William N. Hait. Anticancer drug development: the grand challenges, April 2010.
- [21] Marica Markovic, Jasper Van Hoorick, Katja Hölzl, Maximilian Tromayer, Peter Gruber, Sylvia Nürnberger, Peter Dubruel, Sandra Van Vlierberghe, Robert Liska, and Aleksandr Ovsianikov. Hybrid Tissue Engineering Scaffolds by Combination of Three-Dimensional Printing and Cell Photoencapsulation. *Journal of Nanotechnology in Engineering and Medicine*, 6(2):021004, September 2015.
- [22] Jetze Visser, Ferry P.W. Melchels, June E. Jeon, Erik M. van Bussel, Laura S. Kimpton, Helen M. Byrne, Wouter J.A. Dhert, Paul D. Dalton, Dietmar W. Hutmacher, and Jos Malda. Reinforcement of hydrogels using three-dimensionally printed microfibrils. *Nature Communications*, 6(1), December 2015.
- [23] Jasper Van Hoorick, Peter Gruber, Marica Markovic, Maximilian Tromayer, Jürgen Van Erps, Hugo Thienpont, Robert Liska, Aleksandr Ovsianikov, Peter Dubruel, and Sandra Van Vlierberghe. Cross-Linkable Gelatins with Superior Mechanical Properties

- Through Carboxylic Acid Modification: Increasing the Two-Photon Polymerization Potential. *Biomacromolecules*, 18(10):3260–3272, October 2017.
- [24] An I. Van Den Bulcke, Bogdan Bogdanov, Nadine De Rooze, Etienne H. Schacht, Maria Cornelissen, and Hugo Berghmans. Structural and Rheological Properties of Methacrylamide Modified Gelatin Hydrogels. *Biomacromolecules*, 1(1):31–38, March 2000.
- [25] Maximilian Tromayer, Agnes Dobos, Peter Gruber, Aliasghar Ajami, Roman Dedic, Aleksandr Ovsianikov, and Robert Liska. A biocompatible diazosulfonate initiator for direct encapsulation of human stem cells via two-photon polymerization. *Polymer Chemistry*, 9(22):3108–3117, June 2018.
- [26] Aleksandr Ovsianikov, Ali Khademhosseini, and Vladimir Mironov. The Synergy of Scaffold-Based and Scaffold-Free Tissue Engineering Strategies. *Trends in Biotechnology*, 36(4):348–357, April 2018.
- [27] Rodrigo A. Rezende, Frederico D. A. S. Pereira, Vladimir Kasyanov, Aleksandr Ovsianikov, Jan Torgersen, Peter Gruber, Jurgen Stampfl, Ken Brakke, Júlia A. Nogueira, Vladimir Mironov, and Jorge V. L. da Silva. Design, physical prototyping and initial characterisation of ‘lockyballs’. *Virtual and Physical Prototyping*, 7(4):287–301, December 2012.
- [28] Karina R. Silva, Rodrigo A. Rezende, Frederico D. A. S. Pereira, Peter Gruber, Mellannie P. Stuart, Aleksandr Ovsianikov, Ken Brakke, Vladimir Kasyanov, Jorge V. L. da Silva, José M. Granjeiro, Leandra S. Baptista, and Vladimir Mironov. Delivery of Human Adipose Stem Cells Spheroids into Lockyballs. *PLOS ONE*, 11(11):e0166073, November 2016.
- [29] Aleksandr Ovsianikov, Vladimir Mironov, Jürgen Stampfl, and Robert Liska. Engineering 3d cell-culture matrices: multiphoton processing technologies for biological and tissue engineering applications. *Expert Review of Medical Devices*, 9(6):613–633, November 2012.
- [30] Ksenia Gnedeva, Ekaterina Vorotelyak, Flavio Cimadamore, Giulio Cattarossi, Elena Giusto, Vasiliy V. Terskikh, and Alexey V. Terskikh. Derivation of Hair-Inducing Cell from Human Pluripotent Stem Cells. *PLoS ONE*, 10(1), January 2015.
- [31] C. A. Higgins, J. C. Chen, J. E. Cerise, C. A. B. Jahoda, and A. M. Christiano. Microenvironmental reprogramming by three-dimensional culture enables dermal papilla cells to induce de novo human hair-follicle growth. *Proceedings of the National Academy of Sciences*, 110(49):19679–19688, December 2013.
- [32] A. Ovsianikov, A. Gaidukeviciute, B. N. Chichkov, M. Oubaha, B. D. MacCraith, I. Sakelari, A. Giakoumaki, D. Gray, M. Vamvakaki, M. Farsari, and C. Fotakis. Two-Photon Polymerization of Hybrid Sol-Gel Materials for Photonics Applications, 2008.
- [33] M. Malinauskas, P. Danilevičius, D. Baltriukienė, M. Rutkauskas, A. Žukauskas, ž. Kairytė, G. Bičkauskaitė, V. Purlys, D. Paipulas, V. Bukelskienė, and R. Gadonas. 3d artificial polymeric scaffolds for stem cell growth fabricated by femtosecond laser. *Lithuanian Journal of Physics*, 50(1):75–82, 2010.

Bibliography

- [34] Maria Farsari and Boris N. Chichkov. Materials processing: Two-photon fabrication. *Nature Photonics*, 3(8):450–452, August 2009.
- [35] Nikolay S. Makarov, Mikhail Drobizhev, and Aleksander Rebane. Two-photon absorption standards in the 550–1600 nm excitation wavelength range. *Optics Express*, 16(6):4029–4047, March 2008.
- [36] Aliasghar Ajami, Wolfgang Husinsky, Maximilian Tromayer, Peter Gruber, Robert Liska, and Aleksandr Ovsianikov. Measurement of degenerate two-photon absorption spectra of a series of developed two-photon initiators using a dispersive white light continuum Z-scan. *Applied Physics Letters*, 111(7):071901, August 2017.
- [37] Xiao-Hua Qin, Aleksandr Ovsianikov, Jürgen Stampfl, and Robert Liska. Additive manufacturing of photosensitive hydrogels for tissue engineering applications. *BioNanoMaterials*, 15(3-4), January 2014.
- [38] X. M. Du, Y. Yan, Z. L. Bai, J. P. Zhang, Z. Wang, L. L. Liu, and L. J. Feng. Evaluation of the cytotoxicity of a two photon absorbing fluorescence compound on human HepG2 cells and its application to tracking human hepatic cancer cells in mice. *Biotechnic & Histochemistry: Official Publication of the Biological Stain Commission*, 85(2):107–113, April 2010.
- [39] James S. Oakdale, Jianchao Ye, William L. Smith, and Juergen Biener. Post-print UV curing method for improving the mechanical properties of prototypes derived from two-photon lithography. *Optics Express*, 24(24):27077, November 2016.
- [40] Maria Ann Woodruff and Dietmar Werner Hutmacher. The return of a forgotten polymer—Polycaprolactone in the 21st century. *Progress in Polymer Science*, 35(10):1217–1256, October 2010.
- [41] Marwa Tallawi, Elisabetta Rosellini, Nicoletta Barbani, Maria Grazia Cascone, Ranjana Rai, Guillaume Saint-Pierre, and Aldo R. Boccaccini. Strategies for the chemical and biological functionalization of scaffolds for cardiac tissue engineering: a review. *Journal of The Royal Society Interface*, 12(108):20150254, July 2015.
- [42] Annemie Houben, Patrice Roose, Hugues Van den Bergen, Heidi Declercq, Jasper Van Hoorick, Peter Gruber, Aleksandr Ovsianikov, Dirk Bontinck, Sandra Van Vlierberghe, and Peter Dubruel. Flexible oligomer spacers as the key to solid-state photopolymerization of hydrogel precursors. *Materials Today Chemistry*, 4:84–89, June 2017.
- [43] J. Serbin, A. Egbert, A. Ostendorf, B. N. Chichkov, R. Houbertz, G. Domann, J. Schulz, C. Cronauer, L. Fröhlich, and M. Popall. Femtosecond laser-induced two-photon polymerization of inorganic–organic hybrid materials for applications in photonics. *Optics letters*, 28(5):301–303, 2003.
- [44] Naoto Tsutsumi, Asato Fukuda, Ryotaro Nakamura, Kenji Kinashi, and Wataru Sakai. Fabrication of three-dimensional microstructures in positive photoresist through two-photon direct laser writing. *Applied Physics A*, 123(8), August 2017.

- [45] Sascha Engelhardt, Jenny Tempeler, and Martin Wehner. The voxel onset time as an in situ method to evaluate focal position effects on two-photon-induced lithography. *Applied Physics A*, 121(2):513–519, November 2015.
- [46] Peilong Chen and Jorge Vinals. Amplitude equations and pattern selection in Faraday waves. *Physical Review E*, 60(1):559–570, July 1999. arXiv: ptt-sol/9712003.
- [47] Pu Chen, Zhengyuan Luo, Sinan Güven, Savas Tasoglu, Adarsh Venkataraman Ganesan, Andrew Weng, and Utkan Demirci. Microscale Assembly Directed by Liquid-based Template. *Advanced materials (Deerfield Beach, Fla.)*, 26(34):5936–5941, September 2014.
- [48] Ruth Schmidt-Ullrich and Ralf Paus. Molecular principles of hair follicle induction and morphogenesis. *BioEssays: News and Reviews in Molecular, Cellular and Developmental Biology*, 27(3):247–261, March 2005.
- [49] R. P. Lanza, Robert S. Langer, and Joseph Vacanti, editors. *Principles of tissue engineering*. Academic Press, an imprint of Elsevier, Amsterdam, fourth edition edition, 2014.
- [50] Giuseppe Mazza, Krista Rombouts, Andrew Rennie Hall, Luca Urbani, Tu Vinh Luong, Walid Al-Akkad, Lisa Longato, David Brown, Panagiotis Maghsoudlou, Amar P. Dhillon, Barry Fuller, Brian Davidson, Kevin Moore, Dipok Dhar, Paolo De Coppi, Massimo Malago, and Massimo Pinzani. Decellularized human liver as a natural 3d-scaffold for liver bioengineering and transplantation. *Scientific Reports*, 5(1), October 2015.
- [51] Katja Hölzl, Shengmao Lin, Liesbeth Tytgat, Sandra Van Vlierberghe, Linxia Gu, and Aleksandr Ovsianikov. Bioink properties before, during and after 3d bioprinting. *Biofabrication*, 8(3):032002, 2016.
- [52] Francesco Urciuolo, Giorgia Imparato, Alessandra Totaro, and Paolo A. Netti. Building a Tissue In Vitro from the Bottom Up: Implications in Regenerative Medicine. *Methodist DeBakey Cardiovascular Journal*, 9(4):213–217, 2013.
- [53] Vladimir Mironov, Richard P. Visconti, Vladimir Kasyanov, Gabor Forgacs, Christopher J. Drake, and Roger R. Markwald. Organ printing: tissue spheroids as building blocks. *Biomaterials*, 30(12):2164–2174, April 2009.
- [54] Karen E Kasza, Amy C Rowat, Jiayu Liu, Thomas E Angelini, Clifford P Brangwynne, Gijsje H Koenderink, and David A Weitz. The cell as a material. *Current Opinion in Cell Biology*, 19(1):101–107, February 2007.
- [55] Sangeeta Bhatia. *Microfabrication in Tissue Engineering and Bioartificial Organs*, volume 5 of *Microsystems*. Springer US, Boston, MA, 1999.
- [56] Karoly Jakab, Adrian Neagu, Vladimir Mironov, Roger R. Markwald, and Gabor Forgacs. Engineering biological structures of prescribed shape using self-assembling multicellular systems. *Proceedings of the National Academy of Sciences of the United States of America*, 101(9):2864–2869, March 2004.
- [57] Jens M. Kelm and Martin Fussenegger. Scaffold-free cell delivery for use in regenerative medicine. *Advanced Drug Delivery Reviews*, 62(7-8):753–764, June 2010.

Bibliography

- [58] Anthony P. Napolitano, Dylan M. Dean, Alan J. Man, Jacquelyn Youssef, Don N. Ho, Adam P. Rago, Matthew P. Lech, and Jeffrey R. Morgan. Scaffold-free three-dimensional cell culture utilizing micromolded nonadhesive hydrogels. *BioTechniques*, 43(4):494–500, October 2007.
- [59] Daiki Murata, Satoshi Tokunaga, Tadashi Tamura, Hiroaki Kawaguchi, Noriaki Miyoshi, Makoto Fujiki, Koichi Nakayama, and Kazuhiro Misumi. A preliminary study of osteochondral regeneration using a scaffold-free three-dimensional construct of porcine adipose tissue-derived mesenchymal stem cells. *Journal of Orthopaedic Surgery and Research*, 10, March 2015.
- [60] B. S. Schon, G. J. Hooper, and T. B. F. Woodfield. Modular Tissue Assembly Strategies for Biofabrication of Engineered Cartilage. *Annals of Biomedical Engineering*, 45(1):100–114, January 2017.
- [61] H. W. Müller, H. Wittmer, C. Wagner, J. Albers, and K. Knorr. Analytic Stability Theory for Faraday Waves and the Observation of the Harmonic Surface Response. *Physical Review Letters*, 78(12):2357–2360, March 1997.
- [62] Pu Chen, Sinan Güven, Osman Berk Usta, Martin L Yarmush, and Utkan Demirci. Biotunable acoustic node assembly of organoids. *Advanced healthcare materials*, 4(13):1937–1943, September 2015.
- [63] Toni-Marie Achilli, Julia Meyer, and Jeffrey R. Morgan. Advances in the formation, use and understanding of multi-cellular spheroids. *Expert Opinion on Biological Therapy*, 12(10):1347–1360, October 2012.
- [64] S. Pickard-Holley. The symptom experience of alopecia. *Seminars in Oncology Nursing*, 11(4):235–238, November 1995.
- [65] Alfredo Rossi, Carmen Cantisani, Luca Melis, Alessandra Iorio, Elisabetta Scali, and Stefano Calvieri. Minoxidil use in dermatology, side effects and recent patents. *Recent Patents on Inflammation & Allergy Drug Discovery*, 6(2):130–136, May 2012.
- [66] Michael S. Irwig. Depressive Symptoms and Suicidal Thoughts Among Former Users of Finasteride With Persistent Sexual Side Effects. *The Journal of Clinical Psychiatry*, 73(09):1220–1223, September 2012.
- [67] Peipei Zhang, Russell E Kling, Sudheer K Ravuri, Lauren E Kokai, J Peter Rubin, Jia-ke Chai, and Kacey G Marra. A review of adipocyte lineage cells and dermal papilla cells in hair follicle regeneration. *Journal of Tissue Engineering*, 5:204173141455685, February 2014.
- [68] Andreas Gebhardt. *Generative Fertigungsverfahren: Rapid Prototyping - Rapid Tooling - Rapid Manufacturing*. Hanser, München, 3. aufl edition, 2007. OCLC: 213391925.
- [69] ISO/ASTM 52900:2015: Additive manufacturing – General principles – Terminology (International Organization for Standardization, Geneva, Switzerland).
- [70] Rúben F. Pereira and Paulo J. Bártolo. 3d Photo-Fabrication for Tissue Engineering and Drug Delivery. *Engineering*, 1(1):090–112, March 2015.

- [71] Rachel Elizabeth Saunders and Brian Derby. Inkjet printing biomaterials for tissue engineering: bioprinting. *International Materials Reviews*, 59(8):430–448, November 2014.
- [72] Bertrand Guillotin, Agnès Souquet, Sylvain Catros, Martí Duocastella, Benjamin Pip-penger, Séverine Bellance, Reine Bareille, Murielle Rémy, Laurence Bordenave, Joëlle Amédée, and Fabien Guillemot. Laser assisted bioprinting of engineered tissue with high cell density and microscale organization. *Biomaterials*, 31(28):7250–7256, October 2010.
- [73] Johnson H. Y. Chung, Sina Naficy, Zhilian Yue, Robert Kapsa, Anita Quigley, Simon E. Moulton, and Gordon G. Wallace. Bio-ink properties and printability for extrusion printing living cells. *Biomaterials Science*, 1(7):763, 2013.
- [74] Sean V Murphy and Anthony Atala. 3d bioprinting of tissues and organs. *Nature Biotechnology*, 32(8):773–785, August 2014.
- [75] Sanna M. Peltola, Ferry P. W. Melchels, Dirk W. Grijpma, and Minna Kellomäki. A review of rapid prototyping techniques for tissue engineering purposes. *Annals of Medicine*, 40(4):268–280, January 2008.
- [76] Jos Malda, Jetze Visser, Ferry P. Melchels, Tomasz Jüngst, Wim E. Hennink, Wouter J. A. Dhert, Jürgen Groll, and Dietmar W. Hutmacher. 25th Anniversary Article: Engineering Hydrogels for Biofabrication. *Advanced Materials*, 25(36):5011–5028, September 2013.
- [77] Robert Chang, Jae Nam, and Wei Sun. Effects of Dispensing Pressure and Nozzle Diameter on Cell Survival from Solid Freeform Fabrication–Based Direct Cell Writing. *Tissue Engineering Part A*, 14(1):41–48, January 2008.
- [78] Ph. Bertrand, F. Bayle, C. Combe, P. Goeriot, and I. Smurov. Ceramic components manufacturing by selective laser sintering. *Applied Surface Science*, 254(4):989–992, December 2007.
- [79] Thomas G. Spears and Scott A. Gold. In-process sensing in selective laser melting (SLM) additive manufacturing. *Integrating Materials and Manufacturing Innovation*, 5(1), December 2016.
- [80] William E. Frazier. Metal Additive Manufacturing: A Review. *Journal of Materials Engineering and Performance*, 23(6):1917–1928, June 2014.
- [81] Charles W. Hull. Apparatus for production of three-dimensional objects by stereolithography, March 1986.
- [82] J. R. Ebdon. Introduction to polymers (second edition) R. J. Young and P. A. Lovell Chapman and Hall, London, 1991. pp. 443, price £16.95. ISBN 0-412-30640-9 (PB); ISBN 0-412-30630-1 (HB). *Polymer International*, 27(2):207–208, January 1992.
- [83] Jean-Pierre Fouassier. *Photoinitiation, photopolymerization, and photocuring: fundamentals and applications*. Hanser ; Distributed by Hanser/Gardner Publications, Munich ; New York : Cincinnati, 1995.
- [84] Shawn B. Allin. Introduction to Physical Polymer Science, 3rd Edition (Sperling, L. H.). *Journal of Chemical Education*, 78(11):1469, November 2001.

Bibliography

- [85] Wei-Er Lu, Xian-Zi Dong, Wei-Qiang Chen, Zhen-Sheng Zhao, and Xuan-Ming Duan. Novel photoinitiator with a radical quenching moiety for confining radical diffusion in two-photon induced photopolymerization. *Journal of Materials Chemistry*, 21(15):5650, 2011.
- [86] Xiangquan Wu, Qin Lian, Dichen Li, and Zhongmin Jin. Tilting separation analysis of bottom-up mask projection stereolithography based on cohesive zone model. *Journal of Materials Processing Technology*, 243:184–196, May 2017.
- [87] Hong-Bo Sun and Satoshi Kawata. Two-Photon Photopolymerization and 3d Lithographic Microfabrication. In *NMR 3D Analysis Photopolymerization*, volume 170, pages 169–273. Springer Berlin Heidelberg, Berlin, Heidelberg, 2006.
- [88] Adrian Negrean and Huibert D. Mansvelder. Optimal lens design and use in laser-scanning microscopy. *Biomedical Optics Express*, 5(5):1588–1609, May 2014.
- [89] Fu-Cheng Wang, Kuo-An Wang, Tien-Tung Chung, and Jia-Yush Yen. Fabrication of large-scale micro-structures by two-photon polymerization with a long-stroke precision stage. *Advances in Mechanical Engineering*, 9(4):168781401769575, April 2017.
- [90] Thomas Stichel. Two-photon Polymerization as Method for the Fabrication of Large Scale Biomedical Scaffold Applications. *Journal of Laser Micro/Nanoengineering*, 5(3):209–212, December 2010.
- [91] M. Malinauskas, V. Purlys, A. Žukauskas, M. Rutkauskas, P. Danilevičius, D. Paipulas, G. Bičkauskaitė, L. Bukelskis, D. Baltriukienė, R. Širmenis, A. Gaidukevičiūtė, V. Bukelskienė, R. Gadonas, V. Sirvydis, A. Piskarskas, Nikolaos Vainos, Stelios Couris, Emmanuel Paspalakis, Ioannis Koutselas, and Stavros Pissadakis. Large Scale Laser Two-Photon Polymerization Structuring for Fabrication of Artificial Polymeric Scaffolds for Regenerative Medicine. pages 12–17, Delphi, (Greece), 2010.
- [92] Kotaro Obata, Ayman El-Tamer, Lothar Koch, Ulf Hinze, and Boris N. Chichkov. High-aspect 3d two-photon polymerization structuring with widened objective working range (WOW-2pp). *Light: Science & Applications*, 2(12):e116, December 2013.
- [93] J.P Fouassier, X Allonas, and D Burget. Photopolymerization reactions under visible lights: principle, mechanisms and examples of applications. *Progress in Organic Coatings*, 47(1):16–36, July 2003.
- [94] Natalja E. Fedorovich, Marion H. Oudshoorn, Daphne van Geemen, Wim E. Hennink, Jacqueline Alblas, and Wouter J. A. Dhert. The effect of photopolymerization on stem cells embedded in hydrogels. *Biomaterials*, 30(3):344–353, January 2009.
- [95] Paola Occhetta, Roberta Visone, Laura Russo, Laura Cipolla, Matteo Moretti, and Marco Rasponi. VA-086 methacrylate gelatine photopolymerizable hydrogels: A parametric study for highly biocompatible 3d cell embedding. *Journal of Biomedical Materials Research. Part A*, 103(6):2109–2117, June 2015.

- [96] Niklas Pucher, Arnulf Rosspeintner, Valentin Satzinger, Volker Schmidt, Georg Gescheidt, Jürgen Stampfl, and Robert Liska. Structure-Activity Relationship in in D- π -A- π -D-Based Photoinitiators for the Two-Photon-Induced Photopolymerization Process. *Macromolecules*, 42(17):6519–6528, September 2009.
- [97] Zhiqian Li, Jan Torgersen, Aliasghar Ajami, Severin Mühleder, Xiaohua Qin, Wolfgang Husinsky, Wolfgang Holthöner, Aleksandr Ovsianikov, Jürgen Stampfl, and Robert Liska. Initiation efficiency and cytotoxicity of novel water-soluble two-photon photoinitiators for direct 3d microfabrication of hydrogels. *RSC Advances*, 3(36):15939–15946, August 2013.
- [98] Zhiqian Li, Niklas Pucher, Klaus Cicha, Jan Torgersen, Samuel C. Ligon, Aliasghar Ajami, Wolfgang Husinsky, Arnulf Rosspeintner, Eric Vauthey, Sergej Naumov, Tom Scherzer, Jürgen Stampfl, and Robert Liska. A Straightforward Synthesis and Structure-Activity Relationship of Highly Efficient Initiators for Two-Photon Polymerization. *Macromolecules*, 46(2):352–361, January 2013.
- [99] Maximilian Tromayer, Peter Gruber, Marica Markovic, Arnulf Rosspeintner, Eric Vauthey, Heinz Redl, Aleksandr Ovsianikov, and Robert Liska. A biocompatible macromolecular two-photon initiator based on hyaluronan. *Polymer Chemistry*, 8(2):451–460, 2017.
- [100] Zhiqian Li, Marton Siklos, Niklas Pucher, Klaus Cicha, Aliasghar Ajami, Wolfgang Husinsky, Arnulf Rosspeintner, Eric Vauthey, Georg Gescheidt, Jürgen Stampfl, and Robert Liska. Synthesis and structure-activity relationship of several aromatic ketone-based two-photon initiators. *Journal of Polymer Science Part A: Polymer Chemistry*, 49(17):3688–3699, September 2011.
- [101] Klaus Cicha, Zhiqian Li, Klaus Stadlmann, Aleksandr Ovsianikov, Ruth Markut-Kohl, Robert Liska, and Jürgen Stampfl. Evaluation of 3d structures fabricated with two-photon-photopolymerization by using FTIR spectroscopy. *Journal of Applied Physics*, 110(6):064911, September 2011.
- [102] Klaus Cicha, Thomas Koch, Jan Torgersen, Zhiqian Li, Robert Liska, and Jürgen Stampfl. Young’s modulus measurement of two-photon polymerized micro-cantilevers by using nanoindentation equipment. *Journal of Applied Physics*, 112(9):094906, November 2012.
- [103] Anne-Laure Pénard, Thierry Gacoin, and Jean-Pierre Boilot. Functionalized Sol-Gel Coatings for Optical Applications. *Accounts of Chemical Research*, 40(9):895–902, September 2007.
- [104] Aleksandr Ovsianikov, Jacques Viertl, Boris Chichkov, Mohamed Oubaha, Brian MacCraith, Ioanna Sakellari, Anastasia Giakoumaki, David Gray, Maria Vamvakaki, Maria Farsari, and Costas Fotakis. Ultra-Low Shrinkage Hybrid Photosensitive Material for Two-Photon Polymerization Microfabrication. *ACS Nano*, 2(11):2257–2262, 2008.
- [105] Justinas Mačiulaitis, Milda Deveikytė, Sima Rekštytė, Maksim Bratchikov, Adas Darinškas, Agnė Šimbelytė, Gintaras Daunoras, Aida Laurinavičienė, Arvydas Laurinavičius,

Bibliography

- Rimtautas Gudas, Mangirdas Malinauskas, and Romaldas Mačiulaitis. Preclinical study of SZ2080 material 3d microstructured scaffolds for cartilage tissue engineering made by femtosecond direct laser writing lithography. *Biofabrication*, 7(1):015015, March 2015.
- [106] Enas M. Ahmed. Hydrogel: Preparation, characterization, and applications: A review. *Journal of Advanced Research*, 6(2):105–121, March 2015.
- [107] S. Van Vlierberghe, P. Dubruel, and E. Schacht. Biopolymer-Based Hydrogels As Scaffolds for Tissue Engineering Applications: A Review. *Biomacromolecules*, 12(5):1387–1408, May 2011.
- [108] Aleksandr Ovsianikov, Andrea Deiwick, Sandra Van Vlierberghe, Peter Dubruel, Lena Möller, Gerald Dräger, and Boris Chichkov. Laser Fabrication of Three-Dimensional CAD Scaffolds from Photosensitive Gelatin for Applications in Tissue Engineering. *Biomacromolecules*, 12(4):851–858, April 2011.
- [109] Jasper Van Hoorick, Peter Gruber, Marica Markovic, Mélanie Rollot, Geert-Jan Graulus, Maxime Vagenende, Maximilian Tromayer, Jürgen Van Erps, Hugo Thienpont, José C. Martins, Stefan Baudis, Aleksandr Ovsianikov, Peter Dubruel, and Sandra Van Vlierberghe. Highly Reactive Thiol-Norbornene Photo-Click Hydrogels: Toward Improved Processability. *Macromolecular Rapid Communications*, 39(14):1800181, July 2018.
- [110] Christopher N. LaFratta and Tommaso Baldacchini. Two-Photon Polymerization Metrology: Characterization Methods of Mechanisms and Microstructures. *Micromachines*, 8(4):101, March 2017.
- [111] Z. Bayindir, Y. Sun, M. J. Naughton, C. N. LaFratta, T. Baldacchini, J. T. Fourkas, J. Stewart, B. E. A. Saleh, and M. C. Teich. Polymer microcantilevers fabricated via multiphoton absorption polymerization. *Applied Physics Letters*, 86(6):064105, February 2005.
- [112] Markus Lunzer, Liyang Shi, Orestis G. Andriotis, Peter Gruber, Marica Markovic, Philipp J. Thurner, Dmitri Ossipov, Robert Liska, and Aleksandr Ovsianikov. A Modular Approach to Sensitized Two-Photon Patterning of Photodegradable Hydrogels. *Angewandte Chemie*, 130(46):15342–15347, November 2018.
- [113] J. Bauer, S. Hengsbach, I. Tesari, R. Schwaiger, and O. Kraft. High-strength cellular ceramic composites with 3d microarchitecture. *Proceedings of the National Academy of Sciences*, 111(7):2453–2458, February 2014.
- [114] Lucas R. Meza and Julia R. Greer. Mechanical characterization of hollow ceramic nanolatitices. *Journal of Materials Science*, 49(6):2496–2508, March 2014.
- [115] Lucas R. Meza, Alex J. Zelhofer, Nigel Clarke, Arturo J. Mateos, Dennis M. Kochmann, and Julia R. Greer. Resilient 3d hierarchical architected metamaterials. *Proceedings of the National Academy of Sciences of the United States of America*, 112(37):11502–11507, September 2015.
- [116] Thomas Koch and Sabine Seidler. Mechanical properties of micro-injection moulded components. *Macromolecular Symposia*, 181(1):499–506, May 2002.

- [117] B J Briscoe, L Fiori, and E Pelillo. Nano-indentation of polymeric surfaces. *Journal of Physics D: Applied Physics*, 31(19):2395–2405, October 1998.
- [118] MA Dejun, Chung Wo Ong, LIU Jianmin, and HE Jiawen. Determination of Young's modulus by nanoindentation. *Materials Science*, page 11, 2004.
- [119] Luís Eduardo Silva Soares, Airton Abrahão Martin, and Antonio Luiz Barbosa Pinheiro. Degree of Conversion of Composite Resin: A Raman Study. *Journal of Clinical Laser Medicine & Surgery*, 21(6):357–362, December 2003.
- [120] Christian Decker and Khalil Moussa. A new method for monitoring ultra-fast photopolymerizations by real-time infra-red (RTIR) spectroscopy. *Die Makromolekulare Chemie*, 189(10):2381–2394, October 1988.
- [121] Li Jia Jiang, Yun Shen Zhou, Wei Xiong, Yang Gao, Xi Huang, Lan Jiang, Tommaso Baldacchini, Jean-Francois Silvain, and Yong Feng Lu. Two-photon polymerization: investigation of chemical and mechanical properties of resins using Raman microspectroscopy. *Optics Letters*, 39(10):3034, May 2014.
- [122] Maria Göppert-Mayer. Über Elementarakte mit zwei Quantensprüngen. *Annalen der Physik*, 401(3):273–294, 1931.
- [123] W. Kaiser and C. G. B. Garrett. Two-Photon Excitation in $\text{Ca F}_2 : \text{Eu}^{2+}$. *Physical Review Letters*, 7(6):229–231, September 1961.
- [124] Winfried Denk, James P. Strickler, and Watt W. Webb. Two-photon laser microscopy, July 1991. CIB: G01N21/64; G02B21/00; G11B7/004; G11B7/12; G11B7/135; G01N21/63; (IPC1-7): G01J3/00; G01N21/39.
- [125] W. Denk, J.H. Strickler, and W.W. Webb. Two-photon laser scanning fluorescence microscopy. *Science*, 248(4951):73–76, 1990.
- [126] Helmut J. Koester, Dagmar Baur, Rainer Uhl, and Stefan W. Hell. Ca^{2+} Fluorescence Imaging with Pico- and Femtosecond Two-Photon Excitation: Signal and Photodamage. *Biophysical Journal*, 77(4):2226–2236, October 1999.
- [127] Ingolf V. Hertel and Claus-Peter Schulz. Coherence and Photons. In *Atoms, Molecules and Optical Physics 2*, pages 71–134. Springer Berlin Heidelberg, Berlin, Heidelberg, 2015.
- [128] Bahaa E. A. Saleh. *Fundamentals of photonics*. Wiley series in pure and applied optics. Wiley Interscience, Hoboken, N.J, 2nd ed edition, 2007.
- [129] H. A. Haus. Mode-locking of lasers. *IEEE Journal of Selected Topics in Quantum Electronics*, 6(6):1173–1185, November 2000.
- [130] G. R. Huggett. Mode-locking of cw lasers by regenerative rf feedback. *Applied Physics Letters*, 13(5):186–187, September 1968.
- [131] J.D. Kafka, M.L. Watts, and J.-W.J. Pieterse. Picosecond and femtosecond pulse generation in a regeneratively mode-locked Ti:sapphire laser. *IEEE Journal of Quantum Electronics*, 28(10):2151–2162, October 1992.

Bibliography

- [132] Peter Moulton. Ti-doped sapphire: tunable solid-state laser. *Optics News*, 8(6):9–9, November 1982.
- [133] P. F. Moulton. Spectroscopic and laser characteristics of Ti:Al₂O₃. *Journal of the Optical Society of America B*, 3(1):125–133, January 1986.
- [134] Jean-Claude Diels and Wolfgang Rudolph. *Ultrashort Laser Pulse Phenomena: Fundamentals, Techniques, and Applications on a Femtosecond Time Scale*. Elsevier, September 2006. Google-Books-ID: rDQe81K0d3kC.
- [135] Joachim Fischer, Jonathan B Mueller, Johannes Kaschke, J A Wolf, Andreas-Neil Unterreiner, and Martin Wegener. Three-dimensional multi-photon direct laser writing with variable repetition rate. page 17, 2013.
- [136] Robert Szipöcs, Kárpát Ferencz, Christian Spielmann, and Ferenc Krausz. Chirped multilayer coatings for broadband dispersion control in femtosecond lasers. *Optics Letters*, 19(3):201–203, February 1994.
- [137] C. Soeller and M. B. Cannell. Construction of a two-photon microscope and optimisation of illumination pulse duration. *Pflügers Archiv*, 432(3):555–561, July 1996.
- [138] Yuzo Ishida, Tatsuo Yajima, and Akira Watanabe. A simple monitoring system for single subpicosecond laser pulses using an SH spatial autocorrelation method and a CCD image sensor. *Optics Communications*, 56(1):57–60, November 1985.
- [139] J. Janszky, G. Corradi, and R. N. Gyuzalian. On a possibility of analysing the temporal characteristics of short light pulses. *Optics Communications*, 23(3):293–298, December 1977.
- [140] Michael Bass, Eric W. Van Stryland, David R. Williams, and William L. Wolfe. *Handbook of optics*, volume 2. McGraw-Hill New York, 1995.
- [141] Bo Zhang, Josiane Zerubia, and Jean-Christophe Olivo-Marin. Gaussian approximations of fluorescence microscope point-spread function models. *Applied Optics*, 46(10):1819–1829, April 2007.
- [142] Warren R Zipfel, Rebecca M Williams, and Watt W Webb. Nonlinear magic: multiphoton microscopy in the biosciences. *Nature Biotechnology*, 21(11):1369–1377, November 2003.
- [143] B. Richards and E. Wolf. Electromagnetic diffraction in optical systems, II. Structure of the image field in an aplanatic system. *Proc. R. Soc. Lond. A*, 253(1274):358–379, December 1959.
- [144] Jesper Serbin, Aleksandr Ovsianikov, and Boris Chichkov. Fabrication of woodpile structures by two-photon polymerization and investigation of their optical properties. *Optics Express*, 12(21):5221, 2004.
- [145] Jonathan B. Mueller, Joachim Fischer, Frederik Mayer, Muamer Kadic, and Martin Wegener. Polymerization Kinetics in Three-Dimensional Direct Laser Writing. *Advanced Materials*, 26(38):6566–6571, October 2014.

- [146] Ioanna Sakellari, Elmina Kabouraki, David Gray, Vytautas Purlys, Costas Fotakis, Alexander Pikulin, Nikita Bityurin, Maria Vamvakaki, and Maria Farsari. Diffusion-Assisted High-Resolution Direct Femtosecond Laser Writing. *ACS Nano*, 6(3):2302–2311, March 2012.
- [147] Tiancheng Liu, Lisa Y. Wu, Joseph K. Choi, and Clifford E. Berkman. Targeted photodynamic therapy for prostate cancer: inducing apoptosis via activation of the caspase-8/-3 cascade pathway. *International Journal of Oncology*, 36(4):777–784, April 2010.
- [148] Sehoon Kim, Tymish Y. Ohulchanskyy, Haridas E. Pudavar, Ravindra K. Pandey, and Paras N. Prasad. Organically Modified Silica Nanoparticles Co-encapsulating Photosensitizing Drug and Aggregation-Enhanced Two-Photon Absorbing Fluorescent Dye Aggregates for Two-Photon Photodynamic Therapy. *Journal of the American Chemical Society*, 129(9):2669–2675, March 2007.
- [149] Paras N. Prasad. *Introduction to biophotonics*. Wiley-Interscience, Hoboken, NJ, 2003.
- [150] Hui Zeng, Mengxiong Sun, Chenghao Zhou, Fei Yin, Zhuoying Wang, Yingqi Hua, and Zhengdong Cai. Hematoporphyrin Monomethyl Ether-Mediated Photodynamic Therapy Selectively Kills Sarcomas by Inducing Apoptosis. *PLOS ONE*, 8(10):e77727, October 2013.
- [151] Zheng Huang. A Review of Progress in Clinical Photodynamic Therapy. *Technology in Cancer Research & Treatment*, 4(3):283–293, June 2005.
- [152] FDA Approves PMA for New Photofrin Laser. *Oncology Times*, 38(15):23, August 2016.
- [153] Shaloam Dasari and Paul Bernard Tchounwou. Cisplatin in cancer therapy: molecular mechanisms of action. *European Journal of Pharmacology*, 740:364–378, October 2014.
- [154] Durga Prasad Hari and Burkhard König. Synthetic applications of eosin Y in photoredox catalysis. *Chemical Communications*, 50(51):6688–6699, May 2014.
- [155] Maria Farsari, George Filippidis, Kyriaki Sambani, Theodore S. Drakakis, and Costas Fotakis. Two-photon polymerization of an Eosin Y-sensitized acrylate composite. *Journal of Photochemistry and Photobiology A: Chemistry*, 181(1):132–135, July 2006.
- [156] Mikhail Drobizhev, Yuriy Stepanenko, Yuliya Dzenis, Aliaksandr Karotki, Aleksander Rebane, Peter N. Taylor, and Harry L. Anderson. Understanding Strong Two-Photon Absorption in π -Conjugated Porphyrin Dimers via Double-Resonance Enhancement in a Three-Level Model. *Journal of the American Chemical Society*, 126(47):15352–15353, December 2004.
- [157] Yvette Niamien Konan, Robert Gurny, and Eric Allémann. State of the art in the delivery of photosensitizers for photodynamic therapy. *Journal of Photochemistry and Photobiology. B, Biology*, 66(2):89–106, March 2002.
- [158] Penglei Chen, Xiaoguang Ma, Pengfei Duan, and Minghua Liu. Chirality Amplification of Porphyrin Assemblies Exclusively Constructed from Achiral Porphyrin Derivatives. *ChemPhysChem*, 7(11):2419–2423, November 2006.

Bibliography

- [159] Katherine J Schafer, Joel M Hales, Mihaela Balu, Kevin D Belfield, Eric W Van Stryland, and David J Hagan. Two-photon absorption cross-sections of common photoinitiators. *Journal of Photochemistry and Photobiology A: Chemistry*, 162(2-3):497–502, March 2004.
- [160] Duxia Cao, Zhiqiang Liu, Guozhong Li, Guoqun Liu, and Guohui Zhang. Synthesis and blue-violet two-photon excited fluorescence of a new organoboron compound. *Journal of Molecular Structure*, 874(1):46–50, February 2008.
- [161] Sophie de Reguardati, Juri Pahapill, Alexander Mikhailov, Yuriy Stepanenko, and Aleksander Rebane. High-accuracy reference standards for two-photon absorption in the 680–1050 nm wavelength range. *Optics Express*, 24(8):9053, April 2016.
- [162] Mihaela Balu, Joel Hales, David J. Hagan, and Eric W. Van Stryland. White-light continuum Z-scan technique for nonlinear materials characterization. *Optics Express*, 12(16):3820–3826, August 2004.
- [163] Andrea Gnoli, Luca Razzari, and Marcofabio Righini. Z-scan measurements using high repetition rate lasers: how to manage thermal effects. *Optics Express*, 13(20):7976–7981, October 2005.
- [164] M. Sheik-Bahae, A.A. Said, T.-H. Wei, D.J. Hagan, and E.W. Van Stryland. Sensitive measurement of optical nonlinearities using a single beam. *IEEE Journal of Quantum Electronics*, 26(4):760–769, April 1990.
- [165] Eric W. Van Stryland and Mansoor Sheik-Bahae. Z-scan measurements of optical nonlinearities. *Characterization Techniques and Tabulations for Organic Nonlinear Materials*, pages 655–692, 1998.
- [166] A. Miller and D. M. Finlayson. *Laser Sources and Applications*. CRC Press, January 1997.
- [167] Aleksei Zheltikov, Anne L’Huillier, and Ferenc Krausz. Nonlinear Optics. In Frank Träger Prof, editor, *Springer Handbook of Lasers and Optics*, pages 157–248. Springer New York, 2007.
- [168] Orazio Svelto. *Principles of Lasers*. Springer Science & Business Media, March 2010.
- [169] Eric W. Van Stryland, David J. Hagan, Olga V. Przhonska, Seth R. Marder, Scott Webster, and Lazaro A. Padilha. Nonlinear Absorption Spectroscopy of Organic Dyes. *Nonlinear Opt., Quantum Opt*, 40:95–113, 2010.
- [170] Mauro Falconieri. Thermo-optical effects in Z -scan measurements using high-repetition-rate lasers. *Journal of Optics A: Pure and Applied Optics*, 1(6):662, November 1999.
- [171] R. de Nalda, R. del Coso, J. Requejo-Isidro, J. Olivares, A. Suarez-Garcia, J. Solis, and C. N. Afonso. Limits to the determination of the nonlinear refractive index by the Z-scan method. *Journal of the Optical Society of America B*, 19(2):289, February 2002.

- [172] C. Jacinto, D. N. Messias, A. A. Andrade, S. M. Lima, M. L. Baesso, and T. Catunda. Thermal lens and Z-scan measurements: Thermal and optical properties of laser glasses – A review. *Journal of Non-Crystalline Solids*, 352(32–35):3582–3597, September 2006.
- [173] Richard L. Burden and John Douglas Faires. *Numerical analysis*. Brooks/Cole, Pacific Grove, Calif, 7th ed edition, 2001. OCLC: 247970299.
- [174] Ming-Kuei Hu. Visual pattern recognition by moment invariants. *IRE Transactions on Information Theory*, 8(2):179–187, February 1962.
- [175] José Antonio Martín H., Matilde Santos, and Javier de Lope. Orthogonal variant moments features in image analysis. *Information Sciences*, 180(6):846–860, March 2010.
- [176] Switzerland International Organization for Standardization, Geneva. ISO 11146-2:2005. <https://www.iso.org/standard/33626.html>. Accessed: 2018-10-25.
- [177] A. Weiner. Effect of group velocity mismatch on the measurement of ultrashort optical pulses via second harmonic generation. *IEEE Journal of Quantum Electronics*, 19(8):1276–1283, August 1983.
- [178] A. Ovsianikov, Z. Li, A. Ajami, J. Torgersen, W. Husinsky, J. Stampfl, and R. Liska. 3d grafting via three-photon induced photolysis of aromatic azides. *Applied Physics A*, 108(1):29–34, July 2012.
- [179] Objective plan-apochromat 63x/1.40 oil dic. <https://www.micro-shop.zeiss.com/?a=v&f=o&id=420640-9900-000&l=en&m=a&p=us>. Accessed: 2010-09-30.
- [180] Objective plan-apochromat 20x/0.8 m27. <https://www.micro-shop.zeiss.com/?a=v&f=o&id=420650-9901-000&l=en&m=s&p=us>. Accessed: 2010-09-30.
- [181] Objective plan-apochromat 63x/1.40 oil dic. <https://www.micro-shop.zeiss.com/?p=us&f=o&a=v&m=s&id=440762-9904-000>. Accessed: 2010-09-30.
- [182] Ormocomp | Micro Resist Technology GmbH. <https://www.microresist.de/de/produktwelt/hybridpolymere/uv-imprint-uv-abformung/ormocomp%C2%AE>. Accessed: 2018-09-22.
- [183] Alexander K. Nguyen and Roger J. Narayan. Two-photon polymerization for biological applications. *Materials Today*, 20(6):314–322, July 2017.
- [184] Silanizing Glassware - Seed - 2000 - Current Protocols in Cell Biology - Wiley Online Library. <https://currentprotocols.onlinelibrary.wiley.com/doi/abs/10.1002/0471143030.cba03es08>. Accessed: 2018-10-25.
- [185] Jag Mohan. *Organic Spectroscopy: Principles and Applications*. CRC Press, 2004. Google-Books-ID: fA08Uy5DR0QC.
- [186] R. G. Carpenter. Principles and procedures of statistics, with special reference to the biological sciences. *The Eugenics Review*, 52(3):172–173, October 1960.
- [187] Norman Richard Draper and Harry Smith. *Applied regression analysis*. Wiley series in probability and statistics. Wiley, New York, 3rd ed edition, 1998.

Bibliography

- [188] Julian R. Jones, Olga Tsigkou, Emily E. Coates, Molly M. Stevens, Julia M. Polak, and Larry L. Hench. Extracellular matrix formation and mineralization on a phosphate-free porous bioactive glass scaffold using primary human osteoblast (HOB) cells. *Biomaterials*, 28(9):1653–1663, March 2007.
- [189] David S. Bischoff, Nalini S. Makhijani, and Dean T. Yamaguchi. Constitutive Expression of Human Telomerase Enhances the Proliferation Potential of Human Mesenchymal Stem Cells. *BioResearch Open Access*, 1(6):273–279, December 2012.
- [190] H. W. Kroto, J. R. Heath, S. C. O'Brien, R. F. Curl, and R. E. Smalley. C60: Buckminsterfullerene. *Nature*, 318(6042):162–163, November 1985.
- [191] Yagmur Turgay, Matthias Eibauer, Anne E. Goldman, Takeshi Shimi, Maayan Khayat, Kfir Ben-Harush, Anna Dubrovsky-Gaupp, K. Tanuj Sapra, Robert D. Goldman, and Ohad Medalia. The molecular architecture of lamins in somatic cells. *Nature*, 543(7644):261–264, 2017.
- [192] PHS Policy on Humane Care and Use of Laboratory Animals. <https://olaw.nih.gov/policies-laws/phs-policy.htm>. Accessed: 2018-09-25.
- [193] Anthony E. Siegman. Defining, measuring, and optimizing laser beam quality. In *Laser Resonators and Coherent Optics: Modeling, Technology, and Applications*, volume 1868, pages 2–13. International Society for Optics and Photonics, August 1993.
- [194] Aleksandr Ovsianikov, Severin Mühleder, Jan Torgersen, Zhiquan Li, Xiao-Hua Qin, Sandra Van Vlierberghe, Peter Dubruel, Wolfgang Holthöner, Heinz Redl, Robert Liska, and Jürgen Stampfl. Laser Photofabrication of Cell-Containing Hydrogel Constructs. *Langmuir*, 30(13):3787–3794, April 2014.
- [195] Marianne Labet and Wim Thielemans. Synthesis of polycaprolactone: a review. *Chemical Society Reviews*, 38(12):3484, 2009.
- [196] Dietmar W. Huttmacher, Thorsten Schantz, Iwan Zein, Kee Woei Ng, Swee Hin Teoh, and Kim Cheng Tan. Mechanical properties and cell cultural response of polycaprolactone scaffolds designed and fabricated via fused deposition modeling. *Journal of Biomedical Materials Research*, 55(2):203–216, May 2001.
- [197] Anand Doraiswamy, Aleksandr Ovsianikov, Shaun D. Gittard, Nancy A. Monteiro-Riviere, Rene Crombez, Eva Montalvo, Weidian Shen, Boris N. Chichkov, and Roger J. Narayan. Fabrication of microneedles using two photon polymerization for transdermal delivery of nanomaterials. *Journal of Nanoscience and Nanotechnology*, 10(10):6305–6312, October 2010.
- [198] Jessica M. Williams, Adebisi Adewunmi, Rachel M. Schek, Colleen L. Flanagan, Paul H. Krebsbach, Stephen E. Feinberg, Scott J. Hollister, and Suman Das. Bone tissue engineering using polycaprolactone scaffolds fabricated via selective laser sintering. *Biomaterials*, 26(23):4817–4827, August 2005.
- [199] Michael P. Stocker, Linjie Li, Rafael R. Gattass, and John T. Fourkas. Multiphoton photoresists giving nanoscale resolution that is inversely dependent on exposure time. *Nature Chemistry*, 3(3):223–227, March 2011.

- [200] Sophie Pautot, Claire Wyart, and Ehud Y. Isacoff. Colloid-guided assembly of oriented 3d neuronal networks. *Nature Methods*, 5(8):735–740, August 2008.
- [201] Ying Zheng, Xiabing Du, Wei Wang, Marylene Boucher, Satish Parimoo, and Kurt S. Stenn. Organogenesis From Dissociated Cells: Generation of Mature Cycling Hair Follicles From Skin-Derived Cells. *Journal of Investigative Dermatology*, 124(5):867–876, May 2005.
- [202] Chao-Chun Yang and George Cotsarelis. Review of hair follicle dermal cells. *Journal of Dermatological Science*, 57(1):2–11, January 2010.
- [203] Yizhong Shen, Adam J. Shuhendler, Deju Ye, Jing-Juan Xu, and Hong-Yuan Chen. Two-photon excitation nanoparticles for photodynamic therapy. *Chemical Society Reviews*, 45(24):6725–6741, December 2016.
- [204] Erin Wachter, David K. Heidary, Brock S. Howerton, Sean Parkin, and Edith C. Glazer. Light-activated ruthenium complexes photobind DNA and are cytotoxic in the photodynamic therapy window. *Chemical Communications*, 48(77):9649–9651, 2012.

Curriculum Vitae

Personal

Name: Wolfgang Steiger
Academic degree: Dipl.-Ing.
Nationality: Austria
Date of birth and place: April 15th 1989, Eisenstadt
Phone: +43 (1) 58801 - 308 48
E-Mail: wolfqang.steiger@gmx.at

Education

Sep. 2015 - PhD Candidate, Institute of Material Science and Technology (Group of Prof. A. Ovsianikov) TU Wien
Jun. 2015 - Master Thesis „Design and assembly of an open aperture z-scan setup based on high-power femtosecond oscillator" at Institute of Material Science and Technology (Group of Prof. J. Stampf) TU Wien, Graduated with distinction
Jul., 2011 Project work at Lab for Quantum Chemistry at UPS-Toulouse, France
Oct. 2008-Jun. 2015 Student at TU Wien, graduated with distinction as Dipl.-Ing. in Physics
Sep., 2007- Jun. 2008 Military Service (promoted to rank of Gefreiter)
Sep., 1999- Jun. 2007 High School (BG-Babenbergerring), graduated with distinction

Employment

Sep. 2015 - Project Assistant at the Institute of Material Science and Technology (Group of Prof. A. Ovsianikov) TU Wien
Mar., 2012 – June, 2015 Tutoring at TU-Wien (Fundamentals of Physics, Physics for Geodesics)
Jul. 2014, Jul. 2013 Location Manager at Summa Cum Laude Festival
Jan., 2008 – Jul., 2015 IT-Management at doctor's office Dr. Steiger

Languages

German (mother tongue)
English (fluent)
French (advanced)
Italian (beginner)
Latin (5 years)

Programming Skills

Languages: Python, Fortran, C, C++, C#, Matlab, Mathematica, Visual Basic, Autodesk Inventor, Netfab
Microsoft: Windows and Office
Adobe: Photoshop, Flash, Premiere, After Effects, Illustrator, Audition

Interpersonal Skills

Peer-Mediator
2 years head boy
Tutoring

■ Talks and Poster Presentations

1. *Oral Presentation:* W. Steiger, P. Gruber, M. Tromayer, M. Lunzer, A. Ajami, W. Husinsky, R. Liska, A. Ovsianikov; Fully automated z-scan setup based on a tunable fs-oscillator; DVSPM (Danube Vltava Sava Polymer Meeting), September 5th-8th 2017, Vienna
2. *Poster Presentation:* W. Steiger, P. Gruber, M. Tromayer, A. Dobos, M. Lunzer, R. Liska, and A. Ovsianikov; Fully automated z-scan setup based on a tunable fs-oscillator, AMBA (Advanced Materials for Biomedical Applications), September 27th – 29th 2017, Ghent
3. *Oral Presentation:* W. Steiger, P. Gruber, M. Tromayer, A. Dobos, M. Lunzer, R. Liska, and A. Ovsianikov; Spectral optimization of multiphoton polymerisation for tissue engineering; ViCEM (Vienna Center for Engineering in Medicine), October 10th 2017, Vienna
4. *Oral Presentation:* W. Steiger, P. Gruber, M. Tromayer, A. Dobos, M. Lunzer, R. Liska, and A. Ovsianikov; Fully automated z-scan setup based on a tunable fs-oscillator; BIOS (Biophotonics, Biomedical Optics, and Imaging Conference) at SPIE Photonics West, February 2nd – 7th 2018, San Francisco
5. *Poster Presentation:* Wolfgang Steiger, Peter Gruber, Agnes Dobos, Elise Zerobin, Robert Liska, Aleksandr Ovsianikov, Tuneable z-scan setup as a versatile tool to improve the efficiency of PDT and high resolution 3D printing; ICPEPA11 (11th International Conference on Photo-Excited Processes and Applications), September 10th – 14th 2018

■ Extracurricular activities

Jun. 2018	Performing „Carmina Burana“ as part of the choir „Wiener Singakademie“ at Wiener Konzerthaus
Mai 2018	Graphical Design for “Fabrication of placental barrier structures within a microfluidic device utilizing two-photon polymerization” in International Journal of Bioprinting, 4,2 (2018).
Mar. 2018, Feb. 2018	Performing „Disney in Concert –Frozen“ at Stadthalle, Vienna and Hallenstadion Zurich as part of the choir „Neue Wiener Stimmen“
December 2016	Editing and assembly of promotional Short „Castle on a pencil tip via nano-scale 3D-printing“
Since Nov. 2015	Chairman of „Neue Wiener Stimmen“
Since Apr. 2014	Founder, administrator and host of the first Austria based movie podcast (www.flipthetruck.com)
Mai, 2014, 2015	Performing the opening of Vienna Life Ball as part of the choir „Neue Wiener Stimmen“
Oct., 2012-2015	Performing „Hollywood in Vienna“ as part of the choir „Neue Wiener Stimmen“
Since 2012	Organizing festivals and official events for more than 100 people.
Jun., 2010	Logo Design for the Task Force against human trafficking

■ Interests

Singing (Choir Neue Wiener Stimmen, Wiener Singakademie), Dancing (Standard dance, Gold-Needle) Running (Semi-Marathon 2010, Marathon 2014), Philosophy, Literature